UNIVERSITÉ DU LUXEMBOURG

PhD-FSTM-2022-111
The Faculty of Science, Technology, and Medicine

DISSERTATION

Defence held on 16/09/2022 in Esch-sur-Alzette

to obtain the degree of

DOCTEUR DE L'UNIVERSITÉ DU LUXEMBOURG EN PHYSIQUE

by

Naveen ARUCHAMY
Born on 04 April 1991 in Coimbatore, (India)

FATIGUE AND BREAKDOWN STUDIES OF SOLUTION DEPOSITED OXIDE FERROELECTRIC THIN FILMS

Dissertation defence committee

Dr. Torsten Granzow, Dissertation supervisor
Lead R&T Associate, Luxembourg Institute of Science and Technology

Dr. Anupam Sengupta, Chairman
Professor, Université du Luxembourg

Dr. Sebatjan Glinšek, Vice Chairman
Lead R&T Associate, Luxembourg Institute of Science and Technology

Dr. Kyle Webber
Professor, Friedrich-Alexander-Universität-Nürnberg

Dr. Jurij Koruza
Assist. Professor, Technische Universität Graz

யாதும் ஊரே, யாவரும் கேளிர்..

-கணியன் பூங்குன்றனார்

(புறநானூறு: 192)

Translation:

All the world my home, all the people my kin..

-Kanian Poongundranar

(Puranan ooru: 192)

Abstract

Ferroelectric materials are ubiquitous in several applications and offer advantages for micro-electromechanical systems (MEMS) in their thin film form. However, novel applications require ferroelectric films to be deposited on various substrates, which requires effective integration and know-how of the material response when selecting a substrate for film deposition. As substrate-induced stress can alter the ferroelectric properties of the films, the knowledge of how stress changes the ferroelectric response under different actuation conditions is essential. Furthermore, the stress dependent behavior raises the question of understanding the reliability and degradation mechanisms under cyclic electric loading. Therefore, ferroelectric thin film's fatigue and breakdown characteristics become more relevant.

Lead zirconate titanate (PZT) thin films are popular among other ferroelectric materials. However, there is a tremendous effort made in the direction of finding a lead-free alternative to PZT. Ferroelectric thin films can be deposited using different processing techniques. In this work, the chemical solution deposition route is adapted for depositing PZT thin films on transparent and non-transparent substrates. A correlation between the substrate-induced ferroelectric properties and processing conditions with different electrode configurations is established. Finite element modeling is used to understand the influence of the design parameters of the co-planar interdigitated electrodes for fabricating fully transparent PZT stacks. In-plane and out-of-plane ferroelectric properties of PZT thin films in metal-insulator-metal (MIM) and interdigitated electrode (IDE) geometries, respectively, on different substrates, are compared to establish the connection between the stress-induced effect and the actuation mode. It is shown that the out-of-plane polarization is high under in-plane compressive stress but reduced by nearly four times by in-plane tensile stress. In contrast, the in-plane polarization shows an unexpectedly weak stress dependence. The fatigue behavior of differently stressed PZT thin films with IDE structures is reported for the first time in this study. The results are compared to the fatigue behavior of the same films in MIM geometry. PZT films in MIM geometry, irrespective of the stress state, show a notable

decrease of switchable polarization during fatigue cycling. In contrast, the films actuated with IDEs have much better fatigue resistance. The primary fatigue mechanism is identified as domain wall pinning by charged defects. The observed differences in fatigue behavior between MIM and IDE geometries are linked to the orientation of the electric field with respect to the columnar grain structure of the films.

Hafnium oxide, an emerging and widely researched lead-free alternative to PZT for non-volatile ferroelectric memory application, is also explored in this work. The breakdown properties of chemical solution deposited ferroelectric hafnium oxide thin films are also studied. The structure-property relationship for stabilizing the ferroelectric phase in solution deposited hafnium oxide thin films is established. Furthermore, the effect of processing conditions on the ferroelectric switching behavior and breakdown characteristics are demonstrated and correlated with the possible mechanism.

Acknowledgements

Ph.D. thesis work at the Luxembourg Institute of Science and Technology would not have been possible without all the fantastic people who were there for me. I want to take this opportunity to acknowledge all the people who have helped me in this (more than) four-year-long journey.

Dr. Torsten Granzow, I cannot thank you enough for your mentorship and generosity in the time you have given me from the day I arrived at LIST. You have been patient enough with me, giving me the time to understand the subject and get independent with the work. I am indebted to you for the time you have spent reviewing my writing, discussing scientific matters, and providing constructive criticism to help me grow. I truly appreciate the way you challenged me. You showed a great work ethic and professionalism, and I will remember that all my career. I also want to sincerely thank you for the support and compassion you showed me during times of personal difficulty outside the laboratory. Thank you for believing in me and doing everything you could to help me reach my goals. I wish I knew all the movies, TV series, and songs you quoted to understand the puns you meant.

I cannot get past this line without thanking you, Dr. Sebastjan Glinsek. It has been a true pleasure learning and working with you. You have been my second mentor during all these four years, guiding me on all the thin film deposition-related works. I started at LIST without any prior experience with thin films, and you have been kind enough to teach me many things. I also thank you for your time reviewing my manuscript. Your feedback was always very valuable.

Thank you, Dr. Emmanuel Defay, for all your efforts and guidance during my work at LIST. You have been a great group leader, managing everything to the best of your abilities. Being part of such a dynamic team is truly amazing, and I will definitely miss this.

I would also like to acknowledge the members of my thesis supervisory committee, Dr. Anupam Sengupta, Dr. Jurij Koruza, and Dr. Sebastjan Glinsek, for all of your valuable time following my work during these four years and for providing constructive feedback every time. I also wish to thank the external member of the jury, Prof. Dr. Kyle Webber, for accepting to be part of the

jury. Finally, I thank all the jury members for dedicating their time to reading and assessing my manuscript.

Thank you, Nico, for all your help and guidance during the first year of my Ph.D. You did all the precursor solutions and trained me on various equipment in the lab; I am grateful for your time and efforts. Thank you for all the beers and the fun times!! I must thank Alfredo and Longfei for later helping me with the precursor solution. Thank you, Stephanie, for all the patterning and lithography-related works and for training me later. Thank you, Veronika and Longfei, for the electrode deposition. Thanks to you, Tony, for training me on XRD and all the discussions we had later for hafnia and not-so-hafnia stuff. Thanks to Kevin and Noureddine for all your help in the clean room and off course, outside the clean room too ;) Thanks, Olivier and Pierre, for your help with the instrumentation and Python-related stuff in the lab. I have to thank all the MRT support guys who helped me with several things for my experiments. A special thanks to Hugo, Ashwath, Veronika, Uros, Juliette, and Barnik for (happily) accepting to read the chapters of my thesis and giving feedback quickly. It helped me a lot, guys!

Cosme and Mauro, saying thanks is not enough for both of you. You guys made my time in Luxembourg a memorable one. I still remember Mauro; it all started with that Hollywood party and went on and on from there... Thanks for being the bastard you are. I know how you and Cosme pushed me to move to Grund, which was one of my best decisions. Cosme... you are a great friend, flatmate, and colleague. I will fondly remember all our fun times in the flat, office, trips, shopping, parties, and the list goes on. Thanks for being there, especially during the COVID times. Things would have been way different if not for you guys! I miss your cooking, baking, and desserts. 25, Rue St Ulric, will be missed when I move out from here. Connie, you were a great flatmate and friend. Thanks for all the crazy times and parties. Du bist eine MARKE Connie! John (Johnny-boy), thanks for being a fun flatmate and friend. Thanks for introducing me to American popcorn. You and Andrea kept the fun going. Thank you, Andrea, for keeping everything sane in the house. Thank you, Shameek, for all the fun and cricket.

Thanks to Christina (Youri & Alvar - 'the drama queens'), we all had a great time in the office. Christina, you are a good friend; I will miss our coffee times and conversations. Youri, thanks for all the banters, fun times, and salsa lessons. Youri and Alvar, you guys have to record the song you guys made for me. Alfredo, we had a great time during the Korea trip; thanks for everything! Hugo and Laura, thank you for the 'atelier the cuisine' evenings you guys had with Cosme and me. We should do more. Thanks to you, Veronika, our neighbor, for organizing nice weekend gatherings. Monika, Constance, Mael, Ashwath, Barnik, Sangeetha, Diana, Carlos,

Longfei, Poorani, Uros, Jorge, Rao, Pranab, Natalya, Juliette, Georgy, Andreas, Hala, Marco, thank you all guys for being great colleagues and a team. Finally, to all the other people I have not mentioned here but helped in different ways, Thank you!

Dharini, you are a dear friend to me. Thanks for being there; words will not suffice to thank you. Thank you, Sabari, for being there as a support; it means a lot. Udhayan, Raghav, Ram, Subbu, and Loki, all these years would not have been fun and possible without you guys. The time we spent in Grenoble, Lyon, and all the trips will be a memorable one forever. Thanks a tonne! A special thanks to Ahilan, Divya, and Karthick for being there as my Tamil family in Luxembourg.

Last but not least! I thank my family with all my heart. This would not have been possible without their love, support and sacrifice. Thank you, Amma, Appa, and Kala chitti, for everything! Selva appa, I know you will be proud. Thank you, Akka, machan, and all my cousins and relatives who were there for me. Even though my field of study and work is far removed from the concerns of my upbringing, I would not be where I am today without you and your help!

The Luxembourgish National Research Fund (FNR) is acknowledged for funding.
This manuscript is based on work supported by FNR under the project PRIDE-MASSENA (FNR PRIDE / 15 / 10935404).

Index

Introduction

Ferroelectric thin films have found their application in microelectromechanical systems (MEMS). They have revolutionized the consumer product market due to the ease of their use in the integrated circuit and compatibility in complementary metal-oxide semiconductor (CMOS) technology [1, 2]. $PbZr_xTi_{(1-x)}O_3$ (PZT) is one of the important ferroelectric materials fabricated in thin film form and is used for several applications like ferroelectric field effect transistors, non-volatile memory devices, sensors, print heads, accelerometers, etc. [3]. The thin film compositions close to the morphotropic phase boundary ($x = 0.53$, MPB) exhibit superior ferroelectric and piezoelectric properties over a wide range of operating temperatures [4]. Recent interests in tunable optics for X-ray telescopes [5, 6], interactive touch panels [7], radio frequency (RF) MEMS switches [8], etc. have led research groups to explore the possibility of depositing PZT thin films on transparent substrates with and without bottom electrode.

PZT thin films are deposited by the chemical solution deposition (CSD) technique. CSD is a versatile technique that can be easily modified or adapted for different material and composition ranges. It also offers an economic advantage over the other thin film deposition techniques. The chemistry and microstructure of the films on various substrates can be well controlled with CSD. However, one aspect that invariably changes with different substrates is the residual mechanical stress induced in the film. For the solution deposited thin films, the residual stress stems mainly from the differences in the thermal expansion coefficient of the substrate and the thin film. With the cross-functionality and the ability to be integrated with various other materials, the interplay between the properties of ferroelectric thin film and the substrate has to be considered an important aspect. The effect of the substrate's mechanical and thermal properties can impact the ferroelectric thin film's electrical or other functional properties. Substrate-induced stress can affect the way in which the domains are formed or oriented in the film and can eventually affect the polarization dynamics of the material. In this scenario, understating the reliability aspect like fatigue behavior and breakdown characteristics of the material becomes more important.

By utilizing the substrate-induced material properties and carefully selecting the electrode geometries, one can explore various combinations of functional properties for a specific application. PZT thin films are fabricated with metal-insulator-metal (MIM) and interdigitated electrode (IDE) configurations to probe the out-of-plane and in-plane ferroelectric properties, respectively. Finite element analysis is performed to understand the influence of IDE geometry on the electric field distribution in the ferroelectric layer. The impact of substrate-induced stress on the out-of-plane and in-plane properties is experimentally demonstrated. The film's possible domain orientation is deduced from the stress state and the ferroelectric behavior. A phenomenological model is put forth explaining the observed differences between the in-plane and out-of-plane properties of differently stressed PZT thin film. Bipolar fatigue cycling experiments are performed for all the films on various substrates with different electrode geometries. The long-term cycling behavior of PZT thin films is shown to improve with the specific combination of microstructure, stress state, and electrode design. The impact on domain switching and the role of defects in domain pinning during bipolar fatigue cycling is elucidated.

Hafnium oxide (HfO_2) thin films got the attention of the ferroelectric research community after the recent discovery of voltage-dependent capacitance enhancement in Si-doped HfO_2 thin films [9]. This enhancement in capacitance was linked to a metastable orthorhombic phase of hafnium oxide. From then on, numerous research works have been carried out to understand:

- the root cause for ferroelectricity linked to the structural properties,
- deposition methodologies and processing conditions to stabilize the ferroelectric phase in hafnium oxide, and
- their field cycling behavior to illustrate the reliability issues

A small part of this work also deals with understanding the structure and property relationship of solution deposited La-doped HfO_2 thin films. In addition, the impact of processing conditions on stabilizing the ferroelectric phase in hafnium oxide thin films and their breakdown characteristics are addressed.

This manuscript consists of six chapters and is structured as follows:

In **Chapter 1**, the fundamentals of ferroelectricity with an emphasis on PZT are presented. The domain structure, types, and switching landscapes are discussed. The properties of PZT thin film and the influence of stress on the domain orientation and switching are discussed in

detail. A literature review on stabilizing the ferroelectric phase in HfO_2 thin films is discussed. Different possible thin film deposition techniques are outlined, and the chemical solution deposition technique is discussed in detail. PZT and HfO_2 thin films and the influence of various processing parameters on their structural and functional properties are outlined. Finally, the reliability aspects like fatigue and breakdown properties of PZT and HfO_2 thin films and the governing mechanism behind these issues are summarised. An example of a ferroelectric field effect transistor is used to discuss the application of ferroelectric thin films for non-volatile memories, and the challenges regarding their reliability issues are outlined.

In **Chapter 2**, the thin film deposition methodologies and the structural and ferroelectric characterization techniques used in this work are explained in detail. In particular, the characterization methodology relevant for residual stress quantification, fatigue, and breakdown studies is also discussed.

In **Chapter 3**, the influence of processing parameters on the structure-property relationship of PZT thin film deposited on different substrates is illustrated. The experiments demonstrating the impact of pyrolysis and annealing temperature on the microstructural evolution are shown. In addition, the effect of seed layer solvents and buffer layer on thin film texture and the resulting ferroelectric properties are outlined for the stacks in MIM and IDE configuration, i.e., with and without bottom electrodes, respectively. From the results of these experiments, thin film samples with good ferroelectric properties were chosen for fatigue cycling experiments and further characterizations.

In **Chapter 4**, finite element analysis using COMSOL models is used to understand the electric field distribution in the ferroelectric material with the IDEs. Bulk PZT slabs with the IDEs are modeled initially to establish a base study for an unconstrained system. Later the design conditions of the IDE electrodes are adapted to the thin film stack deposited on various substrates. The limitations of the approximations and the design conditions are discussed with respect to each system.

In **Chapter 5**, the influence of stress state on the domain configuration in PZT thin film deposited on different substrates is summarised. The difference in ferroelectric behavior between the MIM and IDE systems is elaborated, and a model is presented to describe the behavior of each thin film system governed by the stress state and respective electrode configuration. The results of fatigue cycling experiments are presented, and the degradation of ferroelectric properties during bipolar fatigue cycling is elaborated. The impact of bipolar cycling on domain wall motions is postulated with respect to the mechanism of domain pinning by charged defects.

The fatigue-resistant behavior of PZT thin films with IDEs is showcased, and possible mechanisms are proposed.

In **Chapter 6**, the ferroelectric behavior of solution deposited La-doped HfO_2 thin film is shown. The effect of annealing temperature and atmosphere on stabilizing the ferroelectric phase in HfO_2 thin film is demonstrated. The breakdown characteristics of the HfO_2 thin films deposited following different routes are discussed in relation to the processing conditions.

To conclude, all the key results are summarised, and an outlook with a scope for future work is presented.

Chapter 1

Background

This chapter provides an overview of the literature that laid the foundation for the work done in this thesis. The fundamentals of ferroelectricity relating to perovskite structured materials with an emphasis on Pb(Zr,Ti)O_3 (PZT) and the importance of the morphotropic phase boundary (MPB) compositions are presented. The domain structure of PZT and different types of domain walls are introduced. Domain switching landscapes and possible domain reversal processes contributing to polarization are also discussed. The fundamentals of the chemical solution deposition technique for growing PZT and ferroelectric HfO_2 (Hafnium oxide, will be referred to as hafnia) thin films are discussed, and the influence of processing conditions on the ferroelectric properties is outlined. The reliability aspects of ferroelectric thin films focusing on fatigue and breakdown are discussed with their corresponding mechanisms. The current state of the art of fatigue of sol-gel deposited PZT thin film is presented. The wake-up and breakdown characteristics exhibited by hafnia thin films are also discussed. To conclude the chapter, an application interest relevant to this work is presented and discussed with the relevance to the reliability criteria.

1.1 Piezoelectricity, Pyroelectricity and Ferroelectricity

The discovery of the piezoelectric effect in 1880 was based on the experiments conducted on Quartz crystals and Rochelle salt by Pierre and Jacques Curie. They observed the development of electric potential at each end of these crystals (in other words, the material can be polarized) when they were subjected to compression and decompression. This effect was later termed as direct piezoelectric effect [10]. The inverse of this effect was also proved a year later when the material deformation was demonstrated upon application of an electric potential across the opposite faces of the crystal, the converse-piezoelectric effect. The linear relationship between stress and the electric potential (voltage) can be conceived by the notions given below for the direct (equation 1.1) and converse-piezoelectric (equation 1.2) effects where the proportionality constant is called the piezoelectric charge coefficient. Here, P_i is the electric polarization, σ_{jk} is the stress applied on the piezoelectric material and d_{ijk} is the direct piezoelectric coefficient given by the units $(C\,N^{-1})$. In the case of the converse effect, E_k is the electric field applied to the material, and x_{ij} is the strain developed on the piezoelectric material, where d_{kij} is the converse-piezoelectric coefficient given by the units $(m\,V^{-1})$. It can also be written as d^t_{ijk} where t denotes the transposed matrix as the piezoelectric coefficients are third-rank tensors. Due to the thermodynamic consideration, the direct and inverse piezoelectric effects are identical and can be expressed by the same coefficient [11, 12]. In the application context, the direct piezoelectric effect is used in the case of sensors and energy harvesters, where the mechanical energy is converted to electrical energy, and the converse effect is used in actuators.

$$\mathrm{P_i} = \mathrm{d_{ijk}}\sigma_{\mathrm{jk}} \tag{1.1}$$

$$\mathrm{x_{ij}} = \mathrm{d_{kij}E_k} = \mathrm{d^t_{ijk}E_k} \tag{1.2}$$

Although, care should be taken not to confuse piezoelectric materials with electrostrictive materials, which can also convert electrical energy to mechanical energy. The difference is that strain in electrostrictive material is proportional to the square of the electric field but not vice-versa. Whereas the piezoelectric coefficient (d) can be positive or negative and is commonly referred to according to the direction, it is measured with respect to the direction of the applied stress, either parallel (longitudinal coefficient) or perpendicular (transverse coefficient). For a material to exhibit piezoelectricity, it must be non-centrosymmetric, i.e., the material should not

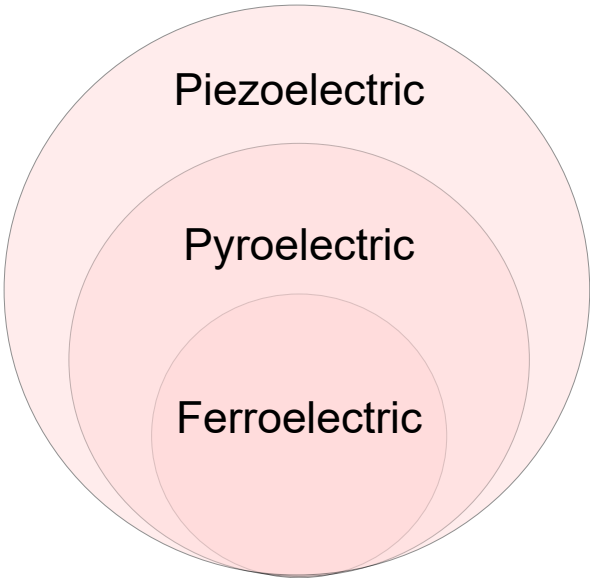

Figure 1.1: Classification and sub-classes of piezoelectric materials.

have an inversion center in its crystalline structure. Out of the 32 crystallographic point groups, 21 point groups lack an inversion center. An exception to this is the point group 432, which is non-centrosymmetric. It does not exhibit piezoelectricity because the movement of charges due to the applied mechanical stress does not induce the appearance of dipole [13]. Therefore, only 20 point groups that are non-centrosymmetric belong to the class of piezoelectric material [14].

Some point groups with low symmetry do not need an external field to produce electric polarization; they exhibit a unique polar axis and are called polar point groups. The materials with polar point groups exhibit spontaneous polarization even in the absence of any external field. Among the 20 point groups that belong to the piezoelectric class, 10 of the polar point group exhibit pyroelectricity, where the spontaneous polarization be changed with the temperature. Pyroelectricity can be written as shown in the equation 1.3, where ΔP_i is the change in polarization and ΔT is the variation in temperature with p_i being the pyroelectric coefficient. The converse pyroelectric effect also exists and is known as the electrocaloric effect.

$$\Delta \mathrm{P_i} = \mathrm{p_i} \Delta \mathrm{T} \tag{1.3}$$

A sub-group of pyroelectric materials exists in which the direction of spontaneous polarization can be changed by applying an external electric field, known as ferroelectric materials. Therefore, all ferroelectric materials belong to the pyroelectric group, but it is not the other way around, as an extremely large electric field is sometimes required to change the spontaneous polarization direction, which can be higher than the dielectric breakdown strength of the material.

According to Poisson's equation, the dielectric displacement (D) is given by the flux density originating due to free charges in the material. Polarization is based on the polarizability ($P = \varepsilon_0 \chi E$, χ is the susceptibility and ε_0 is the vacuum contribution to permittivity) of the material due to the bound charges by dipoles. Therefore, the total charges in the material should be equal to the summation of free charges and the charges bound to the dipole ($\rho_{total} = \rho_{free} + \rho_{bound}$). The bound and free charges in the material are equal and they cancel each other. A phenomenological description of ferroelectricity can be given by using Maxwell equations shown below. For a dielectric material, as in our case, the dielectric displacement can be written as a linear relationship between the electric field and the polarization, as shown in equation 1.5.

$$\begin{aligned} \nabla \cdot \mathrm{D} &= \rho_{\mathrm{free}} \\ \nabla \cdot \mathrm{P} &= -\rho_{\mathrm{bound}} \\ \nabla \cdot \mathrm{E} &= \frac{\rho_{\mathrm{total}} - \nabla \cdot \mathrm{P}}{\varepsilon_0 \varepsilon} \end{aligned} \tag{1.4}$$

$$\mathrm{D} = \varepsilon_0 \varepsilon_{\mathrm{r}} \mathrm{E} + \mathrm{P} \tag{1.5}$$

1.1.1 Ferroelectricity

Ferroelectric materials are broadly classified based on the transition from a high-temperature paraelectric phase to a low-temperature ferroelectric phase. They are either order-disorder or displacive transitions. The order-disorder transition is mostly seen in the materials with hydrogen bonds in which the motion of the protons is related to the ferroelectric properties, and the typical examples of such materials are Rochelle salt ($KNaC_4H_4O_6{\cdot}4H_2O$) and Potassium dihydrogenphosphate or KDP (KH_2PO_4). Among the materials that exhibit displacive transition are the materials with perovskite structure, ex. $BaTiO_3$ [15]. However, many ferroelectric materials exhibit both displacive as well as order-disorder types of transitions [16, 17]. Perovskite materials have a general chemical formula ABO_3 following its prototypical mineral structure $CaTiO_3$, where A and B are the metal cations with different ionic radii ($r_A > r_B$). A large number of cations can be used to form a perovskite structure. According to the geometric consideration of the 'hard sphere model' put forth by Goldschmidt [18], the ionic radii r_A, r_B and r_O should obey the following condition:

$$t = \frac{r_A + r_B}{\sqrt{2}(r_B + r_O)} = 1 \tag{1.6}$$

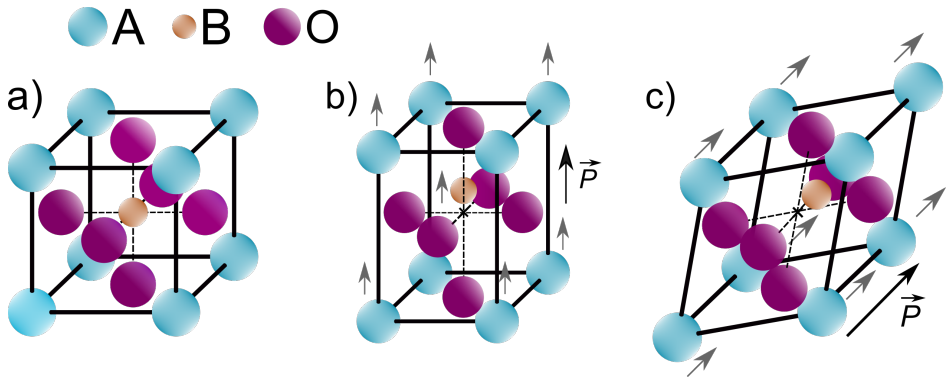

Figure 1.2: Schematics of the (a) Cubic perovskite unit cell, distorted cubic structure resulting in (b) tetragonal and rhombohedral unit cells. The arrows inside the unit cells of (b) and (c) indicates one of the possible displacement of the A and B-site cation from the initial position resulting in net polarization as represented in the figure, in reality all the ions are displaced against each other.

Here, t is the tolerance factor, and a perovskite structure is stable when the value of t is between 0.8 and 1.1. The perovskite structure can be described with a cubic unit cell shown in Figure 1.2 a) where the corners of the cube are occupied by the A cation, and the oxygen (O^{2-}) anions form an octahedral cage occupying the six corners located at the face centers of the cube with B cation at the body center. The cubic perovskite structure is a high-temperature phase that does not exhibit ferroelectricity, but below the transition temperature (Curie temperature T_c), the cubic symmetry is broken, resulting in a distorted unit cell with tetragonal or rhombohedral structure as shown in Figure 1.2 b & c. These distortions result in the displacement of B-site cations relative to the oxygen octahedra creating a permanent dipole moment in the unit cell, resulting in the appearance of spontaneous polarization in the material. For a tetragonal unit cell, there are 6 equivalent directions in which the polarization can be oriented. A rhombohedral unit cell has 8 equivalent polarization directions, and an orthorhombic unit cell has 12 equivalent polarization directions.

The temperature at which ferroelectric materials undergo a phase transformation from a non-polar paraelectric phase to a polar ferroelectric phase is called the Curie temperature (T_C). The dielectric constant above this temperature follows the Curie-Weiss behavior as shown in the equation 1.7, where χ is the dielectric susceptibility and (ε_r) is the relative dielectric permittivity, C is the Curie-Weiss constant, T is the temperature, and T_0 is the Curie-Weiss temperature. The temperature T_0 is the constant obtained by extrapolation, while the Curie temperature (T_C) is the actual temperature where the structural changes happen. Usually, T_0 is not different from

T_C for a material that undergoes a second-order phase transition. In contrast, the material that undergoes a first-order transition T_0 will differ from that of T_C.

$$\chi = (\varepsilon_r - 1) = \frac{C}{T - T_0} \tag{1.7}$$

The material property near the paraelectric-ferroelectric transition region is phenomenologically derived from Landau-Ginzburg-Devonshire formalism. Here the free energy term (F) can be written as a Taylor series expansion of an order parameter. In our case, polarization (P) is considered, which evolves according to the symmetry change from a high-temperature paraelectric phase to a low-temperature ferroelectric phase. The free energy of a ferroelectric system can be written as the following. The odd power terms are not included in the equation as they tend to be zero due to symmetry reasons.

$$F = \frac{\alpha}{2}P^2 + \frac{\beta}{4}P^4 + \frac{\beta}{6}P^6... \tag{1.8}$$

Here, α, β, and γ are the Landau–Devonshire coefficients in the Taylor expansion series. Around the transition temperature, α, associated with the P^2 term, varies linearly with the temperature (i.e., $\alpha = \alpha_0(T - T_0)$). It is important to note that below T_c, the ordered states $+P$ and $-P$ are the same in energy leading to all the odd power terms in the series being zero by symmetry. The sign of β represents the order of the phase transition: $+\beta$ indicates a second order transition where the order parameter (P) evolves continuously below Curie temperature, and $-\beta$ indicates the first order phase transition where there is an abrupt change in the order parameter below T_c [19].

1.2 Domains and domain walls

Spontaneous polarization is developed for ferroelectric materials when the material is cooled down from T_c. This spontaneous polarization in the material will give rise to bound charges on the surface. Due to the surface charges, an electric field in the direction opposite to the spontaneous polarization is produced, called the depolarizing field. Mechanical constraints are imposed on the material due to thermal stress or clamping in the case of thin films during phase transition. To minimize the electrostatic energy associated with the depolarizing field and the elastic energy associated with the stress and clamping, the material breaks down into finite volumes of identical polarization orientation called 'domains.' The boundaries separating these domains are called

domain walls. There is also energy associated with the formation of domain walls. The domain wall energy also has contributions like crystal energy due to polarization in the domain walls. The spontaneous polarization can also contribute to the spontaneous deformation of crystallites due to a change in polarization direction in the domain wall. The elastic energy associated with it also adds to the total energy density. Due to the piezoelectric coupling, there is also electromechanical energy from the mechanical deformations and the electric polarization. All these energies affect domain walls in different ways.

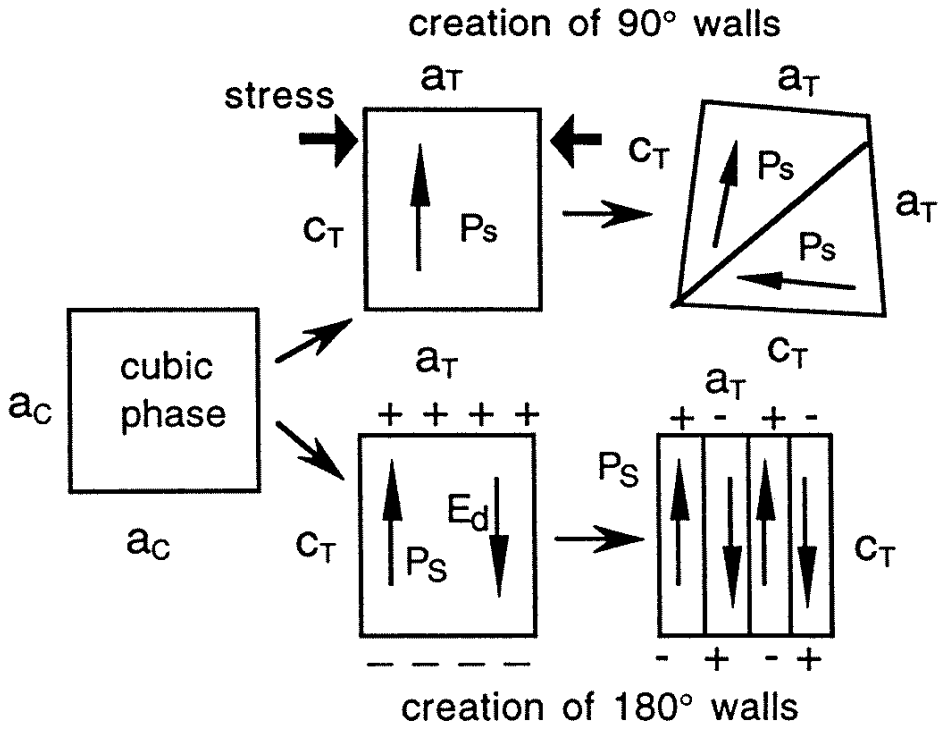

Figure 1.3: Schematic illustrating the formation of different domain walls in a tetragonal perovskite, where a_C represents the sides of the cubic unit cell, c_T and a_T represents the c and a-axis of the tetragonal unit cell, respectively. P_s is the spontaneous polarization and E_d is the depolarizing field [12].

The domains formed due to compensating the electrostatic energy from the depolarizing field will have anti-parallel orientation. The domain walls separating anti-parallel domain orientation are typically 180° domain walls. 90° domain walls are also formed to compensate for both electrostatic and elastic energy [14, 20]. The mechanical strain will not result in anti-parallel domains because positive or negative strain direction denotes either elongation or compression of the crystal axes. However, 90° domain walls are restricted only to the tetragonal system due to the crystallographic angle. For a rhombohedral system, it can form 109° or 71° along with the 180° domain walls that are always possible. Therefore, the 180° domain walls are ferroelectrically active, and the non-180° domain walls are both ferroelectrically and ferroelastically active. For

example, $PbTiO_3$, which is a pure tetragonal system, can develop polarization along six equivalent pseudo-cubic (100) directions. In this case, the domains can be anti-parallel or perpendicular to each other forming 180° or 90° domain walls, respectively. The combination of electrostatic and elastic energy often results in a complex domain structure with mixed 90° and 180° domain walls. A simplified view of different domains and domain wall formation is illustrated in Figure 1.3. Most ferroelectrics will have no net polarization upon cooling due to different polarization orientations in each domain, which cancel each other.

1.2.1 Types of domain walls

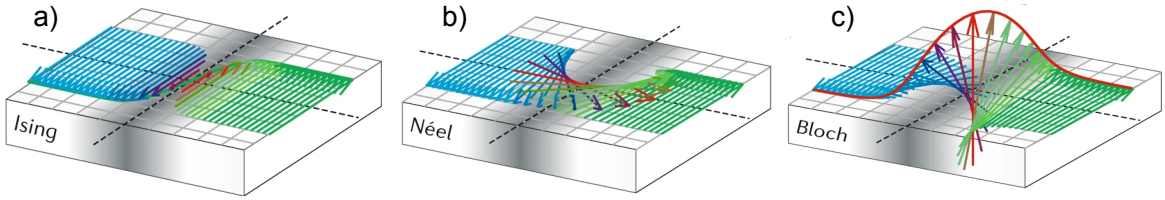

Figure 1.4: Schematic of different types domain walls in a ferroelectric system: a) Ising-type, b) Néel-type and c) Bloch-type. Reused from [21].

Different types of domain walls are present in a ferroelectric system, and the schematics of different possible domain wall types are shown in Figure 1.4. Domains and domain wall formation depend on material properties like crystallite size, shape, orientation, and domain wall formation energy. The size of the ferroelectric domain walls is typically in the order of a few unit cells. The domain walls are regions where the order parameters change their orientation, and based on this signature change, domain walls can be classified into the following three types [22, 23]. First, one is the Ising-type domain walls where the order parameter (in this case polarization) decreases in magnitude through the wall thickness and changes sign across the wall. Néel-type and Bloch-type domain walls where the polarization does not change in magnitude but rotates in the plane and perpendicular to the plane of the domain wall, respectively. Ising-type walls are assumed to be prevalent in ferroelectric materials with 180° domains, but recent studies have pointed out that non-Ising types of walls are also possible in different ferroelectric materials, including PZT [24–27].

1.2.2 Polarization reversal and domain switching

Domain switching can happen in a single step or through multiple consecutive steps, an important characteristic of ferroelectric material. When an electric field is applied to a polycrystalline

sample, the randomly oriented domains can be re-reoriented in the direction of the electric field (a-b), which can be seen in Figure 1.5. At higher fields, the domains with a polarization direction parallel to the applied field become stable. Ideally, the resultant ferroelectric will contain one domain aligned with the electric field direction, as depicted schematically in Figure 1.5. Upon removal of the field (b-c), the material retains its polarization resulting in a remanent polarization (P_r) state. The value of P_r may not equal the maximum polarization achieved with the field due to back switching caused by local strains and electric field [12]. When the electric field is further decreased (c-d), the domains start to nucleate and grow in the opposite direction. The electric field where the polarization passes through zero is the coercive field ($+E_c$ or -E_c). The reversal of polarization direction happens around the coercive field region shown in Figure 1.5 (c-d) & (e-a). When the electric field is increased, the domains continue to grow further in the field direction and saturate at the maximum field value, with all the domains again aligning in the applied field direction. It is understood that two stable orientational states are possible for a ferroelectric material, and it can be reoriented by the electric field. A similar notion can also be defined for a ferroelastic material. A material is ferroelastic if it has two or more stable orientational states in the absence of mechanical stress or electric field and if it can be reproducibly transformed from one to another of these states by the application of mechanical stress [28].

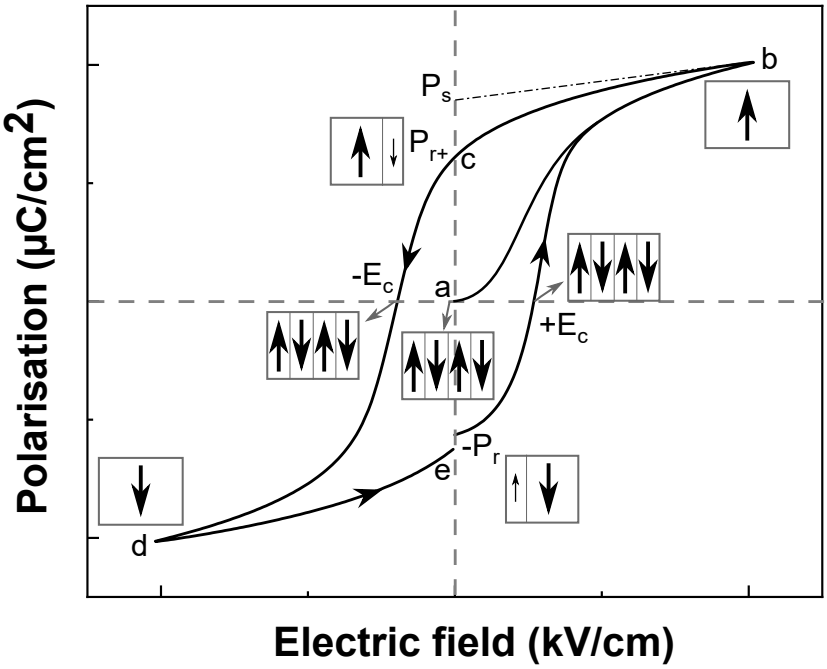

Figure 1.5: Example of a polarization-electric field (P-E) hysteresis loop of macroscopic polarization showing the remanent polarization ($+P_r$ and -P_r), and the coercive fields ($+E_c$ and -E_c). The domain structure of an aligned crystal at various points (a)-(e) on the hysteresis loop are also marked in the figure.

The polarization reversal is, however, more complex than the explanation given above, and it happens in multiple steps, as depicted in Figure 1.6. Domain nuclei are either single local dipoles or ensembles of dipoles that start to appear due to thermal fluctuations in the direction opposite to the macroscopic polarization. These domain nuclei are not stable in the region of oppositely polarized surroundings, and they disappear quickly. When a field of sufficient magnitude is applied opposite to the surrounding polarization direction, the domain nuclei start to grow. Nucleation of new domains is favored at the interface between the electrode and the sample or the defect sites. At very low fields, the polarization is proportional to the applied field. As the field is increased further, the nuclei start to grow forward through the thickness of the sample. The domain nuclei favor a needle shape because of the energetic reason to reduce the depolarizing field. Once the growing needle reaches the opposite side of the sample, the domains start to expand sideways. With the continued increase of the field, the domains expanding sideways encounters a neighboring domain and start to coalesce and grow bigger, resulting in domains with polarization parallel to the field direction. The polarization reversal is nucleation or wall movement limited as these two processes are slower compared to the forward motion of domain walls and coalescence of domains. [21, 22, 29]. The model of domain nucleation and growth are shown in Figure 1.6 is simple for a 180° reversal process, but in reality, there are non-180° domains with the complex switching process. For example, it was identified that 180° switching happens by two consecutive 90° steps than by a single 180° step based on the results from time-resolved X-ray diffraction experiments. Two different time constants were reported reflecting a sequence of domain reorientation steps [30].

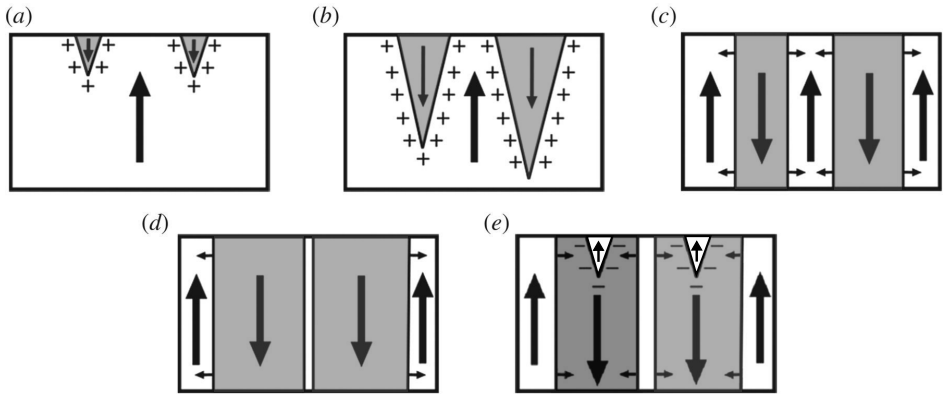

Figure 1.6: Sequence of polarization reversal process (light and dark regions shows the regions of opposite polarization). a) nucleation of new domains, b) forward motion of domain walls, c) side ward expansion of domains, d) coalescence of domains, and e) spontaneous back-switching. Adapted from [29].

1.2.3 Rayleigh studies

As explained above, polarization reversal depends on the amplitude of the electric field; at low fields, the polarization is nucleation limited. When the field is high enough, stable nuclei can appear, and the polarization reversal becomes domain wall movement limited. It takes time for the domain wall to move through the system, and it depends on the magnitude of the applied field. Based on this, the material response to the small and large applied fields should be distinguished and referred to as small-signal and large-signal parameters, respectively. Large-signal parameter mostly depends on the reorientation and growth of domains.

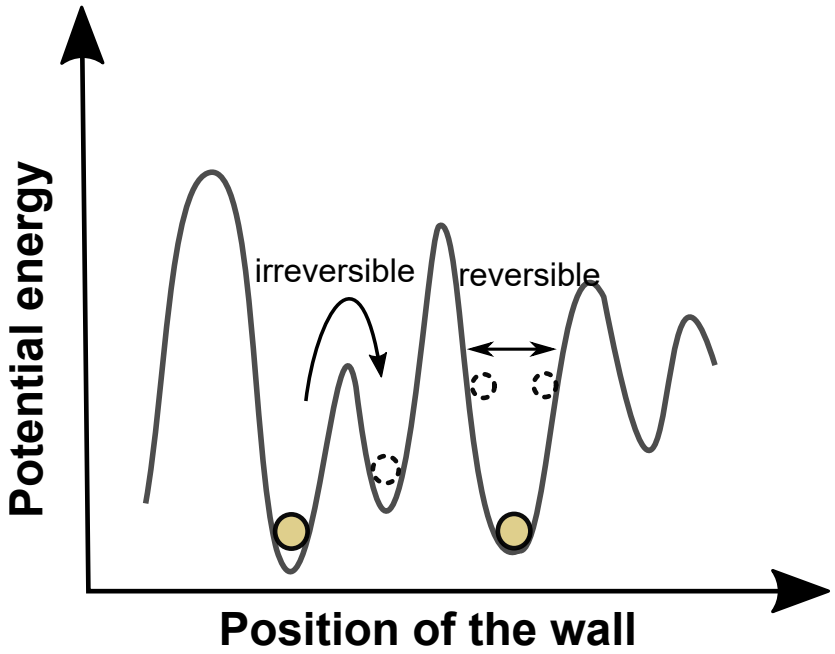

Figure 1.7: Depiction of energy landscape for a domain wall with randomly distributed pinning centres. Adapted from [12].

Small-signal parameters are measured by applying a smaller field that is large enough to cause local changes in the domain structure but does not cause any reorientation. The small-signal response encompasses both intrinsic and extrinsic contributions [31–33]. Intrinsic contributions are due to the deformation of crystal lattice under the applied field. Extrinsic contributions stem from the translation and vibration of domain walls, movement of defects, and field-induced phase changes. Intrinsic contributions are almost always reversible, but extrinsic contributions contain both the reversible and irreversible parts of the polarization changes. At smaller oscillating fields, the domain walls move within their potential well contributing to the reversible part of the polarization as depicted in Figure 1.7. When the field applied is large enough, the domain walls move to the next potential well and will not return to their original position when the field

is removed. This movement of the domain wall from one potential to the other contributes to the irreversible part of the small signal response. Large-signal response relates to polarization hysteresis to the external field. Small-signal behavior relates to the dielectric permittivity response or piezoelectric coefficient response to a small ac-signal [34, 35].

The non-linear dielectric response of a ferroelectric at sub-switching conditions (small ac signal) is often described by first approximation, in terms of the Rayleigh relations [36]. The equation 1.9 indicates the Rayleigh behavior for ferroelectric materials.

$$\varepsilon = \begin{cases} \varepsilon_{init} & forE < E_t \\ \varepsilon_{init} + \alpha(E_0 - E_t) & forE \geq E_t \end{cases} \tag{1.9}$$

Here $\varepsilon_{\mathrm{init}}$ is the permittivity due to intrinsic contributions from lattice distortions and reversible domain wall motion. α represents the Rayleigh coefficient that results from irreversible domain wall motion/displacement, E_0 is the field amplitude at which ε_{33} is measured, and E_{t} is the threshold field amplitude. Rayleigh law paints a picture of the energy landscape (shown in Figure 1.7) within which the domain walls move. These energy landscapes are determined by the defects and the pinning centers in the material. Therefore it is also clear from the equation 1.9 that a threshold field (E_{t}) is required to move the domain walls from its original energy well. Below E_{t} the small signal parameter is constant, and above E_{t} the system is in the 'Rayleigh region' where the small-signal parameters vary linearly with the field. When the field is further increased beyond the coercive field, the system is in the 'high-field region' where long-range domain wall motions are possible and are referred to as large-signal parameters when they vary super-linear with the applied field [32, 37].

1.3 Processing of ferroelectric thin films

1.3.1 Physical methods

Physical and chemical methods can be used to produce ferroelectric thin films. In the physical method, a thin film is formed from the vapor phase of the oxide or metallic species condensing onto the substrate. The targets of metallic or oxide systems are used to create the vapor phase, and the method of forming the vapor depends on the particular technique. For example, the physical vapor deposition (PVD) method includes pulsed laser deposition (PLD) and sputtering techniques.

1.3.2 Pulsed laser deposition

The PLD technique involves using a high-power laser to vaporize the target material under a vacuum creating a plasma plume. A thin film is formed on the heated substrate from the plasma. It requires careful control of processing parameters like laser power, substrate temperature, purity of the target, etc., to maintain the stoichiometry of the resulting thin films. PLD was used to grow doped, and undoped epitaxial PZT thin films on platinized silicon substrates [38, 39]. This technique allows for producing high-quality thin films for research purposes, but scaling it up to the industrial scale is rather challenging [40].

1.3.3 Sputtering

In the sputtering technique, the vapor phase is formed by bombarding the target with an ion produced by ionizing the inert gas in the deposition chamber. Different power sources are used to create plasma between the target and the substrate. The type of power source used determines the sputtering process, which includes DC diode sputtering, radio frequency (RF) sputtering, and magnetron sputtering. Various substrates can be used for depositing high-quality thin films by sputtering technique [5, 41, 42], and a higher growth rate [43] is also reported in some cases.

Although PVD techniques can produce high-quality thin films, they all need vacuum conditions, high-quality targets, and expensive equipment to have control over process quality. The cost associated with it is not attractive for industrial purposes.

1.3.4 Chemical methods

Chemical methods, on the other hand involves the use of metallic precursor in their molecular form. The metallic precursors are deposited onto the substrates, and the decomposition of organic

chemicals forms a crystalline thin film by post-deposition heat treatment steps. Chemical methods include chemical vapor deposition (CVD), atomic layer deposition (ALD), and chemical solution deposition (CSD) techniques.

1.3.5 Chemical vapour deposition

In the CVD process, the substrate is exposed to the precursors in its vapor form. The thin film growth is mediated by the vapor phase reaction and decomposition of the organo-metallic species on the surface of the substrate. Metal-organic CVD (MOCVD) technique was reported to produce high-quality PZT thin films at a higher growth rate [44]. However, precise control of temperature and pressure of the chemical precursors is required during the process. In addition, the use of highly toxic metallic precursors also makes the process extremely challenging [45].

1.3.6 Atomic layer deposition

ALD is also a vapor phase deposition technique that proceeds by sequential step-by-step self-limiting half-reactions on the surface. ALD is well known for its high degree of conformality, subnanometer thickness control, and low deposition temperature [46]. It also allows for deposition on high-aspect-ratio substrates. Ferroelectric doped-HfO_2 thin film is most frequently deposited using ALD [47, 48]. Although the technique has several advantages, ALD-specific narrow temperature range called 'ALD window' is described as the criterion for the process. The temperature should be high enough to enable surface reaction but not too high to cause the decomposition of the precursors. High-quality precursors are needed to produce high-quality thin films. ALD is often poised with carbon contamination from metal-organic precursor [49].

1.3.7 Chemical solution deposition

Chemical solution deposition (CSD) offers a great economic advantage and versatility in processing ferroelectric thin films. Apart from these two key advantages, CSD also offers good control over the composition of the thin films allowing greater flexibility and scalability to the industrial standards. A fine example of this is demonstrated in this work, where the CSD techniques are used to deposit a perovskite-type PZT thin film and a fluorite-type dielectric oxides thin film like HfO_2. The chemical solution deposition process involves a series of steps, from synthesizing a metallorganic chemical solution to the deposition of the solution onto the substrate of choice and then successive heat treatment processes to crystallize the thin film.

The solution synthesis process can be broadly classified into the metallorganic decomposition method (MOD), sol-gel synthesis method, and chelate method, based on the nature of the cation precursor and type of solvent used for the synthesis of the solution [50].

- The MOD method involves the use of carboxylate-based metal precursors (M-$(OOCR)_x$ where M is the metal ion, and OOCR is the carboxylate group with any hydrocarbon chain 'R' at the end) for both the A-site and B-site cations of typical perovskite-type oxides [51].
- Sol-gel synthesis method involves the use of carboxylate-based precursors for A-site and metal alkoxide precursors for B-site cations. It is dissolved in solvents like 2-methoxyethanol, 1,3-propanediol, or 1-methoxy-2-propanol, which allows for the alcohol exchange reactions [52]. Sol-gel method is extensively used in the preparation of solutions for $PbTiO_3$ [53], PZT, $BaTiO_3$ thin films [54, 55].
- Chelate method, also known as the hybrid method, involves using alkoxide-based precursors for B-site cations with chelating agents like acetic acid, acetylacetone, or amine-based compounds [50, 56].

1.3.8 Deposition of thin films by CSD

The deposition step of the CSD process can be done via spin coating, spray coating, or dip coating process. In the spin coating process, the chemical solution is dropped onto the spinning substrate, where the spinning rate of the substrate is maintained based on the solution concentration, viscosity, and thickness requirement. The deposition technique can be adapted according to the choice of substrate and the application requirements.

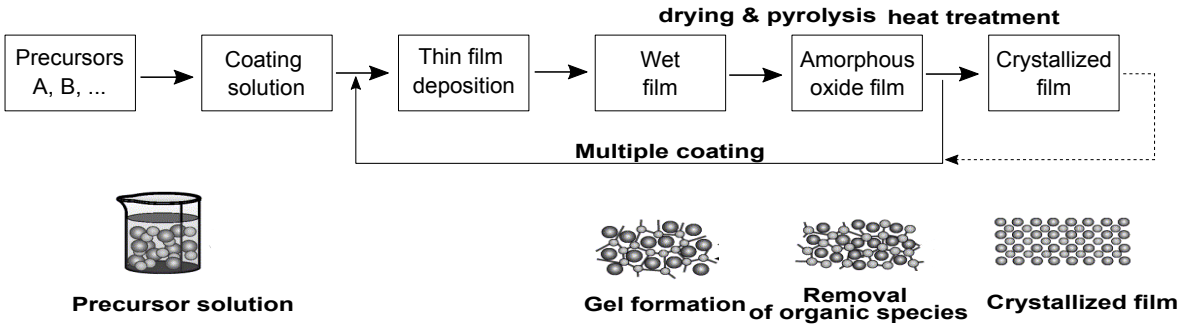

Figure 1.8: Overview of various steps involved in chemical solution deposition (CSD) process. Adapted from [56]

Irrespective of the above-discussed methods, the as-deposited wet films are subjected to a low-temperature drying step at which the solvent evaporates, and gel formation happens. The gel

formation steps lead to a long-range network of chemical structures due to cross-linking reactions. This low-temperature step is followed by a relatively high-temperature heating step, often referred to as the 'pyrolysis' step, where the decomposition of organic species in the chemical solution takes place, and any remaining solvents from the previous step will be removed. A temperature range of 200 to 400 °C is often used for the pyrolysis step, and an amorphous oxide film structure is formed at the end of this step. The drying and pyrolysis steps are often performed on hot plates under the fume hood or closed oven, depending on the evaporating solvents and chemical species. The pyrolysis step is followed by a high-temperature crystallization step in a controlled environment. Crystallization is performed in a conventional or a rapid thermal annealing furnace, and the crystallization temperature typically ranges from 600 - 800 °C. Long-range ordering, phase and microstructural evolution, and densification of the film usually happen during this step. Therefore, it is imperative to control the crystallization temperature and atmosphere to avoid the formation of intermediate phases such as pyrochlore or carbonate phases [56]. Stresses also develop during the film crystallization process, so the heating and cooling rates are equally important to avoid film cracking. By controlling all the different parameters discussed above, right from solution synthesis to the crystallization step, one can obtain thin films of varied microstructure and orientation, which will directly impacts the ferroelectric behavior of these films. Figure 1.8 shows an overview of various steps involved in the CSD process. The film's microstructure is strongly linked to the resulting ferroelectric properties, and it is essential to control the grain size, density, texture, and phase purity. To be integrated on specific substrates, an adhesion layer or buffer layer, or diffusion barrier layer is often used during the thin film deposition process. An adhesion layer or buffer layer is used to improve the thermodynamic and wetting properties of the subsequent layer deposited on the substrate. A diffusion barrier layer is used to prevent the inter-diffusion of metallic species between the film and the substrate and form undesired inter-metallic compounds. A typical example of this is the TiO_x layer used on the Si substrates to act as an adhesion layer for the sputtering of Pt electrode, as well as to prevent the diffusion of Pb into the SiO_2 layer [57]. Often, other oxide and nitride layers like ZrO_x, Al_2O_3, HfO_2, ZrN_x, TiN_x are also used as a buffer or diffusion barrier layer [7, 58]. It is important to note that using buffer or diffusion barrier layers is not limited to the CSD technique but is also used with other deposition processes.

1.4 Lead zirconate titanate

Among the ferroelectric materials, lead-based materials are widely used in many piezoelectric applications such as sensors, actuators, transducers, etc. Lead zirconate titanate, $PbZr_xTi_{1-x}O_3$ (PZT) is a solid solution of $PbTiO_3$ (PTO) and $PbZrO_3$ (PZO). PZT has a perovskite structure with Pb^{2+} ions occupying the A-sites at the corners of the cube and Zr^{4+}/Ti^{4+} cations occupying the B-sites. The oxygen atom occupies the faces of the cube forming an octahedral cage around the B-site cation, as explained in the earlier section. The high-temperature phase of PZT is a cubic paraelectric $(m\bar{3}m)$ phase. Following the phase diagram presented in Figure 1.10, at the temperature below T_c, the cubic structure is distorted, forming a tetragonal phase (point group $4mm$) on the Ti-rich side and a rhombohedral phase (point group $3m$) on the Zr-rich side. The rhombohedral phase is further separated into high temperature ($R3m$) and low temperature ($R3c$) rhombohedral phases based on the tilt of the oxygen octahedra. Anti-ferroelectric orthorhombic phase exists as an end member of $PbZrO_3$ and pure $PbTiO_3$ is a tetragonal ferroelectric phase. The tetragonal phase has 6 polar directions along the $< 001 >$ directions, and the rhombohedral phase has 8 polar directions, including the polarization along the $< 111 >$ direction.

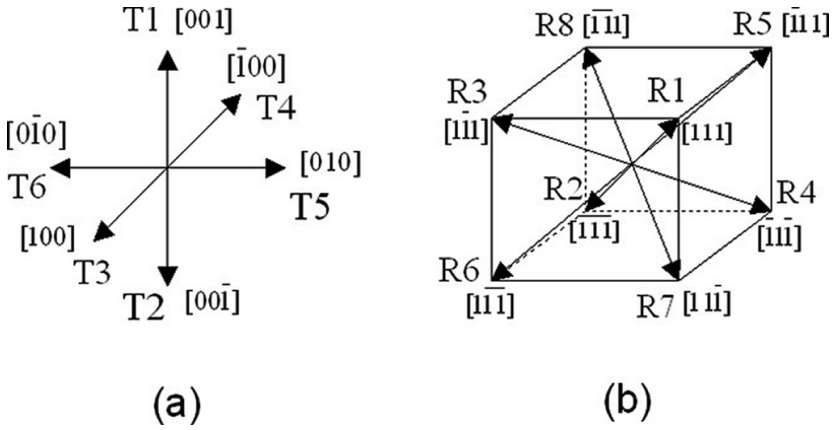

Figure 1.9: Geometric representation of different possibilities of polarization orientation in tetragonal and rhombohedral phases of PZT. Adapted from [59]

1.4.1 Morphotropic phase boundary

In PZT, the phase boundary separating the tetragonal and the rhombohedral regions is the morphotropic phase boundary (MPB) around the composition (x=0.48). The morphotropic boundary is defined as the boundary where structural changes happen in a solid solution with varying composition [60]. This phase boundary is not a well-defined line but a broadened region extending from a composition of $0.47 \leq x \leq 0.53$, where the rhombohedral phase gradually

changes to a tetragonal phase independent of temperature. A later discovery by Noheda et al. [61, 62] on the coexistence of the monoclinic phase as a subgroup of tetragonal and rhombohedral phases along the MPB region is also reported. Although several contradicting arguments to the presence of a monoclinic phase along the MPB region are reported, [63–65]. However, for a ferroelectric material where such a change of symmetry is possible, several important physical properties, including the permittivity, piezoelectric coefficients, and coupling factors, are enhanced around the MPB composition. It is associated with the ease of orientation of polarization with respect to the external field, and it is limited by the crystallographic structure. Material properties are enhanced when there is a better degree of alignment of the polarization with the external field. By a simplified explanation, there are, in total, 14 possible polarization directions (6 from tetragonal and 8 from rhombohedral) due to the combination of tetragonal and rhombohedral phases that exist along the MPB region. When the monoclinic phase is also considered, the polarization can rotate easily along the plane containing the polar axis with minimum energy need. The MPB region extends up to the T_c of 350 °C [4, 60], and the properties are more stable over a wider temperature making this composition range interesting for several commercial piezoelectric applications.

1.5 PZT thin films

Ferroelectric ceramics produced by powder technology are polycrystalline. They can also be fabricated in thin film form and deposited on a specific substrate as needed. The differences in microstructure between the bulk ceramics and the thin films originate from the processing conditions. For instance, the bulk ceramics are sintered at 1200-1300 °C for a few hours, and the thin films deposited by the chemical solution technique are annealed at 700 °C for a few minutes. Therefore the resulting microstructure influences the properties of the resulting thin film to a great degree.

1.5.1 Influence of thin film texture on ferroelectric properties

Thin films offer the possibility to be fabricated in a single crystal (epitaxial) form or as highly textured or as randomly oriented films. Texture in a thin film is defined by its growth in preferred crystallographic orientation. Textured films offer an advantage of achieving better intrinsic ferroelectric properties due to their anisotropic behavior with respect to the preferred crystallographic direction for polarization orientation [66–68]. To have a texture in the thin film, nucleation of

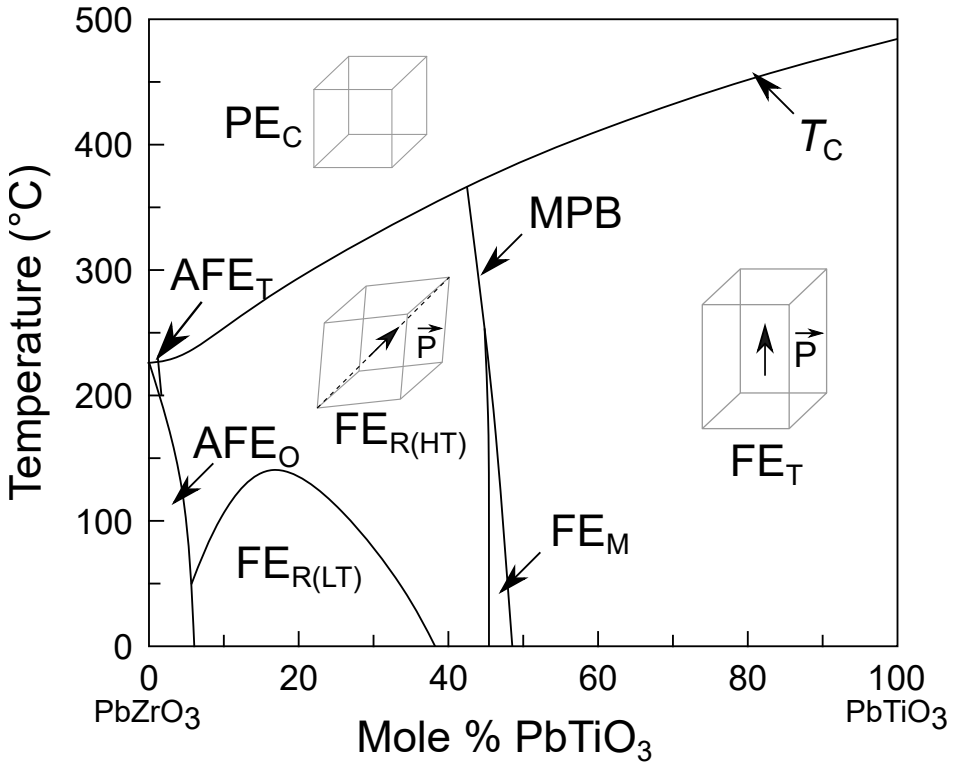

Figure 1.10: Phase diagram of PZT showing various phases. PE_C: paraelectric cubic, $FE_{R(HT)}$ and $FE_{R(LT)}$: ferroelectric high-temperature and low-temperature rhombohedral phases, respectively, FE_T: ferroelectric tetragonal phase, FE_M: ferroelectric monoclinic phase, AFE_O and AFE_T: antiferroelectric orthorhombic and tetragonal phases, respectively. Adapted from Jaffe et al. [60] and modified according to data from Noheda et al. [62].

one particular family of crystallites should be favored over the other during thin film crystallization. Crystallization in PZT thin film is nucleation mediated, and the nucleation is controlled by thermodynamics and kinetics of the crystallization process [69, 70]. Lower surface energy due to thermodynamically controlled process favors $\{100\}$ orientation, and growth controlled by crystallization kinetics favors $\{111\}$ orientation. A very thin seed layer is used to impart particular orientation in the PZT layer to overcome the competition between these two processes. For example, $PbTiO_3$ is used to promote $\{100\}$ orientation [67, 71], TiO_2 [72] and Pt are used for $\{111\}$ orientation [73], and $SrTiO_3$ is used for (110) orientation [74]. Large piezoelectric responses are observed for $\{100\}$ oriented PZT films compared to the ones that are $\{111\}$ or randomly oriented [4]. As shown in Figure 1.11, the $\{100\}$ textured PZT films were reported to have better transverse piezoelectric properties for various compositions, and the $\{111\}$ oriented films have better dielectric permittivity [67].

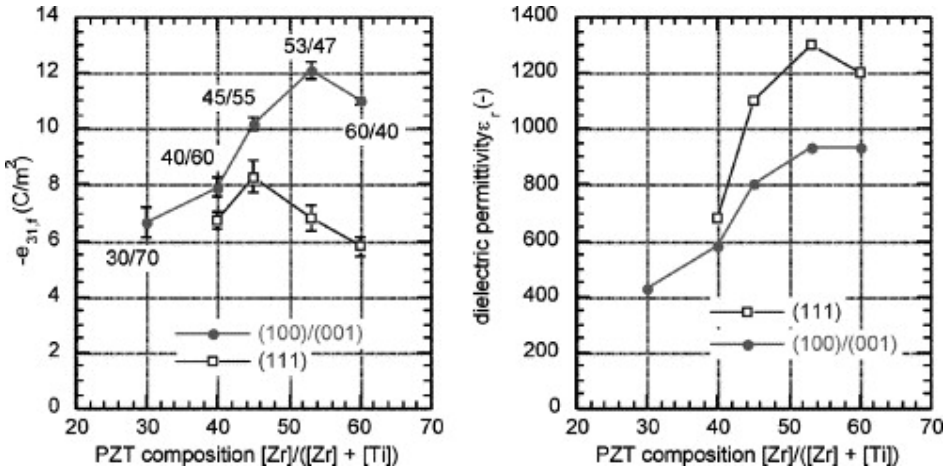

Figure 1.11: Influence of texture on the transverse piezoelectric coefficient ($e_{31,f}$) and dielectric permittivity (ε_r for various PZT compositions, from [67].

1.5.2 Influence of stress on ferroelectric properties

Thin film's properties differ from their bulk counterparts in many ways because the thin films grown on substrates are generally clamped. Thin films are clamped to the substrate due to epitaxial strain, growth stress or thermal strain due to the differences in thermal expansion coefficient between the film and the substrates. The films are subjected to significant residual stresses due to clamping. It depends on the thin film deposition process and the thickness of the film. Although the stresses can relax with the increasing film thickness, the residual stresses are still unavoidable. The stress state in thin films alters its domain structure, and the clamping can affect the domain wall motion, and the poling behavior [68, 75–77]. According to the stress state of the film, the polarization and permittivity in response to the external stimulus such as an electric field or mechanical loading can be enhanced or suppressed. The compressive residual stress can increase the polarization and reduce the permittivity response, while the tensile stress can reduce the polarization and increase the permittivity response [78, 79]. However, this argument is valid only when the electric field is applied perpendicular to the film. The effect of stress on the resulting domain orientation in PZT thin films is well studied by several research groups. They reported that the domain patterns that compensate for the residual tensile stress are predominantly in-plane oriented, growing at the expense of out-of-plane oriented domains. To compensate for the compressive stress, the out-of-plane oriented domains are grown at the expense of in-plane domains [80, 81]. As a result, different domain patterns are possible in thin films with the combination of ferroelastic and ferroelectric domains forming to reduce the elastic energy and the depolarization field, respectively [80]. The domain walls are; however, mobile under the application of electric

field [82, 83], and can contribute to an interesting combination of ferroelectric, piezoelectric, and fatigue-resistant properties according to how domains are oriented with respect to the electric field [84, 85].

1.5.3 Influence of grain size on ferroelectric properties

PZT thin films usually have fine grain microstructure in the range of 65-150 nm restricting the domain sizes in the order of a few tens to hundreds of nanometers [4]. Fine grain microstructure results in reduced intrinsic and extrinsic contributions due to lower mobility of domain walls [86–88]. Increasing the annealing temperature has been shown to increase the grain size in PZT thin films [78, 89]. However, the processing temperature is limited to the thermal properties of the substrate. Higher processing temperature may also lead to increased thermal stress in thin films, which may also be detrimental to the resulting properties [78]. PZT films with fine grain microstructure were also shown to have better resistance to degradation during fatigue cycling [89, 90].

1.5.4 Domain switching dynamics in PZT thin film

During polarization reversal in the thin film, a strain is associated with switching the domain from one direction to the other due to the residual stresses. The residual stress can be due to epitaxial strain, growth, and thermal stress. Therefore, 90° domains (for the case of a tetragonal system) or the a-domains are readily formed in thin films to release the elastic energy associated with the stress [83, 91]. This effect is observed mainly in $Pb(Zr_{0.2}Ti_{0.8})O_3$ epitaxial films but not in polycrystalline thin films or the films with MPB composition. For the a-domains to be formed, the elastic energy relaxation should be higher than that of the electrostatic energy [92]. From the experimental results, it has been shown that the dielectric constant of the films with more a-domains is higher [81]. In addition, a significant enhancement in piezoelectricity was also reported when the a-domains are switched under an electric field along with the c-domains [91, 93].

1.6 Hafnium oxide thin films

Hafnium oxide is well known for its use as a refractory material for a long time [94, 95]. HfO_2 was also well researched as high-k dielectric material alternative to SiO_2 for CMOS application due to its high permittivity [96, 97]. Ferroelectricity was discovered in hafnium oxide-based thin

films in 2011 by the group Boske et al. [9].

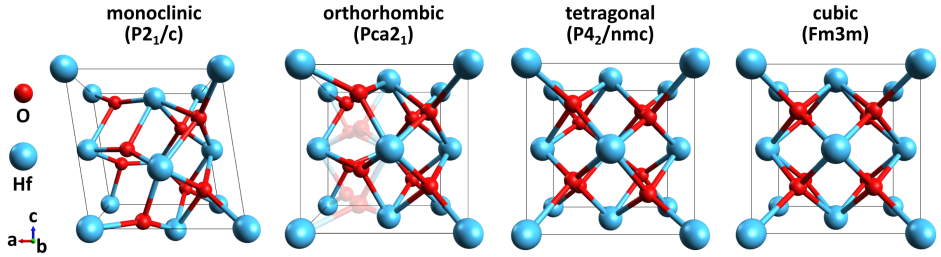

Figure 1.12: Schematics of unit cell structures in (010) view of various polymorphs of hafnium oxide. From [98].

HfO_2 exhibits a monoclinic phase ($P2_1/c$) at room temperature which has a distorted cubic fluorite crystal structure, a tetragonal ($P4_2/nmc$), and a cubic ($Fm3m$) phase at 1700 °C and 2600 °C, respectively. All these phases are non-polar and centrosymmetric; therefore, they do not exhibit ferroelectric behavior [99]. Early findings and experimental confirmation [9, 99] of the orthorhombic ($Pca2_1$) phase in thin films being polar and non-centrosymmetric is responsible for ferroelectric signature. The unit cell images of different phases of HfO_2 are depicted in Figure 1.12. HfO_2 forms a cubic ($Fm3m$) fluorite crystal structure, with Hf^{4+} cations occupying the corners and faces of the cube and O^{2-} anions occupying the eight tetrahedral interstitial sites. The oxygen atom in the ferroelectric phase ($Pca2_1$) shifts along the c-axis relative to the position of Hf, thereby allowing spontaneous polarization. Many research groups have identified several root causes

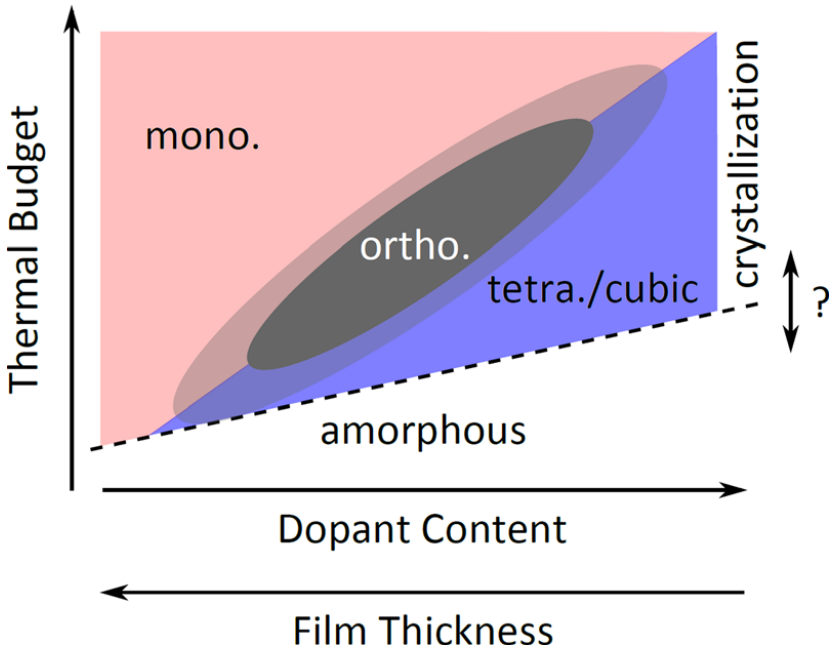

Figure 1.13: Model describing the phase stabilization region for orthorhombic phase of HfO_2 under the influence of various process parameters. From [100].

responsible for stabilizing the orthorhombic phase over the years. The notable causes include the usage of dopants [101, 102], oxygen vacancies [103], field-induced phase transformation [104], stress-induced phase stabilization [9], energy due to surface, interface, or grain boundaries inducing stress in the growing film to stabilize the polar phase [105, 106]. Depending on the deposition process and the nature of the dopant used, one or many of the causes mentioned above can play a crucial role in stabilizing the ferroelectric phase. During thin film deposition, crystallization proceeds by nucleation of the tetragonal phase and a subsequent transformation to a stable monoclinic phase. By appropriate doping, control of film thickness (inducing strain in the film), capping with the top electrode (mechanical confinement), and careful control of process parameters (to control the concentration of oxygen vacancies); the fraction of the monoclinic phase can be reduced, and a metastable orthorhombic phase with a high dielectric constant can be stabilized.

Hoffman et al. [100] performed a comprehensive work to propose a qualitative model to describe the dependence of phase stabilization on the annealing temperature, film thickness, and dopant concentration. The phase stability diagram summarizing the outcome of the model is presented in Figure 1.13.

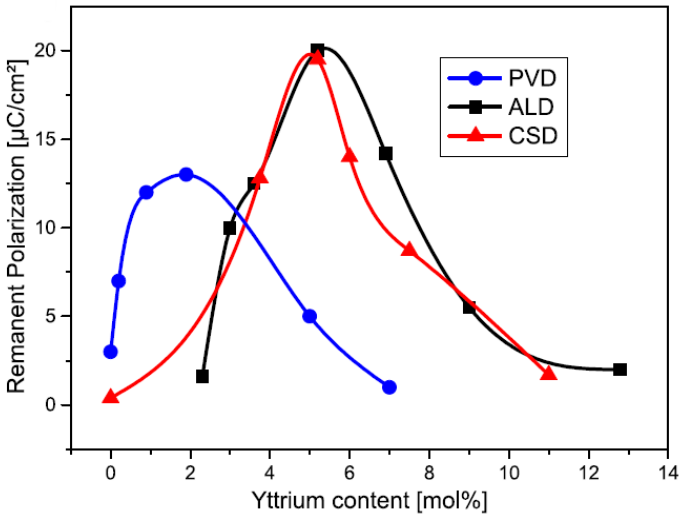

Figure 1.14: Plot comparing the effect of different thin film deposition technique on the remanent polarization values of Y doped HfO_2 thin films as a function of yttrium content. From [107].

A higher annealing temperature, lower dopant concentration, and a higher film thickness stabilize the monoclinic phase in the films, while the opposite stabilizes the tetragonal or cubic phases. The polar orthorhombic phase exists between these two extremes; the dopant concentration and the annealing temperature depend on the deposition process, the dopant used, and the

film thickness. An example of this can be demonstrated using the comparative study presented by Starschich et al. [107] in Figure 1.14 showing the influence of different deposition techniques on the evolution of remanent polarization of Y doped HfO_2 thin films. The films deposited by atomic layer deposition (ALD) [101] and chemical solution deposition (CSD) shows a similar dependence to the yttrium content. However, the properties of sputter deposited [108] film vary significantly from the other two processes and could be attributed to the higher kinetic energy involved during the sputtering process. Furthermore, it was also demonstrated that the heating steps and annealing temperature during the CSD process play an important role in controlling the ferroelectric properties of the resulting thin films [107, 109].

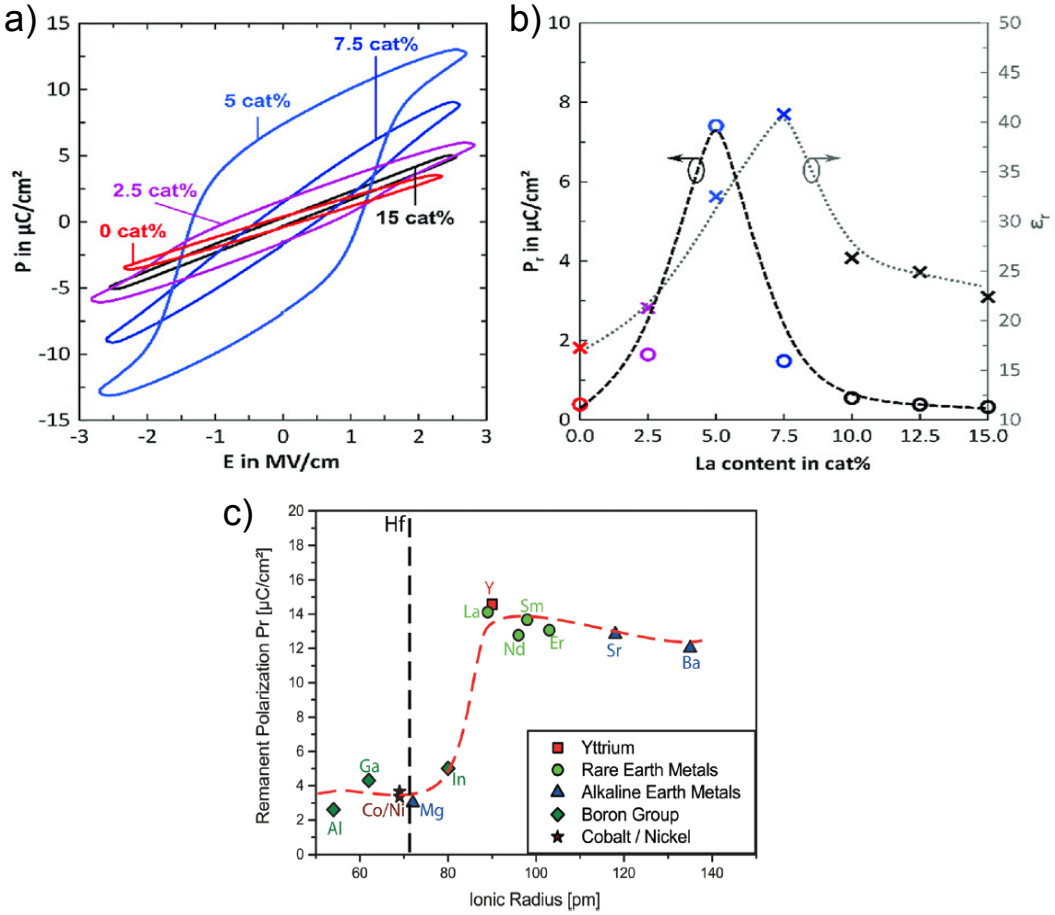

Figure 1.15: (a & b) Evolution of ferroelectric properties of La doped HfO_2 thin films deposited by CSD technique [110], (c) variation of remanent polarization depending of the ionic radii of different dopants [111].

The ferroelectric phase in hafnium oxide can be stabilized by careful doping of HfO_2 with various metal ions. The remanent polarization value varies with the doping concentration. The polarization increases with an increasing dopant concentration for almost all the dopants. It

decreases when a threshold concentration is reached; the effect of La doping is shown in Figure 1.15 (a & b). The actual reason behind such dependence is not yet fully understood. The optimum doping concentration, however, depends on the type of dopant used and its ionic radii. As depicted in Figure 1.15(c), the dopants with ionic radii larger than that of Hf showed a maximum polarization with a doping concentration in the range of 3-6 %. On the other hand, the dopants with smaller radii (like Si and Al) than that of Hf showed a distributed range and often resulted in the stable pinched hysteresis loop [112].

1.7 Fatigue in ferroelectric thin films

A ferroelectric material integrated into devices is expected to maintain a high switchable polarization during many polarization reversals. But the materials in bulk, single crystal, and thin film form are prone to one or several reliability challenges like fatigue, breakdown, leakage, imprint, and retention problems. In ferroelectric materials, 'fatigue' refers to the degradation of desired material properties, typically piezoelectric coefficients, remanent polarization, or electrical permittivity, under cyclically varying external stimulus, typically an electric field.

The application of perovskite ferroelectric thin films for non-volatile memories, aided by integrating these materials onto silicon semiconductor technology as a complementary metal oxide (CMOS), fuelled reliability research during the late 1980s [113]. Identifying one particular mechanism for fatigue is not possible, and a vast amount of work by several research groups can be evidence of this, especially on PZT thin films [114, 115]. However, some important mechanisms that are identified to be the cause of fatigue are listed below:

- The polarization suppression in ferroelectric is mainly due to domain wall pinning by ionic defects, specifically due to the electromigration of oxygen vacancies as the oxygen vacancies are often considered for their high mobility [116, 117]. The charged domain walls and ionic defects can form a stable pattern when the bound charges on the domain are not fully compensated which hinders the domain wall movement or switching [82, 118, 119]. Colla et al. [120] also proposed two different possibilities based on which polarization suppression during fatigue cycling can be explained. One is the pinning of domain walls in the bulk of the film by ionic or electronic charge carriers. The second is the inhibition of domain nucleation at the electrode-ferroelectric interface. The mechanism of polarization suppression at different cycling frequencies is identified to be different. Pinning of domain walls in the bulk of the film by charged defects and defect agglomerates was identified as

the cause of fatigue at low frequency. On the contrary, the polarization suppression was less pronounced when cycled at a higher frequency [120, 121].

- Injection of electronic charge carriers from the metal-ferroelectric interface during electrical cycling [122]. The high field cycling induces charge carriers like free electrons and/or holes by carrier injection or emission over the metal-ferroelectric interface. In turn, the injected charges change the sample's local electric field during electrical cycling and can cause ferroelectric domains to freeze. The lead vacancies can also cause the electronic charge to be trapped in the domain walls. The mobile defects can drift through the lattice to form agglomerates which can potentially pin the domain walls, inhibiting them from further switching [117]. It has also been shown that fatigue with fields smaller than saturation typically results in less degradation [123]. PZT deposited on silicon substrates with metallic electrodes was shown to undergo degradation during fatigue cycling and lose more than 50% of its switchable polarization, in contrast to oxide electrode systems which are less susceptible to fatigue [124, 125]. It was proposed that the oxide electrodes allow easy oxygen diffusion in contrast to the metallic electrodes, thereby reducing the defect entrapment at the film electrode interface. Also, the difference in work function between the ferroelectric and oxide electrode is lower than the ferroelectric and metal electrode interface. The reduced difference in work function lowers the Schottky barrier height, reducing the probability of charge entrapment at the ferroelectric-electrode interface [124, 126, 127]. In contrast, the charge carriers are entrapped at the top and bottom metal-ferroelectric interface because of the Schottky barrier between the metallic electrode and the ferroelectric changes during cycling. The defects or impurities at the interface can also lead to easier charge injection.

- Cycling induces a formation of a 'dead' layer with degraded dielectric properties at the electrode-film interface. This layer can screen the film from the applied electric field to a level insufficient for domain switching. In addition, the low permittivity blocking layer creates a potential drop across the ferroelectric layer, thus inhibiting a maximum possible polarization switching [127].

- Migration of charged defects during cycling creates a depolarizing field. This depolarizing field creates an internal bias that can cause a kinetically frozen domain state. This further affects the domain reversal process and reduces the switchable polarization [128, 129].

- Cycling can induce mechanical degradation such as micro-cracks and dislocations. These deformities can affect the domain wall motion, causing reduced polarization or increased

coercive field values. Electrode delamination during cycling can also be identified as a cause of fatigue [130, 131]. Phase decomposition of ferroelectric films into non-ferroelectric pyrochlore-like phase due to high field bipolar cycling was also proposed. It was highlighted that phase decomposition induces charge injection during switching, preventing domain nucleation.

Any of these different fatigue models are typically valid only for specific systems or driving conditions, where certain mechanisms are dominant over the others and depend on the microstructure, preparation techniques, and processing conditions of the ferroelectric thin films.

1.7.1 Effect of grain size and grain boundaries on fatigue behavior

Grains and grain boundaries play an important role in affecting the functional properties and fatigue behavior of polycrystalline ceramics and thin films. Some of the earlier works point to an increased amount of oxygen vacancies along the grain boundaries [132]. Accumulation of point charges due to charged defects was found along the grain boundaries during bipolar and unipolar cycling experiments. The mobility of these point charges is higher along the grain boundaries than the bulk of the material. Therefore, they can easily diffuse along the grain boundaries to pin the adjacent domain walls that are oppositely charged to effect a reduction in switchable polarization [133, 134]. Variations in grain size can also influence the way in which the material can degrade during fatigue cycling. PZT thin film sample with finer grains showed better fatigue properties compared to the film with larger grains. The authors argue that the films with a smaller fraction of grains touching the electrode showed a decreased fatigue rate. With the larger grains, the probability of accumulating charged point defects underneath the electrodes-film interface is higher in comparison to the fine grain microstructure, thus contributing to a large volume of material that can be affected by modified switching due to the screening of electric field [135, 136].

1.7.2 Effect of texture / orientation on fatigue behavior

The anisotropic nature of PZT with respect to the texture and orientation is an important factor during fatigue cycling. As discussed in the section 1.5, PZT thin films can be grown with different crystallographic textures or orientations using an appropriate substrate or seed layer. The stresses in the film can alter the domain orientation; therefore, the orientation of the electric field with respect to the crystallites or domain orientation has to be considered. The projection

of the electric field onto the major domain orientation determines the effective driving field for the domain switching. According to Pan et al. [137], the pinning force is higher for the domains oriented in the field direction than those not initially oriented in the field direction. It could be due to the directional migration of defects or space charges due to the applied electric field, which results in the build-up of the directional pinning force. They argue that the space charge field created by defects and space charges during the half period of bipolar cycling counteracts the applied field and causes back-switching when the applied field reaches zero. Therefore, the domains that are initially oriented perpendicular to the electric field were observed to be reoriented in the direction of the field in the fatigued state.

1.8 Reliability issues with Hafnia thin films

1.8.1 Wake-up and fatigue behavior

Hafnia thin films exhibit a field cycling behavior where the hysteresis loop opens up (depinching) with an increase in P_r values exhibiting a so-called wake-up effect during initial cycling. The wake-up effect can be distinguished from fatigue. Fatigue is defined as the decrease of switchable polarization (P_r) at higher numbers of switching cycles. In the pristine state, the hysteresis loop is pinched, showing two different switching events that can be seen from the current transient curve in Figure 1.16. Upon cycling, the switching peaks merge, forming one dominant peak. This kind of wake-up behavior will cause instability in memory devices during repeated field cycling [138–140]. The mechanisms behind the field cycling behaviour strongly depends on dopant and processing conditions. An overview of the underlying possibilities are presented here.

In a pristine state, a strong internal bias field is present, causing the pinched hysteresis loop combined with a strong polarization relaxation after switching [141]. Differential degradation of electrode-ferroelectric film interface, i.e., bottom electrode interface is oxidized well during the film deposition and annealing. At the same time, the top electrode interface is not oxidized enough from the post-deposition annealing. This results in an asymmetry in the oxygen vacancies distribution between the top and bottom electrode interface, leading to a strong increase in the internal bias field [142, 143]. High oxygen vacancy concentration was reported along the top electrode interface than the bottom interface. The oxygen vacancies are suspected to diffuse during the electric field cycling, which can cause de-pinning of domains [144, 145]. The field-induced phase transition from a monoclinic or cubic phase to a ferroelectric orthorhombic phase was reported as a reason for the wake-up effect [139, 145]. In the pristine state, portions of

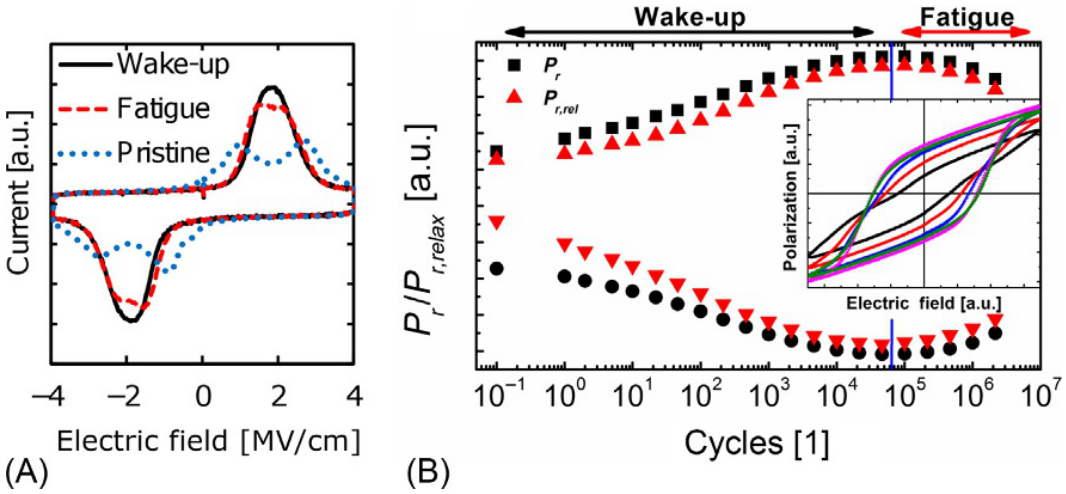

Figure 1.16: (A) Transient current response to the corresponding polarization hysteresis (B-inset) of the ferroelectric Sr-doped HfO_2 thilm film for the pristine, woken-up, and fatigued states. (B) Evolution of positive and negative remanent polarization with switching cycles. From [115].

the monoclinic phase were found in the bulk of the film. For the woken-up and fatigued cases, the monoclinic fractions decreased, and the orthorhombic phase fractions increased significantly. This led to the conclusion that a field cycling-induced phase transition took place. The wake-up effect is reported to be strongly dependent on cycling frequency and not the number of switching cycles. Low cycling frequency requires fewer cycles; therefore, it depends on the overall cycling time. This also indicates a contribution from charged species like ionic charges moving through the lattice during cycling [141, 144].

In the context of fatigue, it was found that the bipolar switching cycles result in an evident degradation of switchable polarization and not the uni-polar cycling. For the bipolar case, suppressed switching can be directly correlated to the increase in defect concentration. The formation of the conductive path along the grain boundaries due to their intrinsically high concentration of oxygen vacancies [146] can also be linked to the cause of fatigue. In addition, the annealing temperature and time were also shown to influence the oxygen vacancy concentration significantly. Higher annealing temperature or time resulted in increased interface oxidation leading to poor fatigue and early breakdown. The redistribution of oxygen vacancies during field cycling will also contribute to subsequent fatigue in films after the wake-up [147–149]. The higher concentration of oxygen vacancies along the grain or domain boundary also results in pinning the domain walls in HfO_2 thin films [150, 151].

1.8.2 Leakage and breakdown in hafnia thin films

Breakdown often follows after a significant increase of leakage current. During field cycling, the oxygen vacancies are diffused and redistributed along the grain boundaries [152]. This, in turn, results in an increase of grain boundary mediated conductivity leading to the formation of a conductive path. When the field is continuously cycled or increased, the conductive path can grow, contributing to the increase in leakage current resulting in a dielectric breakdown. There is also a clear correlation between the higher annealing temperature and time with increased leakage current and earlier dielectric breakdown [146, 153]. It is associated with the oxygen vacancy generation or re-distribution in the film.

On the contrary, some studies also reported that fewer oxygen vacancies are formed in thin films processed in an atmosphere containing nonreactive gas (i.e., argon or nitrogen) during the crystallization or annealing step. In some of the earlier works [154–157] doped and un-doped HfO_2 thin films were deposited by sputtering and solution deposition methods [158] where annealing was performed under varied oxygen and argon atmosphere. It was hinted that a low oxygen growth environment resulted in improved ferroelectric properties. It was also common to use nitrogen atmosphere to anneal HfO_2 thin films. Suzuki et al. [159] reported rapid-thermal annealing of RF-sputtered hafnia thin films under O_2 and N_2 atmosphere. It was demonstrated that the films annealed in an O_2 atmosphere showed an increase in leakage current and exhibited a poor degradation behavior. It was hypothesized that the oxygen-deficient environment during sputter deposition generated oxygen vacancies that, in turn, help to stabilize the ferroelectric phase [159]. On the other hand, the deposition in an oxygen-rich environment creates interstitial oxygen, which can enhance the leakage current.

1.9 Ferroelectric thin film applications

PZT thin films are utilized in various devices that makes use of piezoelectric microelectromechanical systems (piezo-MEMS) which includes sensors [160, 161], actuators [160], transducers [160], energy harvesters [162–164], and memory devices [165, 166]. There is also a growing interest for the transparent electromechanically active stack to be used in interactive touch panels [7], devices that are beneficial for applications such as 5G telecommunications or radio frequency microelectromechanical system (RF-MEMS) switches [167, 168], for IoT, tactile internet and related applications [169]. The discovery of ferroelectricity in HfO_2 has also triggered the research interest to find its application in ferroelectric memories, and ferroelectric field-effect transistors (FE-FET)

[170]. The example of non-volatile memory with a field effect transistor cell is discussed in the following section highlighting the relevance of reliability issues associated with ferroelectric thin films. The discussion is centered around the challenges in using PZT and HfO_2 in a ferroelectric field effect transistor.

1.9.1 Non-volatile ferroelectric memories

The non-volatile ferroelectric random access memory (NV-FERAM) consists of an access transistor and a capacitor that acts as s storage node. The capacitor here is formed by a ferroelectric material typically PZT [171, 172], $Sr_2(Ta,Nb)_2O_7$ [173], BLT ($(Bi,La)_4Ti_3O_{12}$) [174, 175] etc, functioning as a gate dielectric of the transistor. The schematic in Figure 1.17 shows a typical ferroelectric field-effect transistor (FE-FET) forming a 1T memory cell. The ferroelectric layer is usually deposited on the Si layer. The non-linear hysteretic behavior of the ferroelectric capacitor facilitating charge generation upon applying an electric field is utilized for memory applications. 'Writing' is accomplished when the electric field (gate voltage) is applied and the ferroelectric layer is polarized. According to the polarization state, electrons or holes accumulate on the surface of the semiconductor layer. 'Reading' is accomplished when the drain current flows between the source and drain when one type of charge carrier is accumulated in the semiconducting layer. Therefore, the current output is recorded on the 'bit line,' indicating the memory state of the cell. Ferroelectric memories need power only while reading and writing operations, making them a good candidate for low power operation. The energy required for writing a bit of information in FE-FET is $\approx 1\,fJ$ [170].

The hysteresis behavior determines the memory window of the cell, and the stable remanent state is essential for the retention properties; therefore, FERAM retains its data even after the power is turned off. As per the industrial standards [176, 177] NV-FERAMs with PZT should have high endurance and should be operated for more than 10^{15} write and read sequence. The degradation of switchable polarization during fatigue cycling decides the long-term endurance properties of the ferroelectric materials used in these memory cells. PZT is also poised with the problem of scalability since a minimum thickness of 70-100 nm is required to keep the coercive voltage in the reasonable operating range [113, 178].

However, CMOS integration of PZT thin films is challenging due to compatibility issues with the Si substrates. An insulating buffer layer (dielectric layer) is often used between the Si and PZT layer, but the low capacitance of the buffer dielectric layer causes severe degradation of data retention characteristics of the ferroelectric capacitor due to the depolarizing field. Therefore a

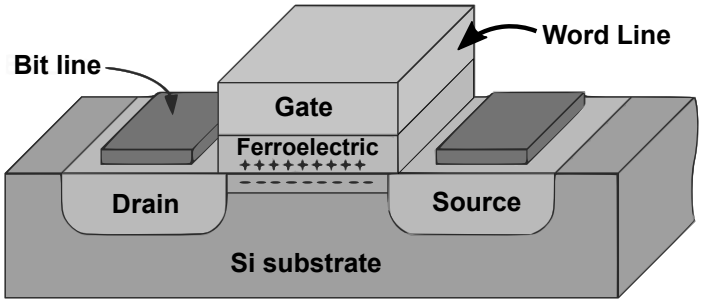

Figure 1.17: Schematic representation of 1T-type memory cell in FeRAM composed of a single ferroelectric-gate FET. Adapted from [179].

thin buffer layer with a high dielectric constant is needed. Apart from this, the ferroelectric and dielectric layers should have low leakage current characteristics. If the leakage current is higher for the ferroelectric and the dielectric layer, the charges between the dielectric-semiconductor interface will be disturbed and the stored data cannot be read by the change in drain current [175]. Several dielectrics like Si_3N_4 [180], $LaAlO_3$ [181], HfAlO [182], and HfO_2 [183] exhibiting low leakage behavior have been used as buffer layer for FE-FETs. Particularly, with the discovery of ferroelectricity in HfO_2, a lot of research efforts have been made to integrate the ferroelectric HfO_2 layer directly onto the semiconductor node of the transistor for the FE-FET owing to the CMOS compatibility and scalability. Ferroelectric HfO_2 also faces challenges like endurance, retention limits, wake-up effect, and breakdown behavior, as discussed in the section 1.8. A retention period longer than 10 years is a requirement for nonvolatile memories and is expected for FE-FET with ferroelectric doped HfO_2 gate oxide. Due to the high coercive field of HfO_2, the operating voltage is close to the breakdown field of the material. Therefore, it is important to optimize the material property to enhance its breakdown strength while scaling down in thickness and retaining the ferroelectric nature of HfO_2.

Therefore, by comparing the perovskite-type and fluorite structure-type ferroelectric thin films as candidates for NV-FERAM application, it can be understood that both films suffer some reliability challenges while scaling down. Furthermore, as of date, processing and material integration for CMOS compatibility combined with the issues of long-term field cycling behavior, retention characteristics, and breakdown strength of the material system limits the widespread use of ferroelectric materials in memory applications.

Chapter 2

Experimental methods

This chapter presents the main experimental methods relevant to the characterization of ferroelectric thin films. In addition, an overview of the synthesis of precursors for chemical solution deposition and a detailed description of the deposition methodologies of PZT and HfO_2 thin films are outlined in the first section. In the latter part, structural characterization methodologies for thin films, orientation, and residual strain quantification by x-ray diffraction-based methods are discussed. Finally, electrical characterization methodologies, including reliability studies like fatigue cycling and breakdown studies, are discussed in the last section.

2.1 Thin film configuration

Two different electrode configurations were used to characterize the thin films used in this study: metal-insulator-metal (MIM) and interdigitated electrodes (IDEs). The MIM geometry includes top and bottom electrodes with a thin film sandwiched between them with the electrode surface area A and the film thickness d. IDEs are planar electrode structures patterned and deposited on the film surface. MIM and IDE designs are schematically depicted in Figure 2.1, along with the electric field direction for each structure. In the case of the MIM configuration, the field is perpendicular to the film plane. For the IDE, it is mainly parallel to the direction film plane, with a slight curvature [184].

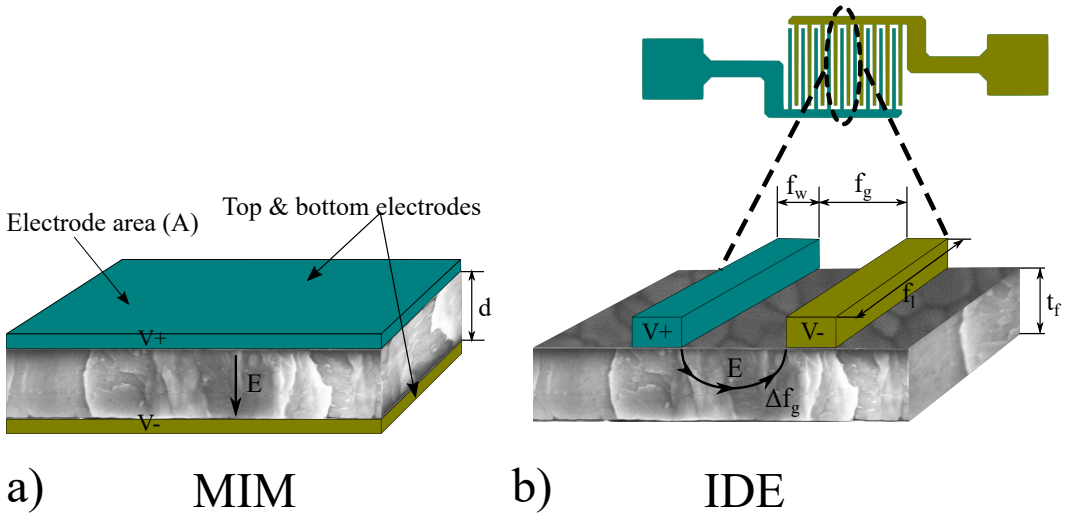

Figure 2.1: Schematic representation of (a) MIM and (b) IDE configuration used in the study. The actual design of the IDE is shown in the magnified view. Adapted from [184].

The finger gap (f_g) and width (f_w) are the critical parameters of the IDE structures, the importance of these dimensions is discussed in detail in Chapter 4. They were chosen in such a way that (f_g) and (f_w) are greater than the film thickness (t_f). The metalization ratio $\mu = f_w/(f_g + f_w)$ is another important parameter that should be taken into consideration to maximise the electric field distribution in the ferroelectric layer. As there will be no field below the fingers, this volume of the ferroelectric layer will not contribute to any charge generation. However, f_w cannot be made comparable to film thickness as this would result in an uneven field distribution between the fingers, and the feature size will be very small for the lithography process. The finger length (f_l) should also be much greater than the gap to achieve better poling and to ensure that no stray field from the tip of the fingers influences the field in between the fingers [184, 185]. The effective electrode area with IDEs is given by $A = (2N - 1)f_l t_f$, where N is the total number of

fingers for each electrode. The effective distance between the electrodes is $\mathrm{d} = \mathrm{f_g} + \Delta \mathrm{f_g}$, where $\Delta f_\mathrm{g} \approx 1.32\, t_\mathrm{f}$: a correction factor derived for curvature and length of the field lines joining fingers of opposite polarity, and Δf_g is proportional to t_f. [184]. With the effective area and electrode distance, the electric field between the fingers will be $E = V/f_\mathrm{g} + \Delta f_\mathrm{g}$, where V is the voltage applied. The capacitance of the ferroelectric film can be derived as follows:

$$C = \varepsilon_f \varepsilon_0 \frac{(2N-1) f_\mathrm{l} t_\mathrm{f}}{f_\mathrm{g} + \Delta f_\mathrm{g}} \tag{2.1}$$

where ε_0 and ε_f are the vacuum permittivity and the film permittivity, respectively.

2.2 Processing of thin films

The chemical solution deposition technique is used for fabricating thin films in this work. This section will describe the methodology of solution synthesis and the deposition steps followed for preparing PZT and HfO_2 thin films. Substrates like silicon, fused silica, and sapphire are used to deposit different sets of thin film stacks.

2.2.1 Precursor solutions for PZT and Hafnia thin films

The details of the solution synthesis methodology can be found in the work of Godard et al. [71, 186] and Schenk et al. [110] for PZT and hafnia, respectively.

Precursors of lead (II) acetate trihydrate (99.5%), titanium (IV) isopropoxide (97%), and zirconium (IV) propoxide (70% in propanol), all Sigma-Aldrich, USA, were used with 2-methoxyethanol (99.8%, Sigma-Aldrich, USA) as solvent to prepare 0.3 M of PZT solution. A similar set of precursors were adapted to prepare a 0.1 M $PbTiO_3$ solution, which was used as a seed layer during the deposition process of PZT films. $PbTiO_3$ solutions were prepared using two different solvent systems, 2-methoxyethanol as well as 1-methoxy-2-propanol (99.8%, Sigma-Aldrich, USA), which was proposed to be safer than 2-methoxyethanol [186]. The metal precursors of lead, titanium, and zirconium were dissolved in 2-methoxyethanol. The mixture of modified metal precursors in the solvent was refluxed, distilled, and diluted to obtain a 0.3 M PZT solution. A similar procedure was adapted for $PbTiO_3$ (PT) seed layer, where lead and titanium metal precursors were mixed in either 2-methoxyethanol or 1-methoxy-2-propanol to obtain a 0.1M PT seed layer solution [71]. $PbTiO_3$ is used to impart $\{100\}$ texture in the PZT thin films [186]. To compensate for the loss of Pb atoms during heat treatment and preserve the final film's required stoichiometry, the PZT and PT spin coating solutions are typically prepared with a 10% and 30% excess Pb content,

respectively.

Metallic precursors, Hf(IV)-acetylacetonate (Alfa Aesar, 97% purity) and La(III)-acetate hydrate (Sigma-Aldrich, 99.9% purity), were dissolved in propionic acid (Sigma- Aldrich, 99.5% purity) for the preparation of La-doped Hafnia metal-organic solutions of varied concentration for the preparation of La-doped HfO_2 thin films. The hafnia solutions were prepared in two different concentrations, 0.25 M and 0.083 M, to be used for two different deposition strategies, namely conventional and layer-by-layer routes, respectively.

2.2.2 Deposition process of PZT thin films

Thin films were deposited using the spin coating technique, and different substrates were used for depositing PZT thin films. The substrates used for depositing PZT and HfO_2 thin films are summarized in Table 2.1. The nomenclature followed during the work referring to the different substrates is also mentioned in the table. Transparent and non-transparent thin film stacks can be fabricated using the given combination of substrates and electrode geometries. Fused silica and sapphire was chosen for their thermal properties; both the substrates have a very high melting point and can easily withstand the high crystallization temperature during PZT deposition.

Table 2.1: List of substrates with their technical details used for PZT thin film deposition in this study

	Substrate	Nomenclature	Supplier	Substrate thickness	Orientation	Oxide layer	Buffer layer	Bottom electrode	Stack
With bottom electrode (MIM)									
1	Si	Pt/Si-Sintef	SINTEF	675 µm	(100)	SiO_2 (500 nm)	TiO_x (20 nm)	Pt (100 nm)	$Si/SiO_2/TiO_x/Pt/PTO/PZT$
2	Si	Pt/Si-in-house	SIEGERT WAFER	725 µm	(100)	SiO_2 (500 nm)	HfO_2 (20-30 nm)	Pt (100 nm)	$Si/SiO_2/HfO_2/Pt/PTO/PZT$
3	Fused silica	Pt/FS	SIEGERT WAFER	500 µm	x	x	HfO_2 (20-30 nm)	Pt (100 nm)	$FS/HfO_2/Pt/PTO/PZT$
4	Sapphire	Pt/SP	SIEGERT WAFER	430 µm	C-Plane (0001)	x	HfO_2 (20-30 nm)	Pt (100 nm)	$SP/HfO_2/Pt/PTO/PZT$
Without bottom electrode (IDE)									
5	Si	Si	SIEGERT WAFER	725 µm	(100)	SiO_2 (500 nm)	HfO_2 (20-30 nm)	x	$Si/SiO_2/HfO_2/PTO/PZT$
6	Fused silica	FS	SIEGERT WAFER	500 µm	x	x	HfO_2 (20-30 nm)	x	$FS/HfO_2/PTO/PZT$
7	Sapphire	SP	SIEGERT WAFER	430 µm	C-Plane (0001)	x	HfO_2 (20-30 nm)	x	$SP/HfO_2/PTO/PZT$

The deposition methodology developed by Godard et al. [71] for PZT thin film on platinized silicon (Pt/Si-Sintef) wafer was followed during this work. Firstly, the as-procured wafers were heated to 400 °C on a hot plate for 5 min to remove the adsorbates and cooled down to room temperature before spin-coating. A 0.1 M $PbTiO_3$ (PTO) solution was first deposited to be used as a seed layer, and the spinning rate of the substrate was maintained at 3000 rpm for 30 s. PTO layer was dried at 130 °C, followed by pyrolysis at 350 °C on hot plates for 3 min each under

the fume hood. Crystallization was carried out in a rapid thermal annealing furnace (RTA AS - Master, Annealsys, France) at 700 °C for 1 min in atmospheric conditions. The PTO seed layer crystallizes as a continuous layer of nanocrystals with well-defined facets distributed across the Pt surface, which can promote the growth and crystallization of the PZT layer in the {100} crystallographic orientation [186]. Then the as-prepared precursor solution of PZT (Zr/Ti = 53/47) with a composition close to the morphotropic phase boundary (MPB) was deposited. The spinning rate for PZT was also maintained at 3000 rpm for 30 s to obtain a layer thickness of approximately 40 nm per spinning step. PZT film was also subjected to drying and pyrolysis steps identical to the PT layer. After four subsequent deposition-drying-pyrolysis cycles, crystallization was performed in a rapid thermal annealing furnace at 700 °C for 5 min resulting in ≈170 nm thick PZT film. These steps were repeated several times to achieve films of required thickness. Figure 2.2 shows the schematic of the PZT thin film deposition process followed during this study. Finally, 100 nm thick platinum was sputtered at room temperature on the PZT films to be used as a top electrode, forming a metal-insulator-metal (MIM) geometry. The top electrodes were patterned into circles of various diameters (from 100 µm to 2 mm) using lift-off photolithography using direct laser writing (MLA, Heidelberg Instruments).

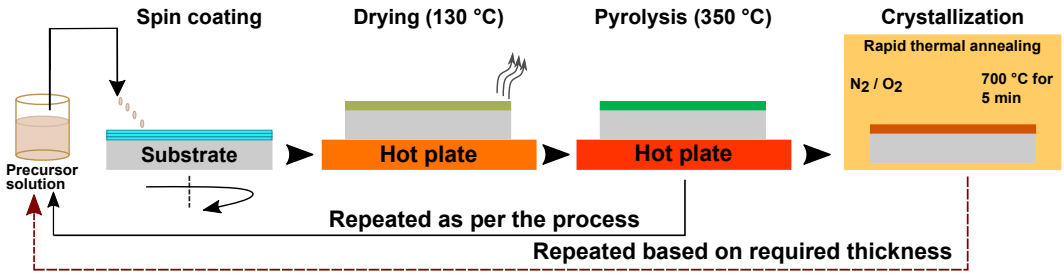

Figure 2.2: Schematic of solution deposition steps for PZT thin films.

Apart from the standard process involving Pt/Si-Sintef wafers, silicon (Si-in-house) wafers with 500 nm thick SiO_2 (grown by wet thermal oxidation) were also used to grow PZT thin films with and without bottom electrodes for this work. In addition, fused silica and sapphire wafers were used to grow PZT thin film with and without the bottom Pt electrode. In order to prepare the substrate, a 20-30 nm thick HfO_2 layer was first deposited either using atomic layer deposition (ALD) or CSD route. This HfO_2 layer is used as a diffusion barrier layer and a buffer layer to promote surface wetting during the deposition steps. The CSD route for using HfO_2 as a buffer layer was developed during this work. Based on the requirement for MIM geometry, 100 nm thick platinum (Pt) bottom electrode is sputtered at room temperature onto fused silica and sapphire wafers after the buffer layer deposition resulting in platinized fused silica (Pt/FS) and platinized

sapphire (Pt/SP) substrates. Then the procedure mentioned above was followed for depositing the PTO seed layer and PZT thin films of required thickness.

PZT thin film stacks without bottom electrodes were patterned with planar interdigitated electrodes (IDEs) to produce transparent stacks on fused silica and sapphire wafers. The deposition process on fused silica (following the above-discussed route) was initially developed by Glinsek et al.[7], and it involved using ALD deposited HfO_2 barrier layer. The same work was also adapted to develop a transparent PZT thin film stack on sapphire. Additionally, PZT film stacks with CSD deposited HfO_2 buffer layer was developed on fused silica and sapphire substrates. Apart from the transparent substrates, PZT thin film stacks without bottom electrodes on Si substrate are also developed during this work. HfO_2 as a barrier layer (both ALD and CSD routes) was used for the first time on Si substrate with 500 nm SiO_2 layer. PZT layers were then deposited and later patterned with IDEs. Schematics of different thin film stacks developed for this study are shown in Figure 2.3.

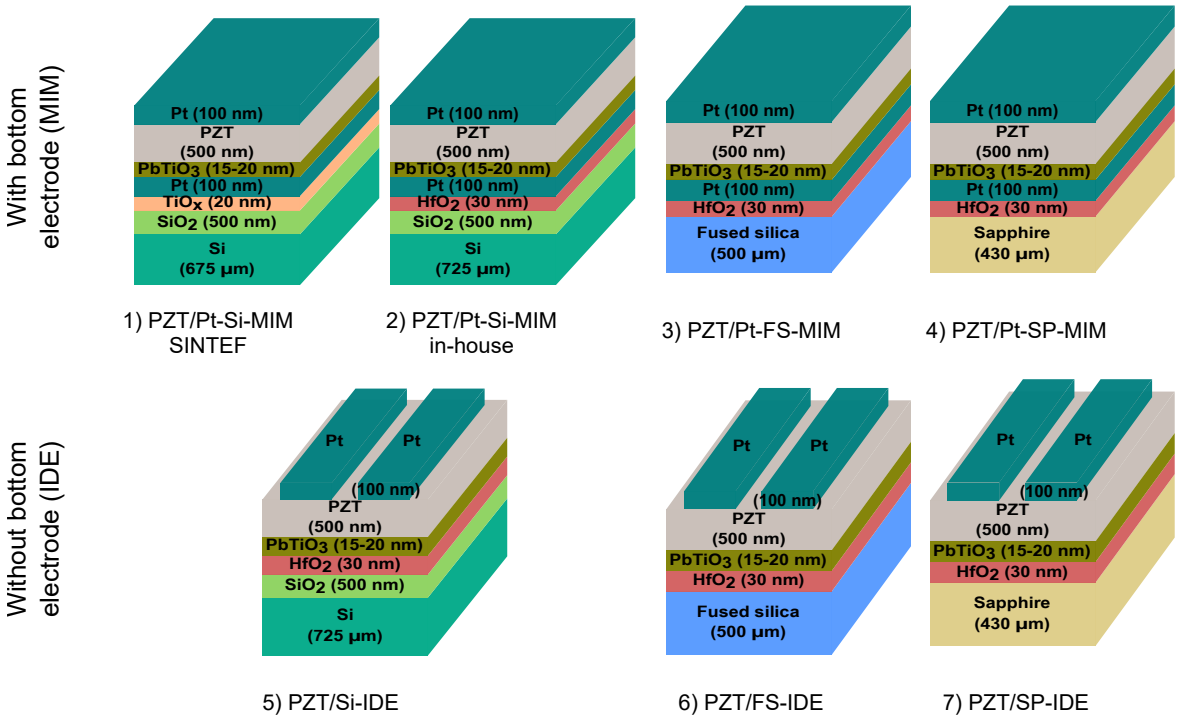

Figure 2.3: Schematic of various thin film stacks developed and used during this work. Note: the dimensions are not to scale.

The circular top electrodes for MIM configuration and the planar IDEs are then patterned on the PZT layer by the lift-off photolithography process. The samples are first cleaned and dried, followed by thermal dehydration. A lift-off resist based on polydimethylglutarimide (LOR-3A, Shipley) is first spin-coated and baked at 160 °C for 5 min. It is followed by coating cresol

formaldehyde resin (photo-resist layer) (S1813, Shipley) and baking at 115 °C for 1 min. Then the photo-resist is exposed to UV illumination by a direct laser writing instrument MLA 150, (Heidelberg Instruments) and developed in tetramethylammonium hydroxide-based developer (MF-319, Microposit) for 40-50 s to remove the exposed part of the photo-resist and generate an undercut in the lift-off resist [187]. Next, the developed samples are sputtered with a Pt layer at room temperature for 3 min 40 s with the sputtering power of 200 W to achieve a thickness of 100 nm. The deposition chamber is maintained under a pressure of $2.1\text{x}10^{-2}$ mbar with 15 sccm argon flow. It is followed by a lift-off step, where the samples are soaked in a resist remover N-methyl-2-pyrrolidone (Remover PG, MicroChem) to remove the unexposed resist along with the metallic layer. This leaves the Pt-layer on the exposed part of the resist intact to realize the required IDE design. The sample is then finally rinsed off with solvents and dried. Figure 2.4 shows a simple schematic explaining the steps of the lithography process.

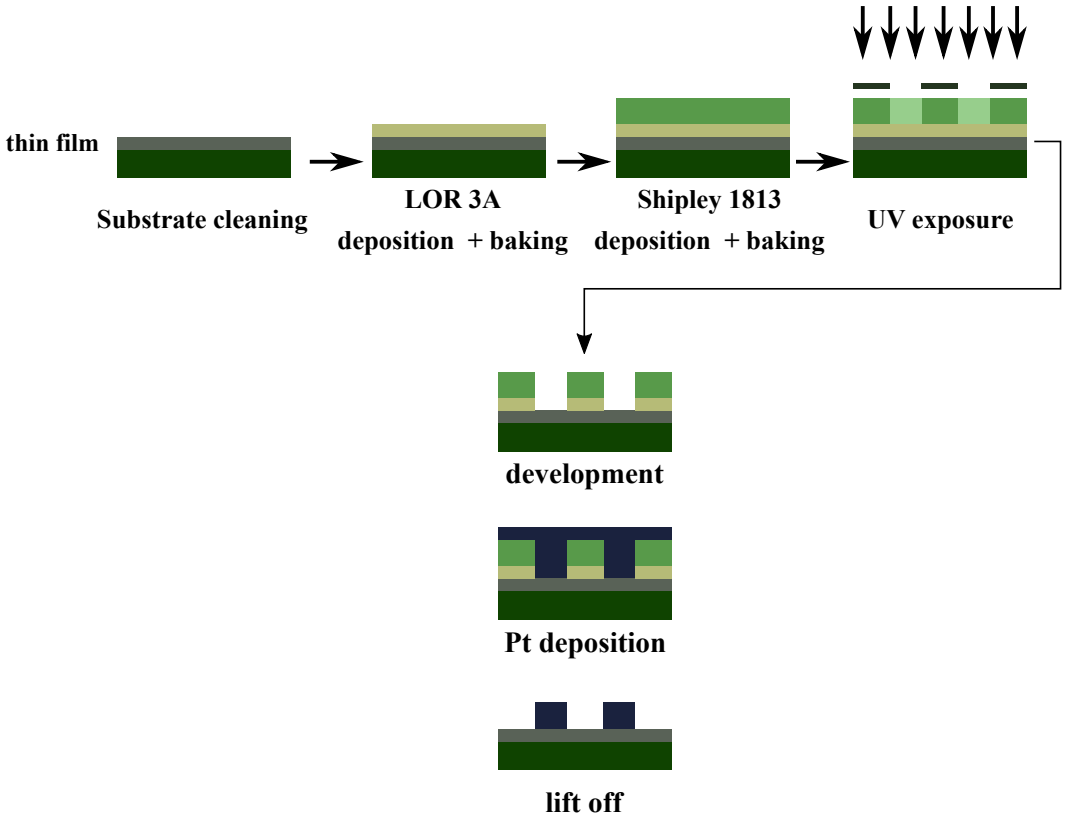

Figure 2.4: Schematic of the process steps followed during lithography for IDE patterning. Adapted from [188, 189]

The MIM and IDE electrodes on all film stacks are finally annealed (post-annealing) at 400 °C for 10 min on hot plate. Based on the need, 80-100 nm thick layer of polymer resist (SU8 3005) is deposited on the surface of the films with IDEs. SU8 is spin coated on the samples at 10000

rpm for 1 min. The SU8 layer is then exposed to UV illumination (1200 mJ/cm^2) with a negative pattern of the used IDE design. After the UV exposure, the sample is heated at 95 °C for 1 min on hot plate at a heating rate of 450 °C/hr, and developed in MF-319 for 40-50 s to remove the unexposed part of SU8. Following this, the patterned SU8 is cured at 150 °C for 30 min. The SU8 layer is mainly used to prevent the interdigitated electrode fingers from getting short-circuited during the application of high fields. Therefore, the interdigitated portion of the IDEs with SU8 is exposed to UV illumination and later developed to remove the unexposed part of the SU8 layer.

2.2.3 Deposition process of Hafnia thin films

Two different deposition routes, namely conventional and layer-by-layer (L/L) methodologies, were followed for depositing HfO_2 thin films. La (5%) doped HfO_2 solutions of two different concentrations (0.25 M and 0.083 M) are used to spin coat on pre-cleaned Pt/Si wafers. The spinning rate is maintained at 3000 rpm for 30 s, to obtain a single layer thickness (SLT) of 15 nm with a 0.25 M solution for conventional route and SLT of 4-5 nm with a 0.083 M solution for films deposited by L/L route for each spinning step. The substrate coated with the precursor solution was subjected to a drying step at 215 °C for 5 min. For the conventional route, the spin coating-drying step is repeated 3 times to achieve a film thickness of 45 nm after the crystallization step. For the L/L route, crystallization is performed after each spinning and drying cycle. Irrespective of the deposition route, the films were crystallized by rapid thermal annealing at 800 °C for 90 s in a 1:1 atmosphere of Ar and O_2. The L/L process was repeated 11 times to obtain a film thickness of 45 nm. The schematic of the HfO_2 deposition process is shown in Figure 2.5. Both conventional and L/L samples are subjected to a post-annealing step after top Pt-electrode deposition. Post-annealing is typically performed to improve the interface between the ferroelectric thin film and the metallic top electrode.

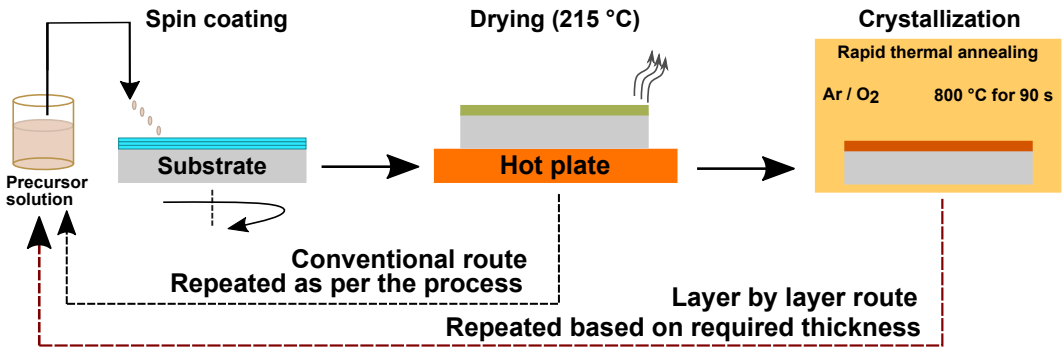

Figure 2.5: Schematic of solution deposition steps for HfO_2 thin films.

2.3 Structural characterization

2.3.1 XRD

The crystal structure and phase fractions of the given polycrystalline thin films are identified by means of x-ray diffraction. The atoms in a crystal lattice are arranged in a periodic array with long-range order. When probed with X-rays of wavelength (λ) that are similar to the distance between atoms in a crystal, diffraction can occur. The incident x-rays with the incident angle (θ) are scattered, producing constructive interference at the angle (2θ), resulting in diffraction patterns. These diffraction patterns contain information about the atomic arrangement within the crystal. This phenomenon of diffraction is based on Bragg's law, which correlates the diffraction angle to the interplanar distance of the diffracting crystallites, which is given by the equation 2.2 where n is the order of reflection, ($\mathrm{d_{(hkl)}}$) is the inter-planar distances of the (hkl) lattice plane and (θ) being the Bragg's angle of diffraction as shown in Figure 2.6.

$$\mathrm{n}\lambda = 2\mathrm{d_{(hkl)}} \sin\theta_{(\mathrm{hkl})} \tag{2.2}$$

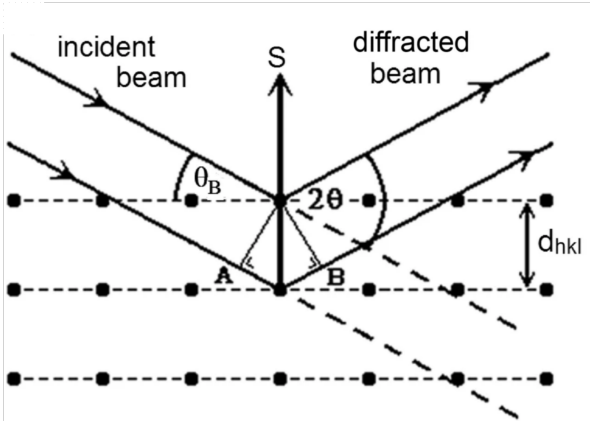

Figure 2.6: Principle of Bragg's diffraction, from [190].

The classical θ-2θ setup and grazing incidence X-ray diffraction (GI-XRD) geometry setup are used based on the thickness of the thin film stacks under investigation. The grazing incidence geometry is used explicitly for thin and ultra-thin films, where the incident angle is fixed to a small angle ($0.5 - 2^\circ$) to limit the penetration depth to maximize the information from the thin films. Caution has to be taken when reporting the GIXRD diffractogram, as the lattice planes contributing to the measured signal are not always parallel to the sample surface, and their orientation continuously changes during the measurement. XRD measurements in this work were performed using a Bruker D8 Discover diffractometer with a 5-axis cradle and a copper anode

X-ray source ($\lambda_{\mathrm{Cu}}(\mathrm{K}_\alpha)$=1.541 84 Å). The $\theta - 2\theta$ scans are used for investigating PZT thin films, and grazing incidence scans with 0.5° incident angle were used mainly for HfO_2 thin films.

For a polycrystalline thin film sample, the Lotgering factor method [191] is used to determine the orientation factor from the measured x-ray diffractogram. The orientation factor for a given family of reflection xyz at a certain 2θ angle can be calculated by the given expression:

$$f_{xyz} = \frac{P_{xyz} - P_0}{1 - P_0} \quad \text{were} \quad P_{xyz} = \frac{\sum I_{xyz}}{\sum I_{hkl}} \quad \text{and} \quad P_0 = \frac{\sum I^0_{xyz}}{\sum I^0_{hkl}} \tag{2.3}$$

$\sum I_{xyz}$ is the sum of the intensities of the (xyz) reflections of the oriented sample, while $\sum I_{hkl}$ is the sum of all the (hkl) intensities of the oriented sample. Similarly, $\sum I^0_{xyz}$ is the sum of intensities of the (xyz) reflections of a randomly oriented reference powder sample, while $\sum I^0_{hkl}$ is the sum of all the (hkl) reflections of the reference (which is typically available from the ICDD database). The orientation factor f can vary from 0 for a randomly oriented sample to 1 for a perfectly oriented sample. The higher the value indicates, the better the orientation of the film in that particular direction. However, the Lotgering factor method has its limitations: it cannot provide any information about the in-plane orientation, it is not linear, and the orientation factor calculated for the same diffraction spectrum is shown to vary as a function of the selected reflections used in the calculation, and the degree of orientation calculation is only qualitative [192].

2.3.2 Strain measurement through XRD by modified $\sin^2(\psi)$ method

Residual stresses in thin films can result from epitaxial strain due to the lattice mismatch between the substrate and the film, growth stresses, and thermal strain because of the difference in thermal expansion coefficient mismatch between the substrate and the film. For non-epitaxial films in this work, only the strain from thermal mismatch is considered. During the crystallization process, when the film is cooled down from the highest temperature, the difference in thermal expansion coefficient causes the substrate and the film to cool down at a different rate. This difference results in residual stress in the film, which can be expressed as

$$\sigma_{th} = \frac{\mathrm{Y_f}}{1 - \nu_f} \times \epsilon = \frac{\mathrm{Y_f}}{1 - \nu_f} \times (\alpha_s - \alpha_f) \times (\mathrm{T} - \mathrm{T_i}) \tag{2.4}$$

where $\mathrm{Y_f}$ and ν_f are the Young's modulus and Poisson ratio of the film. α_s and α_f are the thermal expansion coefficient of the substrate and film, respectively. T and $\mathrm{T_i}$ denote the film crystallization and room temperature, respectively. The stress values obtained from the above

approximation can be slightly higher than the actual value because the film is assumed to be at zero stress during crystallization, which need not be the case. In addition, the temperature dependence of the thermal expansion coefficient of the substrates and the film and stress relaxation due to domain formation during cooling through the Curie temperature is not considered.

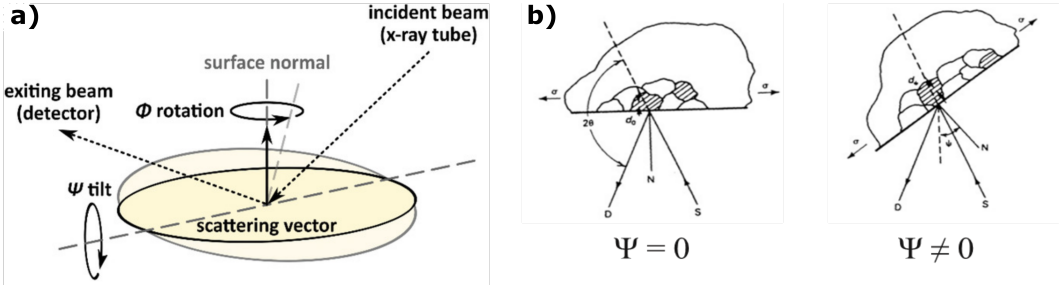

Figure 2.7: Schematic representation of (a) measurement geometry for modified $\sin^2(\psi)$ approach and (b) variation of d-spacing for different stress σ probed at different ψ tilts. Adapted from [193, 194].

Therefore, a modified $\sin^2(\psi)$-approach as described by Schenk *et al.*.[193] was used to quantitatively determine the in-plane stress σ_{11} and out-of-plane stress σ_{33} in the thin films. In the XRD measurement, θ - 2θ scans of certain $\{hkl\}$ peaks are performed for different tilt angles ψ. The schematic of the measurement geometry illustrating various angles in XRD is shown in Figure 2.7. One can plot the shift in 2θ peak position of $\{hkl\}$ family of planes with varying ψ values. This shift is due to substrate-stress induced lattice strain γ_ψ can be calculated from the corresponding lattice plane spacing d_ψ according to the equation below.

$$\gamma_\psi = \frac{d_\psi - d_0}{d_0} = [\gamma_{11} - \gamma_{33}] \times sin^2(\psi) + \gamma_{33} \tag{2.5}$$

where d_0 is the unstrained reference lattice plane spacing and γ_{11} and γ_{33} are the in-plane and the plane-normal strain components, respectively. If the Poisson ratio ν is known, one can substitute γ_{11} for γ_{33} and obtains

$$d_\psi = \frac{(1+\nu)}{(1-\nu)} \times \gamma_{11} \times d_0 \times \sin^2(\psi) + [1 - \frac{2\nu}{1-\nu}\gamma_{11}] \times d_0 \tag{2.6}$$

Then the values of d_{hkl} vs. $\sin^2(\psi)$ can be plotted and it will show a linear behavior. Solving the equation system composed of axis intercept n and slope m of a linear fit of that plot, gives:

$$d_0 = \frac{(1+\nu) \times \eta + 2 \times \nu \times m}{1+\nu} \tag{2.7}$$

$$\gamma_{11} = \frac{(1-\nu) \times m}{(1+\nu) \times \eta + 2 \times \nu \times m} \tag{2.8}$$

This approach guarantees a self-consistent set of strain and stress values respecting basic mechanical principles such as out-of-plane stress $\sigma_{33} = 0$. Often, the lattice parameters did not agree with powder diffraction files, and a proper reference was not readily available [193]. Therefore, this reference-free modified approach relied on the elastic constants of the materials, i.e., the Poisson ratio (ν) for the calculation of strain and Young's modulus (Y) for the subsequent transformation into stress values (in-plane stress (σ_{11}) and plane-normal stress (σ_{33})). The impact of uncertainties in ν and Y on the strains and stresses in the range of a few percent or a few tens of percent was significantly lower than expected from variations in d_0 from a powder diffraction file.

2.4 Scanning Electron Microscopy

The scanning electron microscopy (SEM) utilizes a focused electron beam to scan the specimen's surface systematically and allows for the observation and imaging of microstructural features that cannot be resolved by an optical microscope. The electrons interact with the given sample in different ways resulting in elastic and inelastic scattering producing backscattered electrons, secondary electrons, Auger electrons, x-rays, and cathode-luminescence. All of these signals can be used to form the image or perform elemental analysis of the sample. The secondary electrons mode was mainly used during this work to create a topographical image of the samples. Microstructural characterizations of the surface and cross-sections of the thin films are performed using a Helios NanoLab 650 scanning electron microscope (FEI, USA) in this work. Thin film samples are cleaved and mounted on the specific stubs for cross-sectional and surface imaging. For the films on non-conductive substrates, a very thin layer (5-10 nm) of platinum is sputtered to avoid the accumulation of surface charges when under an electron beam.

2.5 Electrical characterization

Electrical characterization for a ferroelectric thin film capacitor refers to measuring its ferroelectric and dielectric properties, namely polarization, permittivity, and losses. In addition, reliability studies, including the polarization degradation during fatigue cycling and dielectric breakdown, are also considered. Ferroelectric thin film analyzer aixACCT TFA 2000 was used for all these measurements. Probe tips are used for contacting the top and bottom electrodes; for a MIM

sample, contact for the bottom electrode was established using silver paint along the sides of the substrates. Contact pads are specifically designed for the planar IDEs to allow for the ease of contacting the fingers of positive and negative polarity with the probe tips.

A virtual ground method is used for measuring the polarization current, and the current is integrated over a given time of the application of an oscillating field. This measurement method shields the capacitor from any back voltage and parasitic capacitance from the cables. The virtual ground method uses an operational amplifier whose inverting input is connected to the output of the current to voltage converter through a feedback resistor and the ground. The voltage is measured as the difference between the output of the operational amplifier and the ground (the non-inverting input). The voltage difference between the inverting and non-inverting input is ideally zero or negligible; therefore the capacitor under measurement is connected to a virtual ground [195].

2.5.1 Capacitance measurement

For a classical capacitor arrangement with a dielectric material sandwiched between two metal plates, the capacitance of the dielectric layer is given by the ratio of the charges at the surface to the applied voltage $\delta Q/\delta V$. The generated charge is given by $Q = AD$, where D is the displacement, and A is the area. The dielectric displacement is given by

$$D = \varepsilon E + P \tag{2.9}$$

where ε is the dielectric permittivity given by the product of vacuum permittivity ε_0 and the relative permittivity ε_r of the material under investigation, and P is the polarization. Electric field (E) is the measure of the voltage applied over the thickness of the dielectric layer. For a pure dielectric response of the material, the polarization is proportional to the electric field in a linear approximation given by

$$P = \varepsilon_0 \chi_e E \qquad or \qquad D = \varepsilon_0 \varepsilon_r E \tag{2.10}$$

were χ is the dielectric susceptibility, it is related to the relative permittivity by $\chi = \varepsilon_r - 1$. Therefore, the capacitance and permittivity of the given dielectric (ferroelectric) material can be rewritten as,

$$C = \frac{A}{d}\frac{\delta D}{\delta E} = \frac{A}{d}\epsilon_0\epsilon_r \quad \text{and} \quad \epsilon_r = \frac{d}{A\epsilon_0}C \tag{2.11}$$

Permittivity hysteresis (can be referred to as small signal measurements) is obtained by measuring the small signal current response of the material. It gives information about the reversible parts of polarization and the switching process. It is performed by applying a high frequency (in the order of kHz) AC signal of small amplitude superimposed over a DC bias signal. The DC bias signal is applied in a step-by-step fashion, and it is cycled through the hysteresis loop. The small signal measurement sequence is shown schematically in Figure 2.8(a).

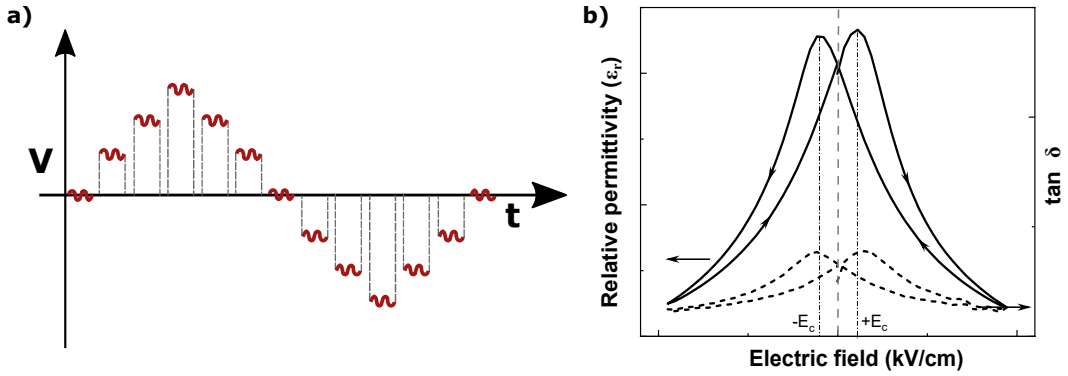

Figure 2.8: (a) Excitation signal for C-V (small-signal) measurement and (b) permittivity hysteresis ($\varepsilon_r - E$) loop as a function of bias field.

The capacitance values are then derived from the AC small signal current response of the sample and expressed as a function of the DC bias field. The permittivity values can be calculated from the capacitance. The loss tangent, a value indicating the measure of dielectric loss, is also usually recorded. As the relative permittivity ($\varepsilon_r = \varepsilon^{'} + j\varepsilon^{''}$) is usually expressed as a complex quantity, where the real part ($\varepsilon^{'}$) corresponds to the electrical energy stored in the material, and the imaginary part ($\varepsilon^{''}$) corresponds to the energy dissipated by the material (losses) [55]. Therefore, the loss tangent is expressed as the ratio of imaginary to the real part of the permittivity ($\tan\delta = \frac{\varepsilon^{''}}{\varepsilon^{'}}$). The permittivity hysteresis exhibits a signature butterfly-shaped loop shown in Figure 2.8(b). As the field is cycled through, the permittivity response at zero fields is recorded to be used as a characteristic value of the material. The maxima are seen around the coercive ($+E_c$ and -E_c) field values, where the domain switching happens.

2.5.2 Polarization measurement

Polarization hysteresis measurement is performed by applying a triangular voltage signal (shown in Figure 2.9(a)) at a given frequency and continuously recording the polarization current

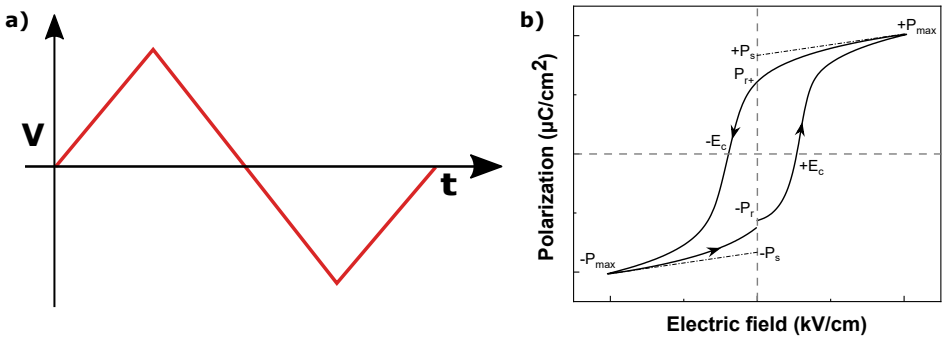

Figure 2.9: (a) Excitation signal for P-E hysteresis measurement, (b) polarization hysteresis loop measured for a single triangular excitation signal.

response. For an ideal, non-leaky ferroelectric capacitor, polarization can be given by:

$$\frac{1}{A}\int_0^{\Delta t} i(t)\ dt = P(\Delta t) - P(0) = \Delta P \tag{2.12}$$

Here, ΔP is the change in polarization over time (Δt). The polarization hysteresis loop in Figure 2.9(b) is obtained by representing P as a function of the electric field E. The remanent polarization ($+/-P_r$), maximum polarization ($+/-\mathrm{P_{max}}$), the saturation polarization ($+/-P_\mathrm{s}$), and the coercive field values ($+/-E_\mathrm{c}$) are indicated in Figure 2.9(b). The shape of the hysteresis loop depends on the frequency at which it is measured. The shape of the loop is altered based on defect chemistry, dopants, mechanical stresses, and poling history [60, 196].

2.5.3 Fatigue measurement

'Fatigue' refers to the degradation of material properties under cycling. In the context of ferroelectric materials, it typically refers to the degradation of piezoelectric coefficients, remanent polarization, or electrical permittivity under cyclically varying electric fields. The fatigue cycling is performed by applying a bipolar or uni-polar excitation signal at a given frequency for several hundred to million cycles. However, the shape and sequence of the excitation signal can be varied to match the specific application requirement. Polarization and permittivity hysteresis is measured in situ at regular intervals during the fatigue cycling to monitor the evolution of material properties. The cycling signal amplitude, frequency, waveform, and the number of switching cycles are chosen in a way that replicates the desired operating conditions. The results of fatigue cycling point to the lifetime of the material or device under test. Usually, higher frequency and cycling amplitudes are chosen to demonstrate the degradation of material properties within a reasonable measurement time, and later the results are extrapolated to the operating conditions. Care must

be taken when choosing a higher frequency for fatigue cycling. One must ensure that there will be complete switching at a higher frequency and monitor the limitations of the measurement device to deliver higher driving power. The schematic of the fatigue measurement sequence and an example of remanent polarization degradation of PZT thin film on Si substrate from this study are shown in Figure 2.10.

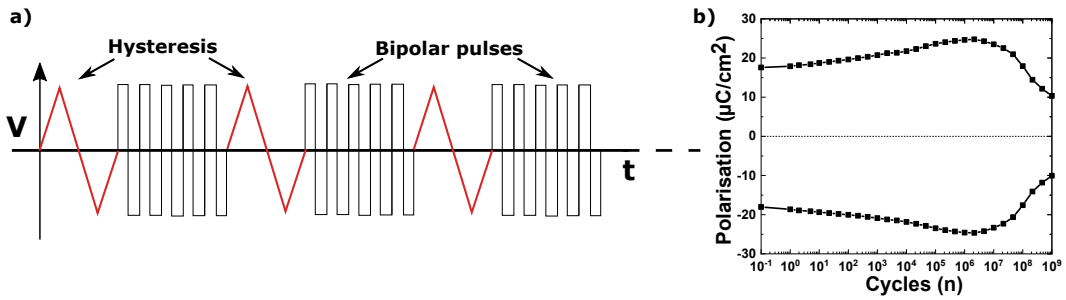

Figure 2.10: Excitation signal for (a) fatigue measurement with bipolar pulses with hysteresis measurement at regular intervals, adapted from [195] (b) Typical result of a fatigue measurement depicted as the remanent polarization versus log cycles of the excitation signal.

2.5.4 Breakdown measurements

In the context of ferroelectric materials, breakdown refers to the dielectric breakdown under the application of a large enough electrical field. The dielectric breakdown strength is governed by the material's intrinsic strength or by the presence of defects and free charge carriers. Breakdown tests are often designed and adapted to understand the effect and mechanism that drives the dielectric breakdown in a given material. There are two ways in which the material's breakdown characteristics can be measured: applying a constant voltage over a period of time and monitoring the evolution of current or applying linearly varying voltage (staircase mode) until the material breaks down. Figure 2.11 shows different breakdown testing sequences.

Both test scenarios can be used to determine the statistical distribution of breakdown strength as a function of applied voltage and current or to estimate the time to breakdown for a given driving condition. During the constant voltage stress (CVS) measurement, the time to breakdown (t_{bd}) value is determined by collecting the leakage current over time which can also be monitored evolution of charge and recording charge to breakdown (Q_{bd}). The dielectric breakdown is marked by a sudden jump in the current value due to a short circuit. With the linear ramp voltage stress test (LRVS), the breakdown voltage (V_{bd}) is determined by monitoring the current at each voltage step and a sudden jump in the current value over a few orders of magnitude indicates the breakdown. It is essential to understand that the breakdown test scenarios have to be defined

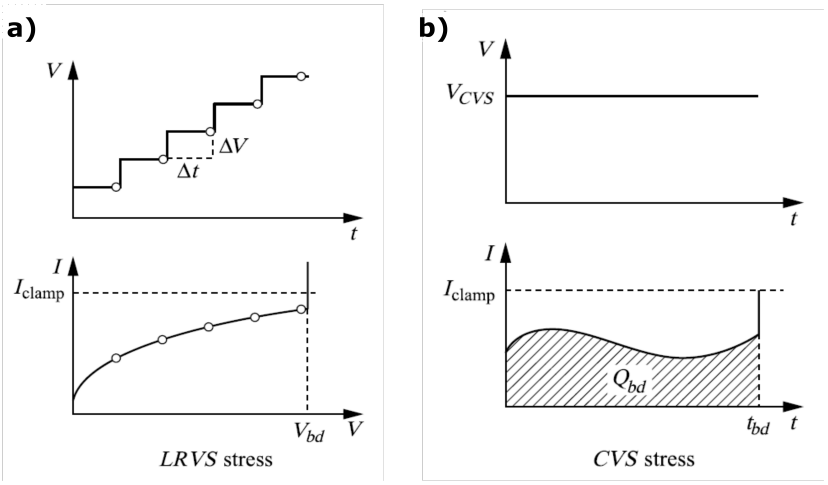

Figure 2.11: Different breakdown measurement types used in this study for (a) Linear ramp voltage stress (LRVS) and (b) Constant voltage stress test (CVS). Adapted from [197]

clearly to meaningfully predict the breakdown conditions and mechanism. For example, with CVS measurement, it is important to indicate the number of capacitors tested, location of the capacitors on the given wafer, temperature conditions, poling history, etc. For an LRVS test, it is important to precisely define the mode of operation, ramp rate (step size and width), temperature conditions, poling state, or history. Often the geometry and type of the electrode also play an important role. The breakdown tests can also be performed in an accelerated way, either by applying higher voltages than the operating voltage or testing the capacitors at elevated temperatures. Under these accelerated conditions, the voltage or temperature dependent breakdown strength can also be determined.

Chapter 3

Effect of thin film deposition process on structural and ferroelectric properties of solution deposited PZT thin films

The influence of deposition parameters on structural and ferroelectric properties of PZT thin films is discussed in this chapter. PZT films are deposited on different substrates, and the process parameters like pyrolysis and annealing temperature are changed to understand the variations in microstructure and their impact on polarization and permittivity. The film's crystallographic texture, grain size, and morphology are compared to arrive at the optimal processing conditions. PZT thin films are deposited with seed layers prepared with two different solvents to study the effect of the seed layer on the texture of the film. Furthermore, a solution deposited HfO_2 buffer layer was developed to replace the ALD deposited HfO_2 layer. The properties of PZT thin films deposited on substrates with CSD-HfO_2 are compared with the film with the ALD-HfO_2 layer. Results of microstructural and ferroelectric characterization from all the experiments are compared. Samples with suitable texture and better ferroelectric properties are chosen for further experiments and reliability studies, which will be discussed in the forthcoming chapters.

3.1 PZT thin films on platinized Silicon (Pt/Si) wafers

3.1.1 Variation of pyrolysis and annealing temperature

The initial development of CSD based process route for PZT thin film was done on platinized silicon (Pt/Si-SINTEF) substrate. The precursor solutions and the deposition process developed by Godard et al. [71] (as outlined in the experimental methods chapter) are followed for this study. The importance and influence of pyrolysis and annealing temperature on the microstructure were discussed in Chapter 1. The microstructural evolution is nucleation mediated, and nucleation can be homogeneous or heterogeneous. Heterogeneous nucleation starts from the surface or the interface between the substrate and the film. It is also governed by the processing conditions such as heating rate, annealing temperature, and annealing atmosphere. Here, the pyrolysis and annealing temperatures are modified to understand the texture and grain size evolution. It was postulated that the changes in grain size could change the way in which the ferroelectric material can degrade during fatigue cycling [198]. Therefore, the texture and grain size evolution are compared for a different combination of pyrolysis and annealing temperatures for the films deposited with and without the $PbTiO_3$ (PTO) seed layer prepared using 2-methoxyethanol (2MoE-PTO).

As a first step, the thin film samples deposited on Pt/Si are subjected to different pyrolysis temperatures from 300 °C to 450 °C, and the annealing temperature is maintained at 700 °C. Later the pyrolysis temperature is maintained at 350 °C, and the annealing temperature is varied between 700 and 800 °C. XRD and SEM analysis was performed on all these samples. It can

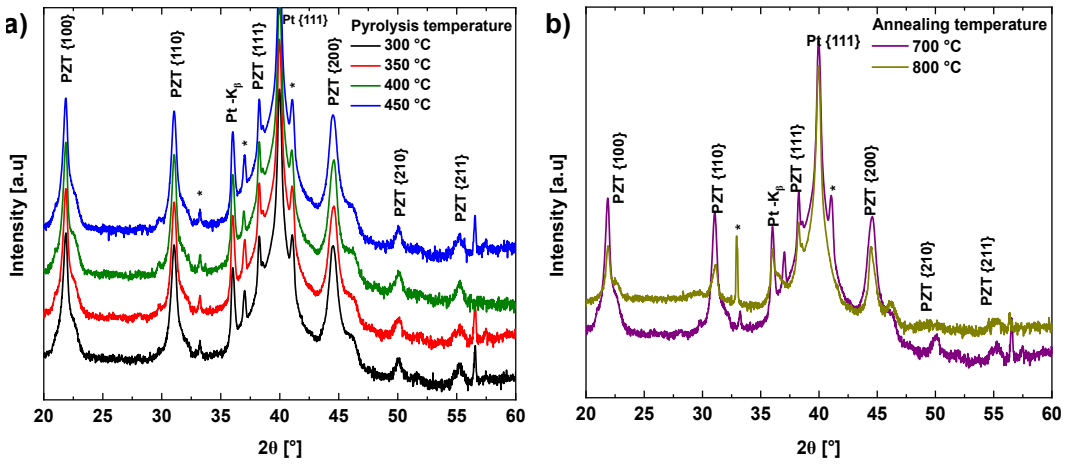

Figure 3.1: X-ray diffractogram of PZT thin films with 2MoE-PTO seed layer on Pt/Si-SINTEF (a) pyrolyzed at different temperatures and annealed at 700 °C, and (b) films pyrolyzed at 350 °C and annealed at different temperatures. *-indicates substrate peaks.

be observed from Figure 3.1(a) that changing the pyrolysis temperature did not change the film

texture from being oriented in $\{100\}$ direction to any considerable extent, and there is no evidence of secondary phases from the X-ray diffractograms. Whereas, from the SEM images in Figure 3.2, it can be observed that there was an increase of secondary phases (pyrochlore) on the surface of the films with increasing pyrolysis temperature without any noticeable change in grain size. The average grain size estimated by the line analysis method for all the PZT samples is in the range of 80-110 nm. The pyrochlore is limited only to the surface of the samples, and it could be due to the loss of Pb during processing; higher temperature leads to more Pb loss. Increasing the annealing temperature to 800 °C with the constant pyrolysis temperature of 350 °C changed the film texture, which can be seen in Figure 3.1(b). The intensities of $\{100\}$ and $\{200\}$ peaks are lower, and the sample appears to be more randomly oriented. Cracks are also visible on the film surface, and that can be observed from the SEM images in Figure 3.3. The annealing temperature was already at the upper limit of the processing temperature for silicon wafers. It was evident that annealing at 800 °C can induce cracking of films due to deformation of the Si substrates. Increasing the pyrolysis temperature above 350 °C can also increase the secondary phases on the surface.

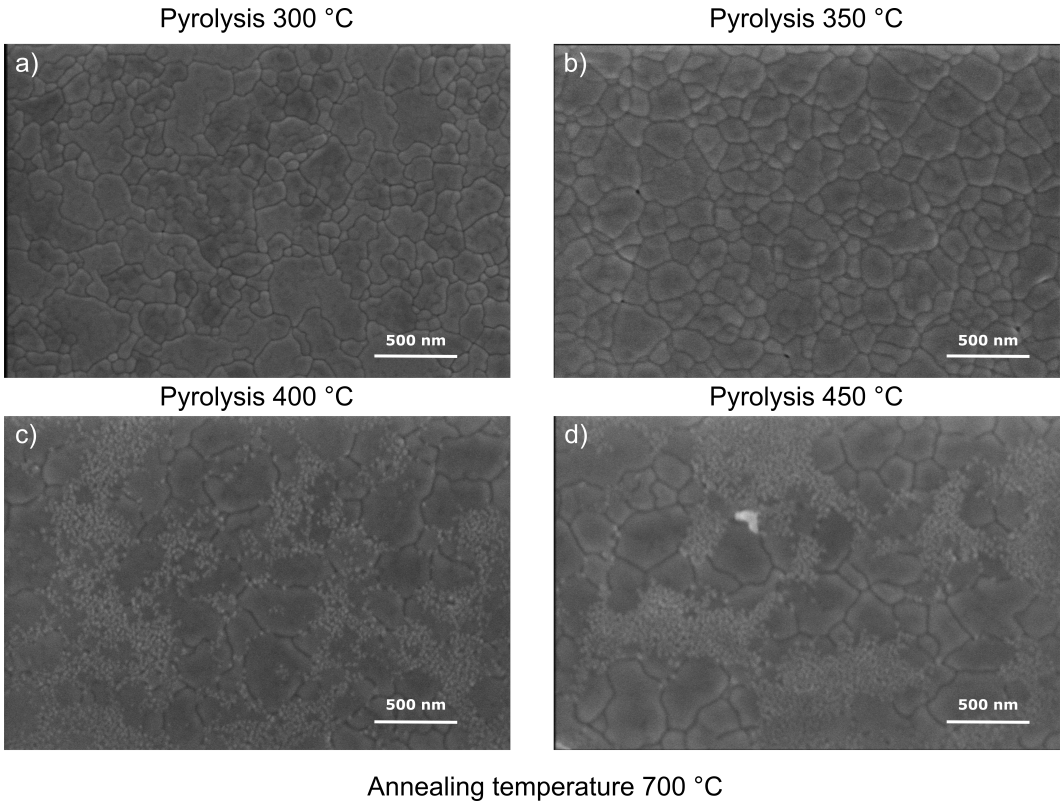

Figure 3.2: SEM topography images of PZT thin films with 2MoE-PTO seed layer on Pt/Si-SINTEF pyrolyzed at different temperatures and annealed at 700 °C.

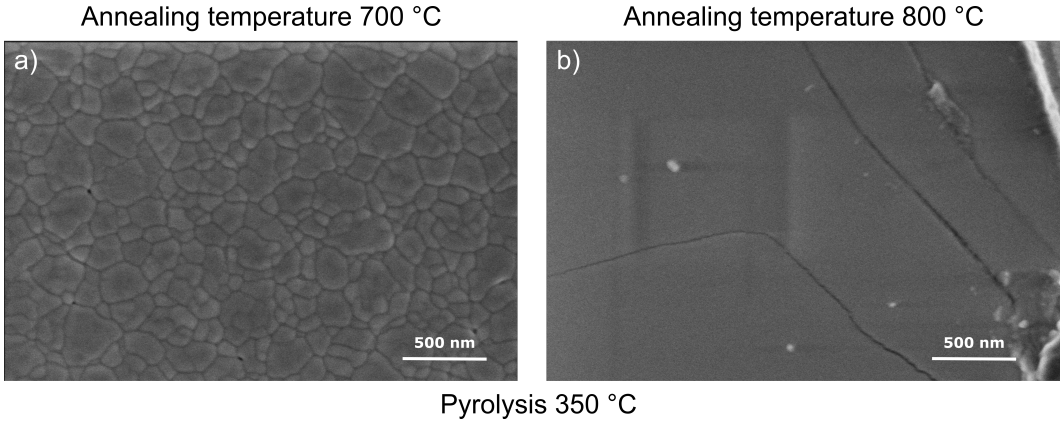

Figure 3.3: SEM topography images of PZT thin films with 2MoE-PTO seed layer on Pt/Si-SINTEF pyrolyzed at 350 °C and annealed at (a) 700 °C and (b) 800 °C. No grains were visible on the cracked surface in (b).

3.1.2 Effect of PTO seed layer

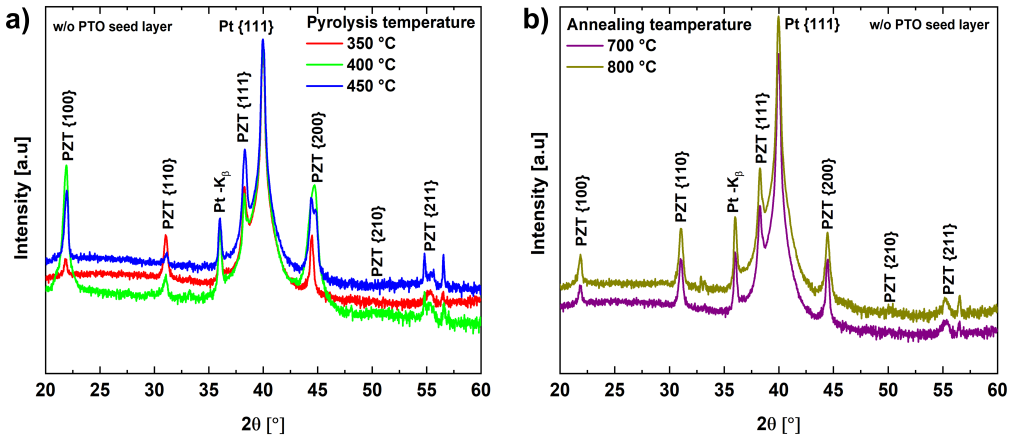

Figure 3.4: X-ray diffractogram of PZT thin films without 2MoE-PTO seed layer on Pt/Si-SINTEF (a) pyrolyzed at different temperatures and annealed at 700 °C, and (b) films pyrolyzed at 350 °C, and annealed at different temperatures.

The next set of experiments is devised with the idea of removing the PTO seed layer. It could be noticed from the XRD patterns in Figure 3.4(a) that the film texture changed from being $\{100\}$ oriented to a random orientation, where the intensities of $\{100\}$ peaks are reduced and all the other PZT peak intensities are increased equally. In comparison to the films with a seed layer, grain sizes also increased (400-600 nm) when the pyrolysis temperature was increased, but not monotonically. Although the grain sizes increased for the samples without seed layer pyrolyzed above 400 °C, several clusters of secondary phases could be observed on the film surface as shown in the SEM images in Figure 3.5. These secondary phases would be detrimental to the ferroelectric

properties of the resulting PZT films. Increasing the annealing temperature to 800 °C without seed layer also altered the film texture and increased the surface pyrochlore on the film as seen in Figures 3.4(b) and 3.6.

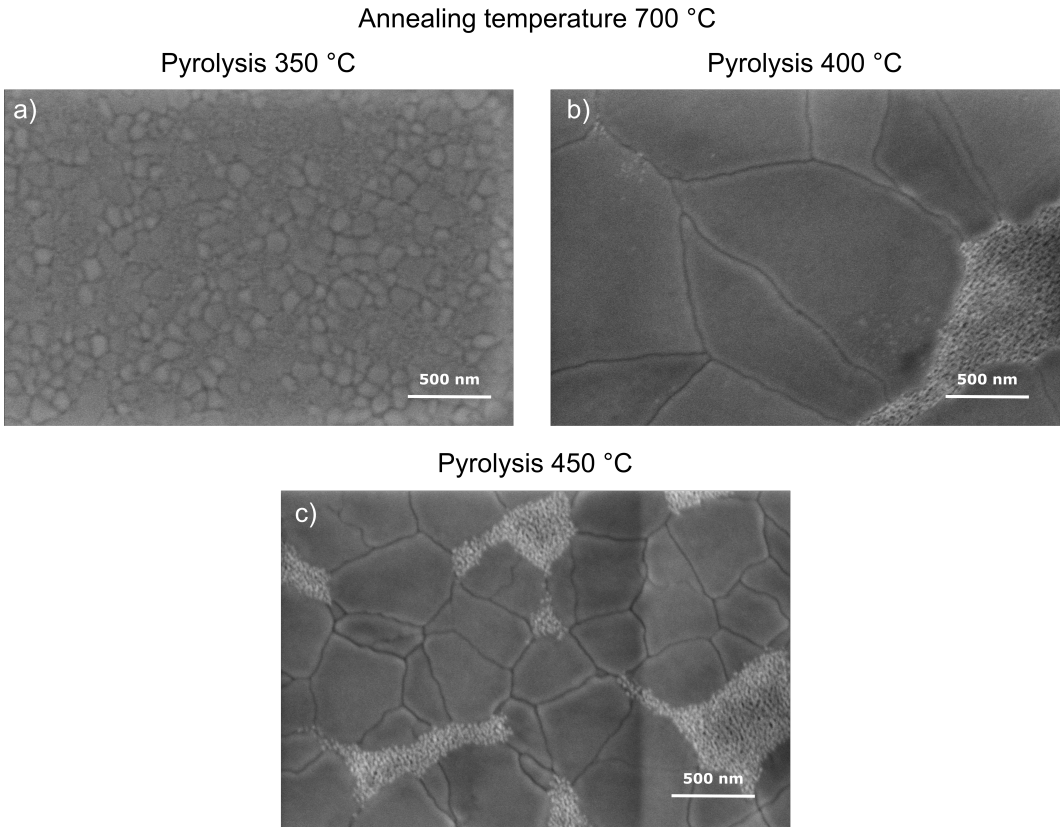

Figure 3.5: SEM topography images of PZT thin films without 2MoE-PTO seed layer on Pt/Si-SINTEF pyrolyzed at different temperatures and annealed at 700 °C.

To summarize the results of the above experiments, the presence of the seed layer is essential to preserve the required texture (i.e., $\{100\}$ orientation) of the PZT films. Increasing the pyrolysis temperature beyond 350 °C without the PTO seed layer increased the secondary phases, although there was an increase in grain sizes due to abnormal grain growth. On the other hand, the annealing temperature could not be increased beyond 800 °C due to the limitation of the processing temperature of Si wafers and the risk of running into practical difficulties of breaking the wafers in the annealing chamber. So, it was understood that the grain size could not be increased without a compromise in ferroelectric properties, which may again be less helpful in increasing the resistance to degradation of switchable polarization during fatigue cycling experiments. Therefore, the pyrolysis temperature of 350 °C and the annealing temperature of 700 °C with the PTO seed layer are chosen for further course of PZT thin film deposition in this study.

The XRD, SEM, and ferroelectric behavior of 500 nm thick PZT film on Pt/Si-SINTEF that

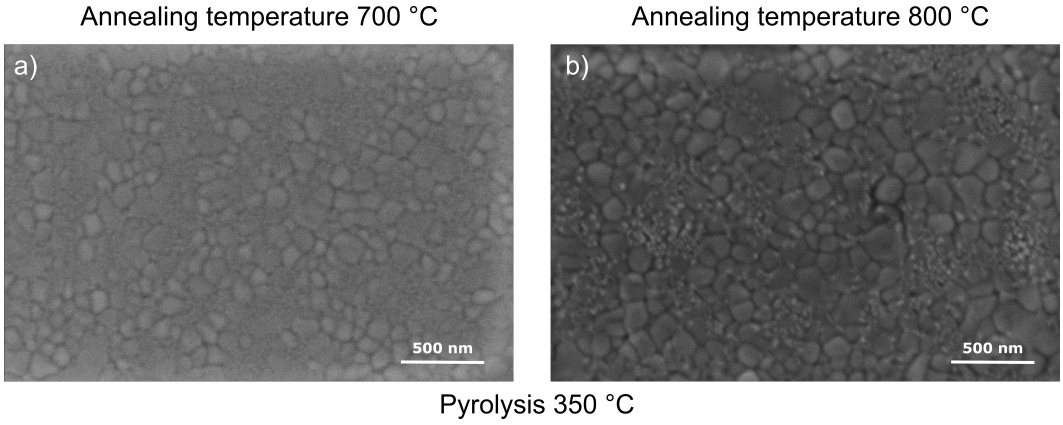

Figure 3.6: SEM topography images of PZT thin films without 2MoE-PTO seed layer on Pt/Si annealed at different temperatures and pyrolyzed at 350 °C.

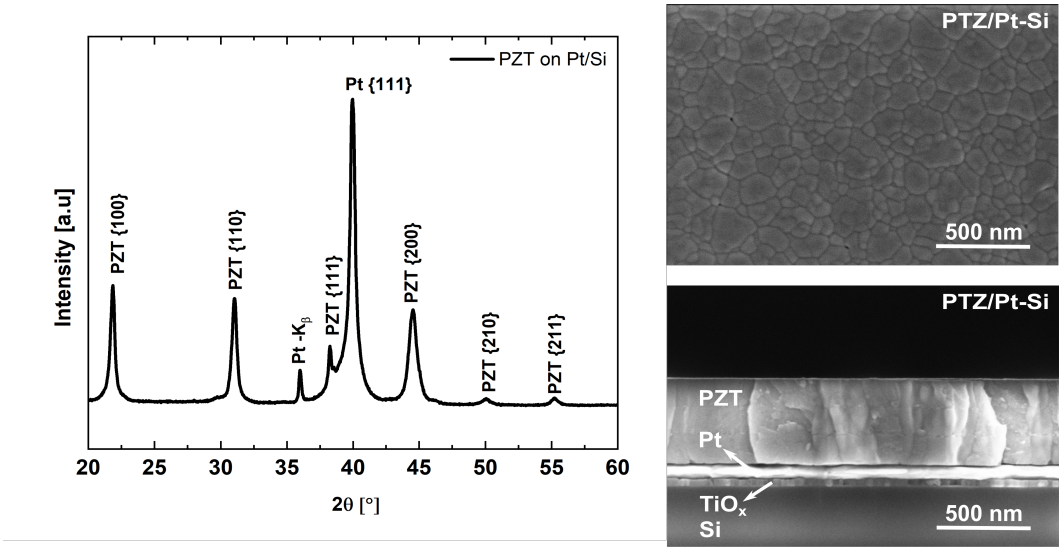

Figure 3.7: X-ray diffractogram (left), and SEM surface (top right) and cross-section (bottom right) images of PZT thin film on Pt/Si-SINTEF.

are prepared following the chosen condition are shown in Figure 3.7. It can be observed from the XRD plot that the PZT film on Pt/Si is preferentially oriented in $\{100\}$ pseudo cubic direction. Furthermore, a dense and columnar microstructure without any secondary phase is observed from the surface and cross-section SEM images. The ferroelectric properties were comparable to the state-of-the-art CSD-based PZT films grown on Pt/Si with P_r of 12-15 μC/cm^2, P_{max} of 30-32 μC/cm^2 and E_c around 50 kV/cm. [74, 199, 200].

3.2 PZT thin film on fused silica and sapphire substrates with bottom electrodes

The naming convention for the films with and without bottom electrode are followed using the electrode configuration (MIM or IDE) and the convention for indicating the substrate on which the PZT was deposited. For example, the PZT film on fused silica with and without a bottom electrode is referred to as PZT/FS-MIM and PZT/FS-IDE, respectively. Similar conventions are followed for other substrates with respective electrode configurations throughout the course of this thesis.

Further to add to the above combinations, PZT thin film stacks on fused silica and sapphire substrates with Pt bottom electrodes were also developed during this study. HfO_2 buffer layer was deposited first on the wafers by ALD, and a 100 nm thick platinum was subsequently sputtered onto the substrates at room temperature to be used as a bottom electrode. A 500 nm thick PZT is then deposited after Pt deposition. The details of the deposition sequence were discussed in Chapter 2 already. Figure 3.8 shows a plot of x-ray diffractogram of PZT films on platinized fused silica (Pt/FS) and sapphire (Pt/SP) compared with film on Pt/Si. Surface and cross-section SEM images of these films were also shown in Figure 3.8. The films are dense and columnar without any sign of porosity and secondary phases in bulk. Surface pyrochlore is seen on the PZT/FS-MIM film and is comparable to the films on Pt/Si pyrolyzed at 400 °C, as shown in the previous section.

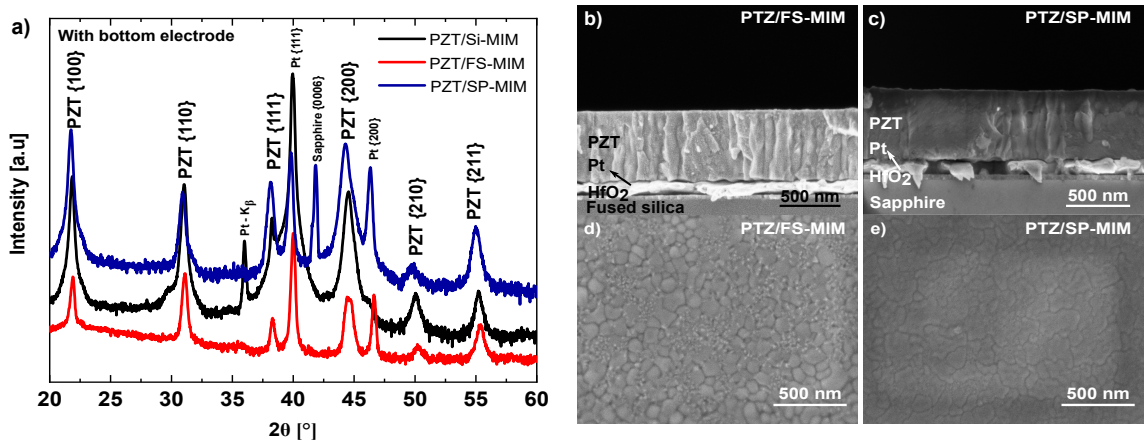

Figure 3.8: XRD patterns (a) and SEM cross section (b, c) and surface images (d, e) of the PZT films with bottom electrodes on different substrates pyrolyzed at 350 °C and annealed at 700 °C.

3.3 PZT thin film on Si, fused silica and sapphire substrates without bottom electrodes

The deposition route for growing PZT thin film on fused silica substrate without a bottom electrode was initially developed by Glinsek et al. [7], following similar processing conditions proposed by Godard et al. [71]. One key difference in the work of Glinsek et al. [7] is the development of a PZT thin film stack without bottom electrodes to be used with planar interdigitated electrodes (IDEs). ALD deposited HfO_2 was used as a diffusion barrier layer between the substrate and the PZT film to prevent the diffusion and reaction of lead with SiO_2 forming lead silicates. The same strategy is used in this work for growing PZT on the fused silica substrate without a bottom electrode. As an extension, silicon and sapphire substrates were also explicitly used for this work to deposit PZT thin films without bottom electrodes, following the methodology outlined in the work of Glinsek et al. [7].

However, using Si substrates with only 500 nm thick SiO_2 (as procured from SIEGERT), along with HfO_2 diffusion barrier layer to deposit PZT film was developed for the first time during this work. The Si substrate acts as a floating electrode when used without a thicker insulating oxide layer or a bottom electrode. However, even with a thicker oxide layer, a diffusion barrier layer is still needed to prevent the inter-diffusion of metallic atoms while depositing thin films. Also, growing a thicker oxide layer in-house needs a special process to be developed. Therefore, using a dielectric HfO_2 layer not only acts as a diffusion barrier layer but also proved beneficial in our case by partially insulating the effect of the floating Si electrode. This process allowed for efficiently integrating PZT thin film on Si wafer and operating it with planar interdigitated electrodes. However, the IDE design had to be optimized for using it with the PZT film on the Si substrate. A schematic of the PZT stack on Si substrates is illustrated in Figure 3.9.

The XRD patterns of PZT films on Si, fused silica, and sapphire substrates are shown in Figure 3.10. All the films are preferentially oriented in $\{100\}$ direction and the SEM images in Figure 3.11 show dense and columnar microstructure with comparable grain sizes.

Surface pyrochlore was often observed on these films due to the loss of Pb during processing. As discussed above, the drying (130 °C), pyrolysis (350 °C), and the crystallization (700 °C) were performed at the same temperature for PZT films on all the substrates. However, the presence of a secondary phase only for PZT on fused silica and not on PZT on Si or sapphire could be attributed to the difference in thermal conductivity of the substrates. For example, thermal conductivity of sapphire (23.2 – 30 W/m-K) [201] is much higher than the thermal conductivity of silicon (3

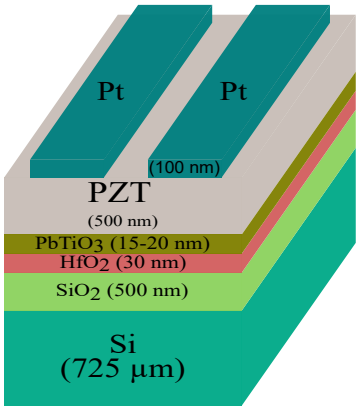

Figure 3.9: Schematic of PZT thin film stack on Si substrate with IDEs, thicknesses of each layers are also indicated. Note: the layers are not to scale.

W/m-K) [202], and fused silica (1.38 W/m-K) [203]. From the view of the thin film crystallization process that has been reported in some of the works related to sol-gel deposited PZT thin films [204–206], crystallization often proceeds through the formation of an intermediate disordered fluorite phase exhibiting a pyrochlore structure. This intermediate phase is then transformed into the thermodynamically stable perovskite phase at higher temperatures. In some cases, the pyrochlore phase can be stabilized where the loss of volatile cations (Pb) is more pronounced due to variations in crystallization temperature, thermal profile, annealing atmosphere, etc. In the current scenario, the differences in the overall thermal profile that can arise due to the difference in thermal conductivities of the substrates can be a reason that some surface pyrochlore is seen on PZT on fused silica but not on others.

3.4 Influence of diffusion barrier layer on PZT thin film texture

The need and importance of a diffusion barrier layer for a PZT thin film stack were discussed in Chapter 1. Based on the preliminary results on the use of ALD deposited HfO_2 as a diffusion barrier or buffer layer, a CSD-based route for the deposition of HfO_2 is developed. This idea is to make the entire stack development process more cost and time efficient. Several research groups have already demonstrated growing HfO_2 thin film by CSD route [107, 207–209] for using it not only as a high k-dielectric layer but also as a ferroelectric material. The work of Schenk et al. [110] was followed for the deposition of HfO_2 by spin coating (also explained in the previous chapter). The CSD deposited HfO_2 layer is annealed at 700 °C for 90 s in 1:1 Ar/O_2 atmosphere in contrast to the ALD deposited HfO_2 layer, which is annealed at 700 °C for 300 s in ambient condition. After the deposition of the HfO_2 layer, the usual processing route explained earlier

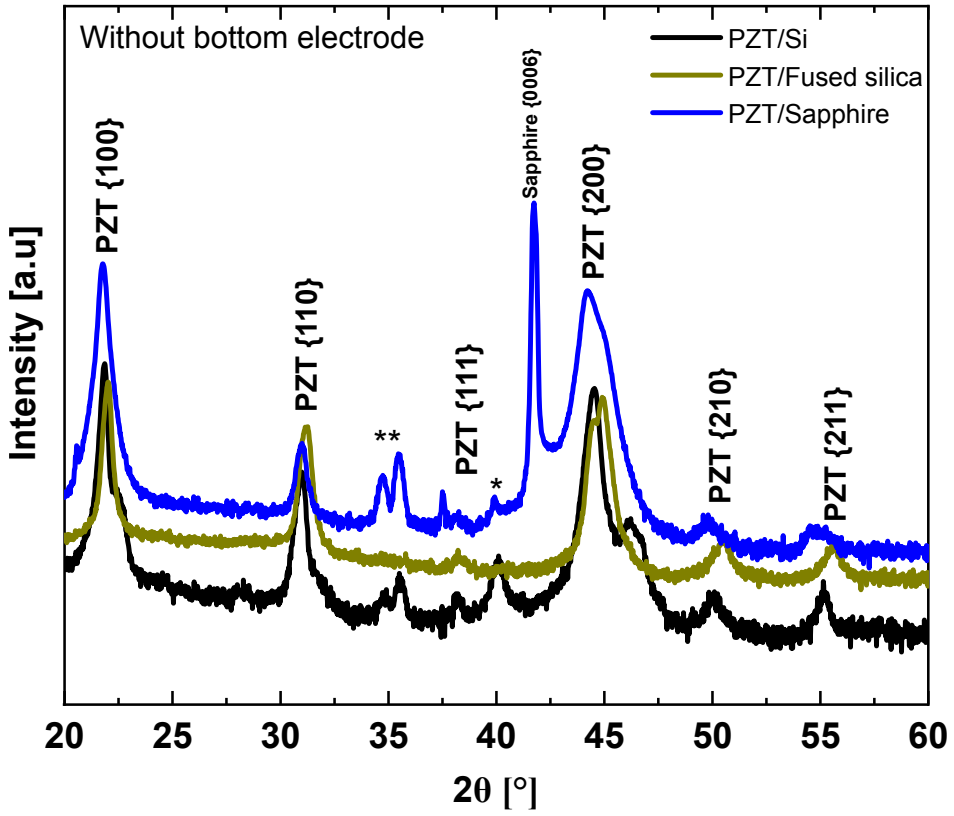

Figure 3.10: XRD patterns of the PZT films without bottom electrodes on different substrates pyrolyzed at 350 °C and annealed at 700 °C. *-indicates substrate peaks.

is followed to deposit PZT thin film with or without the bottom electrode. It is also worth mentioning that having ALD/CSD deposited HfO_2 layer allowed the use of Si wafer with 500 nm thick oxide layer to be sputtered with sputtered Pt-bottom electrode ($Si/SiO_2/HfO_2/Pt$) for MIM configuration opposed to the use of Pt/Si wafer from SINTEF, thus making the process, even more, cost-effective. This resulted in an equivalent set of thin films with the diffusion barrier layer deposited by the ALD or CSD route. The XRD patterns of all these films in comparison to the ones with ALD-HfO_2 are shown in Figure 3.12.

The analysis of the XRD patterns in Figure 3.12 showed that the film stacks with Pt bottom electrode did not show any considerable difference in their respective textures. There were only slight improvements in the texture for the film on Pt-FS with the ALD-HfO_2 and Pt-SP with the CSD-HfO_2. On the other hand, the films without the bottom electrode showed noticeable changes in their textures between the stacks with ALD and CSD deposited diffusion barrier layer. PZT films on all the three substrates showed an improved texture in the $\{100\}$ direction with the ALD-HfO_2 layer. The ferroelectric properties were not considered for analysis and comparison until this point, as the interest was mainly to reduce the processing time and the cost involved in

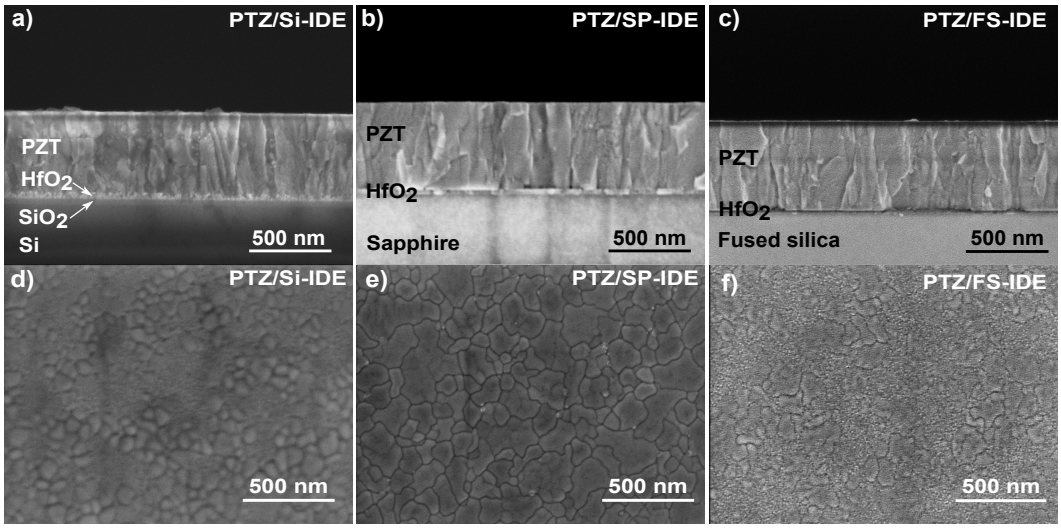

Figure 3.11: SEM cross section (a, b, c) and surface images (d, e, f) of the PZT films without bottom electrodes on different substrates.

developing a CSD-based route for PZT thin film deposition without compromising the structural properties of the film.

3.5 Variation of PTO seed layer solutions

The $PbTiO_3$ (PTO) seed layer solution is modified using a safer solvent, and their impact on crystallographic orientation and ferroelectric properties are analyzed. A safe solvent route for the synthesis of the PTO seed layer was first proposed and developed by Godard et al. [186] for replacing the widely used 2-Methoxyethanol (2MoE) solvent with a relatively safer 1-Methoxy-2-propanal (1M2P). A seed layer is typically used to impart a specific crystallographic orientation to the thin films, although the substrate and the bottom electrode may dictate other orientations [210]. For example, the platinized silicon substrate usually promotes the $\{111\}$ PZT orientation, whereas using a PTO seed layer promotes the $\{100\}$ orientation in the PZT film [4]. A seed layer also provides the benefit of processing the thin films at a lower temperature [211]. The 2MoE and 1M2P share a similar organic backbone with a variation in their functional substituent groups. However, 1M2P results in a less harmful by-product after thermal decomposition by the end of the pyrolysis step. The combined effect of well-defined facets of crystallized nano-islands and the improved orientation of the 1M2P-PTO seed layer was hypothesized to promote an improved texture in the $\{100\}$ orientation for the PZT film [186]. Therefore, the 1M2P-PTO seed layer is used to improve the texture and the ferroelectric properties of the PZT films.

A comparative analysis of X-ray diffractogram and ferroelectric characterization results for the

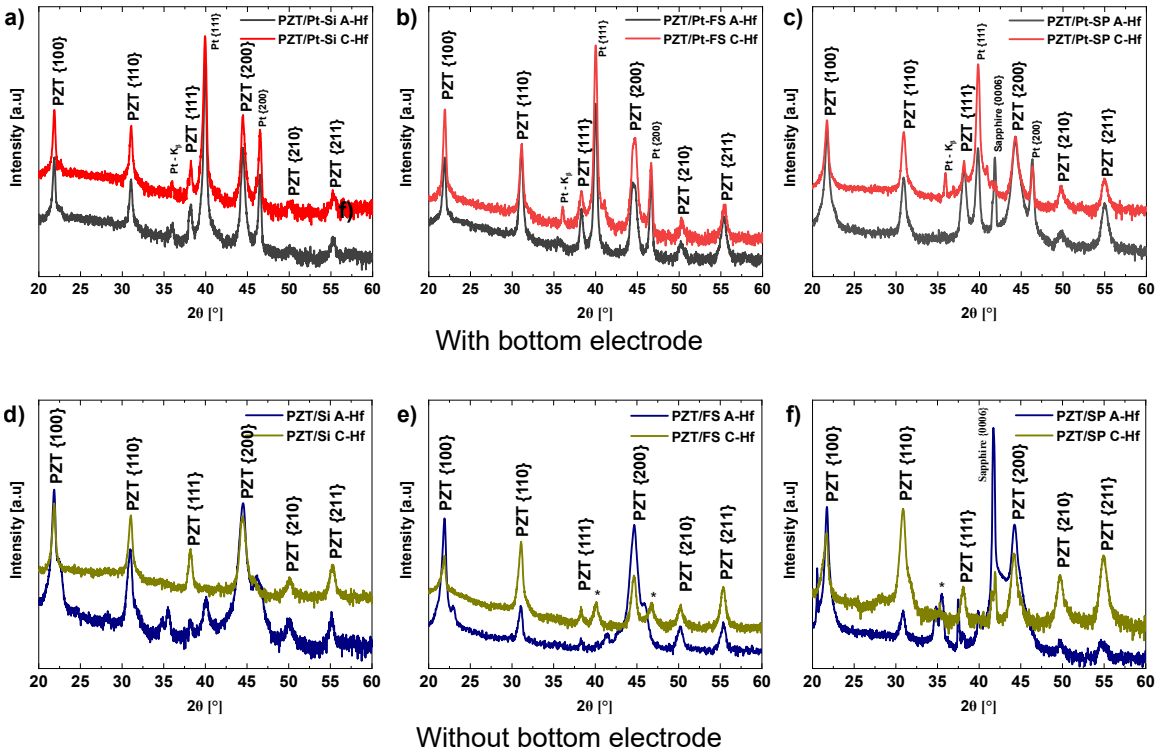

Figure 3.12: XRD patterns of PZT films deposited on different substrates (a), (b) & (c) with and (d), (e) & (f) without bottom electrode, deposited with ALD-HfO_2 (A-Hf) and CSD-HfO_2 (C-Hf) diffusion barrier layer to deposit the rest of the thin film stack. *-indicates substrate peaks.

PZT film on Pt/Si-SINTEF wafer are presented in Figure 3.13. The film with the 1M2P-PTO seed layer showed a stronger orientation and an improved texture in the $\{100\}$ direction compared to the film with the 2MoE-PTO seed layer. The remanent and maximum polarization values are in a comparable range for both the films, and the permittivity and loss values also correspond closely to each other. With these results as a reference, seed layer solutions are also varied for the deposition of PZT on fused silica, sapphire, and in-house developed Si substrates with and without bottom electrodes to understand the influence of seed layer solutions on the structural and ferroelectric properties.

3.5.1 Influence of 2MoE-PTO and 1M2P-PTO seed layer solution on the texture of PZT thin films

As discussed above, PZT thin films were deposited on three different substrates with and without Pt bottom electrodes. Now a new set of PZT thin film stacks with a 1M2P seed layer is also developed on all the substrates to create a combination of better possible texture and ferroelectric properties. The XRD patterns, polarization, and permittivity measurements are

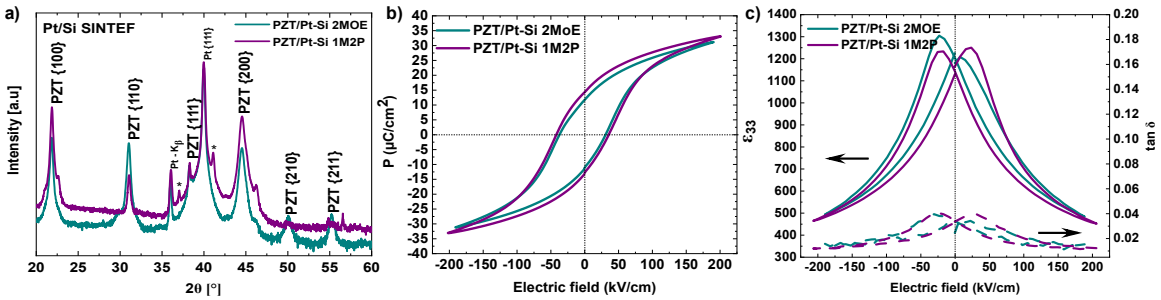

Figure 3.13: (a) X-ray diffraction patterns, (b) and (c) ferroelectric characterization results for the PZT film on Pt/Si substrate with 2MoE and 1M2P-$PbTiO_3$ seed layer. *-indicates substrate peaks in (a). P-E loops recorded at 100 Hz and ε_{33}-E loop recorded at 1 kHz small-signal frequency.

compared among the films on similar set substrates with different seed layers (1M2P-PTO or 2MoE-PTO), and the ones with a good combination of texture and ferroelectric properties are chosen for further investigations.

Figures 3.14, 3.15, and 3.16 compares the X-ray diffractograms, polarization hysteresis P(E), and permittivity measurements ε_{33}(E) of the films with 2MoE and 1M2P-PTO seed layers deposited on each substrates with and without bottom electrodes. Interestingly, using the 1M2P-PTO seed layer did not result in an improved texture in PZT on all the other substrates with the bottom electrode as opposed to the film on PZT/Si-MIM (from SINTEF). The PZT films on Si (PZT/Si-IDE) and fused silica (PZT/FS-IDE) without a bottom electrode followed a similar behavior as mentioned above. On the contrary, the film on sapphire (PZT/SP-IDE) without the bottom electrode showed an improved texture using the 1M2P-PTO seed layer. However, the polarization and permittivity values were not following the trend of texture improvements with the changes in the seed layer for PZT/SP-IDE. The polarization and permittivity values of the film on Si (PZT/Si-IDE) are poised with the effect of parasitic capacitance from the Si substrate and are considered outliers.

All the parameters considered for comparing different thin film stacks with their variations in the seed layer are tabulated in Table 3.1. The Lotgering factor values are considered for quantifying film texture (out-of-plane direction) in the $\{100\}$ pseudo cubic direction for PZT. Remanent and maximum polarization, coercive field, and permittivity values are extracted from the P(E) and ϵ_{33}(E) measurements.

It is interesting to observe the trend in which the polarization and permittivity values changed across the films on different substrates and the variation between the films on the same substrate but with different electrode configurations (i.e., MIM and IDEs). Furthermore, the residual stress,

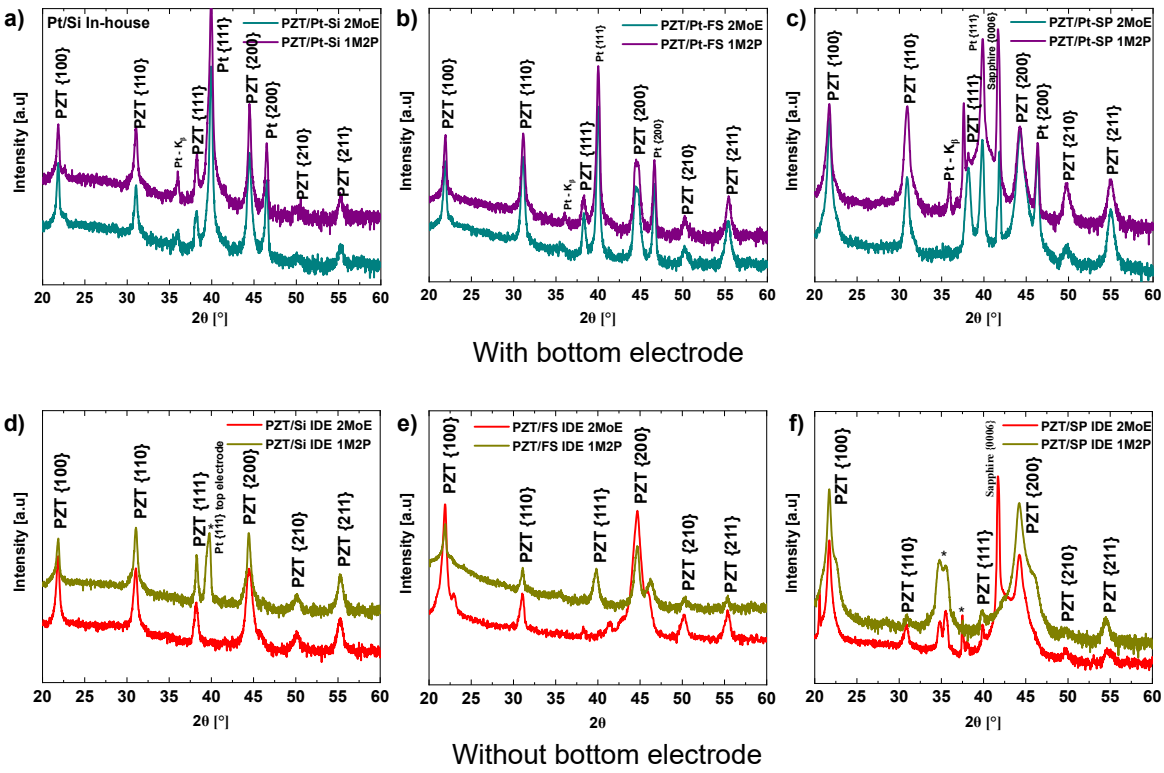

Figure 3.14: X-ray diffraction patterns of PZT film on different substrates (a), (b) & (c) with and (d), (e) & (f) without bottom electrode, deposites with 2MoE and 1M2P-$PbTiO_3$ seed layer to grow PZT over it. *-indicates substrate peaks.

as well as the measurement direction (in-plane or out-of-plane) with respective electrode configurations, altered the way in which the material responds to the large and small excitation signals. The changes in material and functional properties and degradation during fatigue cycling with respect to stress and probing directions are discussed in detail in Chapter 5.

3.6 Inferences and parameter selection

All the above experiments resulted in several sets of thin films on each substrate with the combination of different barrier layers and seed layers. The pyrolysis and annealing temperatures are fixed at 350 °C and 700 °C, respectively, for the entire course of the experiments in this study. The use of ALD or CSD-HfO_2 diffusion barrier layer allowed us to extend and develop the CSD process for depositing PZT thin films on transparent substrates like fused silica and sapphire, both with and without bottom electrode. The process adaption for using Si wafers with only 500 nm thick oxide layer for depositing PZT films without the bottom electrode was only made possible with the use of the HfO_2 diffusion barrier layer.

However, the CSD-HfO_2 diffusion barrier layer was chosen only for selective substrates based

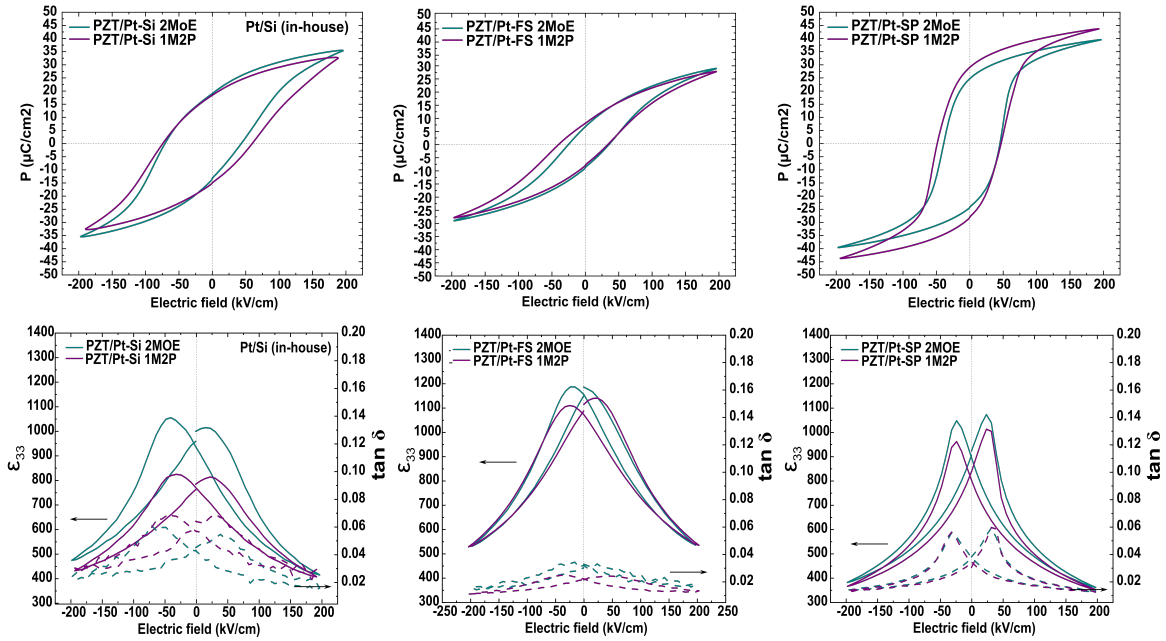

Figure 3.15: P(E) and ϵ_{33}(E) measurement results of PZT film stacks on different substrates with bottom electrode having 2MoE and 1M2P-$PbTiO_3$ seed layers. P-E loops recorded at 100 Hz and ε_{33}-E loop recorded at 1 kHz small-signal frequency.

on the results summarized from Figure 3.12 and Table 3.1. CSD-HfO_2 was only used for PZT/Si-IDE and PZT/SP-IDE, as the other combinations needed further optimization. ALD-HfO_2 was chosen for the rest of the combinations that are studied. With the seed layer selection, 1M2P-PTO was used only for PZT/Si-MIM (Sintef) since it was the only combination that yielded good structural and ferroelectric properties. All the other combinations were retained with the 2MoE-PTO seed layer for the next course of experiments.

3.7 Substrate induced stress due to thermal mismatch

As different substrates were used in this study, it was essential to understand the effect of substrate-induced stress on the PZT thin film. The coefficient of thermal expansion (CTE) mismatch between the substrate and PZT thin film resulted in an in-plane tensile or compressive stress according to the difference in their CTE values. Theoretically estimated values are tabulated in Table 3.2, but they result in an overestimation of the stress or strain values. Therefore, a method based on X-ray diffraction experiments that are self-consistent and independent of the temperature-dependent properties of the material was used to quantify the stress values, as explained in Chapter 2. The X-ray diffraction images in Figures 3.10 and 3.8 illustrated the effect of stress on all the sets of PZT thin film stacks with and without bottom electrodes deposited

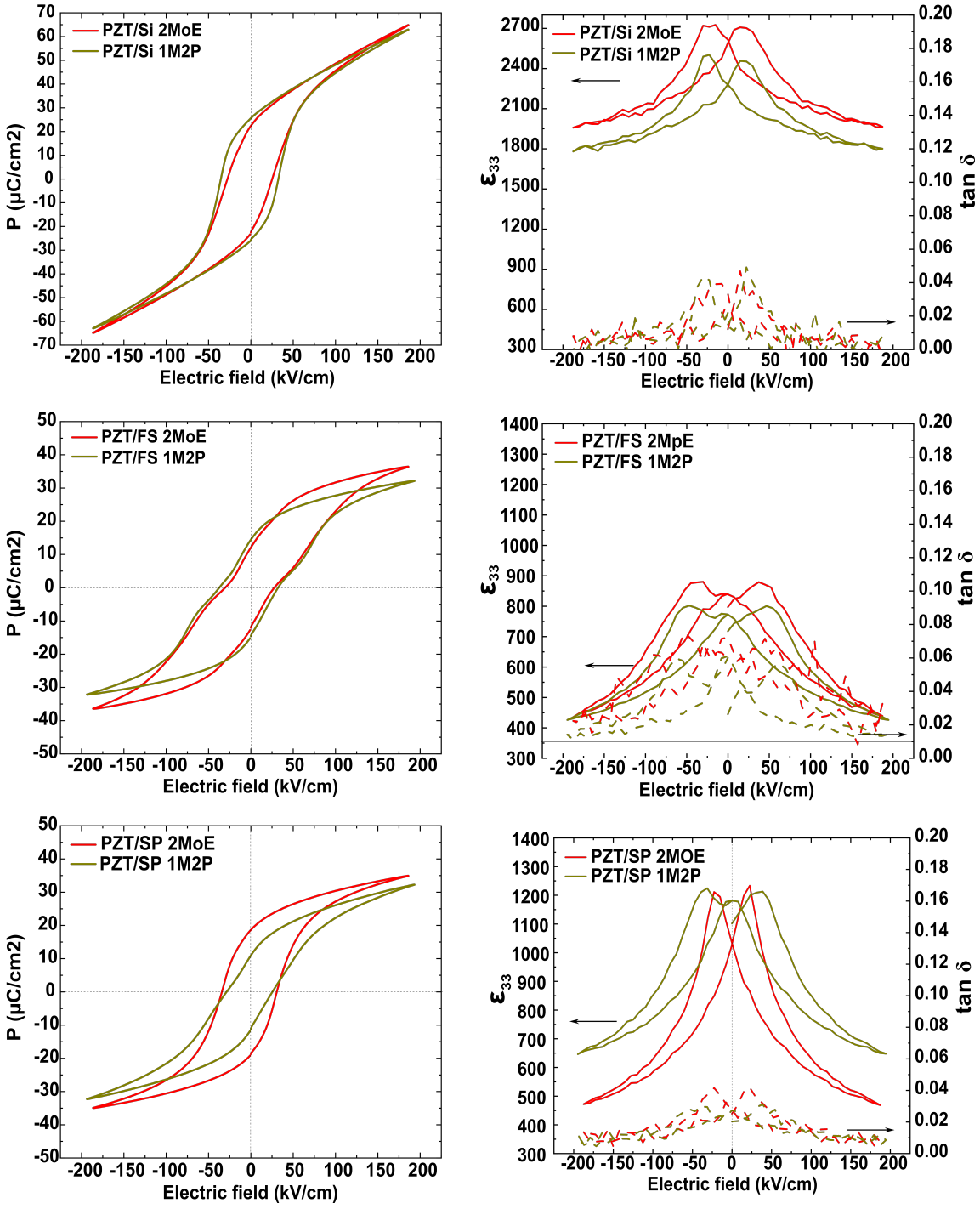

Figure 3.16: P(E) and ϵ_{33}(E) measurement results of PZT film stacks on different substrates without bottom electrode having 2MoE and 1M2P-$PbTiO_3$ seed layers. P-E loops recorded at 100 Hz and ε_{33}-E loop recorded at 1 kHz small-signal frequency.

Table 3.1: Table summarising the main results of above study comparison between the PZT film stacks with 2MoE and 1M2P-PTO seed layer on all the substrates used in this study

	PTO seed layer	Lotgering factor	P_{r} (μCcm^{-2})	$P_{\max}$ (μCcm^{-2})	E_{c} (kV cm^{-1})	$\varepsilon_{33}(0)$
PZT/Si-MIM (SINTEF)	2MoE	0.93	11.8	31.1	36.2	1205
	1M2P	0.55	14.4	33.0	36.2	1164
PZT/Si-MIM (in-house)	2MoE	0.56	19.1	35.3	43.9	999
	1M2P	0.37	18.4	32.5	59.3	784
PZT/FS-MIM	2MoE	0.63	6.9	28.9	36.5	1150
	1M2P	0.40	8.1	27.7	34.5	1073
PZT/SP-MIM	2MoE	0.79	24.8	39.5	47.7	905
	1M2P	0.46	29.1	43.5	47.7	803
PZT/Si-IDE	2MoE	0.54	22.6	64.8	25.3	2592
	1M2P	0.39	25.7	61.9	32.8	2275
PZT/FS-IDE	2MoE	0.94	12.3	36.6	29.1	840
	1M2P	0.67	14.7	32.1	32.2	772
PZT/SP-IDE	2MoE	0.46	18.8	34.9	30.9	1034
	1M2P	0.99	11.2	32.2	26.3	1181

on different substrates. All the films showed a typical shift in their peak positions according to the sign of the residual stresses. Peak positions were shifted to the left for the films under compressive stress and to the right for the films under tensile stress. The film stacks chosen for further experiments after the above-discussed processing parameter selection trials were considered for the stress analysis.

Table 3.2: Table showing the calculated stress values for PZT deposited on different substrates based on their thermal expansion coefficient

Crystallization temperature	700 °C		
($\alpha_{\mathrm{PZT}(53/47)}$ (K^{-1})	5.5x 10^{-6}		
	Si	Fused Silica	Sapphire
($\alpha_{\mathrm{substrates}}$ (K^{-1})	3.5x 10^{-6}	5.5x 10^{-7}	7.0x 10^{-6}
	PZT/Si	**PZT/FS**	**PZT/SP**
Calculated stress (σ) MPa	181	447	-123

3.7.1 Quantification of stress by sin$^2(\psi)$ method

As explained in Chapter 2, the modified sin$^2(\psi)$ technique was used to quantify the residual stress on all films by performing the θ-2θ scans at different tilt angles ψ for $\{111\}$ PZT peaks. Figure 3.17 shows the shift in peak positions of the $\{111\}$ PZT peaks for different tilt angles (ψ).

From these peak positions, values of the inter-planar distance d_{111} were calculated and plotted as a function of $\sin^2(\psi)$ values. The expected linear variation of d_{111} according to the $\sin^2(\psi)$ values are illustrated in Figure 3.18. The slope corresponds to the sign of the stress (positive if tensile and negative if compressive). The slope and intercept values from the linear fit of the above plots were used to calculate the strain and, in turn, the stress values. All the calculated values obtained using the $\sin^2(\psi)$ method are summarized in table 3.3. The Young's modulus $Y = 82.1\,\text{GPa}$ and Poisson's ratio $\nu = 0.39$ of PZT used in the calculation was taken from the work of Casset et al. [212]. It can be noticed that the stress values varied between the films with and without bottom Pt-electrode on a similar substrate.

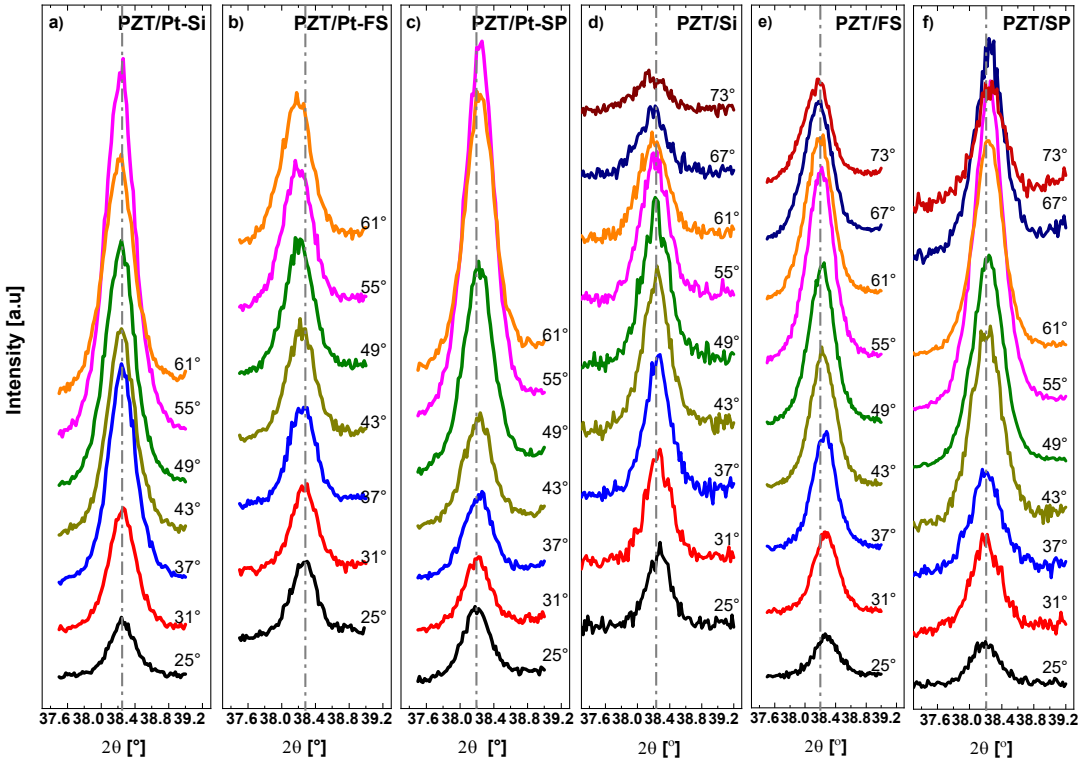

Figure 3.17: X-ray diffraction patterns of PZT {111} peaks measured at different tilt (ψ) angles for (a) PZT/Pt-Si (SINTEF) (b) PZT/Pt-FS (c) PZT/Pt-SP (d) PZT/FS and (e) PZT/SP film stacks.

The d_0 value in the table indicates the unstrained reference lattice plane spacing, and $\gamma_{11/22}$ and γ_{33} are the in-plane and the plane-normal strain components, respectively. The data for PZT on fused silica ranged from $d_\psi = 25° = 234.8\,\text{pm}$ to $d_\psi = 61° = 235.43\,\text{pm}$ and the value from the PDF was 234.77 pm. This meant that the Ψ-dependent data for d varied in the range of 0.25 %. It could already be seen that the reference value for d was not included in the measured

Table 3.3: Comparison of key parametric values of stress measurements for all the PZT films

Young's modulus of PZT Y (GPa)	82.1					
Poisson's ratio of PZT (ν)	0.39					
d_0 (pm) from PDF card (01-070-4264)	234.78					
	PZT/Pt-Si	**PZT/Pt-FS**	**PZT/Pt-SP**	**PZT/Si**	**PZT/FS**	**PZT/SP**
Slope (pm)	0.44	1.07	-0.4	0.68	0.97	-0.4761
Intercept d_{111} (pm)	234.90	234.66	235.42	234.78	234.65	235.43
d_0 (pm)	235.2	235.3	235.2	235.2	235.2	235.2
Strain $\gamma_{11/22}$ (%)	0.08	0.2	-0.75	0.13	0.18	-0.088
Strain γ_{33} (%)	-0.11	-0.26	0.095	-0.16	-0.23	0.11
$\sigma_{11/22}$ (MPa)	110 $\pm$ 11	269 $\pm$ 26	-100 $\pm$ 10	171 $\pm$ 17	245 $\pm$ 24	-120 $\pm$ 12

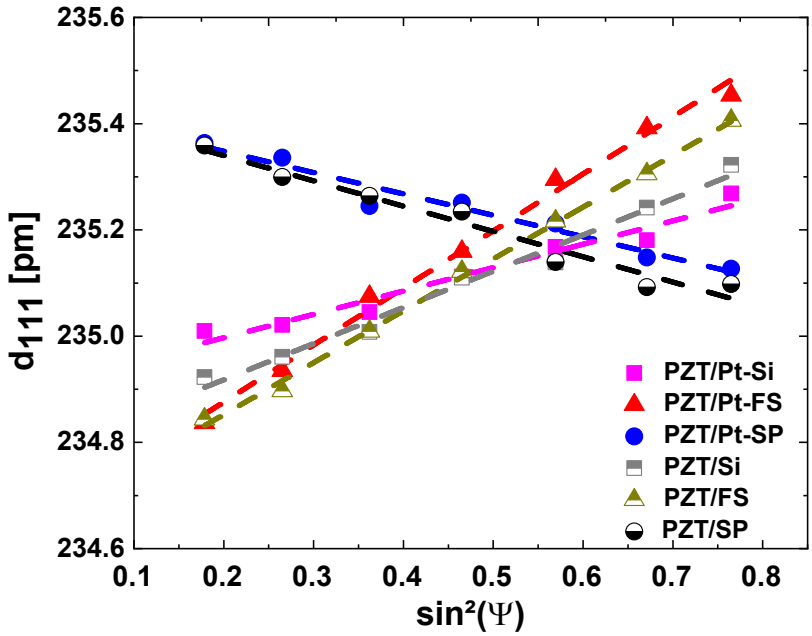

Figure 3.18: d_{111} vs. $\sin^2(\psi)$ plot for all the films used in this study.

range, which pointed to the fact that the lattice parameters of our films were different from those of the reference powder sample in the PDF Card: 01-070-4264 for PZT (53/47). It was obvious that d_0 had a large impact on the calculated Ψ-dependent strain γ_Ψ. The variation stemming from false d_0 values could, therefore, be huge. In our case, using d_0 from the PDF would yield tensile strains and stresses for both the in-plane and the plane-normal directions, which would be physically unreasonable. Moreover, the modified approach used in this work guaranteed a self-consistent set of strain and stress values respecting basic mechanical principles such as $\sigma_{33} = 0$. It was also interesting to note that d_0 values were identical for all the films. The intercept values (d_{111} at $\Psi = 0\,^\circ$) were slightly different in comparison to the $d_{111-\mathrm{ref}}$ (taken from PDF card) which again confirmed the validity of this method.

3.8 Summary

Pyrolysis temperature of 300 °C and 350 °C and annealing temperature of 700 °C were found suitable for PZT deposition on Pt/Si. However, these parameters can be optimized for other substrates with and without the bottom electrode. A very thin layer of 0.1 M $PbTiO_3$ solution can be spin-coated on the PZT films at the end of deposition to avoid surface pyrochlore. This compensates for the loss of Pb-atoms from the surface.

Using the CSD route for HfO_2 deposition could effectively reduce the cost and time of the barrier layer deposition process. However, the CSD route has to be further optimized for each substrate. In addition, it is possible that the structure and crystalline quality of the diffusion barrier layer could impact the way in which the PTO seed layer will be crystallized on them. This can further affect the texture and functional properties of the PZT film.

Using the 1M2P-PTO seed layer resulted in a set of films with an interesting combination of texture and functional properties. The film stack PZT/Si-IDE with 1M2P-PTO seed layer, even with a reduced texture, yielded a comparable polarization value but noticeably lesser permittivity values. Such a combination of properties could be interesting for energy harvesting applications. These aspects were not explored in detail during this study.

Chapter 4

Optimization of interdigitated electrode design for PZT thin films and thick slabs by Finite Element Modeling

COMSOL Multiphysics 5.5 was used to perform finite element analysis to understand the electric field distribution in bulk PZT slabs and PZT thin films with planar interdigitated electrodes (IDEs). Electric field distribution with IDEs on top and bottom faces of the thick slab was analyzed. IDE finger gap, width, and thickness were modified for each case to arrive at the optimal design parameters to achieve homogeneous field distribution and better polarization. Optimization of planar IDE dimension for an unconstrained free-standing slab provides a case study for more constrained systems like multi-layer thin films. PZT thin films deposited on different substrates were analyzed to understand the effect of IDE finger gap and width and the effect of using a semiconductor substrate on the field distribution within the bulk of the ferroelectric layer. The results of these models were used to arrive at the dimensions required for patterning the IDE structures for PZT thin films deposited on different substrates. These IDE patterns were used for ferroelectric characterization during the entire course of this study, and the results are discussed in the forthcoming chapters. The experimental results for the thick slabs are not included in this thesis. However, the results presented in this chapter are mainly used for understanding the effectiveness of the finite element models used during the study and for addressing the limitations of the approximations considered for the use of IDEs with thin films and thicker slabs.

4.1 Finite element analysis for piezoelectric materials with interdigitated electrodes

The interdigitated electrodes are used with thin and thick films for several piezoelectric applications, and particular interest has been shown for energy harvesters and tunable resonators. IDEs have the advantage of utilizing d_{33} mode of actuation by directing the electric field to in-plane directions specifically for the system where the strain is mostly along the length of the ferroelectric material plane. Typically the d_{33} coefficient is twice that of the d_{31} coefficient [213, 214], and the latter is utilized in MIM geometry. But it is only advantageous to use IDEs when the poled fraction of the ferroelectric material is maximized, as one can imagine, there is a significant volume of inactive material under the electrode fingers in the IDE geometry, and a large poling voltage is required. The non-uniform field distribution between the electrode fingers also poses an additional challenge. At the same time, the finger gap can be adjusted to several times the film thickness, and materials with a large dielectric constant like PZT are typically used with IDEs [57, 215]. Therefore, this requires careful optimization of the electrode design with respect to the thickness of the active ferroelectric layer to achieve maximum polarization. The electrode design should also be adapted for specific applications. For example, in the case of energy harvesters, the electrode gap needs to be optimized to have a lower capacitance in order to maximize the voltage output, but having large gaps needs a higher driving voltage for poling process. In the following sections, the finite element model is mainly used to understand the effective field distribution in the PZT slab and thin film on different substrates for various IDE dimensions to achieve maximum polarization in the active ferroelectric layer.

In order to understand the effective field distribution with the IDEs, a simplified assumption is followed, considering IDEs as equivalent to MIM configuration. The IDE fingers are assumed to run through the thickness of the ferroelectric layer, and the field is uniformly distributed in the plane of the ferroelectric layer going from the fingers of positive to negative polarity. But in reality, the electrodes are present only on the surface, and there will be a non-uniform electric field distribution resulting in a curvature of the field lines starting from the edge of the fingers before becoming a straight line through the finger gap (f_g) and curving again towards the finger of opposite polarity. The field curvature is given by the approximation Δf_g and it is proportional to the thickness of the ferroelectric layer, where $\Delta f_g = \alpha t_f$ and α is the pre-factor defined based on methods outline in the studies done by Gevorgian et al. [216] and Igreja et al. [217]. Therefore, the effective gap between the finger for calculating the field can be written as $f_g + \Delta f_g$. The

details of this approximation and the comparison of the pre-factor with the finite element modeling are discussed in detail for thick and thin films in the earlier studies [2, 184, 185, 213, 218].

4.2 Design of PZT slabs with interdigitated electrodes

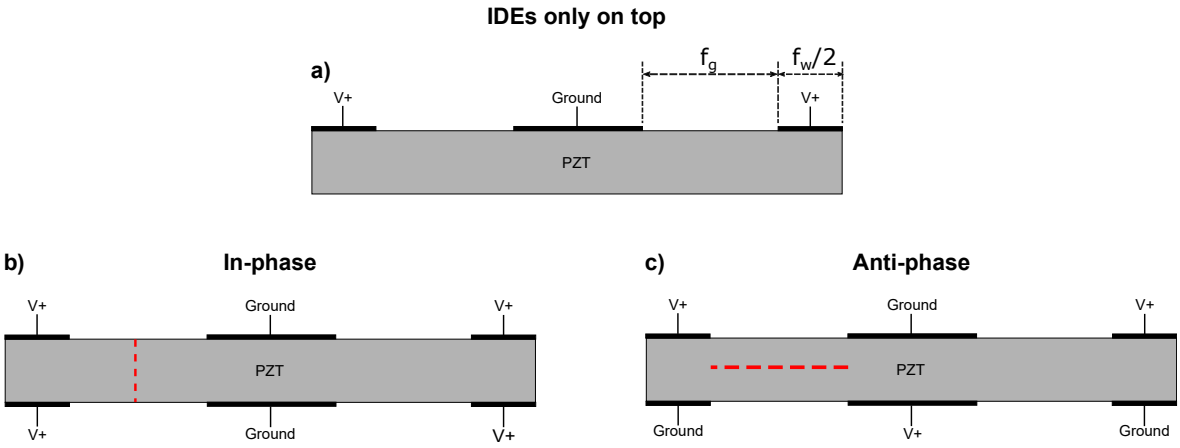

Figure 4.1: Schematics of thick PZT slab used in this study with (a) IDEs only on top, (b) IDEs on top and bottom with same polarity and (c) IDEs on top and bottom with opposite polarity. Red dotted lines in (b) and (c) shows the cut planes in the mid-section between the fingers and mid-section through the thickness of the ferroelectric layer at which the field distribution is analyzed.

The PZT slabs were intended to be used for energy harvesting applications. To increase the harvesting efficiency, a homogeneous field distribution throughout the thickness of the slab is needed to achieve maximum possible polarization with IDEs. Finite element models were developed with planar electrodes on one and both sides of the PZT slab, with different electrode geometries. The represented electrodes indicate a set of IDE fingers which is the interdigitation zone. The gap between the electrode fingers (f_g), and the electrode width (f_w) was adapted according to the input parameter for the simulation. In addition to this, the electrodes on top and bottom faces of the slab are maintained at in-phase (i.e., top and bottom sets of IDEs are in the same polarity) and anti-phase (i.e., top and bottom sets of IDEs are in opposite polarity) to understand the effective design scenario to achieve a maximum effective field and homogeneity in field distribution to achieve a maximum polarization for the given material. Figure 4.1 illustrates various schematics of the model geometry used in COMSOL. A permittivity value of 2000 and the thickness of 0.5 mm is fixed in the model following the specifications of the PZT sample from the supplier. The properties of the platinum (Pt) electrode are defined from the COMSOL library with infinite conductivity. Potential of 1000 V is applied on the electrode(s) maintained at a positive potential, and the other electrode(s) are grounded. The fingers on each side have periodicity

and are considered identical. The built-in COMSOL function was used to choose a finer mesh size for the given geometry, and the electrostatics physics interface was used to analyze the field distribution. The finger gap and width were varied systematically to understand the effective field distribution in the samples.

4.2.1 IDEs only on top of the slab

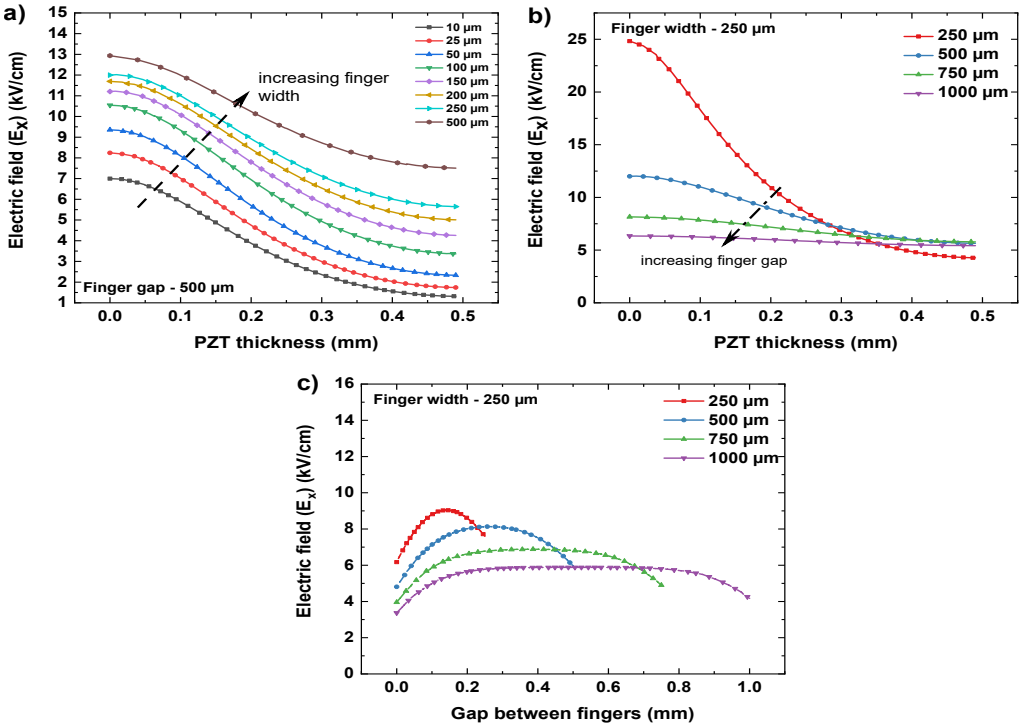

Figure 4.2: Electric field distribution in x-direction for the PZT slab with IDEs only on top showing the (a) finger width (b) finger gap dependence for fixed gap and width, respectively plotted for the mid-section between the IDE fingers. (c) E_x in gap between the fingers plotted at the mid-section of the slab for various finger gaps and a given finger width.

The finite element model for the PZT slab with IDEs only on top was considered, and the effective field distribution in the bulk of the sample for various combinations of finger gaps (f_g) and widths (f_w) are plotted. The field distribution in x-direction (i.e. perpendicular to the finger) at the mid-section between the fingers and the mid-section through the thickness of the sample was analyzed. As shown in Figure 4.2, the effective field value and the distribution clearly depend on both finger width and the gap. It can be seen that with larger finger width, the field amplitude is higher, and the distribution is more homogeneous.

However, a compromise should be found between the finger width and the metallization ratio ($\eta = \frac{f_w}{(f_g+f_w)}$), to keep the electroded area to a minimum as the material volume beneath the

electrode is inactive and do not contribute to net polarization. The field amplitude is higher for smaller gap values, but the distribution is less homogeneous through the thickness of the sample. At the same time, with larger gaps, a very high voltage is needed to achieve a higher effective field and eventually better polarization. As the material volume situated below the electrode fingers is inactive, a given electrode design with larger finger width will have a reduced power output. Applying very high voltages can also cause an early breakdown or short-circuiting of the electrodes. Therefore a balance between minimizing η and increasing f_g is essential to keep the driving voltage reasonably low and achieve better polarization by increasing the active material volume.

4.2.2 IDEs on both faces of the slab

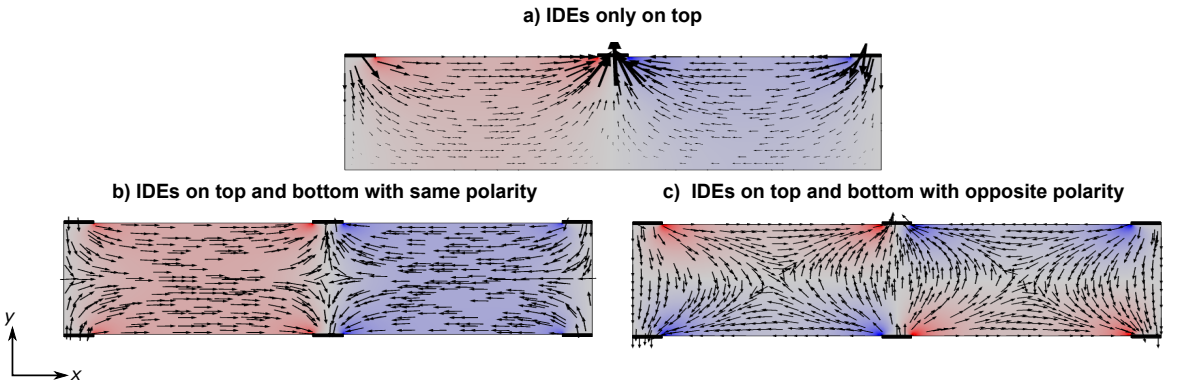

Figure 4.3: Modeled field distribution in PZT slab with the arrows indicating the field direction through the thickness of the sample with $f_w = 250\,\mu$m and $f_g = 1000\,\mu$m for (a) IDEs only on top, (b) IDEs on top and bottom with same polarity and (c) IDEs on top and bottom with opposite polarity.

The IDE patterns are now incorporated on both sides of the PZT slabs, allowing the electric field to effectively penetrate halfway through the thickness of the sample and thus allowing the use of smaller gaps and eventually lower driving voltage. Figure 4.3 shows the field distribution in both x and y-direction through the bulk of the sample with IDE patterns only on top of the slab and patterns on both top and bottom of the slab maintained at the same polarity (in-phase) and opposite polarity (anti-phase) between the top and bottom sides. It is interesting to note that the field distribution with the IDEs maintained at the same polarity is much better compared to the case where the top and bottom pairs of IDEs are in opposite polarity. It can be seen that the field lines cancel each other near the mid-section through the thickness of the sample creating an inactive zone. This will also be detrimental to the piezoelectric response of the structure.

The dependence of finger width and gap is also demonstrated for the samples with top and

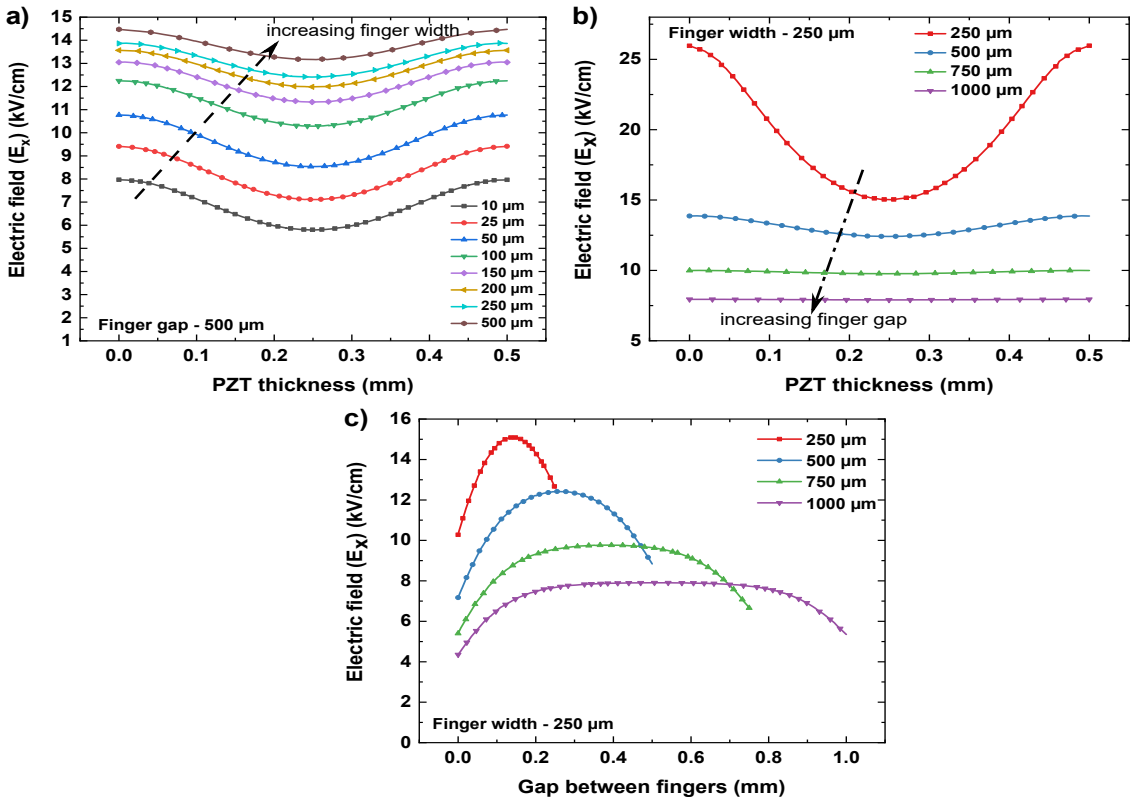

Figure 4.4: Electric field distribution in x-direction for the PZT slab with IDEs on both the sides of the slab with same polarity showing the (a) finger width (b) finger gap dependence for fixed gap and width, respectively plotted for the mid-section between the IDE fingers. (c) E_x in between the fingers plotted at the mid-section of the slab for various finger gaps and a given finger width.

bottom IDEs as shown in Figures 4.4 and 4.5.

It can be seen clearly that the effective field value is higher for the case of IDEs maintained in-phase, and the in-homogeneity in field distribution is also less pronounced for smaller finger gaps when compared to the case with IDE patterns only on the top of the sample. The finger gap dependence is similar for the samples with IDEs only on top and both faces of the sample at the same polarity. For a given set of finger gap and width and driving voltage, the effective field is higher for the case where IDE patterns are on both faces and are maintained at the same polarity.

4.3 PZT thin film stack with interdigitated electrodes

Following the understanding from the modeling of IDEs for thick slabs, design optimization was attempted for multi-layer thin film stacks. Two-dimensional models with interdigitated fingers are created with periodic boundary conditions. The thickness of fused silica (FS), sapphire (SP),

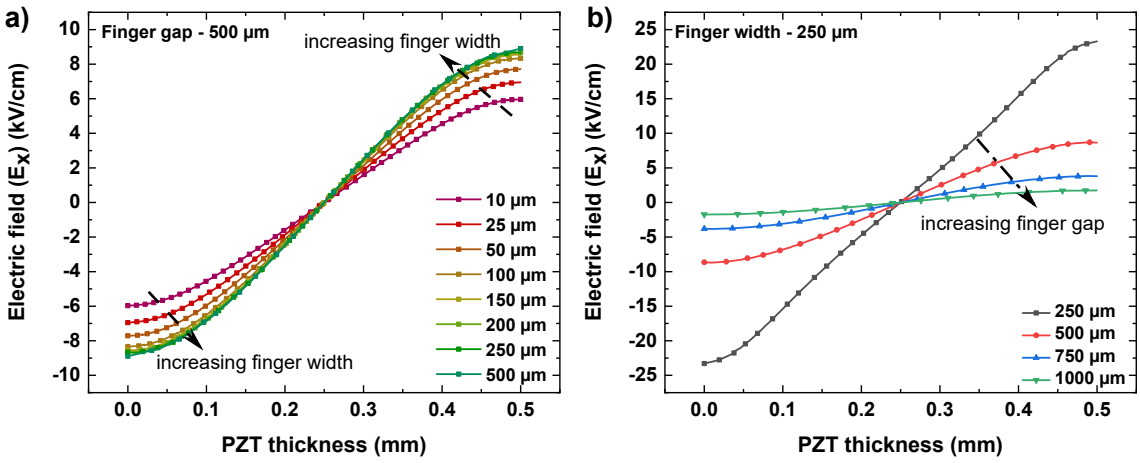

Figure 4.5: Electric field distribution in x-direction for the PZT slab with IDEs on both the sides of the slab with opposite polarity showing the (a) finger width (b) finger gap dependence for fixed gap and width, respectively plotted for the mid-section between the IDE fingers. (c) E_x in between the fingers plotted at the mid-section of the slab for various finger gaps and a given finger width.

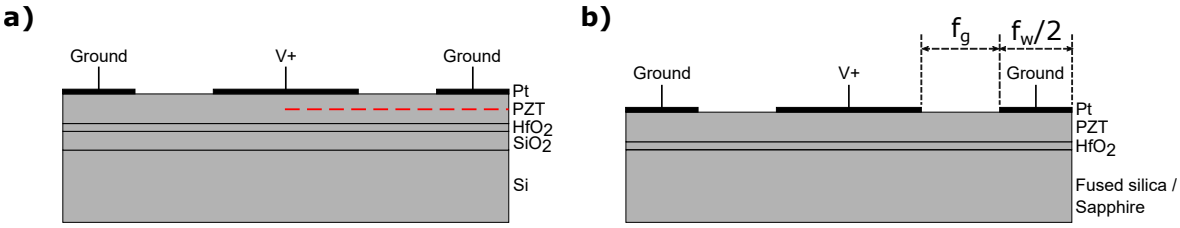

Figure 4.6: Schematics of the model geometry for finite element analysis in COMSOL for film stacks on different electrodes.

and silicon (Si) substrates were used as per the specification; however, the substrate thickness will not have any effect in the model. The COMSOL model was constructed in a multi-layer configuration using the actual thicknesses of 0.5 μm for PZT, 30 nm for HfO_2 layer, and 0.5 μm for SiO_2 layer (only for Si substrate) as per the actual film stack. The permittivity values of each layers were also defined in the model, the in-built values from COMSOL were used for substrates, and oxide layers: $\varepsilon_{\mathrm{FS}}$= 4.2, $\varepsilon_{\mathrm{SP}}$= 9.8, $\varepsilon_{\mathrm{SiO_2}}$= 4.2 and $\varepsilon_{\mathrm{HfO_2}}$= 25. A user-defined permittivity value taken from the measured values reported in the previous chapter ($\varepsilon_{\mathrm{PZT}}$= 1000) was used for the PZT layer. The properties of Pt electrode are defined from the COMSOL library as explained in the previous section. Figure 4.6 illustrates the schematics of the model geometry constructed for the finite element analysis. The electrodes represented on the top of the film indicate a set of IDE fingers which is the interdigitation zone. The f_g and f_w were chosen according to the design choice, and the fingers on each side have the periodicity and are considered identical. A positive

voltage (100 V) is applied to the electrode finger in the middle, and the fingers on either side are grounded. The electrostatics physics interface was used to perform a stationary and time-dependent study to analyze the field distribution in the film. The effect of electrode width and the gap between the electrodes on the electric field distribution in the PZT layer was analyzed. The interface between the Si substrate and SiO_2 was defined as floating potential to replicate the parasitic capacitance contribution from the substrate. In reality, due to the semiconducting nature of the Si substrate (with low resistance), each IDE finger can be considered connected to the Si substrate through a series of capacitors formed by each dielectric layer (PZT, HfO_2, SiO_2). This capacitor formed by the IDE finger and Si substrate will be connected in parallel to the capacitor formed by PZT between the IDE fingers, thus contributing to the parasitic capacitance. A reasonably thicker (0.5 μm) oxide layer (i.e., SiO_2) - along with a thin dielectric HfO_2 layer was used as opposed to a much thicker oxide layers (1-2 μm) like SiO_2 and MgO_2 in other works [184]. Therefore, the effect of SiO_2 layer thickness and the dielectric layer on the electric field distribution in PZT film is also analyzed. These studies were not needed for the film stacks on insulating substrates like fused silica and sapphire.

4.3.1 Effect of finger gap and width on electric field distribution in thin film

The finger gap and width was varied systematically to understand the effect on the electric field distribution within the film. From the plots in Figure 4.7, for a given voltage, the effective field reduces as the gap between the fingers increases. When the finger gap is reduced, the field distribution is less homogeneous and will not penetrate through the entire thickness of the film, which was evident from the study shown with the thicker slabs. From Figure 4.7(c), unlike thicker slab, it is clear that there was little to no change in effective field values with the change in the finger width for the films on all three substrates. It was also apparent from 4.7(a) and (b) that there was a drop in electric field value at the midsection with increasing finger gap. This means a higher voltage will be required to achieve the same polarization when the finger gap is made larger. When using a conductive substrate like Si, the drop in electric field through the PZT layer's thickness is much higher than the films deposited on non-conductive substrates. This will, in turn, result in an in-homogeneous polarization of the material for a given voltage. Although there are no changes in E_x while changing the finger width, the finger width cannot be reduced too much even if it will be beneficial to have a less inactive area of the PZT (under the electrode finger). Reducing the finger width to 5 μm and less will pose practical implications for patterning the electrodes by lithography. The sign of polarization between the adjacent fingers can cancel

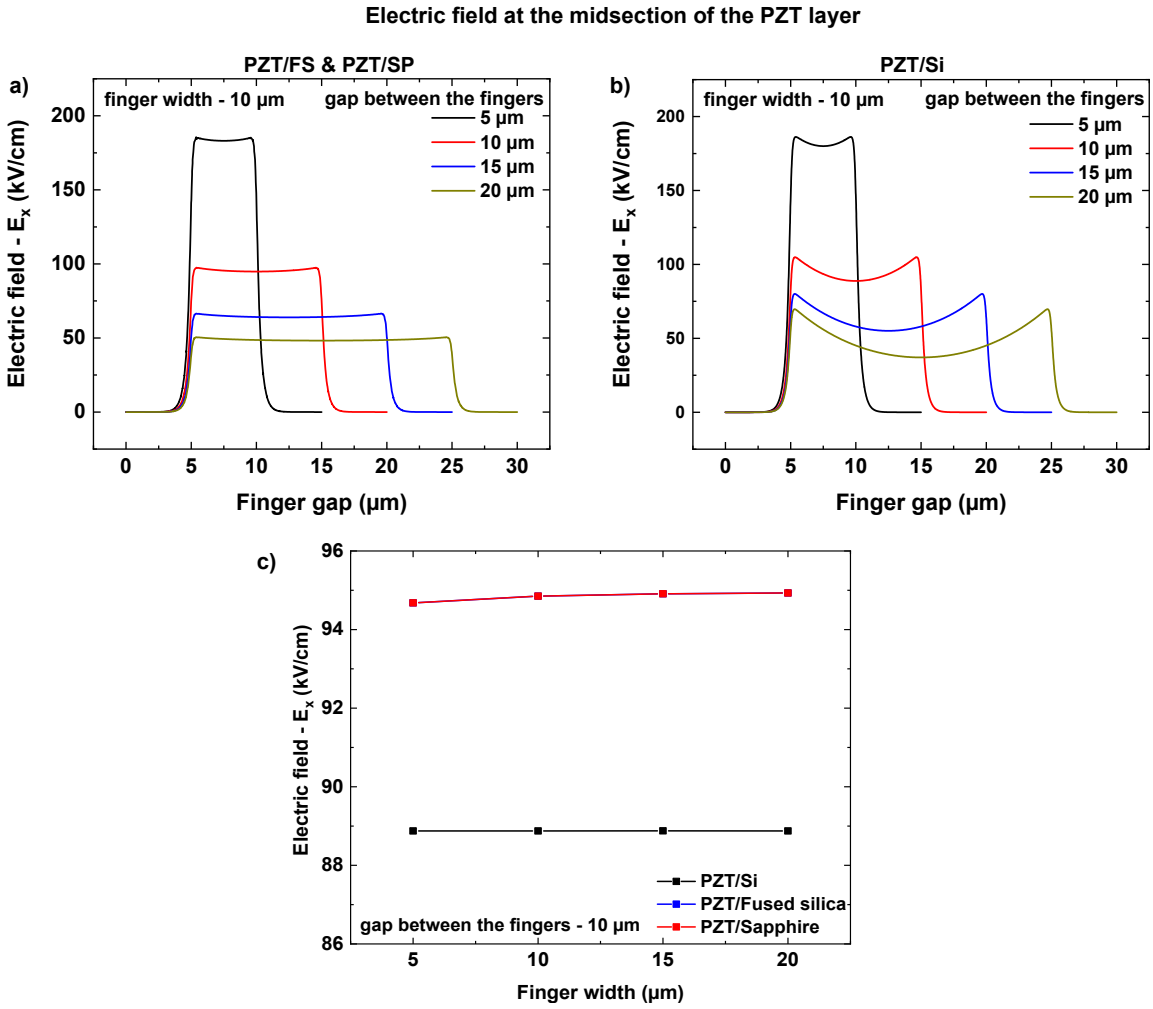

Figure 4.7: Electric field (E_x) at the mid-section of the PZT layer when the finger gap was changed at constant finger width for the film stack on (a) fused silica and sapphire and (b) Si. (c) E_x for different finger width with a constant finger gap

each other when the finger width is much smaller than $2t_f$ [218]. Therefore, the IDE finger width and the gap was maintained at 10 μm for the PZT films deposited on all the substrates during this study. The modeling was also performed by removing the HfO_2 barrier layer, but there were no changes in field distribution observed for this case. The HfO_2 layer acts only as a barrier to prevent the inter-diffusion of Pb atoms to the SiO_2 layer. There were also no noticeable changes in field distribution with the change in HfO_2 and SiO_2 thicknesses. Hence, those results are not presented here.

4.3.2 Field distribution in thin films with interdigitated electrodes

The electric field distribution in the PZT layer for the films on fused silica, sapphire, and silicon is analyzed. Figure 4.8 shows the electric field distribution in x-direction and Figure 4.9

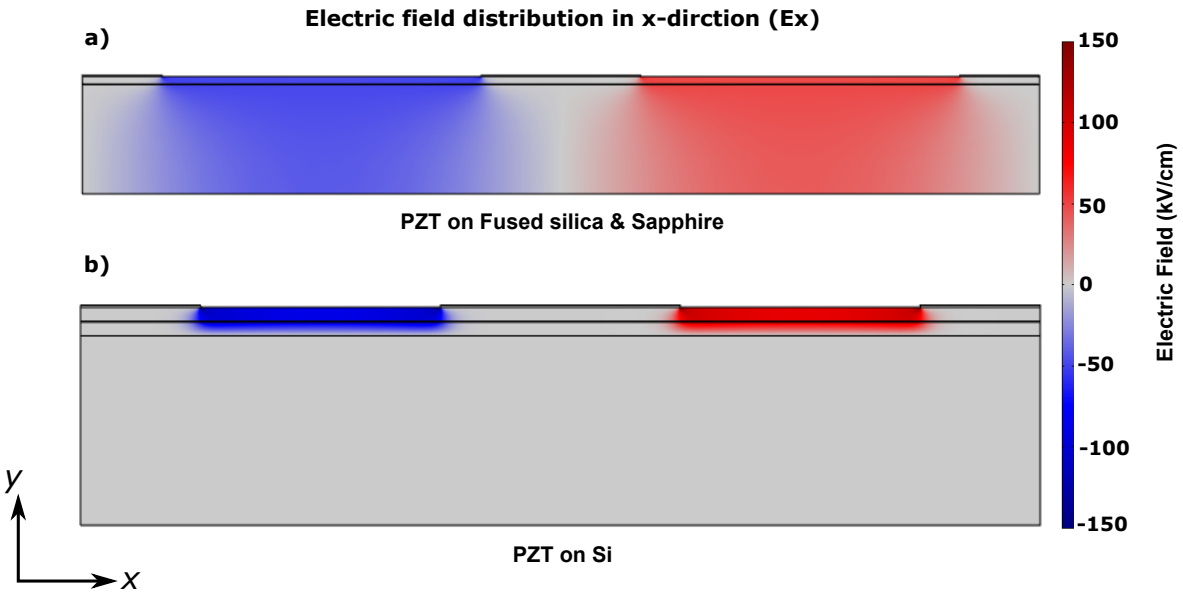

Figure 4.8: Electric field distribution in x-direction (E_x) for the film on (a) fused silica & sapphire, and (b) on silicon substrates. Note: Figures are not to scale as used in the model.

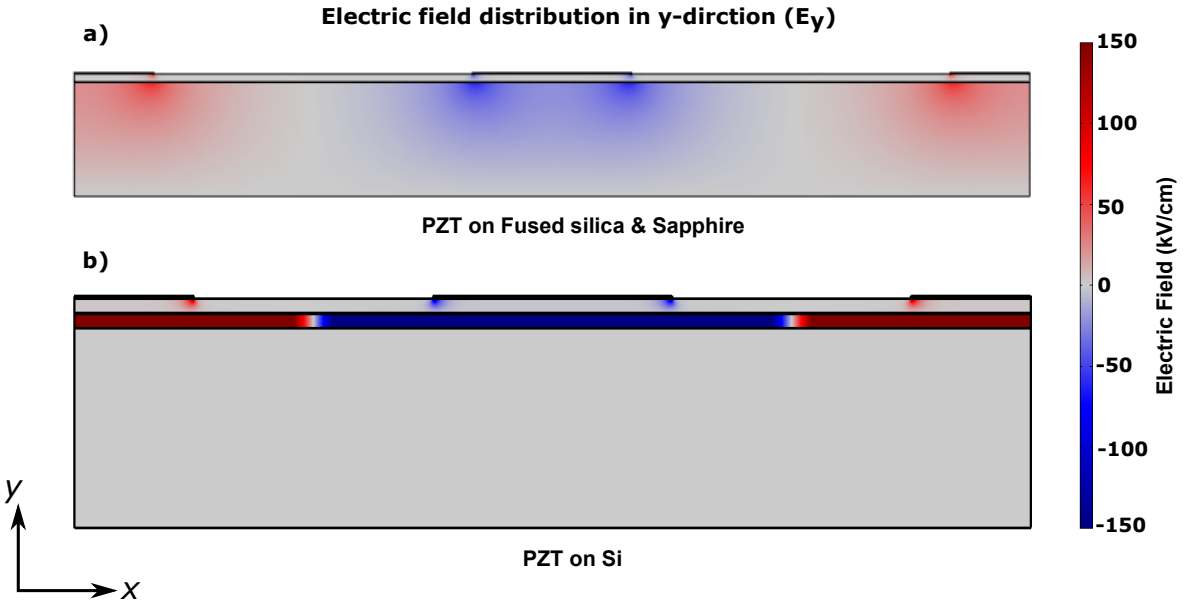

Figure 4.9: Electric field distribution in y-direction (E_y) for the film on (a) fused silica & sapphire, and (b) on silicon substrates. Note: Figures are not to scale as used in the model.

shows the distribution in *y*-direction (i.e direction parallel to the fingers) for the films on all three substrates. The electric field distribution in both x and y directions for the stacks on fused silica and sapphire looks very much similar. For the film on silicon, the field is confined to the PZT and the oxide layers because of the low resistance of Si substrate. It is also interesting to note that there is no field distribution directly under the electrodes but only in the gap between the electrodes. However, this is different in the case of film on the silicon substrate; a non-zero field is observed under the electrode finger. This can be seen in Figure 4.10. To understand this, the x and y components of the electric field in the midsection through the thickness of the PZT layer are plotted. Figure 4.10(a) shows the field distribution in x-direction (E_x) for all the stacks. For the given f_g and f_w PZT on fused silica and sapphire shows a slight drop in E_x between the fingers, and it is in close agreement with the expected field values from the approximation of the finger gap for accommodating the curved field lines right below the edge of the electrode fingers [184]. On the other hand, for the films on Si, the drop in E_x in between the finger is more pronounced, the field value is higher closer to the edge of the finger, and it dropped continuously through the mid-gap between the electrodes. It is mainly due to the difference in capacitance below the finger and the capacitance through the gap as explained in the previous section. The field distribution along y-direction (E_y) in Figure 4.10(b) also shows the effect of Si substrate acting as a floating potential. Comparing E_y values between the PZT film on Si and the other two substrates, it can be noted that there is a non-zero value underneath the electrode and a higher value close to the edge of the fingers.

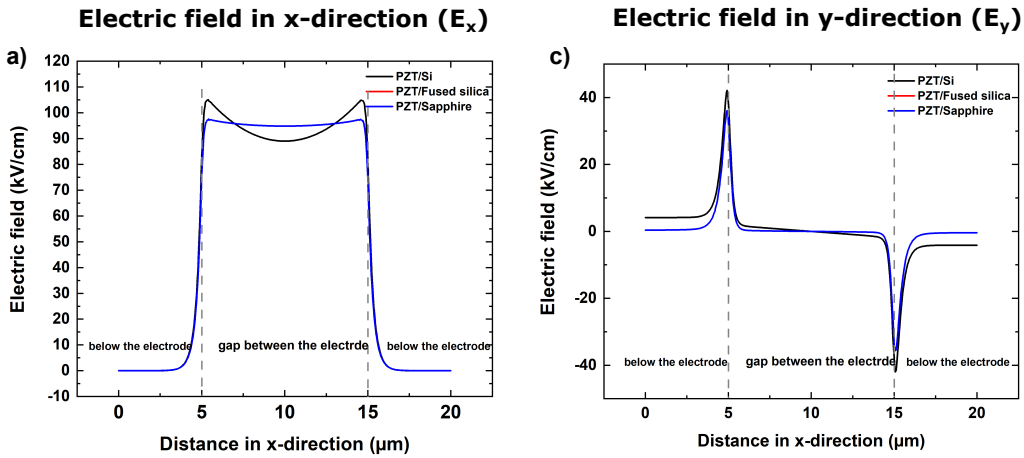

Figure 4.10: Electric field distribution in x and y-direction, (a) E_x and (b) E_y plotted along the cut-plane through mid-section of the PZT layer in all the film stacks, with f_g & $f_w = 10\,\mu$m.

To summarise, it can be seen that for the given f_g value of $10\,\mu$m, there was no significant variation in field distribution with the change in f_w, as the finger gap is sufficiently higher than

the film thickness. There is more flexibility with the design parameters for the films deposited on non-conductive substrates. For PZT deposited on Si, the field value drops in the mid-gap between the fingers as the gap increases. It can be understood that the gap cannot be increased invariably to achieve complete poling as it needs a much higher driving voltage, and it may result in short-circuiting of the electrode and the substrate and an upper limit of the gap should be established in this case. At the same time, f_g can be reduced to less than 10 μm without affecting the homogeneity of field distribution, and in this case, the capacitance of the PZT between the fingers gap will be higher than the parasitic capacitance from the substrates. But the trade-off between the capacitance and the voltage output needs to be considered for specific applications. A lower limit for the gap should also be established, considering the field penetration through the film thickness and the limitations of the lithography process.

4.4 Summary

One important difference between having IDEs on thin films and thicker slabs is the ratio of the gap to thickness (f_g/t_f) and the width to thickness (f_w/t_f). As we saw in the case of thin films, the field distribution was not much affected by variation in finger width and was following the first approximation of $E = V/(f_g + \Delta f_g)$ for various gap values where the ratio f_g/t_f was very high. Also, for the same reason, there was little to no gap dependence on absolute field value and distribution. As it was found that for a given film thickness t_f, a homogeneous field distribution can be achieved by having finger gap and width at least ten times more than that of t_f. The approximation of effective area A = (2N-1)$f_l t_f$ and an effective gap $f_g = \mathrm{f}_g + \Delta f_g$ holds true when the above condition is satisfied. This is not the case for thicker slabs where the ratio f_g/t_f is lesser for several gap values that are compared. The effective field value for a given f_g and f_w is nearly two times lower than that of the values obtained from the approximation for thin films. For these limiting cases where the gap and width to thickness ratio are smaller, the maximum effective field value can be approximated to $\frac{1}{2}V/(f_g + \Delta f_g)$, where $\Delta f_g = \alpha t_f$ provided the field distribution is homogeneous through the gap between the IDE fingers. This has to be taken into consideration for using IDEs with thick slabs. For the given slab, the thickness is 0.5 mm, theoretically the finger gap should be in the order of 5 mm, but having such a large gap means a very high driving voltage, and that will pose a practical limitation. Therefore, it can be inferred from our results that for thicker slabs, the conditions $f_g/t_f \geq 1.5$ and $f_w/t_f \geq 0.4$ should be satisfied to achieve a homogeneous field distribution between the fingers and throughout the

thickness of the slab. However, the trade-off between metallization ratio and driving voltage also has to be taken care of to achieve optimal efficiency.

Chapter 5

Influence of stress on the ferroelectric properties of PZT thin films

In this chapter, the effect of substrate stress on the in-plane and out-of-plane ferroelectric properties of the PZT thin films deposited on various substrates is discussed. The configurations with top and bottom electrodes (MIM) and the planar interdigitated electrodes (IDE) allowed probing of the out-of-plane and in-plane ferroelectric properties, respectively. A phenomenological model of these properties depending on stress and film texture is presented. In addition, the degradation of polarization and permittivity values during fatigue cycling is discussed in detail. Small-signal and large-signal permittivity analysis was performed on all the samples to understand and explain the consequences of bipolar fatigue cycling on reversible and irreversible domain wall motions. Most of the discussions presented in this chapter are already published in our works [84, 85]. The findings on degradation resistant behavior of solution deposited (CSD) PZT thin films with interdigitated electrodes (probing the in-plane properties) are reported. Hypotheses for such degradation-resistant properties are also postulated and discussed.

5.1 Effect of residual stress on the ferroelectric behaviour of PZT thin films

Residual stresses in thin films can be a result of various factors that are discussed in Chapter 1. In the case of sol-gel deposited poly-crystalline thin films, it is primarily due to the difference in thermal expansion mismatch between the substrate and thin film. When the substrate's coefficient of thermal expansion (CTE) is larger than that of the deposited film, the film experiences compressive stress. In contrast, there is tensile stress on the film when the CTE of the substrate is smaller than that of the film. The residual stresses can affect the way in which the domains are formed, consequently, the dielectric and ferroelectric responses of the material are altered [81, 219].

When the projection of the polarization vector of a ferroelectric domain onto the film plane is larger than the projection to the direction perpendicular to that plane, the domains will be referred to as 'in-plane' or *a*-domains with 180° and non-180° walls between them. If the projection of the polarization vector of a ferroelectric domain perpendicular to the film plane is larger than the projection to the direction onto the film plane, the domain is an out-of-plane or *c*-domain with 180° walls between them. The walls separating *c*-and *a*-domains must be non-180° walls, between different *a*-domains, both 180° walls and non-180° walls can exist [91, 220]. For an MPB-PZT composition, there could exist rhombohedral unit cells, and there are 71°, 109° and 180° domain walls. For the sake of brevity, the 71°, 109° will be referred to as 90 ° domain walls throughout the discussion. Since our films are not perfectly textured, this nomenclature is only an approximation of the real orientation of the polarization vector in the domains. In the present case, PZT on sapphire with compressive stress will have the highest *c*-domain population, while the degree of *a*-domains will progressively increase for PZT on Si and fused silica with the increasing tensile stress.

The XRD patterns in Figures 3.8 and 3.10 shown in Chapter 3 illustrate the effect of residual stress on PZT thin films deposited on different substrates. The shift in peak positions is clearly visible from (100) and (200) peaks; the peak position is shifted to a lower 2θ angle for compressively strained films and higher 2θ angles for the films under tensile stress. In addition to quantifying the stress values by the $\sin^2(\psi)$ method, it is important to understand the effect of stress on the ferroelectric domain configuration in each of these films. To elucidate this, the films with two extreme conditions of stress values were considered, and the $\{200\}$ family of peaks were fitted using a pseudo-Voigt function. A close-up-of $\{200\}$ peaks with the fitted data are depicted

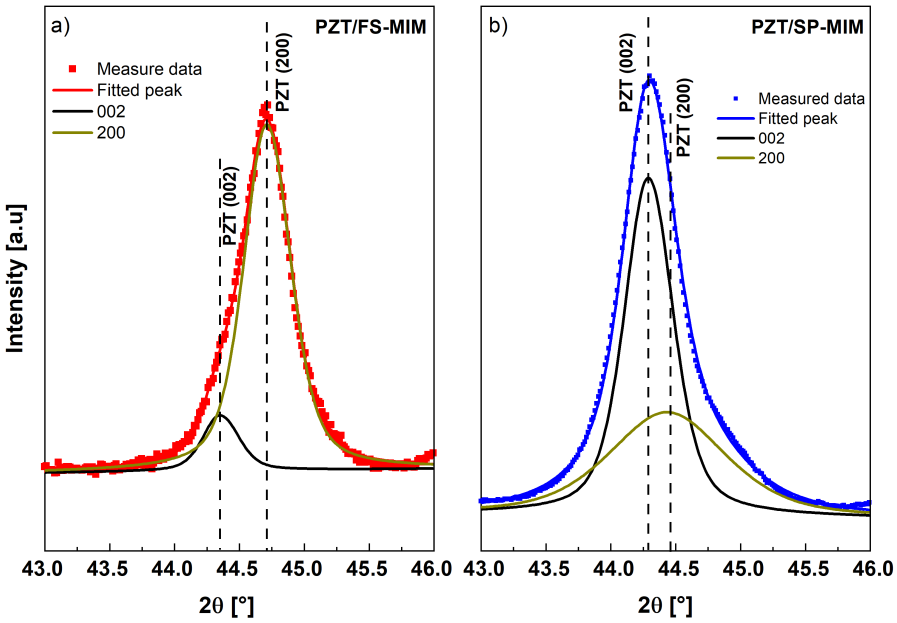

Figure 5.1: A close-up of {200} XRD peaks for (a) PZT/FS-MIM and (b) PZT/SP-MIM with fitted peaks showing splitting in a (200) and a (002) component: experimental data are shown with filled symbols and fitted peaks are shown with continuous lines.

in Figure 5.1. There is an apparent splitting into a (200) and (002) component, originating from domains oriented parallel and perpendicular to the plane of the film, respectively. The peak area is proportional to the volume fraction of the corresponding domain type. The area under each peak was integrated and normalized to the corresponding peak intensities of the powder diffraction data of the tetragonal PZT (PDF Card: 01-070-4264), as the XRD peaks align well with the tetragonal system although it was an MPB composition. The ratio of domains with orientation perpendicular to those oriented parallel to the film was calculated to be 0.79:0.21 for PZT/SP-MIM and 0.25:0.75 for PZT/FS-MIM, respectively. These values correspond closely to the above discussion that PZT films on sapphire with compressive stress have a higher *c*-domain population than *a*-domains, while the amount of *a*-domains is larger than *c*-domains for PZT films on fused silica under tensile stress. A similar analysis could not be performed for the PZT/Si-MIM films because a visible splitting could not be observed for the {200} family of peaks. It also aligns closely with the established understanding that there could be a presence of mixed domain structure for moderately stressed (110 MPa) films on Si with a preferential *a*-domain population, but lower in comparison to the film on fused silica with a stress of 263 MPa. It is also important to mention that this analysis holds true for all the PZT thin film stacks on each substrate, i.e., the stacks with and without bottom electrodes.

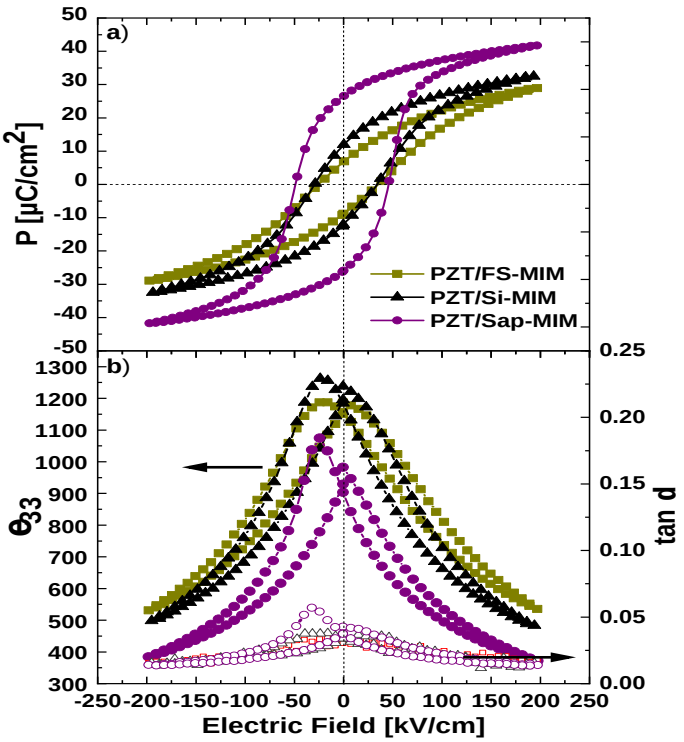

Figure 5.2: (a) Polarization hysteresis measured at 100 Hz. (b) Small-signal permittivity and loss tangent as a function of applied DC bias field at 1 kHz small-signal frequency.

Apart from the structural variations and changes in domain orientation, the ferroelectric properties of the PZT films on different substrates also vary according to the sign and magnitude of the residual stresses. Polarization (P(E)) and small-signal hysteresis $\varepsilon_{33}(E)$ are depicted in Figure 5.2 for the films on Si, fused silica, and sapphire substrates.

All the key values are tabulated in Table 5.1. Maximum and remanent polarization increased from PZT/FS-MIM over PZT/Si-MIM to PZT/SP-MIM, following the order given by the relative increase in *c*-domains and the improved alignment of the *c*-domains along the film normal. The measurement, in this case, detects the polarization component perpendicular to the film surface; therefore, this observation confirms that PZT/SP-MIM contains more *c*-domains with a high out-of-plane polarization component, while PZT/FS-MIM has more *a*-domains with predominantly in-plane polarization component. The intermediate values of PZT/Si-MIM indicate that it contains an admixture of *c*-and *a*-domain population with predominantly an in-plane polarization component due to the tensile stress. The fact that a ferroelectric hysteresis with non-zero remanent polarization is still seen even for PZT/FS-MIM with very high tensile stress indicates that some *c*-domains exist even in the systems under tensile stress. The films can therefore be assumed to have mixed *a*/*c*-domain configurations. This has also been reported earlier for films

having in-plane and out-of-plane domains under tensile and compressive residual stress, respectively [81, 113]. The zero-field permittivity ($\varepsilon_{33}(0)$) should be higher for PZT/FS-MIM with

Table 5.1: Key values of PZT films in MIM and IDE configurations on all three substrates.

	PZT/Si-MIM	PZT/Si-IDE	PZT/FS-MIM	PZT/FS-IDE	PZT/SP-MIM	PZT/SP-IDE
Lotgering factor	0.55	0.54	0.65	0.94	0.78	0.96
Stress $\sigma_{11/22}(\mathrm{MPa})$	110±11	171±17	269±26	245±24	-100±10	-120±12
P_{r} (μC cm^{-2})	12	23	7	21	27	19
P_{max} (μC cm^{-2})	32	65	29	36	42	35
ε_{33}	1180	2592	1156	959	923	1230

more *a*-domains followed by PZT/Si-MIM with *a*/*c*-domains and then PZT/SP-MIM with comparatively lesser *a*-domains than the former two systems. The increased permittivity for in-plane domain configuration that several research groups also observed [79, 81] can be rationalized by a higher domain wall density, equivalent to a reduced domain size [221, 222]. Under compressive in-plane stress, a single out-of-plane domain without any domain walls can be energetically stable. Under tensile in-plane stress, this is not the case: the domain configuration has to accommodate stress both in the (100) and (010) direction, which requires multiple domains. However, the ($\varepsilon_{33}(0)$) values for PZT/FS-MIM and PZT/Si-MIM are very close to each other (Figure 5.2(b)) and that could be due to the increased domain wall density between the *c* and *a*-domains in PZT/Si-MIM. The dielectric loss tangent ($\tan\,\delta$) values are similar for all the films within the range of $\approx$0.03 – 0.05.

5.1.1 Comparison of PZT films in MIM and IDE configuration

Planar interdigitated electrodes (IDEs) are used in this study, where the electric field can be applied in the direction parallel to the film plane. To understand and compare the IDE and MIM geometry, it is imperative to define the directions pertinent to the following discussion. In this context, 'c' is defined as the direction of the film normal, and 'a' and 'b' are mutually perpendicular directions in the plane of the film. For a MIM geometry, the 'a' and 'b' directions are equivalent, as our films do not exhibit any preferential in-plane texture. But, for an IDE geometry, the direction 'a' is perpendicular to the IDE fingers, and 'b' is the direction parallel to the fingers. In the case of samples with MIM configuration, the electric field is applied in the 'c' direction, and for the samples with IDEs electric field is applied in 'a' direction (perpendicular to the fingers). Our discussions in the previous section showed that the domain orientation is dictated by the sign and magnitude of the stress in the PZT film on the respective substrates. Therefore, it is also essential to consider the orientation of the electric field with respect to the

major domain orientation.

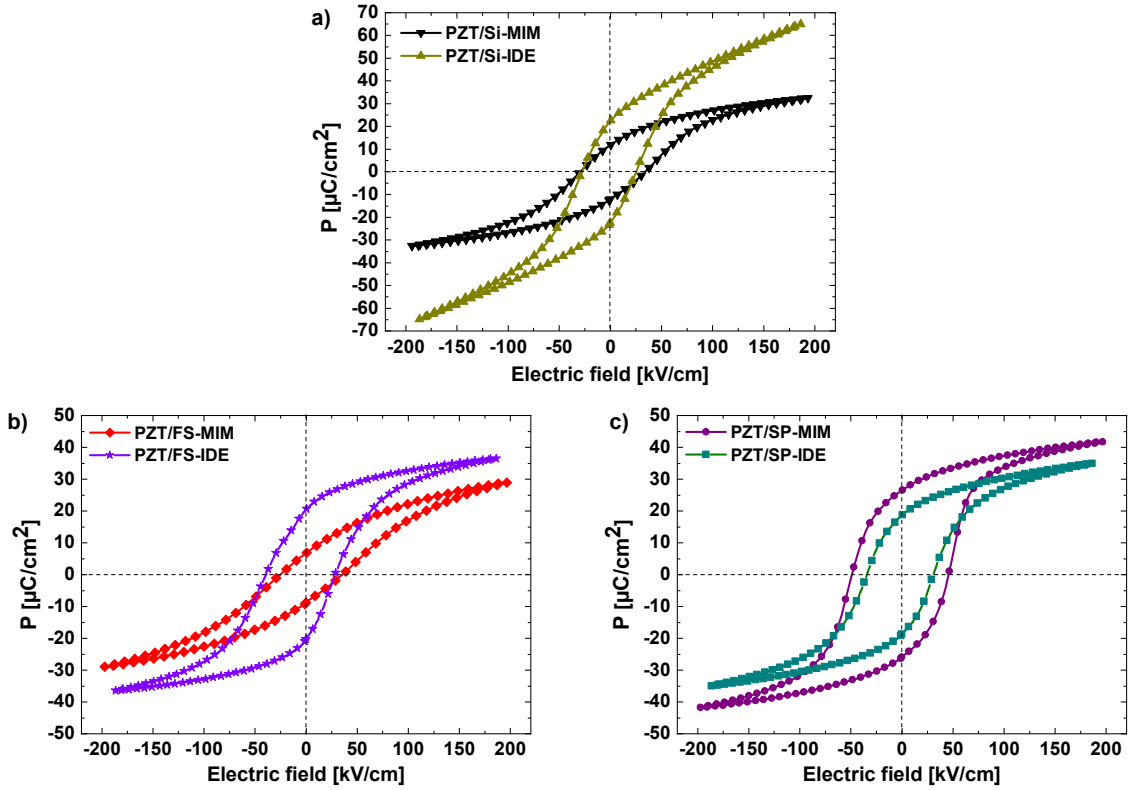

Figure 5.3: Comparison of polarization hysteresis of PZT films in IDE and MIM configuration on (a) Si, (b) fused silica and (c) sapphire substrates. All the measurements were performed at 100 Hz.

Figure 5.3 and 5.4 show the comparison plot of polarization hysteresis $P(E)$ and permittivity measurements $\varepsilon_{33}(E)$, respectively for the films in MIM and IDE configuration on all the substrates. The characteristic values of remanent polarization (P_{r}), maximum polarization (P_{max}) and zero-field permittivity ($\varepsilon_{33}(0)$) of all the films are compared in Table 5.1. From the first observation in Figure 5.3 it is clear that the polarization and permittivity values between the MIM and IDE samples are reversed, except for the PZT/Si-IDE. The high P_{max} and $\varepsilon_{33}(0)$ value for PZT/Si-IDE is due to the influence of parasitic capacitance from semiconducting Si substrate. As it is a clear outlier, the PZT/Si-IDE will not be considered for further discussion.

PZT/SP-MIM has the highest P_{r} value and the smallest ε_{33} among all the samples. The PZT/FS-MIM sample shows the smallest P_{r} of all the samples and a comparatively higher ε_{33} value. On the other hand, the PZT/FS-IDE sample shows a higher P_{r} and lower ε_{33} values in comparison to PZT/FS-MIM and PZT/SP-IDE sample. These differences can be explained by the electric field direction, with the major domain orientation of the particular sample dictated

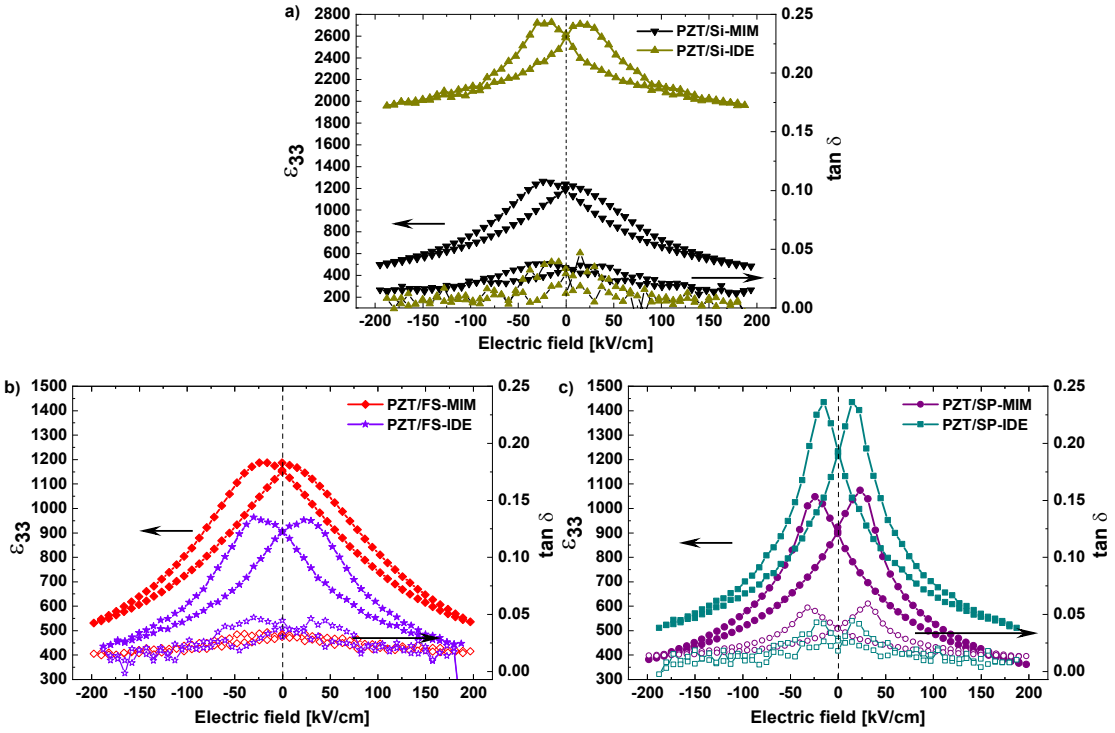

Figure 5.4: Comparison of permittivity hysteresis and loss tangent as function of applied DC bias field at 1 kHz small-signal frequency for the PZT films in IDE and MIM configuration on (a) Si, (b) fused silica and (c) sapphire substrates.

by its stress. For the films on sapphire, the electric field is applied parallel to major domain orientation (out-of-plane domains) in MIM configuration and perpendicular in the case of the IDE configuration. In contrast, for the film on fused silica, the electric field is applied parallel to major domain orientation (in-plane domains) in IDE configuration and perpendicular in the case of MIM configuration. PTZ/Si-MIM shows polarization and permittivity values between the extreme cases of PZT on sapphire and fused silica due to the intermediate tensile stress, resulting in a mixed *a*/*c*-domain configuration. The loss tangent values were similar for all films, in the range of 0.05.

In the following section, a model is presented to explain the observed differences between the in-plane and out-of-plane properties of PZT films in IDE and MIM configurations, respectively. In addition, this model considers the effect of stress (resulting in certain domain configuration) and texture on each substrate in their respective configurations. The following discussion was published in our work [85].

5.2 In-plane and out-of-plane ferroelectric properties

The initial discussion will be based on the following five assumptions; it will be seen later how far these points can be considered valid and what modifications are necessary if a point does not apply:

a) All films are perfectly textured in the $\{100\}_{\mathrm{pc}}$-direction out of the plane and randomly oriented in the plane. With Lotgering factors of 96 %, and 94 % respectively, for the films without Pt bottom electrodes (in IDE configuration) on sapphire and fused silica, this approximation is very good. However, it is less precise for the films with Pt bottom electrodes (in MIM configuration) with Lotgering factors of 78 %, 65 %, and 55 % for sapphire, fused silica, and silicon, respectively.

b) The mechanical stress is large enough to clamp all domains in-plane for PZT/FS with tensile stress and out-of-plane for PZT/SP with compressive stress, even under a high external electric field. The coercive stress of 'soft' bulk PZT is around 50 MPa, that of 'hard' PZT around 150 MPa [223]. The assumption, therefore, is most plausible for low fields and PZT/FS, with substrate stress of more than 240 MPa, and even holds some validity for PZT/SP with a stress of 100 MPa or above. For the case of PZT/Si-MIM under moderate tensile stress of 110 MPa, it is still good enough to clamp all the in-plane domains at low fields. However, at high electric field levels, the blocking force will exceed the clamping stress, and domains will be able to switch between in-plane and out-of-plane directions.

c) The electric field is perpendicular to the film plane for the MIM configuration, and in-plane for the IDE configuration [184]. The first assumption is certainly valid, the second only an approximation: there will be an out-of-plane field component in the IDE configuration due to the curvature of the field lines between the fingers.

d) The ratio of tetragonal to rhombohedral phase is m/n, with $m, n \geq 0$ and $m+n=1$. For a true MPB composition, $m = n = 0.5$; it will be discussed below why the situation may not be so simple here [224].

e) The absolute value of the dipole moment of a unit cell of a given symmetry does not depend on stress. For the tetragonal parts of the film, the polarization is $\vec{P}^T = (P_a^T, P_b^T, P_c^T)$, with $|\vec{P}^T| = P^T$. For the rhombohedral parts, it is $\vec{P}^R = (P_a^R, P_b^R, P_c^R)$, the absolute value is $|\vec{P}^R| = P^R$. The total polarization is $\vec{P} = (P_a, P_b, P_c) = m * \vec{P}^T + n * \vec{P}^R$.

With these assumptions, the polarization vector of the tetragonal parts of PZT/SP is $\vec{P}^T = (0, 0, P_c^T = \pm P^T)$, that of the rhombohedral parts is $\vec{P}^R = \frac{P^R}{\sqrt{3}}(\pm 1, \pm 1, \pm 1)$. Thus, the polar-

ization change during domain reversal in PZT/SP-MIM is $\Delta P_{\mathrm{SP-MIM}} = 2\left(\mathrm{mP^T} + \frac{\mathrm{n}}{\sqrt{3}}\mathrm{P^R}\right)$ and PZT/SP-IDE is $\Delta P_{\mathrm{SP-IDE}} = \frac{2\mathrm{n}}{\sqrt{3}}\mathrm{P^R}$.

The polarization vector of the tetragonal parts of PZT/FS is $\vec{P}^T = \frac{P^T}{\sqrt{2}}(\pm 1, \pm 1, 0)$, that of the rhombohedral parts remains $\vec{P}^R = \frac{P^R}{\sqrt{3}}(\pm 1, \pm 1, \pm 1)$. The polarization change during domain reversal in PZT/FS-MIM is $\Delta P_{\mathrm{FS-MIM}} = \frac{2\mathrm{n}}{\sqrt{3}}\mathrm{P^R}$ and PZT/FS-IDE is $\Delta P_{\mathrm{FS-IDE}} = 2\left(\frac{\mathrm{m}}{\sqrt{2}}\mathrm{P^T} + \frac{\mathrm{n}}{\sqrt{3}}\mathrm{P^R}\right)$.

For PZT/Si, the polarization vector of the tetragonal parts is $\vec{P}^T = \frac{P^T}{\sqrt{3}}(\pm 1, \pm 1, \pm 1)$, and that of the rhombohedral parts remains $\vec{P}^R = \frac{P^R}{\sqrt{3}}(\pm 1, \pm 1, \pm 1)$. Then the polarization change during domain reversal is the same for both MIM and IDE configuration because of the mixed domain configuration and is given by $\Delta P_{\mathrm{Si-MIM/IDE}} = 2\left(\frac{\mathrm{m}}{\sqrt{2}}\mathrm{P^T} + \frac{\mathrm{n}}{\sqrt{3}}\mathrm{P^R}\right)$.

It is interesting to note that for perfect $\{100\}_{\mathrm{pc}}$-texture (condition (a)), $\vec{P}^R$ is independent of the stress state: all of the eight possible dipole directions in the unit cell have the same projection on the $\{100\}_{\mathrm{pc}}$ axis, so neither tensile nor compressive stress makes one of them energetically favorable. P_a and P_b are identical for symmetry reasons since the grains are randomly oriented in-plane. As the electric field is perpendicular to the film in MIM configuration, polarization switching, in this case, means the reversal of the sign of the c- component of $\vec{P}$. In contrast, in the IDE configuration, the sign of the a- component is reversed. Switching between in-plane and out-of-plane polarization is impossible due to condition (b) for the tetragonal parts.

With these arguments, the magnitude of switchable polarization should follow the trend $\Delta P_{\mathrm{SP-MIM}} > \Delta \mathrm{P}_{\mathrm{FS-IDE}} \approx \Delta \mathrm{P}_{\mathrm{Si-IDE}} > \Delta \mathrm{P}_{\mathrm{Si-MIM}} > \Delta \mathrm{P}_{\mathrm{SP-IDE}} \approx \Delta \mathrm{P}_{\mathrm{FS-MIM}}$. Higher polarization also implies better domain orientation and fewer domain walls. This decreases the potential extrinsic contribution to the dielectric permittivity ε_{33}. Neglecting intrinsic contributions, the behavior of ε_{33} should be inverse to that of ΔP: $\varepsilon_{\mathrm{SP-IDE}} \approx \varepsilon_{\mathrm{FS-MIM}} > \varepsilon_{\mathrm{Si-MIM}} > \varepsilon_{\mathrm{FS-IDE}} \approx \varepsilon_{\mathrm{Si-IDE}} > \varepsilon_{\mathrm{SP-MIM}}$. Both relations are well reflected in the data in Table 5.1, with the exception of the proposed equality of $\Delta P_{\mathrm{SP-IDE}}$ and $\Delta P_{\mathrm{FS-MIM}}$. This shows the limitations of the picture based on the five conditions listed above. Similarly the $\varepsilon_{\mathrm{FS-MIM}}$ must be higher than that of $\varepsilon_{\mathrm{Si-MIM}}$, but here the $\varepsilon_{\mathrm{Si-MIM}}$ values are slightly higher or very close to $\varepsilon_{\mathrm{FS-MIM}}$. This could be because of the high domain wall density between the in-plane and out-of-plane domains, as the films on Si have a mixed *a/c*-domain configuration.

The effects of any deviations of the Lotgering factor from the ideal value of 1 (condition (a))

should be low: grains not perfectly oriented along the $\{100\}_{\mathrm{pc}}$ direction will result in a lowering of the effective out-of-plane polarization of the tetragonal fraction of the film since the projection of the local dipole moment of the $\{001\}_{\mathrm{pc}}$ axis is no longer ideal. At the same time, the projection of the local dipole moment of at least one of the polarization states of the rhombohedral phase fraction will increase, compensating for the loss of polarization in the tetragonal phase. Condition (b) that prohibits switching between in-plane and out-of-plane domains is more critical. The absolute value of in-plane stress in PZT/SP-IDE and PZT/Si-MIM is only 120 MPa, and 110 MPa, respectively, while it is 269 MPa in PZT/FS-MIM. Some remanent domain switching between the three orientations should therefore be possible in PZT/SP-IDE accounting for the higher P_{r}. For PZT/Si-MIM, switching between in-plane and out-of-plane oriented domains involves movement of non-180° domain walls that are not parallel to the electric field direction, which in turn leads to higher ε_{33} values. At high fields, the clamping criterion is not fully met by any of the samples; the relative difference between the $P_{\max}$ values of all the samples is, therefore, lower than that of the zero-field P_{r}. At the higher field, the domains that can be switched should be aligned in the field direction, thus reducing the difference in $P_{\max}$ values of all the samples. Incomplete fulfillment of condition (c) is another point that may account for unexpectedly high polarization values in PZT/SP-IDE. Near the electrodes of the IDE structure, the electric field has a non-zero out-of-plane component [184]. This adds a contribution of the out-of-plane tetragonal domains to the measured polarization, increasing the measured values. COMSOL simulations in Chapter 4 show that the volume fraction under the out-of-plane field is less than 5 % of the total volume between the electrode fingers, which would be the order of magnitude with which P^T contributes to the measured polarization. A similar effect does not occur in PZT/Si-MIM or PZT/FS-MIM, as the field does not have an in-plane component that would allow additional polarization switching of the predominantly in-plane tetragonal domains.

The validity of condition (d) is difficult to assess. First, the phase composition is not homogeneous throughout the film. As $PbTiO_3$ has a lower crystallization entropy, it will tend to nucleate first, making parts of the film closer to the substrate Ti-rich and thus more tetragonal at each crystallization step compared to layers further away from the substrate [225–227]. Then, the phase composition is influenced by the local stress [228] which is also not homogeneous but highest at the interface and lower at the free surface. Last, the phase composition may not be constant during hysteresis cycling but can change under the externally applied electric field [224, 229]. While the first two phenomena can be accounted for by the correct choice of the parameters m and n, the possible electric field-induced phase transition would lead to a field-dependence of

the parameters that is beyond the scope of the present phenomenological model. Lastly, with respect to condition (e), the change of the local dipole moments due to stress-induced deformation of the unit cells, equivalent to the intrinsic piezoelectric effect, also can account for some of the observed discrepancy: using a very rough estimation and assuming $d_{33,\mathrm{eff}} \approx 150\,\mathrm{pC/N}$ and $d_{31,\mathrm{eff}} \approx -50\,\mathrm{pC/N}$ [224, 230], about half of these values are due to intrinsic contributions [231–233]. Taking into account the stresses in Table 5.1, the intrinsic piezoelectric effect then induces an additional switchable polarization of $0.25\,\mu\mathrm{C/cm^2}$ in PZT/SP-MIM and of $1.8\,\mu\mathrm{C/cm^2}$ in PZT/FS-IDE, but reduces the polarization in PZT/SP-IDE by $0.9\,\mu\mathrm{C/cm^2}$ and by $0.67\,\mu\mathrm{C/cm^2}$ in PZT/FS-MIM. This helps to explain the deviation of the observed relation of ΔP_{SP-IDE} and ΔP_{FS-MIM}, while for the ΔP_{SP-MIM} the effects would be minor.

5.3 Degradation of ferroelectric properties in PZT thin films with bottom electrode

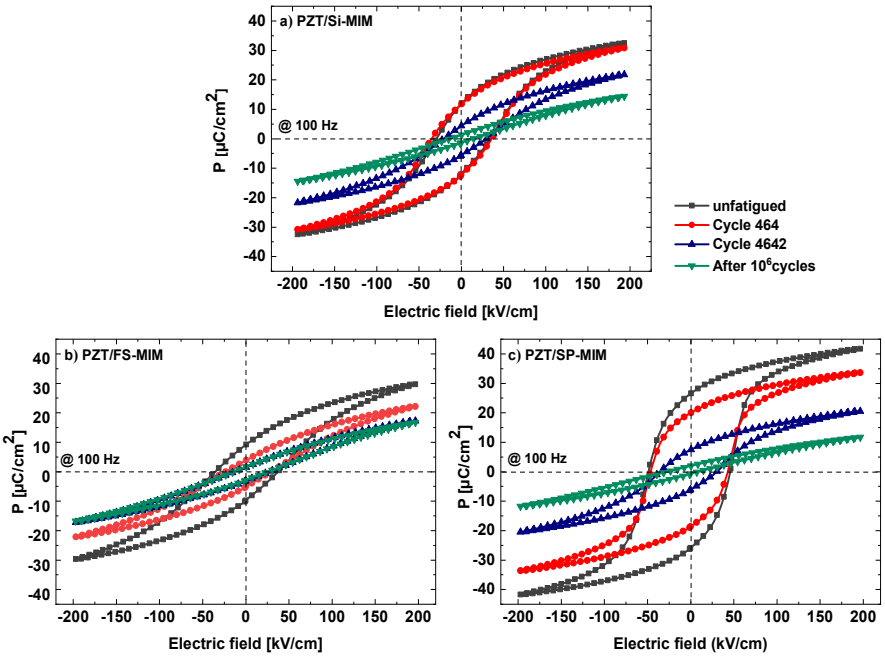

Figure 5.5: Degradation of polarization hysteresis during bipolar fatigue cycling at 100 Hz frequency for the sample in MIM configuration, P-E loops shown in the figures were recorded at 100 Hz for all the samples.

5.3.1 Fatigue mechanism

Bipolar fatigue cycling was performed on all the MIM samples (whose P-E loops are shown in Figure 5.5) by applying a triangular waveform at 100 Hz with 200 kV cm^{-1} amplitude for 1 million cycles. Polarization hysteresis and permittivity values were measured in-situ at regular intervals during fatigue cycling. Degradation of remnant polarization during bipolar fatigue cycling is illustrated in Figure 5.6, which shows the variation of normalized remnant polarization (norm $2P_{\mathrm{r}}$) over switching cycle number (n) in log scale. PZT/FS-MIM underwent a gradual degradation in contrast to PZT/Si-MIM and PZT/SP-MIM, which had a sudden onset of degradation around 10^3 cycles. All three films lost 75% or more of switchable polarization ($2P_{\mathrm{r}}$) by the end of 10^6

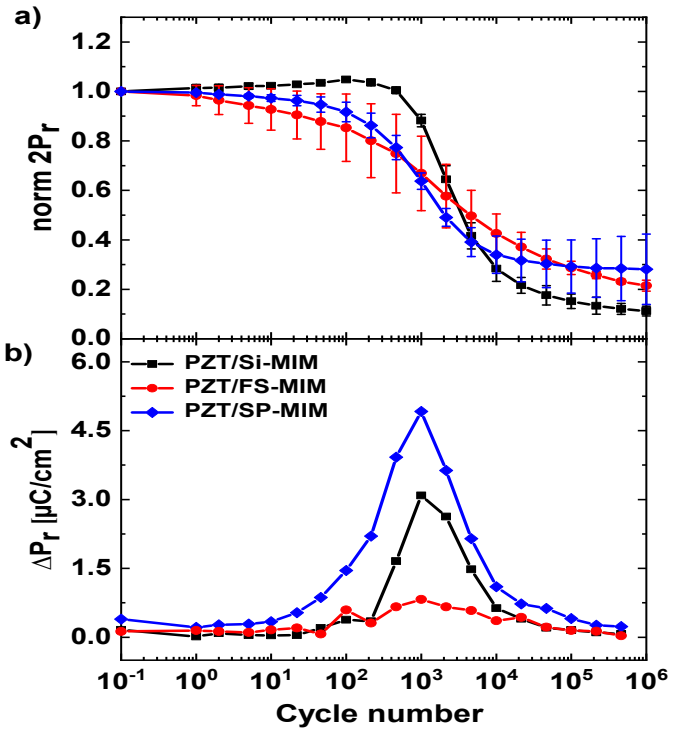

Figure 5.6: (a) Comparison of switched remanent polarization relative to the starting value (norm $2P_{\mathrm{r}}$) versus cycle number (n) for up to a million cycles between PZT films in MIM configuration on all three substrates (error bars were introduced from measuring fatigue degradation of three different electrodes) (b) Absolute polarization change (ΔP_r) with respect to the respective previous measurement.

cycles in Figure 5.6. The change in polarization (ΔP_r) to the previous characterization cycle, i.e., the first derivative of the polarization vs. switching cycle, is also depicted in Figure 5.6(b). Correlated to the sudden drop of polarization, there is a sharp maximum of this derivative for PZT/SP-MIM and PZT/Si-MIM at 10^3 cycles, indicating the inflection point of the norm $2P_{\mathrm{r}}$(n) curve where most of the polarization loss happens. Interestingly, the derivative peaks at the same

point for PZT/FS-MIM, even though the maximum is far less pronounced than for the other two substrates.

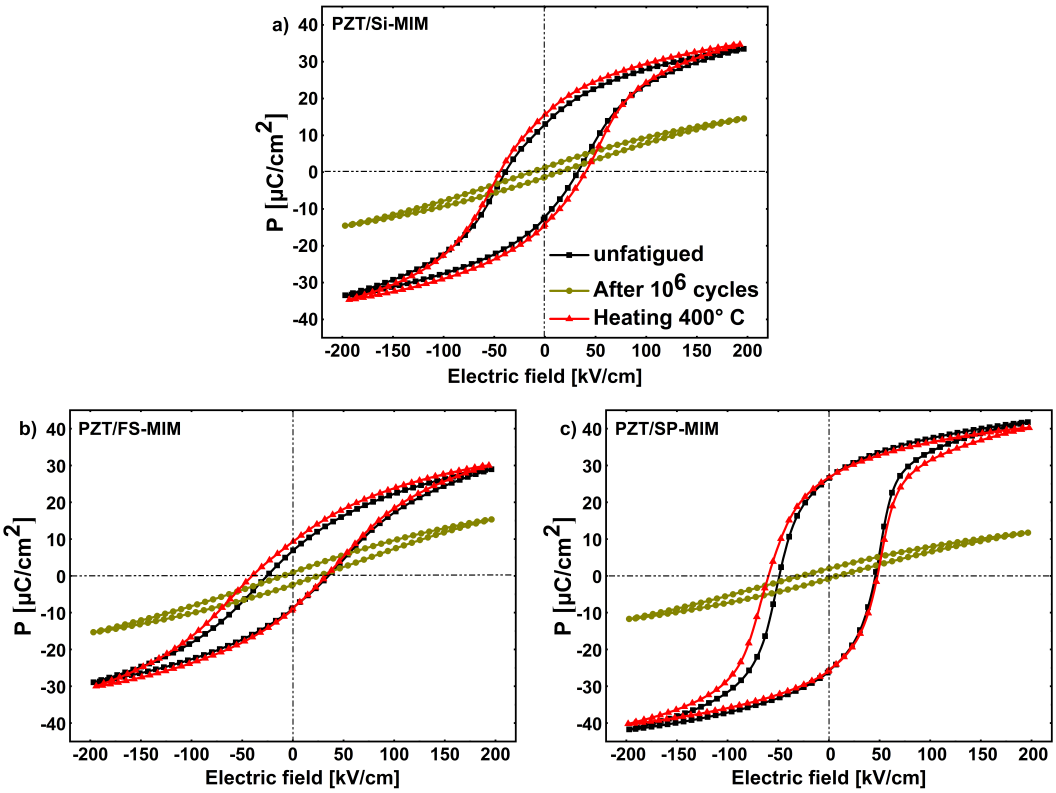

Figure 5.7: Polarization hysteresis for (a) PZT/Si-MIM, (b) PZT/FS-MIM and (c) PZT/SP-MIM before and after fatigue cycling, and showing recovery after thermal treatment. P-E loops were measured at 100 Hz.

In order to understand the mechanism of degradation and to study the recovery of the polarization lost during fatigue cycling, all samples were heated to 400 °C for 5 minutes, i.e., above the Curie temperature of ≈ 390 °C [234]. As shown in Figure 5.7, the polarization hysteresis curves show complete recovery after the thermal treatment on all three samples. The fatigue-induced degradation in switchable polarization is completely removed by heating above T_C [122]. The recovery of switchable polarization after heating cannot be explained based on charge injection at the electrodes or mechanical degradation. However, the degraded electrode/ferroelectric interface can also be a source of defects [127]. Of all the mechanisms proposed in the literature, the pinning of domain walls at charged defects, such as oxygen vacancies or defect agglomerates, is the most plausible [235, 236]. Heating into the paraelectric phase above T_C removes all domain walls. During re-cooling to the ferroelectric phase, a new domain structure develops that is not attached

to the charged defects. This creates a 'clean-slate' for the ferroelectric hysteresis measurements, starting the fatigue process from a fresh state.

As seen in Figure 5.6, the polarization loss sets in rather suddenly around 10^3 cycles in PZT/SP-MIM and PZT/Si-MIM, with the absolute change highest in PZT/SP-MIM, while the relative change is slightly more pronounced in PZT/Si-MIM. In contrast, the degradation is more gradual in PZT/FS-MIM, starting during the first few cycles, and extending to 10^6 cycles. However, as shown in Figure 5.6(b), the polarization loss also has a weak maximum at 10^3 cycles for PZT/FS-MIM, just as for the other two systems. As discussed earlier, the relative amount of *c*-domains decreases from PZT/SP-MIM over PZT/Si-MIM to PZT/FS-MIM. This indicates that the sudden onset of degradation is linked to the higher *c*-domain population.

5.3.2 Polarization Reversal

For a stress-free film, polarization reversal can occur either by a single 180° switching process or by two successive 90° switching [30, 91, 93, 219]. This is true for the tetragonal component of the domains. As discussed in Chapter 1 section 1.4.1, our films with MPB composition should have a 50/50 tetragonal and rhombohedral composition. Therefore, 180°, 109° and 71° switching processes should also be possible. It has been described before that polarization reversal in polycrystalline PZT happens by two consecutive 90° switching steps [237]. However, with high enough tensile stress, the switching from in-plane to out-of-plane or out-of-plane to in-plane becomes less favorable. For PZT/SP-MIM under compressive in-plane stress, forming in-plane domains is energetically unfavorable. If the stress is high enough, switching out-of-plane domains to an in-plane orientation becomes completely suppressed. Therefore, for PZT/Si-MIM and PZT/FS-MIM under high tensile in-plane stress, switching of tetragonal components will be suppressed. The switching event is dominated by pre-existing domain walls in this case, and no nucleation of new domains is needed. This behavior should be even more pronounced in PZT/Si-MIM and PZT/FS-MIM under high tensile in-plane stress, as the stress favors in-plane domains.

A minority of domains can be oriented out-of-plane, but they will be bounded by in-plane domains with 90° domain walls between them. In PZT/SP-MIM, polarization reversal under an electric field anti-parallel to the current poling direction will occur by nucleation of new domains with negative polarization, forming 180° walls to the predominant domain orientation. The nuclei will grow by the forward motion of the walls, forming needle-shaped wedges with negative polarization, followed by sideways expansion and growth of the existing domains [29]. Two-step polarization reversal (i.e., in-plane to out-of-plane and vice-versa) may be possible in PZT/Si-

MIM if the driving electric field can overcome the bi-axial tensile stress, but not in PZT/FS-MIM. It can be estimated that only single-step polarization reversal contributes to the total polarization in PZT/SP-MIM and PZT/FS-MIM. With a change of the configuration which prefers *c*-domains to *a*-domains, the prevalence of 180° polarization reversal processes will decrease in favor of non-180° reversal processes. Consequently, pinning of non-180° domain walls which dominate in PZT/FS-MIM, can start right from the first cycle, whereas pinning of 180° domain walls that are relatively more prevalent in PZT/SP-MIM and PZT/Si-MIM can start only after a sufficient number of defect agglomerates has formed.

In addition, the substrate stress can have a direct influence on defect migration and agglomeration: first-principles calculations of oxygen vacancy migration in perovskites indicate that tensile stress – as present in PZT/FS-MIM – facilitates their migration while a comparatively smaller tensile stress in PZT/Si-MIM and compressive stress – as present in PZT/SP-MIM hinders it [238–241]. This also agrees with the observed immediate start of fatigue in PZT/FS-MIM, while PZT/Si-MIM and PZT/SP-MIM take more cycles until fatigue sets in.

The polarization degradation trend in Figure 5.6 shows that 90° domain walls get pinned slowly and continuously, while 180° domain walls get pinned nearly instantaneously at 10^3 cycles. It has been suggested that 90° domain walls get pinned by defects regularly present in the sample [242] while pinning of 180° domain walls requires modifications of defect structure, such as the formation and migration of oxygen vacancy agglomerates to be trapped along the domain walls that are temporarily charged during fatigue cycling [243]. It is also noteworthy that the fatigue resistance of the PZT thin films reported here is lower than that reported in the literature for solution-deposited PZT thin films [127, 128, 244–247]. This is owed to the fact that the PZT films used in this study are un-doped. At the same time, a comparably low cycling frequency and high cycling amplitude are used in the present study in contrast to most literature studies (amplitude less than $3\times E_c$ and frequency from kHz to MHz range). Therefore, domain walls have more time to interact and get pinned by charged defects like oxygen or lead vacancies. As a result, the overall range of domain wall motion is higher, making a larger volume available for pinning.

5.3.3 Evolution of reversible and irreversible processes during fatigue cycling

In describing the polarization response to an external field, it is customary to distinguish between intrinsic and extrinsic contributions [248, 249]. The intrinsic contributions stem from field-induced distortions of the crystal lattice, and extrinsic contributions result from the motion

of ferroelectric domain walls, movement of defects, or field-induced phase changes.

In particular, domain-wall motion can be either reversible or irreversible. Reversible means that the low-amplitude ac field causes a domain wall movement around an equilibrium position, while irreversible processes lead to a permanent movement of domain walls. In contrast, intrinsic contributions to polarization response are typically always considered reversible. The evolution or degradation of reversible and irreversible processes during fatigue cycling can be understood by analyzing the small-signal dielectric permittivity ε_{33} and the large-signal permittivity ε_{ls}. The ε_{ls} is computed from the slope of polarization hysteresis, as shown in the equation given below [250, 251].

$$\varepsilon_{ls} = \frac{1}{\varepsilon_0}(\frac{\partial P}{\partial E}) \tag{5.1}$$

The evolution of small-signal permittivity during fatigue cycling is illustrated in Figure 5.8 by comparing the ε_{33} curves for various cycles between all the films. ε_{33} degradation in all films during fatigue follows a similar trend. PZT/FS-MIM and PZT/Si-MIM ended with comparable values at the end of fatigue. In contrast, PZT/SP-MIM, which had a lower ε_{33} value from the start, ended up with even lower values than the films on the other two substrates after 10^6 cycles. Figure 5.9 demonstrates the evolution of large-signal permittivity ($\varepsilon_{ls}(E)$) over the applied electric field for all films during fatigue cycling. Larger differences in the magnitude of ε_{ls} were observed around the coercive field region (E_c) for the unfatigued case. In contrast, the values were comparable at high field regions between the film systems. The degradation trend of ε_{ls} is also clearly visible in these plots; all three films show similarly degraded values at the end of fatigue cycling. The small-signal permittivity ε_{33} stems almost exclusively from reversible polarization changes, both intrinsic and extrinsic, while the large signal permittivity ε_{ls} combines the effects of both reversible and irreversible contributions [250].

Figures 5.8 and 5.9 points to the fact that there is a larger difference between the magnitude of ε_{33} and ε_{ls} in the unfatigued state. It indicates that the extrinsic irreversible processes are more pronounced than the reversible processes. In bulk systems, there are usually two maxima of ε_{33} around the coercive field: the density of domain walls is highest in the region of domain reversal, leading to an increase of reversible extrinsic contributions to the small-signal permittivity [32, 252]. However, from Figure 5.8, it can be observed that the two maxima are displaced towards the zero-field region, almost merging into a single maximum. In the thin-film systems, the increase of ε_{33} is not mainly due to extrinsic effects but intrinsic reversible processes such as ionic and electronic displacement [221, 252]. The maxima of ε_{ls} seen in Figure 5.9 around the coercive field region represents the irreversible processes corresponding to the reorientation

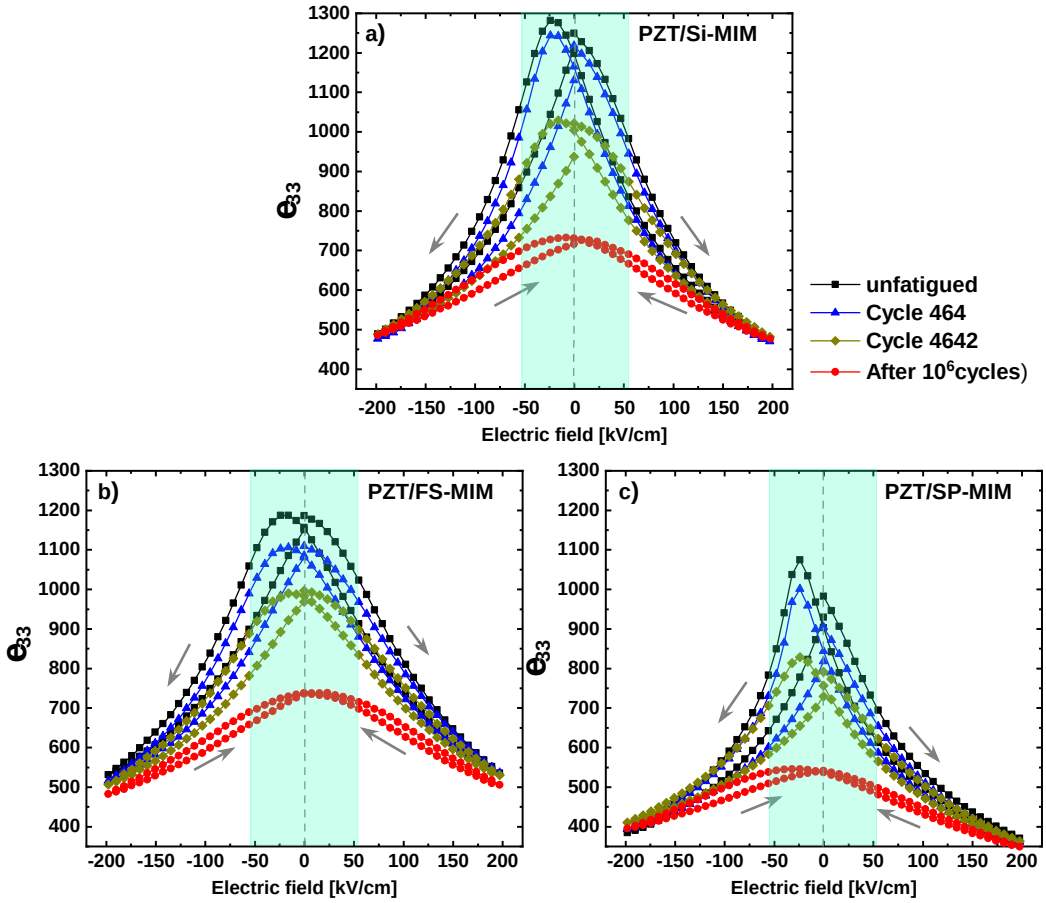

Figure 5.8: Variation of small-signal permittivity hysteresis for (a) PZT/Si-MIM and (b) PZT/FS-MIM and (c) PZT/SP-MIM for the unfatigued state, cycle 464, cycle 4642 and after 10^6 cycles, arrows indicating the direction of change in electric field. The highlighted regions indicate the two maxima that are displaced towards the zero-field region, almost merging into a single maximum. Small-signal permittivity measured at 1 kHz small-signal frequency.

of domains. The maxima are highest for PZT/SP-MIM, followed by PZT/Si-MIM and PZT/FS-MIM, again indicating that there are more pronounced irreversible domain reorientation processes in systems with higher *c*-domain content. The comparison of ε_{33} and ε_{ls} reveals that the pinning reduces irreversible domain wall motion much more strongly than reversible domain wall motion and intrinsic contributions to permittivity.

5.3.4 Ratio of small to large-signal permittivity ξ

It can be understood clearly from the above discussion that both reversible and irreversible polarization processes are affected by fatigue in all the systems. To compare and separate the influence of fatigue on reversible and irreversible processes, the ratio of small to large-signal

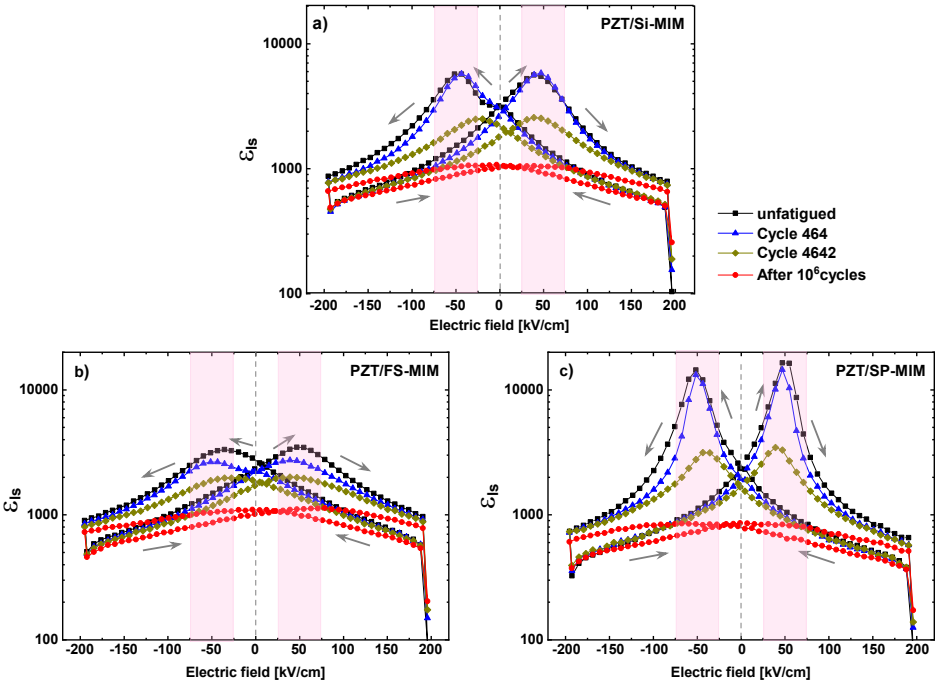

Figure 5.9: Variation of large-signal permittivity hysteresis for (a) PZT/Si-MIM and (b) PZT/FS-MIM and (c) PZT/SP-MIM for the unfatigued state, cycle 464, cycle 4642 and after 10^6 cycles, arrows indicating the direction of change in electric field. The highlighted parts indicate the two distinct maxima around the coercive field region

permittivity $\xi = \varepsilon_{33}/\varepsilon_{ls}$ is plotted as a function of the electric field in Figure 5.10. If only reversible processes are present in the system, the ratio ξ will be 1, while for systems with exclusively irreversible processes, ξ will become zero. In the unfatigued state, ξ values are lowest for PZT/Sap-MIM ($\xi \approx 0.3$ at zero field and $\xi \approx 0.05$ around the coercive field) compared to PZT/Si-MIM ($\xi \approx 0.4$ at zero field and $\xi \approx 0.2$ around the coercive field) and PZT/FS-MIM, ($\xi \approx 0.45$ at zero field and $\xi \approx 0.3$ around the coercive field). At very high field amplitudes, ξ is even higher for all three systems, increasing nearly to unity on decreasing field. In this region, the systems are poled as completely as possible, no further irreversible domain wall motion is possible, and all polarization changes result from reversible intrinsic effects. Consequently, $\varepsilon_{33} \approx \varepsilon_{ls}$ in this high field region and ξ approaches 1.

The low values in the coercive field region indicate that, as expected, irreversible processes dominate during polarization reversal. Reversible processes become more relevant at zero field and for very high field amplitudes. Higher values of ξ are directly correlated with a decrease in the importance of irreversible domain wall motion compared to reversible processes [253]. The ratio ξ in PZT/SP-MIM is similar to that of bulk systems, where $\xi \approx 0.3$ at zero field and $\xi \approx 0$ around

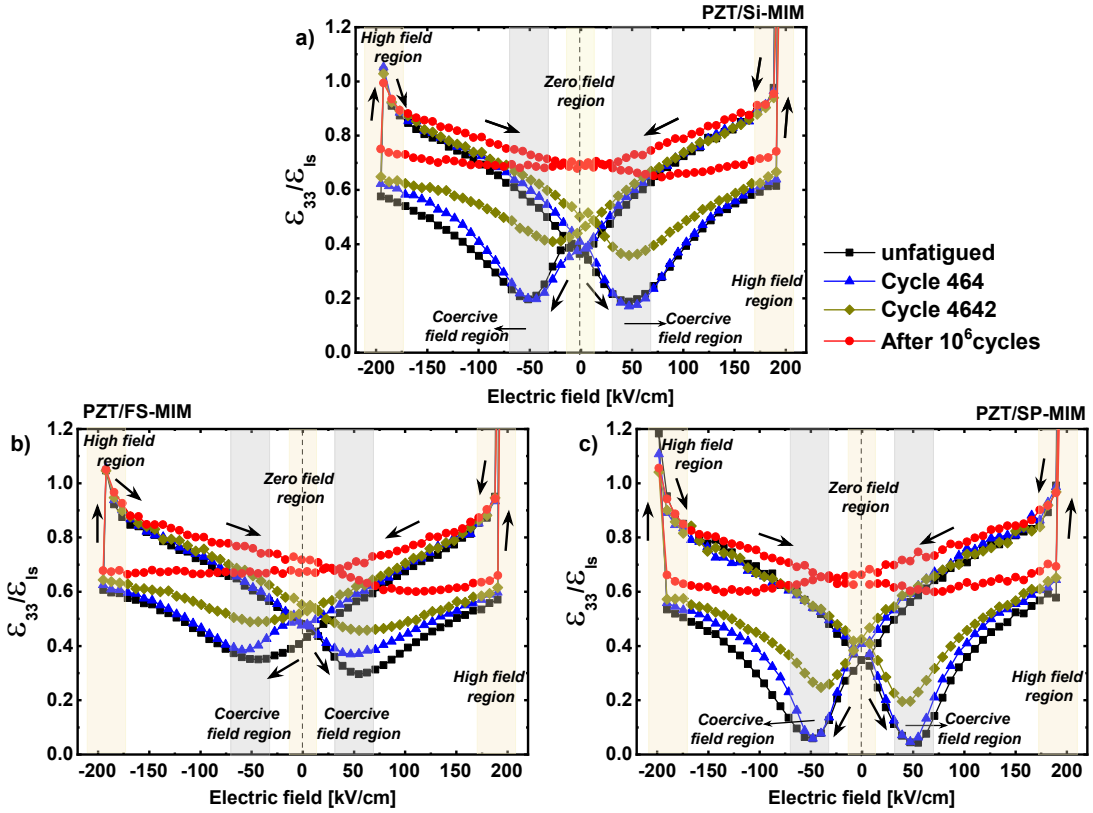

Figure 5.10: Ratio of small-signal to large-signal permittivity variation over applied electric field for PZT thin film on (a) Si and (b) fused silica and (c) sapphire substrates in MIM configuration for the unfatigued state, cycle 464, cycle 4642 and after 10^6 cycles. Different regions of interest are highlighted and marked in the figure.

the coercive field were reported [250], while it is much higher in both PZT/Si-MIM and PZT/FS-MIM. In the two latter systems under high tensile stress, there is far less irreversible domain wall motion and domain switching than the unstressed bulk piezo-ceramics or the compressively stressed PZT/SP-MIM. By the end of the fatigue cycling, ξ is similar for all three systems. The peaks around the coercive field have evolved into a kind of plateau, with ξ values of ≈ 0.7 at zero fields and $\approx 0.60 - 0.65$ around the positive coercive field. The decrease of ε_{33} and ε_{ls} in both sample types shows that both reversible and irreversible processes of polarization reversal are suppressed by fatigue, but the overall increase of ξ in all the samples shows that the irreversible processes are more strongly affected by fatigue than the reversible ones. In the fatigued state, the long-range domain wall movement is reduced to the degree that even for PZT/SP-MIM in the coercive field region, a significant amount of polarization change stems from reversible effects such as unit cell deformation. However, reversible effects are dominant for PZT/SP-MIM outside the coercive field region and for PZT/Si-MIM and PZT/FS-MIM across the entire field range. Though much less pronounced, a similar phenomenon has been observed during the fatigue of

bulk PZT when pinning of domain walls is the dominant fatigue mechanism [250].

5.4 Fatigue-free behaviour of PZT films with IDEs

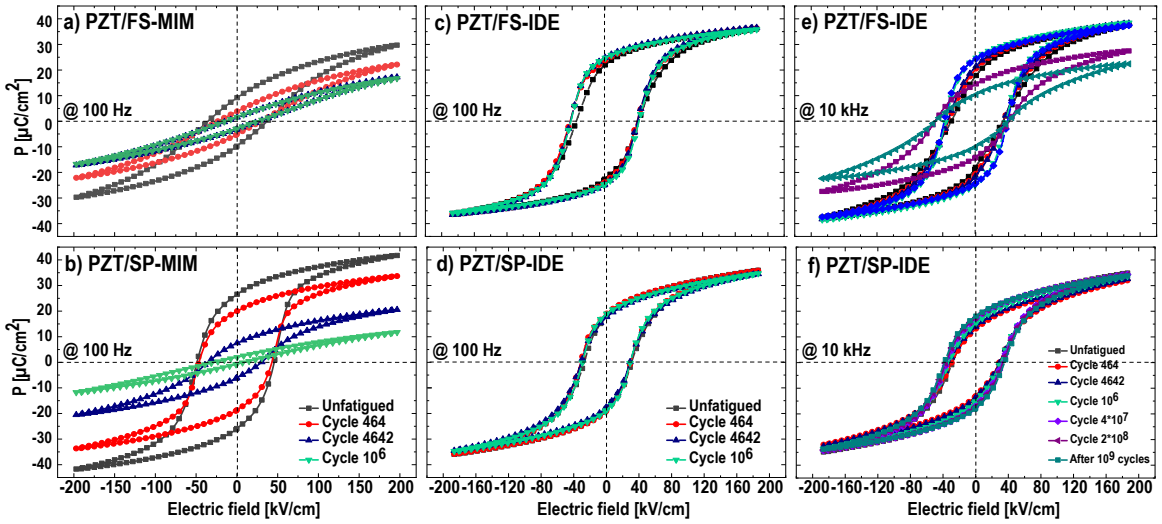

Figure 5.11: Degradation of polarization hysteresis during bipolar fatigue cycling at 100 Hz; (a & b) samples in MIM configuration, (c & d) samples in IDE configuration, and (e & f) samples in IDE configuration subjected to bipolar fatigue cycling at 10 kHz. P-E loops shown in the figures were recorded at 100 Hz for all the samples.

The PZT films on fused silica and sapphire in IDE configuration were also subjected to fatigue cycling. Bipolar fatigue cycling was performed by applying a triangular waveform with a maximum amplitude of 200 kV cm^{-1} at different frequencies up to 10^9 cycles. P(E) measurements were performed in-situ at regular intervals during cycling. Figures 5.11 and 5.12 compare the change in P-E and ε_{33}-E loops during bipolar fatigue cycling of all the samples. In the unfatigued state, PZT/SP-MIM shows the highest P_r value and the smallest ε_{33} among all the samples. On the other hand, the PZT/FS-MIM sample shows the smallest P_r of all the samples and a comparatively higher ε_{33} value. On the other hand, the PZT/FS-IDE sample shows higher P_r and lower ε_{33} values than the PZT/SP-IDE sample.

The evolution of normalized switchable polarization (norm $2P_\mathrm{r}$) is compared between the MIM and IDE samples. From Figure 5.13, it can be observed that the films with IDEs do not show pronounced degradation in switchable polarization as is in the case of MIM samples. The polarization degradation in the case of MIM samples on all three substrates had set in early during the cycling, around 1000 cycles, irrespective of the domain orientation (as discussed in the previous sections). On the other hand, the onset of degradation began only after 10^7 cycles

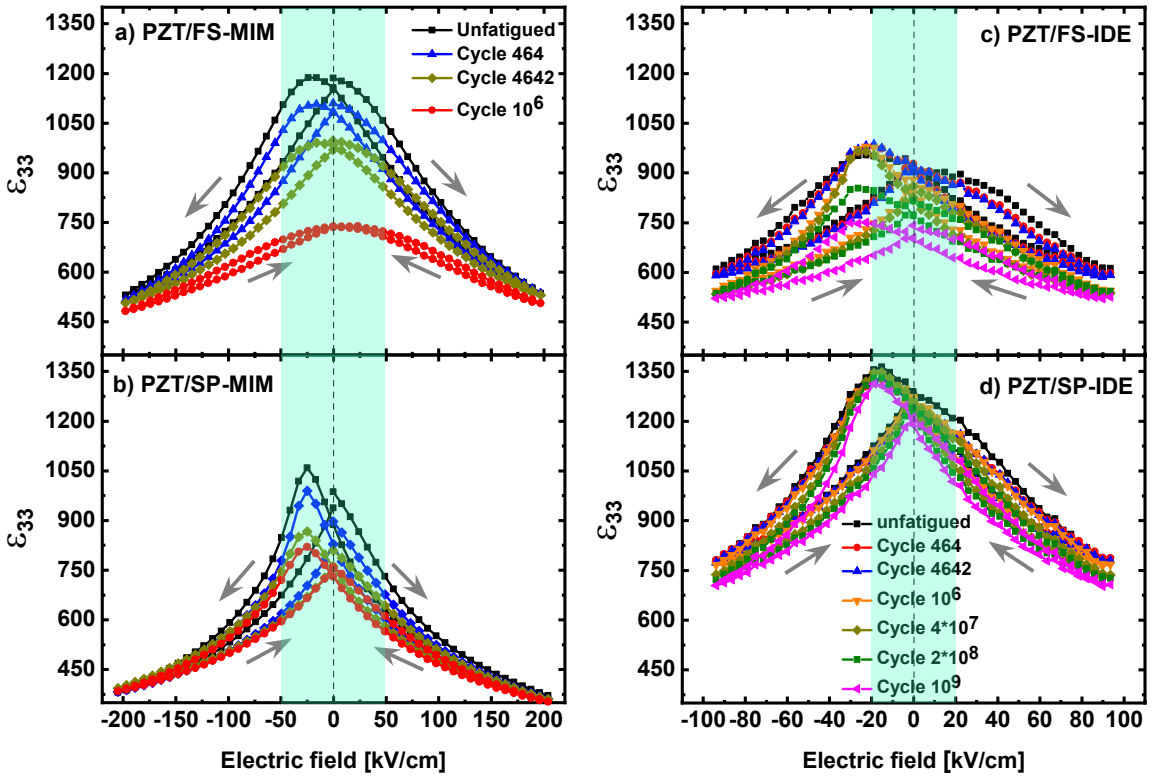

Figure 5.12: Comparison of small-signal permittivity ($\varepsilon_{\rm ss}$) variation during fatigue cycling for (a & c) MIM and (b & d) IDE samples (loops are shown only for the samples cycled at 10 kHz) , arrows indicate the direction of change in electric field. Note: the small signal permittivity measurements for IDE samples were performed only upto 100 kV/cm to avoid short circuiting of the IDE electrodes under high DC bias field during long term cycling.

for PZT/FS-IDE and PZT/Si-IDE, but there is no visible degradation in PZT/SP-IDE sample even after 10^9 cycles. This indicates that with the change in orientation of the electric field with respect to the major domain orientation in the film, the degradation in switchable polarization reduced substantially for the same cycling conditions.

By comparing the evolution of switchable polarization during bipolar cycling in IDE samples, it can be seen that $P_{\rm r}$ increases gradually in PZT/FS-IDE before the onset of degradation and decreases initially for PZT/SP-IDE before increasing again to the original value around 10^7 cycles. However, this increase is not seen in Figure 5.12 where the change in small signal permittivity is plotted for various cycles during fatigue cycling. Only the decrease in ε_{33} is observed after 10^7 cycles for PZT/FS-IDE, and at the same time, no observable changes in ε_{33} are observed for PZT/SP-IDE. In contrast, the large signal ($\varepsilon_{\rm ls}$) permittivity variation shown in Figure 5.14 for the PZT/FS-IDE sample clearly shows an increase in ε_{ls} after a few hundred cycles and decreases after the onset of degradation. This indicates an increase in domain switching from the pristine state

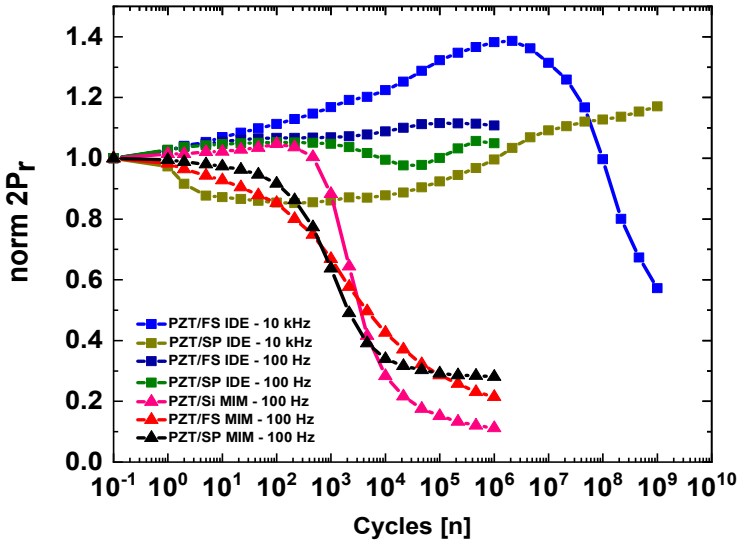

Figure 5.13: Degradation of switchable polarization during bipolar fatigue cycling with 200 kV cm-1 at 100 Hz and 10 kHz for the PZT films in IDE configuration, compared with PZT films in MIM configuration cycled at 200 kV cm-1 at 100 Hz.

before the onset of degradation. It is possible that the domains that are initially clamped by high tensile stress were released progressively during cycling, thus contributing to higher switchable polarization. The evolution of $\varepsilon_{\mathrm{ls}}$ also shows that domain switching is reduced after 200 million cycles. In contrast the changes seen from norm-$2P_r$ during cycling for PZT/SP-IDE are not so apparent from the $\varepsilon_{\mathrm{ls}}$ plot in Figure 5.14(d).

Apart from the observed differences in the $\varepsilon_{\mathrm{ls}}$ values between the MIM and IDE samples, it was also evident enough to understand the differences in switching dynamics between the MIM and IDE samples. Considering the case of PZT/SP-MIM and PZT/FS-IDE, where the electric field is aligned with the major domain orientation, polarization reversal occurs predominantly by 180° switching process (i.e., one-step switching). Whereas, in PZT/SP-MIM, both 90° and 180° switching processes (i.e., one-step and two-step switching) is possible for PZT/FS-IDE. The switching process in these two cases includes nucleation of new domains and forward motion of the domains, followed by side-ward expansion and growth of the existing domains. In the case of PZT/FS-MIM and PZT/SP-IDE, where the electric field is aligned perpendicular to the major domain orientation, it predominantly follows one step switching process through 109° or 71° switching. The switching event is dominated by pre-existing domain walls in this case, and no new domain nucleation event is needed.

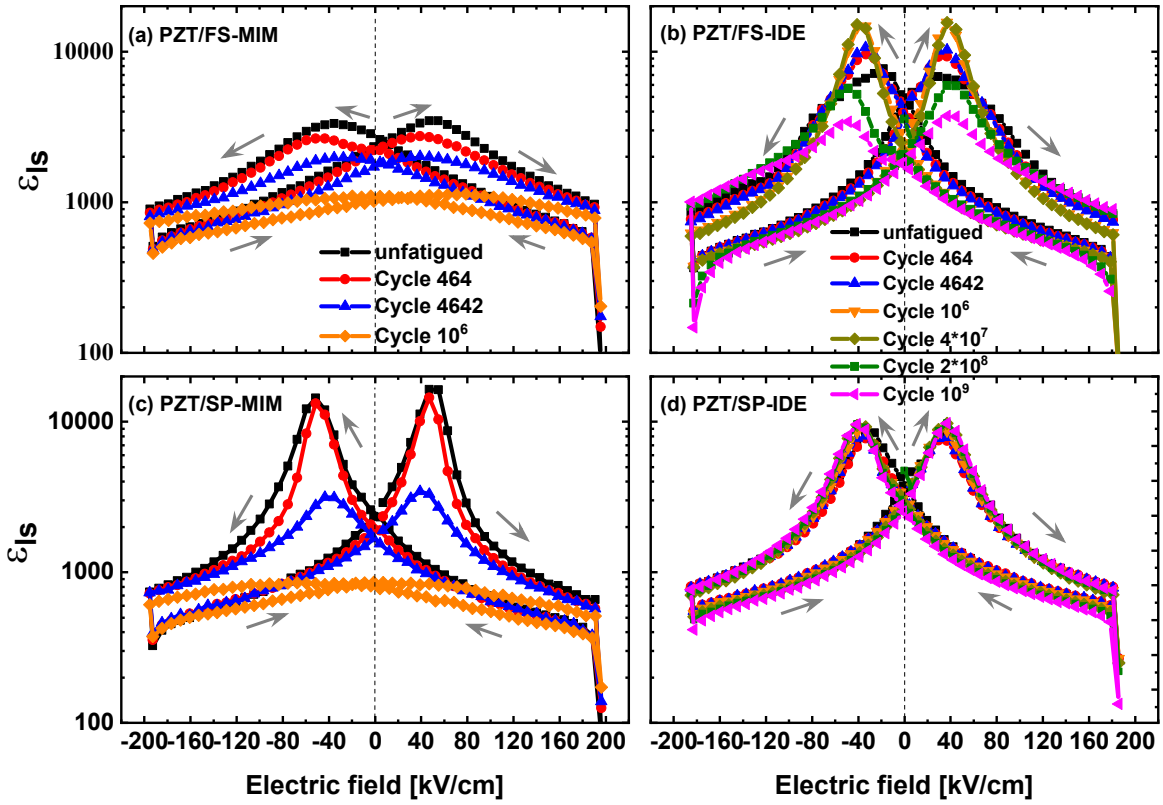

Figure 5.14: Comparison of large signal permittivity ϵ_{ls} variation during the fatigue cycling for (a & c) MIM and (b & d) IDE samples (loops are shown only for the samples cycled at 10 kHz) on fused silica and sapphire, arrows indicate the direction of change in electric field.

5.4.1 Proposed mechanisms

The dominant polarization fatigue mechanism in the case of MIM samples was experimentally identified and discussed in our previous sections as pinning of domain walls by oxygen vacancy agglomerates [84]. In the case of IDE samples, the oxygen vacancies do not seem to affect the long-term switching behavior. It is possible that the grain boundaries can act as oxygen vacancy traps, preventing them from pinning the domain walls. It was clear from the SEM cross-section images from Figures 3.7, 3.8, and 3.11 in Chapter 3 that all the films have dense and columnar microstructure. Therefore, the applied electric field in the IDE configuration encounters more grain boundaries in its path in contrast to the columnar grains with fewer grain boundaries in the case of the MIM configuration. Several studies suggest that in perovskite oxide ceramics [254, 255] as well as in metallic-oxides [256], grain boundaries can act as potential barriers for oxygen vacancy diffusion. Some literature further indicates the segregation of oxygen vacancies along the grain boundaries [257].

Grain boundaries trapping the positively charged oxygen vacancies can, in turn, alter the

electrical properties of the material. For perovskites such as PZT with oxygen vacancies, grain boundaries impeding their diffusion and acting as potential trapping sites can prevent the vacancies from diffusing towards the domain walls and eventually pinning them during cyclic operation. However, the PST/FS-IDE sample shows an increase in P_{r} from the first cycle. A sudden degradation is observed after 10^7 cycles, and the sample loses 50% of its initial value at the end of 10^9 cycles. This could indicate two different things: firstly, the domains are initially clamped by bi-axial tensile stress, and high field cycling can overcome this stress to switch the domain in the field direction contributing to an increase in P_{r}. Secondly, during cycling, the pre-existing domain walls can move from one pinning center to another, and this movement can contribute to the increase in P_{r}. The sudden drop in P_{r} denotes a threshold beyond which the domains are pinned by defect agglomerates. Once the threshold is reached, it could indicate that all the domains are possibly pinned. Therefore, further cycling beyond this point aids field-induced diffusion and migration of defects towards the domain walls and eventually pin them. It is also logical to correlate the effect of residual stress in each thin film system on the activation and diffusion energies of the oxygen vacancies present. Some earlier works [238–241] on model ferroelectric systems shows that the compressive strain in the crystal lattice can increase the formation and migration energies of the oxygen vacancies. In contrast, the tensile strain reduces their migration energies. With this hypothesis in mind, one can argue that the combined effect of electrode design with the microstructure and the compressive strain gradient due to the displacement field could potentially contribute to the fatigue-resistant behavior of the PZT/SP-IDE thin films.

5.5 Summary

The high tensile stress in PZT on fused silica increases the prevalence of *a*-domains, while the compressive stress in PZT on sapphire induced a predominantly *c*-domain structure and larger values of polarization. In contrast, PZT on silicon endures moderate tensile stress smaller than that of the film on fused silica and produces a mixed *a*/*c*-domain structure. Two different electrode configurations (MIM and IDE) were devised to have a comparative study on the out-of-plane and in-plane ferroelectric properties. In addition, a phenomenological model explaining the underlying relationship between the orientation of the electric field, substrate stress, and the domain orientation in PZT thin films was proposed for the first time.

The out-of-plane polarization showed a much higher susceptibility to the stress state of the film, while the in-plane polarization has a much lower stress dependence. Bipolar fatigue cycling

studies showed that the PZT films in MIM configuration on all the three substrates, irrespective of their stress states, lost more than 80% of their switchable polarization after 10^6 cycles. In a compressively stressed PZT/SP-MIM system, fatigue occurs suddenly after 10^3 cycles, while polarization decreases in PZT/FS-MIM and PZT/Si-MIM under tensile stress were more gradual. Fatigue recovery studies indicated that polarization degradation is dominated by the pinning of domain walls by charged defects. Polarization reversal shifts from being dominated by 180° domain switching processes to predominantly 90° domain switching processes with a shift from a *c*-domain to *a*-domain population. It is proposed that fatigue in the latter systems (PZT/FS-MIM) occurs through pinning of 90° domain walls on isolated charged defects and could be initiated already from the first cycle.

In contrast, fatigue in PZT/SP-MIM is based on the formation of oxygen vacancy agglomerates by defect migration, followed by pinning of 180° domain walls on the defect agglomerates. The comparison of large and small-signal permittivity indicated that polarization changes in PZT/SP-MIM and PZT/Si-MIM initially were based more on irreversible processes than in PZT/FS-MIM. Fatigue leads to a drastic reduction of irreversible processes, nearly eliminating all long-range domain wall movement.

On the other hand, the films with planar IDEs did not show any degradation in switchable polarization until 10 million cycles under the same cycling conditions as the MIM samples. PZT/SP-IDE films in particular, did not show any loss in P_{r} values even after 10^9 cycles. The electrode configuration combined with the columnar microstructure in the direction normal to the plane of the film was shown to have a decisive influence on the fatigue-resistant behavior of the thin film. The given set of thin films with columnar microstructure was shown to have more grain boundaries along the path of the electric field in the case of IDE configuration. These grain boundaries could act as trapping sites for oxygen vacancies that are mobile under the influence of an electric field. The compressive stress state induced by the substrates can also increase the migration and diffusion energies of the oxygen vacancies, which further aids the fatigue-resistant nature of the PZT/SP-IDE films. These collective influences of IDEs, along with the correctly engineered microstructure of the thin films, could enhance the lifetime and reliability of the PZT thin films under bipolar switching conditions.

5.5.1 Perspectives and open questions

This work demonstrates the possibilities of engineering the functional properties of ferroelectric thin films by adapting the substrate and mode of actuation by specific electrode configurations. The direction with which the material is probed provides control over the properties and the lifetime of the resulting thin film stack for a given application. The findings presented in this study can possibly be extended to the other ferroelectric material systems that can be used with IDEs.

However, some open questions remain to be answered in this study, which could be helpful in understanding the switching dynamics and the defect distribution in the film during the cycling.

- Studies to quantify and prove the localization of oxygen vacancies in the thin film systems.
- PZT films with non-columnar microstructure or with equiaxed grains should be prepared and subjected to fatigue cycling. These studies could allow us to understand the role of film microstructure on the degradation behavior and, in turn, their long-term stability.
- Experimental study of field-induced defects or oxygen vacancy diffusion in the films should be performed. This could throw some light on supporting our hypothesis on grain boundaries acting as oxygen vacancy traps.

Chapter 6

Solution deposited Hafnia thin films

This chapter deals with the chemical solution deposited ferroelectric La-doped HfO_2 thin film. The deposition routes developed by Schenk et al. [258] are followed throughout this work. Conventional and layer-by-layer (L/L) routes are followed for deposition. The influence of annealing temperature and atmosphere on structural and ferroelectric properties is studied. The correlation between the processing conditions and ferroelectric switching behavior was established. Dielectric breakdown studies were performed to understand the effect of different deposition routes and processing conditions.

6.1 Solution deposited Hafnia thin films

The importance of deposition methodology and the processing parameters for stabilizing the ferroelectric phase in hafnia thin films were discussed in detail in Chapter 1. HfO_2 films prepared by sol-gel routes were prone to problems of low density, contributing to the deterioration in electrical properties and poor breakdown characteristics. The film density is typically governed by the film crystallization route, and the crystallization is generally nucleation mediated. The nucleation process can be homogeneous or heterogeneous depending on the origin of nucleation, either from the bulk of the film in the former case or from the interface or surface in the latter case. Heterogeneous nucleation is thermodynamically preferred and can result in columnar microstructure or with equiaxed grains [210, 259]. The columnar microstructure was reported to be responsible for enhanced dielectric properties in ferroelectric thin films. Heterogeneous nucleation can be initiated by different approaches, which can eventually promote a denser microstructure. The approaches to promote heterogeneous nucleation are well developed and demonstrated by several research groups. Some of the established routes include: selection of substrate to match the lattice parameters of the thin film [56], using seed layer to promote nucleation, using a secondary phase to promote crystallization at lower temperature [210], and by using solutions with very low concentration and performing crystallization after every deposition steps [260, 261]. Using a seed layer to promote nucleation is not yet completely understood or attempted for HfO_2 thin films. At the same time, the films produced following the crystallization scheme after depositing several layers (i.e., conventional route) were not sufficiently dense [110]. Therefore, a layer-by-layer deposition route was developed, where crystallization was performed for every layer deposited using a solution of low concentration compared to the conventional route [258]. The details of deposition methodology are discussed in Chapter 2.

6.1.1 Conventional vs layer-by-layer deposition scheme

The key difference between the conventional and layer-by-layer (L/L) deposition schemes is the crystallization frequency. A 0.25 M solution was used for the conventional route, and crystallization (annealing) was performed after every three deposition and drying steps. For the layer-by-layer route, 0.083 M solution was used, and crystallization was performed after each deposition and drying step (detailed description of the deposition scheme can be found in Chapter 2, Section 2.2.3). With these modifications, the thickness of each crystallized layer, single layer thickness (SLT), was significantly different, as evident from the deposition scheme. The conventional

films resulted in an SLT of 45 nm, while the SLT of L/L films was 4-5 nm each for the given concentration. 45 nm thick films are mainly used for this study. It is reported in an earlier study [258] that the change in deposition scheme from conventional to layer-by-layer resulted in denser films. The overall density of the films improved from 8.0 g/cm^3 (83%) to 8.4 g/cm^3 (87%) for the films produced by conventional and L/L routes, respectively. It is proposed that the improvement in density is associated with the super-structure (alternating layers with higher and lower densities) in the film obtained via the L/L route [258]. A deeper investigation to understand the microstructure by means of secondary ion mass spectroscopy (SIMS) and X-ray reflectivity (XRR) was performed by Schenk et al., the details of the study are, however, not discussed here as it is not the scope of this work.

6.2 Effect of processing conditions on structure and properties

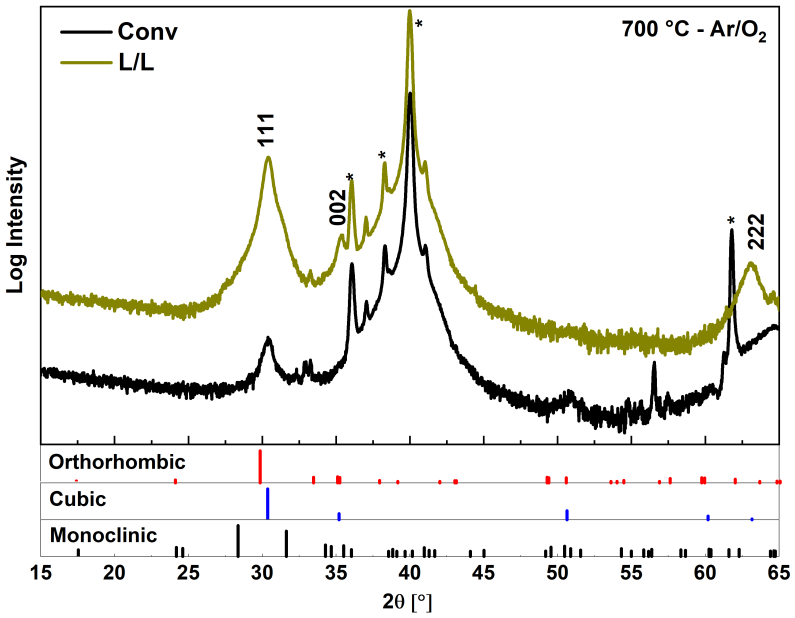

Figure 6.1: GI-XRD patterns for the conventional and the L/L samples, annealed at 700 °C in 1:1 mixture of Ar/O_2 atmosphere, *-indicates substrate peaks

6.2.1 Variation of annealing atmosphere and temperature

As discussed in Section 1.8 in Chapter 1, the reliability issues like wake-up behavior and poor breakdown characteristics are associated with the processing conditions of the solution deposited thin films. In an attempt to understand the effect of annealing atmosphere on the ferroelectric properties of our films, a 1:1 mixture of Ar/N_2 and a 1:1 mixture of Ar/O_2 is used. As some studies

also suggest that the annealing temperature in the range of 600 - 800 °C works well for both pure and doped HfO_2 thin films [107, 109]. To gain further insight, the annealing temperature was also varied between 700 °C and 800 °C in combination with the atmosphere to demonstrate their influence on structural, ferroelectric, and breakdown behavior of resulting HfO_2 thin films by both conventional and L/L methods.

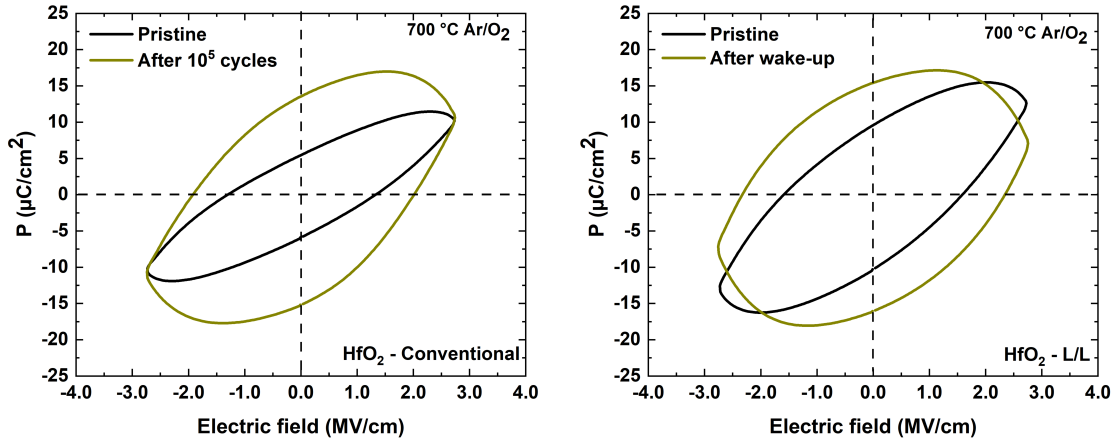

Figure 6.2: P-E loops (at 3 kHz) for the conventional and the L/L samples, annealed at 700 °C in 1:1 mixture of Ar/O_2 atmosphere.

The annealing atmosphere and temperature were varied for both conventional and L/L deposition routes. Figure 6.1 shows the GI-XRD patterns of the conventional and L/L films annealed in an atmosphere 1:1 mixture of Ar/O_2 at 700 °C. The GI-XRD pattern only shows only {111} peak for both conventional and L/L films, while the P-E loops in Figure 6.2 do not show any sign of ferroelectric switching in a pristine state and after cycling. Each of these plots shows the polarization vs. electric field (P-E) loops of the films in their pristine as well after wake-up cycling. Polarization hysteresis of the conventional and L/L films was measured at 3 kHz, and wake-up cycling was performed by applying a series of triangular pulses identical to the ones applied during the P-E measurement.

In the following experiment, the annealing temperature is maintained at 700 °C, and the atmosphere is changed to a 1:1 mixture of Ar/N_2. The GI-XRD patterns of the conventional and the L/L films in Figure 6.3 shows both {111} and {002} peaks. The {002} peak for the conventional film does not align closely with the orthorhombic phase and also with the peak of the L/L film. The peak intensities are also enhanced for the L/L films, while the conventional films showed a low-intensity {111} peak. The P-E loops in Figure 6.4 show signatures of ferroelectric switching. Both samples exhibit wake-up behavior, showing an increase in polarization from an

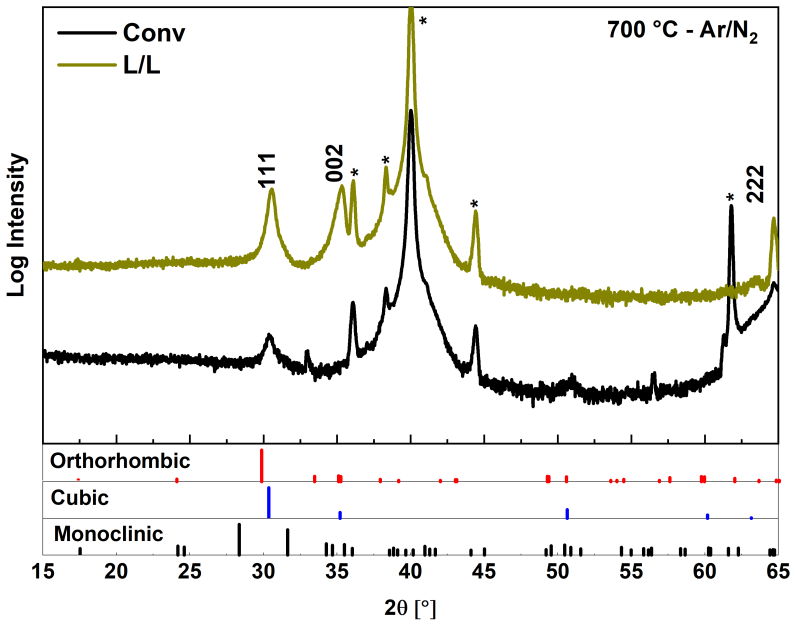

Figure 6.3: GI-XRD patterns for the conventional and the L/L samples, annealed at 700 °C in 1:1 mixture of Ar/N_2 atmosphere, *-indicates substrate peaks.

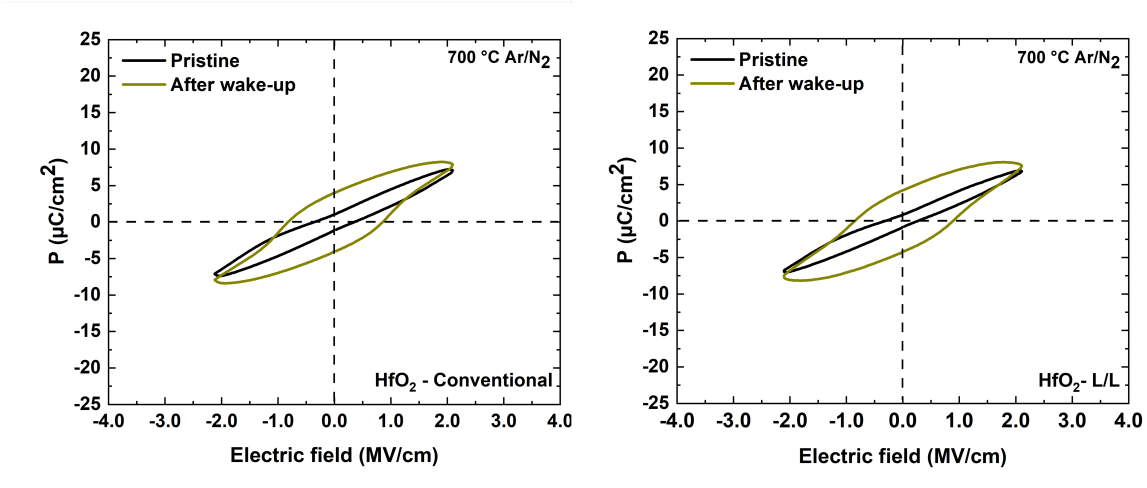

Figure 6.4: P-E loops (at 3 kHz) for the conventional and the L/L samples, annealed at 700 °C in 1:1 mixture of Ar/N_2 atmosphere.

initially pinched hysteresis state. The ferroelectric signature can be associated with the presence of $\{111\}$, and $\{002\}$ peaks as they correspond closely to the orthorhombic phase, which is responsible for ferroelectricity in hafnia [100, 170]. Here the GI-XRD analysis is mainly used to identify the evolution of peaks corresponding to the ferroelectric phase in hafnia. However, the GI-XRD patterns cannot be used for analyzing the texture of any given film, and the differences between the conventional and the L/L films are rather subtle and hard to interpret. So the orientation corresponding to the orthorhombic phase cannot be singled out with these results. Texture comparison was performed in one of the earlier works [110] on 100 nm thick La-HfO_2 films. The L/L samples were shown to have a mixed $\{111\}$ and $\{002\}$ preferential orientation with much stronger peak intensities than conventional films.

In the next step, the annealing temperature is changed to 800 °C while the annealing atmosphere is maintained at a 1:1 Ar/N_2 mixture. The orthorhombic $\{002\}$ peak is absent for both the conventional and the L/L samples, as shown in Figure 6.5. Instead, the conventional film shows a low-intensity $\{111\}$ peak compared to the L/L film, as is the case of samples annealed at 700 °C in $Ar//N_2$ atmosphere. However, the P-E loops in Figure 6.6 do not show any ferroelectric signature in both pristine states and after wake-up cycling.

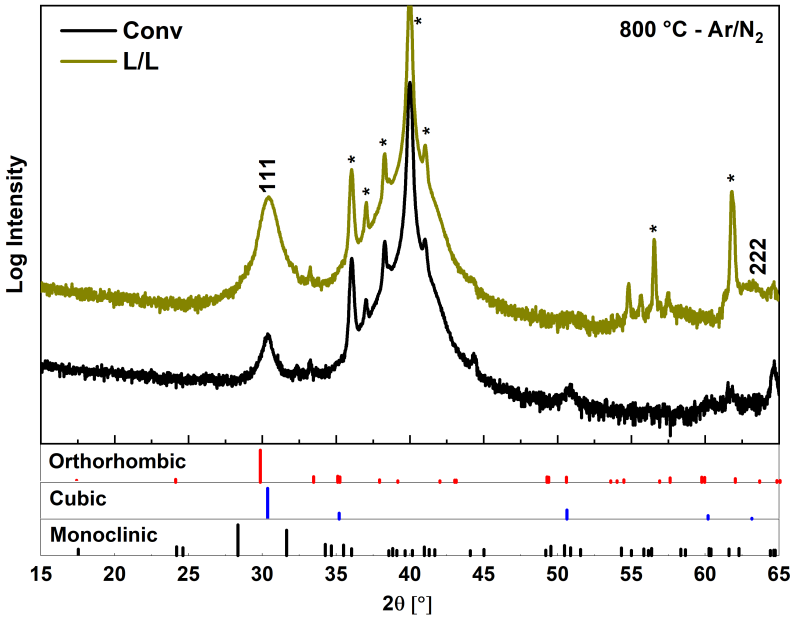

Figure 6.5: GI-XRD patterns for the conventional and the L/L samples, annealed at 800 °C in 1:1 mixture of Ar/N_2 atmosphere, *-indicates substrate peaks.

Finally, the annealing atmosphere is changed to a 1:1 mixture of Ar/O_2 while the temperature is maintained at 800 °C. GI-XRD analysis of the conventional and L/L films show differences in

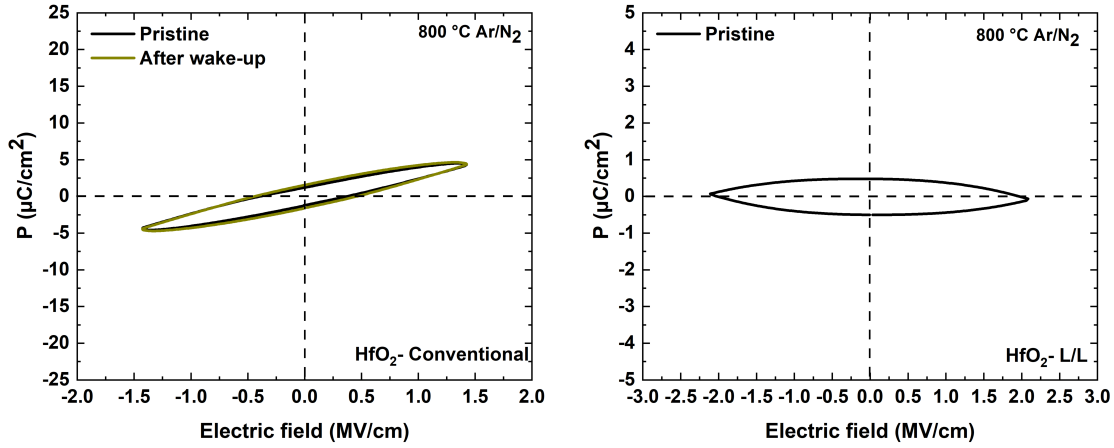

Figure 6.6: P-E loops (at 3 kHz) for the conventional and the L/L samples, annealed at 800 °C in 1:1 mixture of Ar/N_2 atmosphere. Note: scale is different in both the plots as the samples broke beyond 1.5 and 2 MV/cm.

relative intensities between the {111} and {002} or {022} and {113} peaks as shown in Figure 6.7, the {222} peak is absent in the L/L counterpart. The P-E loops in Figure 6.8 show a clear switching signature after wake-up cycling. The P_{r} values of both the conventional and L/L films are comparatively much higher in this case than the films annealed at 700 °C in Ar/N_2 atmosphere. The L/L sample, however, shows an increase in remanent (P_{r}) and maximum (P_{max}) polarization in comparison to the conventional sample. It is also important to note that the maximum applied field E_{max} is increased from 2.9 MV/cm for the conventional sample to 4 MV/cm for the L/L sample. Both these films could withstand cycling in higher fields.

From all these above experiments, it is evident that the appearance of ferroelectric switching is associated with the presence of {002} orthorhombic polar peaks. It can be understood that the lower annealing temperature works in the case of an Ar/N_2 atmosphere. In comparison, the presence of oxygen during annealing required a higher temperature to stabilize the orthorhombic phase. Annealing temperature appears to be critical when changing the atmosphere. In the case of N_2 atmosphere, the {002} peaks appear when annealed at 700 °C but not at 800 °C, and similar behavior was seen for the ferroelectric signature. Although, the polarization values of the samples annealed in Ar/N_2 were much lower than those annealed in Ar/O_2. It is also noteworthy that the post-annealing of top electrodes was carried out at 400 °C for 5 min in ambient environment. It could be possible that the post-annealing process would have altered the defect concentration and structure in these thin films, further altering any changes resulting from the variations in temperature and atmosphere during annealing. Therefore, no clear correlation

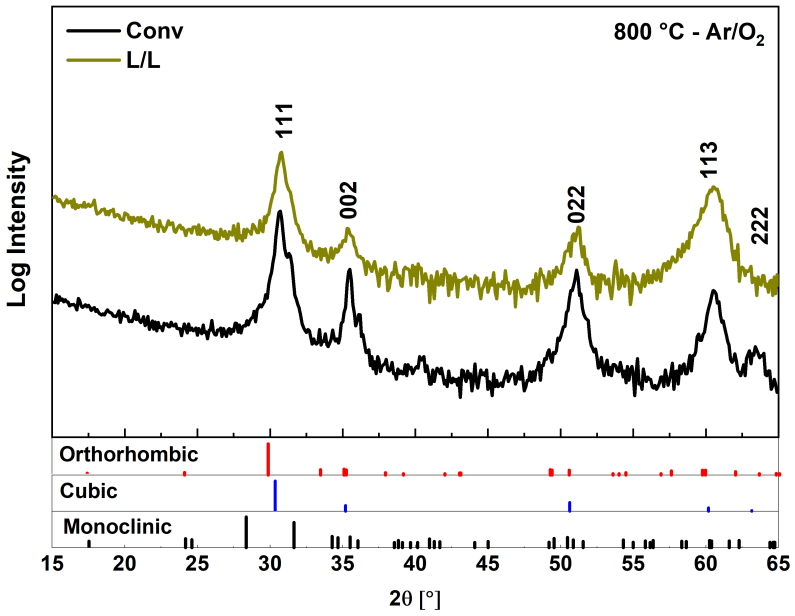

Figure 6.7: GI-XRD pattern of the conventional and the L/L samples annealed at 800 °C in Ar/O_2.

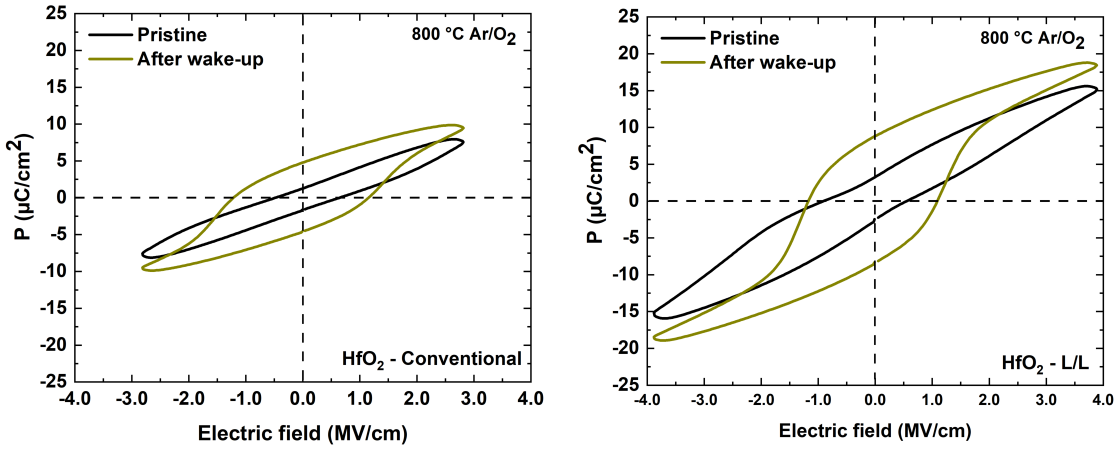

Figure 6.8: P-E loops (at 3 kHz) for the conventional and the L/L samples, annealed at 800 °C in 1:1 mixture of Ar/O_2 atmosphere.

between the processing condition and the possible defect concentrations in these films could be drawn.

6.2.2 Breakdown studies comparing conventional and L/L films

As noted in the previous section from the P-E loops of the films annealed at 800 °C in Ar/O_2 atmosphere, $E_{\max}$ for the conventional film was 2.9 MV/cm and beyond which the samples were breaking down. At the same time, $E_{\max}$ of the L/L film was 4 MV/cm; this already indicates an improvement in the breakdown strength of the L/L samples. In order to quantify the breakdown characteristics, several capacitors from both samples were subjected to a linear ramp voltage test in their pristine state. A ramp rate of 0.05 V/s was chosen, and several capacitors with 200 μm circular electrodes were tested. The plot in Figure 6.9 shows the evolution of current as a function of applied field in representative sets of capacitors from both the samples, going through a breakdown.

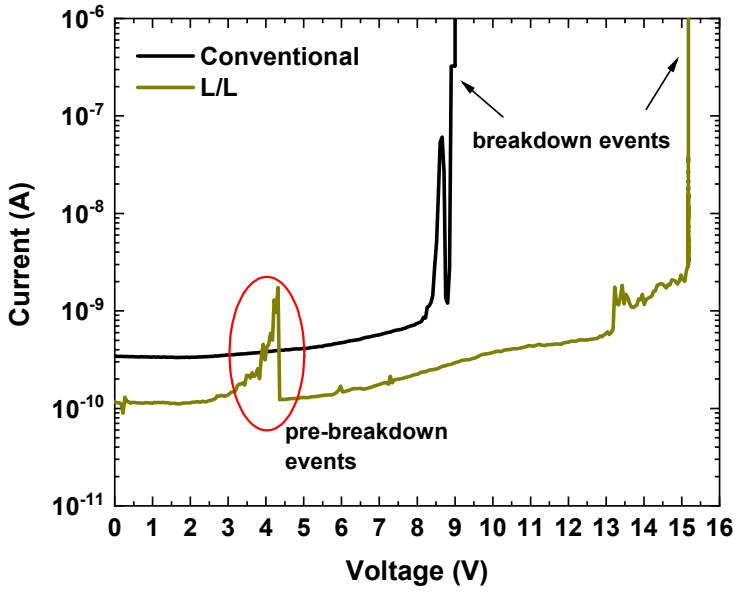

Figure 6.9: Plot showing the breakdown characteristics of the representative capacitors of conventional and L/L samples subjected to a linear ramp voltage test. Pre-breakdown and breakdown events are marked in the plots.

The breakdown voltage is defined as the voltage at which the current value increases more than two orders of magnitude within a short span of change in the voltage (0.1 V or less). The current curve also shows some anomalies where there was an increase in current value but returned to the previous values before going through the breakdown. These anomalies are termed as

pre-breakdown events. The pre-breakdown events could arise from the conductive paths due to the porous microstructure. Most conventional samples broke at a lower voltage than the L/L samples. Statistical analysis is presented in Figure 6.10, which shows the distribution of breakdown voltages for both sets of samples. Among 13 capacitors subjected to a breakdown test from the conventional sample, 9 capacitors showed a prominent pre-breakdown event. On the other hand, only 4 out of 13 L/L samples showed a noticeable pre-breakdown event. The breakdown voltage for the conventional sample was only around 10.1 V (2.2 MV/cm), while it was around 14.5 V (3.2 MV/cm) for the L/L samples. As the ramp rate is much slower than the polarization hysteresis and wake-up cycling, the breakdown voltages were lower compared to the cycling voltage.

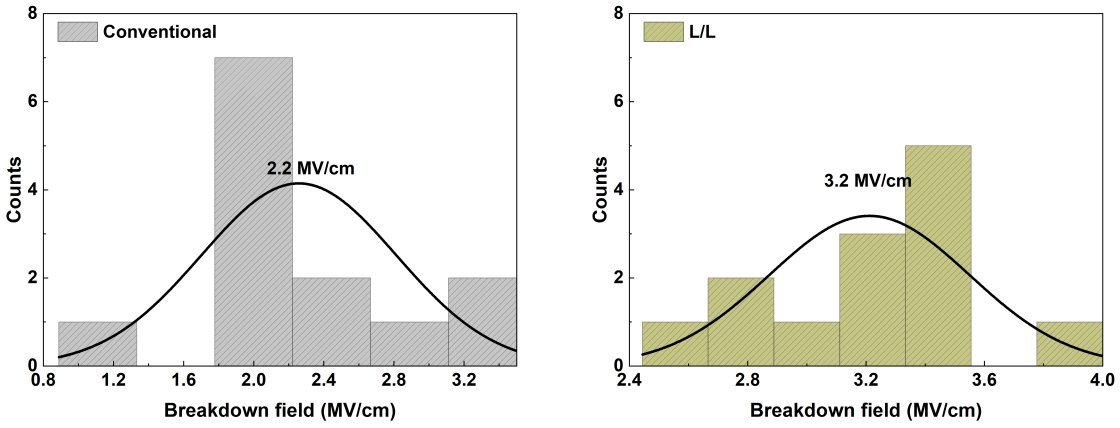

Figure 6.10: Statistical distribution of breakdown voltage for conventional and L/L samples, tested on 13 different capacitors, the mean breakdown voltage is also indicated in the plots

However, the breakdown mechanism cannot be determined clearly from these measurements. One could argue that the transport mechanism should remain the same for both conventional and L/L samples as the current-voltage curves in Figure 6.9 look similar. However, the lower breakdown voltage of the conventional samples indicates that the available current transport path could be larger than the L/L samples. The L/L samples showed an improvement in relative density by only 3%, and this may not be the only reason for the improved breakdown characteristics. The improved breakdown characteristics of the L/L samples can also be logically correlated to the proposed superstructure [258] of the film as a result of an alternating high and low-density layer. The high-density capping layer could pose a resistance in the current path formed by the vertically aligned pores in the alternating low-density layers. As the grain or crystallites size is also in the order of layer thickness in the high-density layer, it could also mean that there are densely packed grains which could increase the dielectric strength of these layers.

6.3 Summary

Stabilizing the ferroelectric phase in HfO_2 thin film is sensitive to annealing temperature and atmosphere changes. It can be seen that the presence of oxygen in the annealing atmosphere requires a higher temperature to stabilize the ferroelectric phase. Although the films annealed in a nitrogen atmosphere showed the signature of the ferroelectric phase and switching, the polarization values were very low compared to those annealed in an oxygen atmosphere. It can be associated with the improved breakdown characteristics of the film annealed in oxygen, allowing for cycling at a higher field. Among the samples annealed at 800 °C in Ar/O_2 atmosphere, the L/L samples exhibited better ferroelectric properties and showed an improved breakdown strength compared to the conventional sample. Post-annealing after electrode deposition could have played a detrimental role in altering the thin film's defect structure, resulting in poor or no sign of ferroelectric properties in the other set of films. It can also be understood from the experiments that apart from the dopant ions themselves, the intrinsic oxygen vacancies during processing impact the phase stability and, in turn, the ferroelectric behavior.

6.4 Perspectives and open questions

Processing trails can be repeated further to stabilize the ferroelectric phase. As the process is susceptible to temperature and atmosphere, further experiments had to be performed by carefully varying the annealing atmosphere and temperature to understand their co-relation with the defect structure.

Post-annealing studies can be carried out at successive steps from lower to a higher temperatures to understand the trade-off between the interface quality and the changes in defect structure that might influence the ferroelectric switching. This can further throw some light on the effect of the post-annealing step on the deterioration of ferroelectric properties.

More breakdown testing to be carried out to establish the correlation between the processing parameters and the defect structure mediated properties.

Summary and outlook

High-quality PZT (53/47) thin films were fabricated by the chemical solution deposition (CSD) technique on transparent and non-transparent substrates during this work. The ferroelectric properties of the films are comparable to the state-of-the-art values of chemical solution deposited un-doped PZT thin films. The possibility of using the HfO_2 buffer layer deposited by CSD and atomic layer deposition (ALD) for integrating PZT on different substrates (Si, fused silica & sapphire) was demonstrated. The influence of different seed layer solvents in affecting the texture and functional properties of the PZT films were experimentally illustrated. PZT thin films with metal-insulator-metal (MIM) geometry and co-planar interdigitated geometry were fabricated on transparent and non-transparent substrates. It allowed us to probe the out-of-plane and the in-plane ferroelectric properties of the PZT thin films on different substrates were probed. The influence of finger width (f_w) and the gap between the fingers (f_g) in the interdigitated electrodes (IDEs) geometry was studied using finite element modeling. The electric field distribution was analyzed for different combinations of f_w and f_g for the PZT thin film deposited on various substrates. The limitation of the design approximations is verified by comparing the non-constrained bulk system with the constrained multi-layer thin film system. It was found that for a given film thickness t_f, a homogeneous field distribution could be achieved by having a finger gap and width at least ten times more than that of t_f. However, this was not the case for the bulk system, where the ratio f_g/t_f is smaller for several values of f_g that were compared. The effective field value for a given f_g and f_w was nearly two times lower than that of the values obtained from the approximation for thin films.

It was demonstrated that different stress states were induced in PZT films by choice of substrates, and the stress values were quantified by the $\sin^2\psi$ method using XRD. The ferroelectric characterization results also confirmed the hypothesis that high tensile stress in PZT/FS induced the prevalence of a-domains. In contrast, the compressive stress in PZT/SP induced a predominantly c-domain structure, and the intermediate tensile stress state in PZT/Si produced a mixed

domain structure. Furthermore, it was shown that the out-of-plane polarization was susceptible to the stress state of the film. A higher possible polarization was achieved for PZT/SP-MIM film under in-plane compressive stress but reduced by a factor of nearly 4 for PZT/FS-MIM film under in-plane tensile stress. On the contrary, the in-plane polarization showed an unexpectedly weak stress dependence. It was only 10% larger for PZT/FS-IDE under tensile stress than PZT/SP-IDE film under compressive stress. Based on the experimental observation, a phenomenological model was proposed to explain the underlying relationship between the substrate stress and the domain orientation to understand the in-plane and out-of-plane ferroelectric properties of the PZT thin films. Bipolar cycling experiments yielded a significant difference in the fatigue behavior of the thin films. PZT films in MIM geometry lost more than 80% of their switchable polarisation at the end of 10^6 cycles, irrespective of the substrate they were deposited on. PZT films with interdigitated electrodes showed increased resistance to degradation during cycling. PZT/FS-IDE did not show degradation until 10^8 cycles, and PZT/SP-IDE showed no degradation even after 10^8 cycles. The primary fatigue mechanism was identified as the pinning of domain walls by oxygen vacancies and other defect agglomerates. The switching dynamics of different domains were affected differently by bipolar cycling. The pinning of 90° domain walls initiated early, and the degradation was gradual, but the system with more 180° domain walls underwent a sudden degradation after 1000 cycles. Irrespective of the domain configuration, fatigue affected the irreversible contribution to polarization by eliminating the long-range domain wall motion in all the systems. It was proposed that the columnar microstructure, in combination with the IDEs, contributed to the fatigue-resistant behavior of the PZT thin films. In the case of IDEs, the electric field is applied in a direction normal to the columnar grains. In such a case, the electric field encounters more grain boundaries in its path than the case in the MIM configuration. It was known that oxygen vacancies and other defects diffuse in the electric field direction. Therefore, the grain boundaries in the path can prevent the defects from diffusing towards the domain walls and even eventually pinning the domain walls.

For a given thin film microstructure and the crystallographic orientation, the direction with which the material is probed provides control over the functional properties and long-term switching abilities. The collective influence of planar IDEs along with the columnar microstructure of the thin films was shown to enhance the lifetime and reliability of the PZT thin films under bipolar switching conditions. Furthermore, the possibility of engineering the functional properties of ferroelectric thin films by adapting the substrate and mode of actuation by specific electrode configurations was demonstrated in this study.

Hafnium oxide thin film, the incipient ferroelectric system, is also studied during this work. The structure-property relationship was established by stabilizing the ferroelectric phase in La-doped HfO_2 thin films deposited by the chemical solution deposition technique. Two different deposition routes were followed, and the influence of annealing temperature and atmosphere on achieving ferroelectric switching properties was demonstrated. It was clear that the ferroelectric properties of HfO_2 thin films are sensitive to annealing temperature and atmosphere. The layer-by-layer deposited films showed an improvement in the breakdown behavior compared to the films deposited by the conventional route. The results are linked to the density improvement in the layer-by-layer deposited films and the intrinsic oxygen vacancies formed during processing under specific conditions. It could be inferred that the differences in temperature seen by the bottom and top electrodes during processing create a weak interface between the top electrode and the film. As pointed out in the literature, it could result in an inhomogeneity in the oxygen vacancy distribution, which is a primary cause of wake-up, fatigue, and early breakdown in hafnia thin films. Therefore, post-annealing of top electrodes could be carried out in a controlled atmosphere and successive temperature steps to improve the film electrode interface. Breakdown studies could be performed to establish a correlation between annealing steps and defect distribution.

Appendix A

List of publications and patents

Articles in peer-reviewed journals

1 **N. Aruchamy**, T. Schenk, S. Girod, S. Glinsek, E. Defay, T. Granzow, Influence of substrate stress on in-plane and out-of-plane ferroelectric properties of PZT films, Journal of Applied Physics. 131 (2022) 014101.

2 **N. Aruchamy**, T. Schenk, V. Kovacova, S. Glinsek, E. Defay, T. Granzow, Influence of tensile vs. compressive stress on fatigue of lead zirconate titanate thin films, Journal of the European Ceramic Society. 41 (2021) 6991–6999.

3 S. Manikandan, **N. Aruchamy**, L. Allirol, S. Girod, S. Glinsek, E. Defay, T. Granzow, Dielectric relaxations of lead zirconate titanate films up to millimeter-wave frequencies, Journal of the American Ceramic Society. (2022) jace.18535.

4 T. Schenk, A. Bencan, G. Drazic, O. Condurache, N. Valle, B.E. Adib, **N. Aruchamy**, T. Granzow, E. Defay, S. Glinsek, Enhancement of ferroelectricity and orientation in solution-derived hafnia thin films through heterogeneous grain nucleation, Applied Physics Letter. 118 (2021) 162902.

5 A. Blázquez Martínez, N. Godard, **N. Aruchamy**, C. Milesi-Brault, O. Condurache, A. Bencan, S. Glinsek, T. Granzow, Solution-processed $BiFeO_3$ thin films with low leakage current, Journal of the European Ceramic Society. 41 (2021) 6449–6455.

Patents:

1 **Naveen ARUCHAMY**, Torsten GRANZOW, Emmanuel DEFAY, Sebastjan GLINSEK, 'Ferroelectric capacitor on Si-substrate with extended lifetime based on planar electrodes (PE) - Material deposition method and microsystem therewith obtained', WO2022/152804 (2022).

List of Figures

List of Tables

References

[1]P. Muralt, "Piezoelectric thin films for mems", Integrated Ferroelectrics **17**, 297–307 (1997).

[2]H. Ræder, F. Tyholdt, W. Booij, F. Calame, N. P. Østbø, R. Bredesen, K. Prume, G. Rijnders, and P. Muralt, "Taking piezoelectric microsystems from the laboratory to production", Journal of Electroceramics **19**, 357–362 (2007).

[3]P. Muralt, "Recent Progress in Materials Issues for Piezoelectric MEMS", Journal of the American Ceramic Society **91**, 1385–1396 (2008).

[4]S. Trolier-McKinstry and P. Muralt, "Thin Film Piezoelectrics for MEMS", Journal of Electroceramics **12**, 7–17 (2004).

[5]R. H. Wilke, R. L. Johnson-Wilke, V. Cotroneo, W. N. Davis, P. B. Reid, D. A. Schwartz, and S. Trolier-McKinstry, "Sputter deposition of pzt piezoelectric films on thin glass substrates for adjustable X-ray optics", Applied Optics **52**, 3412–3419 (2013).

[6]C. T. DeRoo, D. N. Burrows, E. N. Hertz, E. D. Schwartz, J. Walker, M. Tendulkar, P. B. Reid, R. Allured, S. Trolier-McKinstry, T. N. Jackson, T. Liu, and V. Cotroneo, "Design and fabrication of prototype piezoelectric adjustable x-ray mirrors", Optics Express **26**, 27757–27772 (2018).

[7]S. Glinsek, M. A. Mahjoub, M. Rupin, T. Schenk, N. Godard, S. Girod, J.-B. Chemin, R. Leturcq, N. Valle, S. Klein, C. Chappaz, and E. Defay, "Fully transparent friction-modulation haptic device based on piezoelectric thin film", Advanced Functional Materials **30**, 2003539 (2020).

[8]R. R. Benoit, R. Q. Rudy, J. S. Pulskamp, and R. G. Polcawich, "Piezoelectric rf mems switches on si-on-sapphire substrates", Journal of Microelectromechanical Systems **29**, 1087–1090 (2020).

[9]T. S. Böscke, J. Müller, D. Bräuhaus, U. Schröder, and U. Böttger, "Ferroelectricity in hafnium oxide thin films", Applied Physics Letters **99**, 102903 (2011).

[10]S. Katzir, "The beginnings of piezoelectricity: a study in mundane physics", (2006).

[11]D. Damjanovic, "Stress and frequency dependence of the direct piezoelectric effect in ferroelectric ceramics", Journal of Applied Physics **82**, 1788–1797 (1997).

[12]D. Damjanovic, "Ferroelectric, dielectric and piezoelectric properties of ferroelectric thin films and ceramics", Reports on Progress in Physics **61**, 1267–1324 (1998).

[13]E. Defaÿ, Integration of ferroelectric and piezoelectric thin films (ISTE, 2011).

[14]R. E. Newnham, "Properties of materials: anisotropy, symmetry, structure", (2005).

[15]C. Kittel, Introduction to solid state physics, 8th ed (Wiley, Hoboken, NJ, 2005).

[16]M. Stachiotti, A. Dobry, R. Migoni, and A. Bussmann-Holder, "Crossover from a displacive to an order-disorder transition in the nonlinear-polarizability model", Physical Review B **47**, 2473 (1993).

[17]K. Roleder, I. Jankowska-Sumara, G. E. Kugel, M. Maglione, M. D. Fontana, and J. Dec, "Antiferroelectric and ferroelectric phase transitions of the displacive and order-disorder type in $PbZrO_3$ and $Pb(Zr_{1-x}Ti_x)O_3$ single crystals", **71**, 287–306 (2006).

[18]G. V. M, Geochemische verteilungsgesetze der elemente vii (Skrifter utgitt av det Norske Videnskaps-Akademi, 1926), pp. 5–116.

[19]D. Damjanovic, "Contributions to the piezoelectric effect in ferroelectric single crystals and ceramics", Journal of the American Ceramic Society **88**, 2663–2676 (2005).

[20]M. E. Lines and A. M. Glass (Oxford University Press, Feb. 2001).

[21]G. F. Nataf, M. Guennou, J. M. Gregg, D. Meier, J. Hlinka, E. K. H. Salje, and J. Kreisel, "Domain-wall engineering and topological defects in ferroelectric and ferroelastic materials", Nature Reviews Physics **2**, 634–648 (2020).

[22]V. Y. Shur, "Kinetics of ferroelectric domains: Application of general approach to $LiNbO_3$ and $LiTaO_3$", Journal of Materials Science **41**, 199–210 (2006).

[23]D. M. Evans, V. Garcia, D. Meier, and M. Bibes, "Domains and domain walls in multiferroics", Physical Sciences Reviews **5** (2020).

[24]D. Lee, R. K. Behera, P. Wu, H. Xu, Y. L. Li, S. B. Sinnott, S. R. Phillpot, L. Q. Chen, and V. Gopalan, "Mixed Bloch-Néel-Ising character of 180° ferroelectric domain walls", Physical Review B **80**, 060102 (2009).

[25]X.-K. Wei, C.-L. Jia, T. Sluka, B.-X. Wang, Z.-G. Ye, and N. Setter, "Néel-like domain walls in ferroelectric Pb(Zr,Ti)O_3 single crystals", Nature Communications **7**, 12385 (2016).

[26]G. De Luca, M. D. Rossell, J. Schaab, N. Viart, M. Fiebig, and M. Trassin, "Domain wall architecture in tetragonal ferroelectric thin films", Advanced Materials **29**, 1605145 (2017).

[27]S. Cherifi-Hertel, H. Bulou, R. Hertel, G. Taupier, K. D. Dorkenoo, C. Andreas, J. Guyonnet, I. Gaponenko, K. Gallo, and P. Paruch, "Non-Ising and chiral ferroelectric domain walls revealed by nonlinear optical microscopy", Nature Communications **8**, 15768 (2017).

[28]S. C. Abrahams, "Ferroelasticity", Materials Research Bulletin **6**, 881–890 (1971).

[29]V. Y. Shur, E. V. Pelegova, A. P. Turygin, M. S. Kosobokov, and Y. M. Alikin, "Forward growth of ferroelectric domains with charged domain walls. Local switching on non-polar cuts", Journal of Applied Physics **129**, 044103 (2021).

[30]J. E. Daniels, C. Cozzan, S. Ukritnukun, G. Tutuncu, J. Andrieux, J. Glaum, C. Dosch, W. Jo, and J. L. Jones, "Two-step polarization reversal in biased ferroelectrics", Journal of Applied Physics **115**, 224–104 (2014).

[31]A. von Hippel, "Ferroelectricity, domain dtructure, and phase transitions of Barium Titanate", Reviews of Modern Physics **22**, 221–237 (1950).

[32]D. Damjanovic and M. Demartin, "Contribution of the irreversible displacement of domain walls to the piezoelectric effect in barium titanate and lead zirconate titanate ceramics", Journal of Physics: Condensed Matter **9**, 4943–4953 (1997).

[33]D. A. Hall, "Review Nonlinearity in piezoelectric ceramics", Journal of Materials Science **36**, 4575–4601 (2001).

[34]D. V. Taylor and D. Damjanovic, "Evidence of domain wall contribution to the dielectric permittivity in PZT thin films at sub-switching fields", Journal of Applied Physics **82**, 1973–1975 (1997).

[35]D. V. Taylor, D. Damjanovic, E. Colla, and N. Setter, "Fatigue and nonlinear dielectric response in sol-gel derived lead zirconate titanate thin films", Ferroelectrics **225**, 91–97 (1999).

[36]D. Damjanovic and M. Demartin, "The Rayleigh law in piezoelectric ceramics", Journal of Physics D: Applied Physics **29**, 2057–2060 (1996).

[37]N. Bassiri Gharb, S. Trolier-McKinstry, and D. Damjanovic, "Piezoelectric non-linearity in ferroelectric thin films", Journal of Applied Physics **100**, 044107 (2006).

[38]J. S. Horwitz, K. S. Grabowski, D. B. Chrisey, and R. E. Leuchtner, "In situ deposition of epitaxial $PbZr_xTi_{(1-x)}O_3$ thin films by pulsed laser deposition", Applied Physics Letters **59**, 1565 (1998).

[39]M. D. Nguyen, M. Dekkers, E. Houwman, R. Steenwelle, X. Wan, A. Roelofs, T. Schmitz-Kempen, and G. Rijnders, "Misfit strain dependence of ferroelectric and piezoelectric properties of clamped (001) epitaxial $Pb(Zr_{0.52},Ti_{0.48})O_3$ thin films", Applied Physics Letters **99**, 252904 (2011).

[40]J. Schwarzkopf and R. Fornari, "Epitaxial growth of ferroelectric oxide films", Progress in Crystal Growth and Characterization of Materials **52**, 159–212 (2006).

[41]E. Defaÿ, B. Semmache, C. Dubois, M. Leberre, and D. Barbier, "Compositional gradient in and mechanical stability of rf-sputtered and rta annealed $Pb(Zr,Ti)O_3$ thin films", Sensors and Actuators A: Physical **74**, 77–80 (1999).

[42]H. G. Yeo, T. Xue, S. Roundy, X. Ma, C. Rahn, S. Trolier-Mckinstry, H. G. Yeo, T. Xue, S. Roundy, X. Ma, C. Rahn, and S. Trolier-Mckinstry, "Strongly (001) oriented bimorph pzt film on metal foils grown by RF-sputtering for wrist-worn piezoelectric energy harvesters", Advanced Functional Materials **28**, 1801327 (2018).

[43]H. Jacobsen, K. Prume, B. Wagner, K. Ortner, and T. Jung, "High-rate sputtering of thick PZT thin films for MEMS", Journal of Electroceramics **25**, 198–202 (2010).

[44]M. Okada, K. Tominaga, T. Araki, S. Katayama, and Y. Sakashita, "Metalorganic chemical vapor deposition of c-axis oriented PZT thin films", Japanese Journal of Applied Physics **29**, 718–722 (1990).

[45]E. H. Kim, C. W. Moon, J. G. Lee, M. S. Lah, and S. M. Koo, "Synthesis and characterization of lead (iv) precursors and their conversion to PZT materials through a CVD process", Polyhedron **177**, 114270 (2020).

[46]S. M. George, "Atomic layer deposition: an overview", Chemical Reviews **110**, 111–131 (2010).

[47]J. Aarik, A. Aidla, A. Kikas, T. Käämbre, R. Rammula, P. Ritslaid, T. Uustare, and V. Sammelselg, "Effects of precursors on nucleation in atomic layer deposition of HfO_2", Applied Surface Science **230**, 292–300 (2004).

[48]H. A. Hsain, Y. Lee, M. Materano, T. Mittmann, A. Payne, T. Mikolajick, U. Schroeder, G. N. Parsons, and J. L. Jones, "Many routes to ferroelectric HfO_2: a review of current deposition

methods", Journal of Vacuum Science & Technology A: Vacuum, Surfaces, and Films **40**, 010803 (2021).

[49]G. N. Parsons, S. M. George, and M. Knez, "Progress and future directions for atomic layer deposition and ald-based chemistry", MRS Bulletin **36**, 865–871 (2011).

[50]R. W. Schwartz, "Chemical solution deposition of perovskite thin films", Chemistry of Materials **9**, 2325–2340 (1997).

[51]J. Xu, A. Shaikh, and R. Vest, "High K $BaTiO_3$ films from metalloorganic precursors", IEEE Transactions on Ultrasonics, Ferroelectrics and Frequency Control **36**, 307–312 (1989).

[52]J. Zha and H. Roggendorf, "Sol-gel science, the physics and chemistry of sol-gel processing, Ed. by C. J. Brinker and G. W. Scherer, Academic Press, Boston", Advanced Materials **3**, 522–522 (1991).

[53]R. Vest and Xu Jiejie, "$PbTiO_3$ films from metalloorganic precursors", IEEE Transactions on Ultrasonics, Ferroelectrics and Frequency Control **35**, 711–717 (1988).

[54]K. Budd, S. Dey, and D. Payne, "Sol-gel processing of $PbTiO_3$, $PbZrO_3$, PZT, and PLZT thin films.", in British ceramic proceedings, edited by B. Steele (1985), pp. 107–121.

[55]S. Dey, K. Budd, and D. Payne, "Thin-film ferroelectrics of PZT of sol-gel processing", IEEE Transactions on Ultrasonics, Ferroelectrics and Frequency Control **35**, 80–81 (1988).

[56]R. W. Schwartz, T. Schneller, and R. Waser, "Chemical solution deposition of electronic oxide films", Comptes Rendus Chimie **7**, 433–461 (2004).

[57]P. Muralt, M. Marzencki, B. Belgacem, F. Calame, and S. Basrour, "Vibration Energy Harvesting with PZT Micro Device", Procedia Chemistry **1**, 1191–1194 (2009).

[58]N. R. Parikh, J. Todd Stephen, M. L. Swanson, and E. R. Myers, "Study of diffusion barriers for PZT deposited on Si for non-volatile random-access memory technology", MRS Online Proceedings Library **200**, 193–198 (1990).

[59]X. L. Zhou and F. X. Li, "Simulations of domain evolution in morphotropic ferroelectric ceramics under electromechanical loading using an optimization-based model", Journal of Applied Physics **109**, 84–107 (2011).

[60]B. Jaffe, W. R. Cook, and H. Jaffe, Piezoelectric Ceramics, edited by Roberts J. P and Popper P, 1st ed. (Academic Press INC. (London) LTD, London, Nov. 1971).

[61]B. Noheda, D. E. Cox, G. Shirane, J. A. Gonzalo, L. E. Cross, and S.-E. Park, "A monoclinic ferroelectric phase in the $Pb(Zr_{1-x}Ti_x)O_3$ solid solution", Applied Physics Letters **74**, 2059–2061 (1999).

[62]B. Noheda, D. E. Cox, G. Shirane, R. Guo, B. Jones, and L. E. Cross, "Stability of the monoclinic phase in the ferroelectric perovskite $Pb(Zr_{1-x}Ti_x)O_3$", Physical Review B **63**, 014103 (2000).

[63]G. A. Rossetti, W. Zhang, and A. G. Khachaturyan, "Phase coexistence near the morphotropic phase boundary in lead zirconate titanate ($PbZrO_3$-$PbTiO_3$) solid solutions", Applied Physics Letters **88**, 072912 (2006).

[64]K. A. Schönau, L. A. Schmitt, M. Knapp, H. Fuess, R. A. Eichel, H. Kungl, and M. J. Hoffmann, "Nanodomain structure of $Pb[Zr_{1-x}Ti_x]O_3$ at its morphotropic phase boundary: investigations from local to average structure", Physical Review B - Condensed Matter and Materials Physics **75**, 184117 (2007).

[65]A. M. Glazer, P. A. Thomas, K. Z. Baba-Kishi, G. K. Pang, and C. W. Tai, "Influence of short-range and long-range order on the evolution of the morphotropic phase boundary in $Pb(Zr_{1-x}Ti_x)O_3$", Physical Review B - Condensed Matter and Materials Physics **70**, 1–9 (2004).

[66]S. Kalpat and K. Uchino, "Highly oriented lead zirconium titanate thin films: Growth, control of texture, and its effect on dielectric properties", Journal of Applied Physics **90**, 2703–2710 (2001).

[67]N. Ledermann, P. Muralt, J. Baborowski, S. Gentil, K. Mukati, M. Cantoni, A. Seifert, and N. Setter, "{100}-Textured, piezoelectric $Pb(Zr_x,Ti_{1-x})O_3$ thin films for MEMS: integration, deposition and properties", Sensors and Actuators A: Physical **105**, 162–170 (2003).

[68]L. M. Denis, G. Esteves, J. Walker, J. L. Jones, and S. Trolier-McKinstry, "Thickness dependent response of domain wall motion in declamped $\{001\}$ $Pb(Zr_{03},Ti_{0.7})O_3$ thin films", Acta Materialia **151**, 243–252 (2018).

[69]P. Muralt, "Texture control and seeded nucleation of nanosize structures of ferroelectric thin films", Journal of Applied Physics **100**, 051605 (2006).

[70]C. K. Kwok and S. B. Desu, "Low temperature perovskite formation of lead zirconate titanate thin films by a seeding process", Journal of Materials Research **8**, 339–344 (1993).

[71]N. Godard, S. Glinsek, and E. Defay, "Inkjet-printed silver as alternative top electrode for lead zirconate titanate thin films", Journal of Alloys and Compounds. **783**, 801–805 (2019).

[72]P. Muralt, T. Maeder, L. Sagalowicz, S. Hiboux, S. Scalese, D. Naumovic, R. G. Agostino, N. Xanthopoulos, H. J. Mathieu, L. Patthey, and E. L. Bullock, "Texture control of $PbTiO_3$ and $Pb(Zr,Ti)O_3$ thin films with TiO_2 seeding", Journal of Applied Physics **83**, 3835–3841 (1998).

[73]K. G. Brooks, I. M. Reaney, R. Klissurska, Y. Huang, L. Bursill, and N. Setter, "Orientation of rapid thermally annealed lead zirconate titanate thin films on (111) pt substrates", Journal of Materials Research **9**, 2540–2553 (1994).

[74]D. Ambika, "Deposition of PZT thin films with (001), (110), and (111) crystallographic orientations and their transverse piezoelectric characteristics", Advanced Materials Letters **3**, 102–106 (2012).

[75]G. A. C. M. Spierings, G. J. M. Dormans, W. G. J. Moors, M. J. E. Ulenaers, and P. K. Larsen, "Stresses in $Pt/Pb(Zr,Ti)O_3/Pt$ thin-film stacks for integrated ferroelectric capacitors", Journal of Applied Physics **78**, 1926–1933 (1995).

[76]R. J. Ong, D. A. Payne, and N. R. Sottos, "Processing Effects for Integrated PZT: Residual Stress, Thickness, and Dielectric Properties", Journal of the American Ceramic Society **88**, 2839–2847 (2005).

[77]T. A. Berfield, R. J. Ong, D. A. Payne, and N. R. Sottos, "Residual stress effects on piezoelectric response of sol-gel derived lead zirconate titanate thin films", Journal of Applied Physics **101**, 024102 (2007).

[78]F. Griggio and S. Trolier-McKinstry, "Grain size dependence of properties in lead nickel niobate-lead zirconate titanate films", Journal of Applied Physics **107**, 024105 (2010).

[79]K. Coleman, J. Walker, T. Beechem, and S. Trolier-McKinstry, "Effect of stresses on the dielectric and piezoelectric properties of PZT thin films", Journal of Applied Physics **126**, 034101 (2019).

[80]A. L. Roitburd, "Equilibrium structure of epitaxial layers", Physica Status Solidi (a) **37**, 329–339 (1976).

[81]J. S. Speck, A. Seifert, W. Pompe, and R. Ramesh, "Domain configurations due to multiple misfit relaxation mechanisms in epitaxial ferroelectric thin films. II. Experimental verification and implications", Journal of Applied Physics **76**, 477–483 (1994).

[82]G. Arlt and N. A. Pertsev, "Force constant and effective mass of 90° domain walls in ferroelectric ceramics", Journal of Applied Physics **70**, 2283–2289 (1991).

[83]V. Nagarajan, A. Roytburd, A. Stanishevsky, S. Prasertchoung, T. Zhao, L. Chen, J. Melngailis, O. Auciello, and R. Ramesh, "Dynamics of ferroelastic domains in ferroelectric thin films", Nature Materials **2**, 43–47 (2003).

[84]N. Aruchamy, T. Schenk, V. Kovacova, S. Glinsek, E. Defay, and T. Granzow, "Influence of tensile vs. compressive stress on fatigue of lead zirconate titanate thin films", Journal of the European Ceramic Society **41**, 6991–6999 (2021).

[85]N. Aruchamy, T. Schenk, S. Girod, S. Glinsek, E. Defay, and T. Granzow, "Influence of substrate stress on in-plane and out-of-plane ferroelectric properties of PZT films", Journal of Applied Physics **131** (2022).

[86]M. O. Eatough, D. Dimos, B. A. Tuttle, W. L. Warren, and R. Ramesh, "A study of switching behavior in Pb(Zr,Ti)O_3 thin films using X-ray diffraction", MRS Proceedings **361**, 111 (1994).

[87]C. A. Randall, N. Kim, J.-P. Kucera, W. Cao, and T. R. Shrout, "Intrinsic and extrinsic size effects in fine-grained morphotropic-phase-boundary Lead Zirconate Titanate ceramics", Journal of the American Ceramic Society **81**, 677–688 (2005).

[88]Y. Bastani, T. Schmitz-Kempen, A. Roelofs, and N. Bassiri-Gharb, "Critical thickness for extrinsic contributions to the dielectric and piezoelectric response in lead zirconate titanate ultrathin films", Journal of Applied Physics **109**, 014115 (2011).

[89]J. K. Yang, W. S. Kim, and H. H. Park, "Effect of grain size of Pb($Zr_{0.4}Ti_{0.6}$)O_3 sol–gel derived thin films on the ferroelectric properties", Applied Surface Science **169-170**, 544–548 (2001).

[90]F. Yan, P. Bao, H. L. Chan, C. L. Choy, and Y. Wang, "The grain size effect of Pb($Zr_{0.3}Ti_{0.7}$)O_3 thin films", Thin Solid Films **406**, 282–285 (2002).

[91]C. S. Ganpule, V. Nagarajan, H. Li, A. S. Ogale, D. E. Steinhauer, S. Aggarwal, E. Williams, R. Ramesh, and P. De Wolf, "Role of 90° domains in lead zirconate titanate thin films", Applied Physics Letters **77**, 292–294 (2000).

[92]L. Chen, J. Ouyang, C. S. Ganpule, V. Nagarajan, R. Ramesh, and A. L. Roytburd, "Formation of 90° elastic domains during local 180° switching in epitaxial ferroelectric thin films", Applied Physics Letters **84**, 254 (2004).

[93]A. Roelofs, U. Böttger, R. Waser, F. Schlaphof, S. Trogisch, and L. M. Eng, "Differentiating 180° and 90° switching of ferroelectric domains with three-dimensional piezoresponse force microscopy", Applied Physics Letters **77**, 3444–3446 (2000).

[94]J. Wang, H. P. Li, and R. Stevens, "Hafnia and hafnia-toughened ceramics", Journal of Materials Science **27**, 5397–5430 (1992).

[95]K. Matsumoto, Y. Itoh, and T. Kameda, "EB-PVD process and thermal properties of hafnia-based thermal barrier coating", Science and Technology of Advanced Materials **4**, 153–158 (2003).

[96]A. Navrotsky, "Thermochemical insights into refractory ceramic materials based on oxides with large tetravalent cations", Journal of Materials Chemistry **15**, 1883 (2005).

[97]A. Navrotsky and S. V. Ushakov, "Thermodynamics of oxide systems relevant to alternative gate dielectrics", edited by A. A. Demkov and A. Navrotsky, 57–108 (2005).

[98]T. Schenk, "Formation of ferroelectricity in hafnium oxide based thin films", (2017).

[99]X. Sang, E. D. Grimley, T. Schenk, U. Schroeder, and J. M. LeBeau, "On the structural origins of ferroelectricity in HfO_2 thin films", Applied Physics Letters **106**, 162905 (2015).

[100]M. Hoffmann, U. Schroeder, T. Schenk, T. Shimizu, H. Funakubo, O. Sakata, D. Pohl, M. Drescher, C. Adelmann, R. Materlik, A. Kersch, and T. Mikolajick, "Stabilizing the ferroelectric phase in doped hafnium oxide", Journal of Applied Physics **118**, 072006 (2015).

[101]J. Müller, U. Schröder, T. S. Böscke, I. Müller, U. Böttger, L. Wilde, J. Sundqvist, M. Lemberger, P. Kücher, T. Mikolajick, and L. Frey, "Ferroelectricity in yttrium-doped hafnium oxide", Journal of Applied Physics **110**, 114113 (2011).

[102]S. Mueller, C. Adelmann, A. Singh, S. Van Elshocht, U. Schroeder, and T. Mikolajick, " Ferroelectricity in Gd-doped HfO_2 thin films ", ECS Journal of Solid State Science and Technology **1**, N123–N126 (2012).

[103]D. Zhou, J. Müller, J. Xu, S. Knebel, D. Bräuhaus, and U. Schröder, "Insights into electrical characteristics of silicon doped hafnium oxide ferroelectric thin films", Applied Physics Letters **100**, 10.1063/1.3688915 (2012).

[104]D. Martin, J. Müller, T. Schenk, T. M. Arruda, A. Kumar, E. Strelcov, E. Yurchuk, S. Müller, D. Pohl, U. Schröder, S. V. Kalinin, and T. Mikolajick, "Ferroelectricity in Si-Doped HfO_2 revealed: A binary lead-free ferroelectric", Advanced Materials **26**, 8198–8202 (2014).

[105]E. Yurchuk, J. Müller, S. Knebel, J. Sundqvist, A. P. Graham, T. Melde, U. Schröder, and T. Mikolajick, "Impact of layer thickness on the ferroelectric behaviour of silicon doped hafnium oxide thin films", Thin Solid Films **533**, 88–92 (2013).

[106]M. H. Park, H. J. Kim, Y. J. Kim, W. Lee, T. Moon, K. D. Kim, and C. S. Hwang, "Study on the degradation mechanism of the ferroelectric properties of thin $Hf_{0.5}Zr_{0.5}O_2$ films on TiN and Ir electrodes", Applied Physics Letters **105**, 1–6 (2014).

[107]S. Starschich, D. Griesche, T. Schneller, and U. Böttger, "Chemical solution deposition of ferroelectric hafnium oxide for future lead free ferroelectric devices", ECS Journal of Solid State Science and Technology **4**, 419–423 (2015).

[108]T. Olsen, U. Schröder, S. Müller, A. Krause, D. Martin, A. Singh, J. Müller, M. Geidel, and T. Mikolajick, "Co-sputtering yttrium into hafnium oxide thin films to produce ferroelectric properties", Applied Physics Letters **101**, 082905 (2012).

[109]S. Starschich, D. Griesche, T. Schneller, R. Waser, and U. Böttger, "Chemical solution deposition of ferroelectric yttrium-doped hafnium oxide films on platinum electrodes", Applied Physics Letters **104**, 202903 (2014).

[110]T. Schenk, N. Godard, A. Mahjoub, S. Girod, A. Matavz, V. Bobnar, E. Defay, and S. Glinsek, "Toward thick piezoelectric HfO_2-based films", Physica Status Solidi - Rapid Research Letters **14**, 1–6 (2020).

[111]S. Starschich and U. Boettger, "An extensive study of the influence of dopants on the ferroelectric properties of HfO_2", Journal of Materials Chemistry C **5**, 333–338 (2017).

[112]U. Schroeder, E. Yurchuk, J. Müller, D. Martin, T. Schenk, P. Polakowski, C. Adelmann, M. I. Popovici, S. V. Kalinin, and T. Mikolajick, "Impact of different dopants on the switching properties of ferroelectric hafnium oxide", Japanese Journal of Applied Physics **53**, 08LE02 (2014).

[113]J. F. Scott and C. A. Paz De Araujo, "Ferroelectric memories", Science **246**, 1400–1405 (1989).

[114]A. K. Tagantsev, I. Stolichnov, E. L. Colla, and N. Setter, "Polarization fatigue in ferroelectric films: Basic experimental findings, phenomenological scenarios, and microscopic features", Journal of Applied Physics **90**, 1387–1402 (2001).

[115]X. J. Lou, "Polarization fatigue in ferroelectric thin films and related materials", Journal of Applied Physics **105**, 024101 (2009).

[116]M. Dawber and J. F. Scott, "A model for fatigue in ferroelectric perovskite thin films", Applied Physics Letters **76**, 1060–1062 (2000).

[117]I. K. Yoo and S. B. Desu, "Mechanism of fatigue in ferroelectric thin films", Physica Status Solidi (a) **133**, 565–573 (1992).

[118]U. Robels and G. Arlt, "Domain wall clamping in ferroelectrics by orientation of defects", Journal of Applied Physics **73**, 3454–3460 (1993).

[119]C. Brennan, "Model of ferroelectric fatigue due to defect/domain interactions", Ferroelectrics **150**, 199–208 (2011).

[120]E. L. Colla, D. V. Taylor, A. K. Tagantsev, and N. Setter, "Discrimination between bulk and interface scenarios for the suppression of the switchable polarization fatigue in Pb(Zr,Ti)O_3 thin films capacitors with Pt electrodes", Applied Physics Letters **72**, 2478–2480 (1998).

[121]A. Q. Jiang, Y. Y. Lin, and T. A. Tang, "Charge injection and polarization fatigue in ferroelectric thin films", Journal of Applied Physics **102**, 1–10 (2007).

[122]W. L. Warren, D. Dimos, B. A. Tuttle, G. E. Pike, R. W. Schwartz, P. J. Clews, and D. C. McIntyre, "Polarization suppression in Pb(Zr,Ti)O_3 thin films", Journal of Applied Physics **77**, 6695–6702 (1995).

[123]W. Shepherd, "Fatigue and aging in sol- gel derived pzt thin films", MRS Online Proceedings Library 1990 200:1 **200**, 277–288 (1990).

[124]H. N. Al-Shareef, O. Auciello, and A. I. Kingon, "Electrical properties of ferroelectric thin-film capacitors with hybrid (Pt, RuO_2) electrodes for nonvolatile memory applications", Journal of Applied Physics **77**, 2146–2154 (1995).

[125]R. Bouregba, N. Sama, C. Soyer, G. Poullain, and D. Remiens, "Interface depolarization field as common denominator of fatigue and size effect in Pb($Zr_{0.54}Ti_{0.46}$)O_3 ferroelectric thin film capacitors", Journal of Applied Physics **107**, 104102 (2010).

[126]D. P. Vijay and S. B. Desu, "Electrodes for $PbZr_xTi_{1-x}O_3$ ferroelectric thin films", Journal of The Electrochemical Society **140**, 2640–2645 (1993).

[127]W. I. Lee and J. key Lee, "Dopant effects on the grain structure and electrical property of PZT thin films prepared by sol-gel process", Materials Research Bulletin **30**, 1185–1191 (1995).

[128]A. L. Kholkin, E. L. Colla, A. K. Tagantsev, D. V. Taylor, and N. Setter, "Fatigue of piezoelectric properties in Pb(Zr,Ti)O_3 films", Applied Physics Letters **68**, 2577–2579 (1996).

[129]V. Y. Shur, E. L. Rumyantsev, E. V. Nikolaeva, E. I. Shishkin, and I. S. Baturin, "Kinetic approach to fatigue phenomenon in ferroelectrics", Journal of Applied Physics **90**, 6312–6315 (2001).

[130]D. J. Johnson, D. T. Amm, E. Griswold, K. Sreenivas, G. Yi, and M. Sayer, "Measuring fatigue in PZT thin films", MRS Proceedings **200**, 289 (1990).

[131]K. Khachaturyan, "Mechanical fatigue in thin films induced by piezoelectric strains as a cause of ferroelectric fatigue", Journal of Applied Physics **77**, 6449–6455 (1995).

[132]R. F. Klie and N. D. Browning, "Atomic scale characterization of oxygen vacancy segregation at $SrTiO_3$ grain boundaries", Applied Physics Letters **77**, 3737–3739 (2000).

[133]J.-S. Lee and S.-K. Joo, "Enhanced fatigue and data retention characteristics of $Pb(Zr,Ti)O_3$ thin films by the selectively nucleated lateral crystallization method", Japanese Journal of Applied Physics **40**, 229–233 (2001).

[134]C. Verdier, D. Lupascu, and J. Rödel, "Unipolar fatigue of ferroelectric lead–zirconate–titanate", Journal of the European Ceramic Society **23**, 1409–1415 (2003).

[135]F. Yan, P. Bao, H. L. W. Chan, C.-L. Choy, X. Chen, J. Zhu, and Y. Wang, "Effect of grain size on the fatigue properties of $Pb(Zr_{0.3}Ti_{0.7})O_3$ thin films prepared by metalorganic decomposition", Ferroelectrics **252**, 209–216 (2001).

[136]S. Hu, G. Hu, X. Meng, G. Wang, J. Sun, S. Guo, J. Chu, and N. Dai, "The grain size effect of the $Pb(Zr_{0.45}Ti_{0.55})O_3$ thin films deposited on $LaNiO_3$-coated silicon by modified sol–gel process", Journal of Crystal Growth **260**, 109–114 (2004).

[137]W. Pan, C.-F. Yue, and S. Sun, "Tfl15: Domain orientation change induced by ferroelectric fatigue process in lead zirconate titanate ceramics", Ferroelectrics **133**, 97–102 (1992).

[138]D. Zhou, J. Xu, Q. Li, Y. Guan, F. Cao, X. Dong, J. Müller, T. Schenk, and U. Schröder, "Wake-up effects in Si-doped hafnium oxide ferroelectric thin films", Applied Physics Letters **103**, 192904 (2013).

[139]M. Pešić, F. P. G. Fengler, L. Larcher, A. Padovani, T. Schenk, E. D. Grimley, X. Sang, J. M. LeBeau, S. Slesazeck, U. Schroeder, and T. Mikolajick, "Physical mechanisms behind the field-cycling behavior of HfO_2-based ferroelectric capacitors", Advanced Functional Materials **26**, 4601–4612 (2016).

[140]F. P. G. Fengler, R. Nigon, P. Muralt, E. D. Grimley, X. Sang, V. Sessi, R. Hentschel, J. M. LeBeau, T. Mikolajick, and U. Schroeder, "Analysis of performance instabilities of Hafnia-based ferroelectrics using modulus spectroscopy and thermally stimulated depolarization currents", Advanced Electronic Materials **4**, 1700547 (2018).

[141]F. P. G. Fengler, M. Pesic, S. Starschich, T. Schneller, U. Bottger, T. Schenk, M. H. Park, T. Mikolajick, and U. Schroeder, "Comparison of hafnia and PZT based ferroelectrics for future non-volatile FRAM applications", in 2016 46th European Solid-State Device Research Conference (ESSDERC) (Sept. 2016), pp. 369–372.

[142]T. Schenk, M. Hoffmann, J. Ocker, M. Pešić, T. Mikolajick, and U. Schroeder, "Complex internal bias fields in ferroelectric Hafnium oxide", ACS Applied Materials & Interfaces **7**, 20224–20233 (2015).

[143]P. D. Lomenzo, Q. Takmeel, C. Zhou, C. M. Fancher, E. Lambers, N. G. Rudawski, J. L. Jones, S. Moghaddam, and T. Nishida, "TaN interface properties and electric field cycling effects on ferroelectric Si-doped HfO_2 thin films", Journal of Applied Physics **117**, 134105 (2015).

[144]S. Starschich, S. Menzel, and U. Böttger, "Evidence for oxygen vacancies movement during wake-up in ferroelectric hafnium oxide", Applied Physics Letters **108**, 032903 (2016).

[145]M. H. Park, H. J. Kim, Y. J. Kim, T. Moon, K. D. Kim, Y. H. Lee, S. D. Hyun, and C. S. Hwang, "Study on the internal field and conduction mechanism of atomic layer deposited ferroelectric $Hf_{0.5}Zr_{0.5}O_2$ thin films", Journal of Materials Chemistry C **3**, 6291–6300 (2015).

[146]M. Lanza, G. Bersuker, M. Porti, E. Miranda, M. Nafría, and X. Aymerich, "Resistive switching in hafnium dioxide layers: Local phenomenon at grain boundaries", Applied Physics Letters **101**, 193502 (2012).

[147]M. H. Park, D. H. Lee, K. Yang, J.-Y. Park, G. T. Yu, H. W. Park, M. Materano, T. Mittmann, P. D. Lomenzo, T. Mikolajick, U. Schroeder, and C. S. Hwang, "Review of defect chemistry in fluorite-structure ferroelectrics for future electronic devices", Journal of Materials Chemistry C **8**, 10526–10550 (2020).

[148]A. Chouprik, D. Negrov, E. Y. Tsymbal, and A. Zenkevich, "Interplay between oxygen defects and dopants: effect on structure and performance of HfO_2 based ferroelectrics", Nanoscale **8**, 11635–11678 (2021).

[149]A. Chouprik, D. Negrov, E. Y. Tsymbal, and A. Zenkevich, "Defects in ferroelectric HfO_2", Nanoscale **13**, 11635–11678 (2021).

[150]M. Masuduzzaman and M. A. Alam, "Hot atom damage (HAD) limited TDDB lifetime of ferroelectric memories", in Technical Digest - International Electron Devices Meeting, IEDM (2013).

[151]M. Masuduzzaman, D. Varghese, J. A. Rodriguez, S. Krishnan, and M. A. Alam, "Observation and control of Hot atom damage in ferroelectric devices", IEEE Transactions on Electron Devices **61**, 3490–3498 (2014).

[152]M. Masuduzzaman, S. Xie, J. Chung, D. Varghese, J. Rodriguez, S. Krishnan, and M. Ashraful Alam, "The origin of broad distribution of breakdown times in polycrystalline thin film dielectrics", Applied Physics Letters **101**, 153511 (2012).

[153]C. Richter, T. Schenk, M. H. Park, F. A. Tscharntke, E. D. Grimley, J. M. LeBeau, C. Zhou, C. M. Fancher, J. L. Jones, T. Mikolajick, and U. Schroeder, "Si doped Hafnium oxide—A "Fragile" ferroelectric system", Advanced Electronic Materials **3**, 1700131 (2017).

[154]R. Batra, T. D. Huan, G. A. Rossetti, and R. Ramprasad, "Dopants promoting ferroelectricity in hafnia: insights from a comprehensive chemical space exploration", Chemistry of Materials **29**, 9102–9109 (2017).

[155]Y. H. Lee, H. J. Kim, T. Moon, K. D. Kim, S. D. Hyun, H. W. Park, Y. B. Lee, M. H. Park, and C. S. Hwang, "Preparation and characterization of ferroelectric $Hf_{0.5}Zr_{0.5}O_2$ thin films grown by reactive sputtering", Nanotechnology **28**, 305703 (2017).

[156]M. G. Kim and S.-i. Ohmi, "Ferroelectric properties of undoped HfO_2 directly deposited on Si substrates by RF magnetron sputtering", Japanese Journal of Applied Physics **57**, 11UF09 (2018).

[157]Q. Luo, H. Ma, H. Su, K.-H. Xue, R. Cao, Z. Gao, J. Yu, T. Gong, X. Xu, J. Yin, P. Yuan, L. Tai, D. Dong, S. Long, Q. Liu, X.-S. Miao, H. Lv, and M. Liu, "Composition-dependent ferroelectric properties in sputtered $Hf_XZr_{1-X}O_2$ thin films", IEEE Electron Device Letters **40**, 570–573 (2019).

[158]Mohit, T. Murakami, K.-i. Haga, and E. Tokumitsu, "Impact of annealing environment on electrical properties of yttrium-doped hafnium zirconium dioxide thin films prepared by the solution process", Japanese Journal of Applied Physics **59**, SPPB03 (2020).

[159]T. Suzuki, T. Shimizu, T. Mimura, H. Uchida, and H. Funakubo, "Epitaxial ferroelectric Y-doped HfO_2 film grown by the RF magnetron sputtering", Japanese Journal of Applied Physics **57**, 11UF15 (2018).

[160]P. Muralt, R. G. Polcawich, and S. Trolier-McKinstry, "Piezoelectric thin films for sensors, actuators, and energy harvesting", MRS Bulletin **34**, 658–664 (2009).

[161]N. M. Shorrocks, R. W. Whatmore, and P. C. Osbond, "Lead scandium tantalate for thermal detector applications", Ferroelectrics **106**, 387–392 (1990).

[162]S. Lang and S. Muensit, "Review of some lesser-known applications of piezoelectric and pyroelectric polymers", Applied Physics A **85**, 125–134 (2006).

[163]S. P. Alpay, J. Mantese, S. Trolier-McKinstry, Q. Zhang, and R. W. Whatmore, "Next-generation electrocaloric and pyroelectric materials for solid-state electrothermal energy interconversion", MRS Bulletin **39**, 1099–1111 (2014).

[164]C. B. Roundy and R. L. Byer, "Sensitive $LiTaO_3$ pyroelectric detector", Journal of Applied Physics **44**, 929–931 (1973).

[165]H. Kohlstedt, Y. Mustafa, A. Gerber, A. Petraru, M. Fitsilis, R. Meyer, U. Böttger, and R. Waser, "Current status and challenges of ferroelectric memory devices", Microelectronic Engineering **80**, 296–304 (2005).

[166]N. Izyumskaya, Y.-I. Alivov, S.-J. Cho, H. Morkoç, H. Lee, and Y.-S. Kang, "Processing, structure, properties, and applications of PZT thin films", Critical Reviews in Solid State and Materials Sciences **32**, 111–202 (2007).

[167]K. Tsubouchi and N. Mikoshiba, "Zero-temperature-coefficient SAW devices on AlN epitaxial films", IEEE Transactions on Sonics and Ultrasonics **32**, 634–644 (1985).

[168]R. R. Benoit, R. Q. Rudy, J. S. Pulskamp, and R. G. Polcawich, "Piezoelectric RF-MEMS switches on Si-on-Sapphire substrates", Journal of Microelectromechanical Systems **29**, 1087–1090 (2020).

[169]J. Iannacci, "Internet of things (IoT); internet of everything (IoE); tactile internet; 5G – A (not so evanescent) unifying vision empowered by EH-MEMS (energy harvesting MEMS) and RF-MEMS (radio frequency MEMS)", Sensors and Actuators A: Physical **272**, 187–198 (2018).

[170]"Ferroelectricity in doped hafnium oxide", Woodhead Publishing series in Electronic and Optical materials, edited by U. Schroeder, C. S. Hwang, and H. Funakubo (2019).

[171]T. Nakamura, Y. Nakao, A. Kamisawa, and H. Takasu, "Ferroelectric memory FET with Ir/IrO_2 electrodes", Integrated Ferroelectrics **9**, 179–187 (1995).

[172]J. Rodriguez, K. Remack, K. Boku, K. Udayakumar, S. Aggarwal, S. Summerfelt, F. Celii, S. Martin, L. Hall, K. Taylor, T. Moise, H. McAdams, J. McPherson, R. Bailey, G. Fox, and M. Depner, "Reliability Properties of low-voltage ferroelectric capacitors and memory arrays", IEEE Transactions on Device and Materials Reliability **4**, 436–449 (2004).

[173]Y. Fujimori, T. Nakamura, and A. Kamisawa, "Properties of ferroelectric memory FET using $Sr_2(Ta,Nb)_2O_7$ thin film", Japanese Journal of Applied Physics **38**, 2285–2288 (1999).

[174]H. Ishiwara and B.-E. Park, "Recent progress in ferroelectic-gate FETs", MRS Proceedings **747**, T4.5/U9.5 (2002).

[175]H. Ishiwara, "Current status of ferroelectric-gate Si transistors and challenge to ferroelectric-gate CNT transistors", Current Applied Physics **9**, S2–S6 (2009).

[176]MSP430 microcontrollers — TI.com.

[177]I. T. AG, F-RAM (Ferroelectric RAM) - Infineon Technologies.

[178]J. F. Scott, L. Kammerdiner, M. Parris, S. Traynor, V. Ottenbacher, A. Shawabkeh, and W. F. Oliver, "Switching kinetics of lead zirconate titanate submicron thin-film memories", Journal of Applied Physics **64**, 787–792 (1988).

[179]K. Eshraghian, "Evolution of Nonvolatile Resistive Switching Memory Technologies: The Related Influence on Hetrogeneous Nanoarchitectures", Transactions on Electrical and Electronic Materials **11**, 243–248 (2010).

[180]Kwang-Ho Kim, Jin-Ping Han, Soon-Won Jung, and Tso-Ping Ma, "Ferroelectric DRAM (FE-DRAM) FET with metal $SrBi_2Ta_2O_9$/SiN/Si gate structure", IEEE Electron Device Letters **23**, 82–84 (2002).

[181]B.-E. Park and H. Ishiwara, "Fabrication and characterization of (Bi, La)$_4$, Ti_3O_{12} films using $LaAlO_3$ buffer layers for MFIS structures", Integrated Ferroelectrics **62**, 141–147 (2004).

[182]S. Sakai and R. Ilangovan, "Metal Ferroelectric Insulator Semiconductor memory FET with long retention and high endurance", IEEE Electron Device Letters **25**, 369–371 (2004).

[183]K. Aizawa, B.-E. Park, Y. Kawashima, K. Takahashi, and H. Ishiwara, "Impact of HfO_2 buffer layers on data retention characteristics of ferroelectric-gate field-effect transistors", Applied Physics Letters **85**, 3199–3201 (2004).

[184]R. Nigon, T. M. Raeder, and P. Muralt, "Characterization methodology for lead zirconate titanate thin films with interdigitated electrode structures", J. Appl. Phys. **121**, 204101 (2017).

[185]N. Chidambaram, "Advanced sol-gel processing of PZT thin films for piezoelectric MEMS structures", **6338** (EPFL-Thesis, 2014).

[186]N. Godard, P. Grysan, E. Defay, and S. Glinšek, "Growth of 100-oriented lead zirconate titanate thin films mediated by a safe solvent", Journal of Materials Chemistry C **9**, 281–287 (2021).

[187]D. Sette, S. Girod, R. Leturcq, S. Glinsek, and E. Defay, "Transparent ferroelectric capacitors on glass", Micromachines **8**, 313 (2017).

[188]M. Museau, C. Masclet, and S. Tichkiewitch, "Integrated design of MEMS: aiming at manufacturability", International Journal on Interactive Design and Manufacturing (IJIDeM) **1**, 127–134 (2007).

[189]J. Nath, D. Ghosh, J.-P. Maria, A. Kingon, W. Fathelbab, P. Franzon, and M. Steer, "An electronically tunable microstrip bandpass filter using thin-film Barium-Strontium-Titanate (BST) varactors", IEEE Transactions on Microwave Theory and Techniques **53**, 2707–2712 (2005).

[190]M. A. Moram and M. E. Vickers, "X-ray diffraction of III-nitrides", Reports on Progress in Physics **72**, 036502 (2009).

[191]F. Lotgering, "Topotactical reactions with ferrimagnetic oxides having hexagonal crystal structures—I", Journal of Inorganic and Nuclear Chemistry **9**, 113–123 (1959).

[192]J. L. Jones, E. B. Slamovich, and K. J. Bowman, "Critical evaluation of the lotgering degree of orientation texture indicator", Journal of Materials Research **19**, 3414–3422 (2004).

[193]T. Schenk, C. M. Fancher, M. H. Park, C. Richter, C. Künneth, A. Kersch, J. L. Jones, T. Mikolajick, and U. Schroeder, "On the origin of the large remanent polarization in La:HfO_2", Advanced Electronic Materials **5**, 1900303 (2019).

[194]Crystallographic Texture & Orientations — Lambda Technologies Group.

[195]R. Waser, U. Böttger, and S. Tiedke, Polar Oxides, edited by R. Waser, U. Böttger, and S. Tiedke (Wiley, Dec. 2004), pp. 1–387.

[196]T. Schenk, E. Yurchuk, S. Mueller, U. Schroeder, S. Starschich, U. Böttger, and T. Mikolajick, "About the deformation of ferroelectric hystereses", Applied Physics Reviews **1**, 41103 (2014).

[197]E. Defaÿ, ed., Ferroelectric dielectrics integrated on silicon, eng (ISTE, London, 2011).

[198]F. Yan, P. Bao, H. L. W. Chan, C.-L. Choy, X. Chen, J. Zhu, and Y. Wang, "Effect of grain size on the fatigue properties of $Pb(Zr_{0.3},Ti_{0.7})O_3$ thin films prepared by metalorganic decomposition", Ferroelectrics **252**, 209–216 (2001).

[199]U. Selvaraj, K. Brooks, A. V. Prasadarao, S. Komarneni, R. Roy, and L. E. Cross, "Sol-Gel Fabrication of $Pb(Zr_{0.52}Ti_{0.48})O_3$ thin films using lead acetylacetonate as the lead Source", Journal of the American Ceramic Society **76**, 1441–1444 (1993).

[200]D. S. Paik, A. V. Prasada Rao, and S. Komarneni, "Sol-gel fabrication of oriented PZT thin films: Effect of buffer layer in promoting epitaxial growth", Ferroelectrics **211**, 141–151 (1998).

[201]E. R. Dobrovinskaya, L. A. Lytvynov, and V. Pishchik, "Properties of sapphire", Sapphire, 55–176 (2009).

[202]A. C. Sparavigna, "Thermal Conductivity of the Crystalline Silicon", Philica, 1143 (2017).

[203]I. M. Abdulagatov, S. N. Emirov, T. A. Tsomaeva, K. A. Gairbekov, S. Y. Askerov, and N. A. Magomedova, "Thermal conductivity of fused quartz and quartz ceramic at high temperatures and high pressures", Journal of Physics and Chemistry of Solids **61**, 779–787 (2000).

[204]A. D. Polli, F. F. Lange, and C. G. Levi, "Metastability of the Fluorite, Pyrochlore, and Perovskite Structures in the PbO-ZrO_2-TiO_2 System", Journal of the American Ceramic Society **83**, 873–881 (2004).

[205]J. Pérez, P. M. Vilarinho, A. L. Kholkin, J. M. Herrero, and C. Zaldo, "Effect of processing conditions on the piezoelectric properties of sol-gel derived $Pb(Zr,Ti)O_3$ films for micromechanical applications", Journal of Materials Research **20**, 1428–1435 (2005).

[206]K. Nittala, S. Mhin, K. M. Dunnigan, D. S. Robinson, J. F. Ihlefeld, P. G. Kotula, G. L. Brennecka, and J. L. Jones, "Phase and texture evolution in solution deposited lead zirconate titanate thin films: Formation and role of the Pt_3Pb inter-metallic phase", Journal of Applied Physics **113**, 244101 (2013).

[207]J. Y. Lee, G. Anoop, H. J. Lee, J. H. Kwak, and J. Y. Jo, "Structural properties of solution-processed $Hf_{0.5}Zr_{0.5}O_2$ thin films", Current Applied Physics **17**, 704–708 (2017).

[208]K. N. Woods, T.-H. Chiang, P. N. Plassmeyer, M. G. Kast, A. C. Lygo, A. K. Grealish, S. W. Boettcher, and C. J. Page, "High-κ lanthanum zirconium oxide thin film dielectrics from aqueous solution precursors", ACS Applied Materials & Interfaces **9**, 10897–10903 (2017).

[209]S. Nakayama, H. Funakubo, and H. Uchida, "Crystallization behavior and ferroelectric property of HfO_2 – ZrO_2 films fabricated by chemical solution deposition", Japanese Journal of Applied Physics **57**, 11UF06 (2018).

[210]N. Bassiri-Gharb, Y. Bastani, and A. Bernal, "Chemical solution growth of ferroelectric oxide thin films and nanostructures", Chemical Society Reviews **43**, 2125–2140 (2014).

[211]B. Malic and H. Suzuki, "Low-temperature processing of solution-derived ferroelectric thin films", Journal of the Ceramic Society of Japan **122**, 1–8 (2014).

[212]F. Casset, A. Devos, S. Sadtler, A. L. Louarn, P. Emery, G. L. Rhun, P. Ancey, S. Fanget, and E. Defay, "Young modulus and poisson ratio of PZT thin film by picosecond ultrasonics", IEEE International Ultrasonics Symposium, IUS, 2180–2183 (2012).

[213]R. R. Knight, C. Mo, and W. W. Clark, "MEMS interdigitated electrode pattern optimization for a unimorph piezoelectric beam", Journal of Electroceramics **26**, 14–22 (2011).

[214]N. Chidambaram, D. Balma, R. Nigon, A. Mazzalai, R. Matloub, C. S. Sandu, and P. Muralt, "Converse mode piezoelectric coefficient for lead zirconate titanate thin film with interdigitated electrode", Journal of Micromechanics and Microengineering **25**, 045016 (2015).

[215]Y. Jeon, R. Sood, J.-h. Jeong, and S.-G. Kim, "MEMS power generator with transverse mode thin film PZT", Sensors and Actuators A: Physical **122**, 16–22 (2005).

[216]S. Gevorgian, T. Martinsson, P. Linner, and E. Kollberg, "CAD models for multilayered substrate interdigital capacitors", IEEE Transactions on Microwave Theory and Techniques **44**, 896–904 (1996).

[217]R. Igreja and C. Dias, "Analytical evaluation of the interdigital electrodes capacitance for a multi-layered structure", Sensors and Actuators A: Physical **112**, 291–301 (2004).

[218]R. Nigon, "Internal electric fields and electrode effects in ferroelectric thin films for piezoelectric energy harvesting", (EPFL-Thesis, 2017).

[219]B. A. Tuttle, T. J. Headley, D. Dimos, and M. O. Eatough, "Relationships between ferroelectric 90° domain formation and electrical properties of chemically prepared Pb(Zr,Ti)O_3 thin films", in Science and technology of electroceramic thin films, edited by O. Auciello and R. Waser (Kluwer Academic Publisher, 1995), pp. 117–132.

[220]W. Cao and L. E. Cross, "Theory of tetragonal twin structures in ferroelectric perovskites with a first-order phase transition", Physical Review B **44**, 5–12 (1991).

[221]D. Damjanovic and M. Demartin, "Contribution of the irreversible displacement of domain walls to the piezoelectric effect in barium titanate and lead zirconate titanate ceramics", Journal of Physics Condensed Matter **9**, 4943–4953 (1997).

[222]P. Gao, J. Britson, C. T. Nelson, J. R. Jokisaari, C. Duan, M. Trassin, S.-H. Baek, H. Guo, L. Li, Y. Wang, Y.-H. Chu, A. M. Minor, C.-B. Eom, R. Ramesh, L.-Q. Chen, and X. Pan, "Ferroelastic domain switching dynamics under electrical and mechanical excitations", Nature Communications **5**, 3801 (2014).

[223]M. Marsilius, K. G. Webber, E. Aulbach, and T. Granzow, "Comparison of the temperature-dependent ferroelastic behavior of hard and soft lead zirconate titanate ceramics", Journal of the American Ceramic Society **93**, 2850–2856 (2010).

[224]V. Kovacova, N. Vaxelaire, G. Le Rhun, P. Gergaud, T. Schmitz-Kempen, and E. Defay, "Correlation between electric-field-induced phase transition and piezoelectricity in lead zirconate titanate films", Physical Review B **90**, 140101 (2014).

[225]J.-F. Li, Z.-X. Zhu, and F.-P. Lai, "Thickness-dependent phase transition and piezoelectric response in textured Nb-doped $Pb(Zr_{0.52}Ti_{0.48})O_3$ thin films", The Journal of Physical Chemistry C. Chem. C **114**, 17796–17801 (2010).

[226]M. Nishide, S. Yokoyama, H. Funakubo, T. Katoda, and K. Nishida, "Impact of stress on the crystal structural nonuniformity along the film thickness direction by micro fabrication of $Pb(ZrTi)O_3$ islands with morphotropic phase boundary composition", Journal of the Ceramic Society of Japanam. Soc. Jpn. **127**, 123–126 (2019).

[227]H. Lu, S. Glinsek, P. Buragohain, E. Defay, J. Iñiguez, and A. Gruverman, "Probing antiferroelectric-ferroelectric phase transitions in $PbZrO_3$ capacitors by piezoresponse force microscopy", Advanced Functional MaterialsFunct. Mater. **30**, 2003622 (2020).

[228]Y.-H. Seo, D. J. Franzbach, J. Koruza, A. Benčan, B. Malič, M. Kosec, J. L. Jones, and K. G. Webber, "Nonlinear stress-strain behavior and stress-induced phase transitions in soft $Pb(Zr_xTi_{1-x})O_3$ at the morphotropic phase boundary", Physical Review B **87**, 094116 (2013).

[229]A. K. Kalyani, L. K. V, A. R. James, A. Fitch, and R. Ranjan, "Unraveling the nature of electric field- and stress- induced structural transformations in soft PZT by a new powder poling technique", J. Phys.: Condens. Matter **27**, 072201 (2015).

[230]F. Chu, F. Xu, J. Shepard, and S. Trolier-McKinstry, "Thickness dependence of the electrical properties of sol-gel derived lead zirconate titanate thin films with (111) and (100) texture", MRS Proceedings **493**, 409 (1997).

[231]D.-J. Kim, J.-P. Maria, A. I. Kingon, and S. K. Streiffer, "Evaluation of intrinsic and extrinsic contributions to the piezoelectric properties of $Pb(Zr_xTi_{1-x})O_3$ thin films as a function of composition", J. Appl. Phys. **93**, 5568–5575 (2003).

[232]G. Robert, "Extrinsic contributions to the piezoelectric response of lead-based ferroelectrics", (2005).

[233]C. Zhao, D. Hou, C.-C. Chung, H. Zhou, A. Kynast, E. Hennig, W. Liu, S. Li, and J. L. Jones, "Deconvolved intrinsic and extrinsic contributions to electrostrain in high performance, nb-doped $Pb(Zr_xTi_{1-x})O_3$ piezoceramics ($0.50 \leq x \leq 0.56$)", Acta Materialia **158**, 369–380 (2018).

[234]F. Xu, R. A. Wolf, T. Yoshimura, and S. Trolier-McKinstry, "Piezoelectric films for MEMS applications", Proceedings - International Symposium on Electrets, 386–396 (2002).

[235]K. Amanuma, T. Hase, and Y. Miyasaka, "Fatigue Characteristics of Sol-Gel Derived $Pb(Zr,Ti)O_3$ Thin Films", Japanese Journal of Applied Physics **33**, 5211–5214 (1994).

[236]Y. Wang, K. F. Wang, C. Zhu, and J.-M. Liu, "Polarization fatigue of ferroelectric $Pb(Zr_{0.1}Ti_{0.9})O_3$ thin films: Temperature dependence", Journal of Applied Physics **99**, 044109 (2006).

[237]S. Li, C.-Y. Huang, A. S. Bhalla, and L. E. Cross, "90°- Domain reversal in $Pb(Zr_xTi_{1-x})O_3$ ceramics", Ferroelectrics Letters Section **16**, 7–19 (1993).

[238]U. Aschauer, R. Pfenninger, S. M. Selbach, T. Grande, and N. A. Spaldin, "Strain-controlled oxygen vacancy formation and ordering in $CaMnO_3$", Physical Review B **88**, 054111 (2013).

[239]R. Al-Hamadany, J. P. Goss, P. R. Briddon, S. A. Mojarad, M. Al-Hadidi, A. G. O'Neill, and M. J. Rayson, "Oxygen vacancy migration in compressively strained $SrTiO_3$", Journal of Applied Physics **113**, 024108 (2013).

[240]U. Aschauer and N. A. Spaldin, "Interplay between strain, defect charge state, and functionality in complex oxides", Applied Physics Letters **109**, 031901 (2016).

[241]Q. Yang, J. X. Cao, Y. Ma, Y. C. Zhou, L. M. Jiang, and X. L. Zhong, "Strain effects on formation and migration energies of oxygen vacancy in perovskite ferroelectrics: A first-principles study", Journal of Applied Physics **113**, 184110 (2013).

[242]D. Su, Q. Meng, C. A. F. Vaz, M.-G. Han, Y. Segal, F. J. Walker, M. Sawicki, C. Broadbridge, and C. H. Ahn, "Origin of 90° domain wall pinning in $Pb(Zr_{0.2}Ti_{0.8})O_3$ heteroepitaxial thin films", Applied Physics Letters **99**, 102902 (2011).

[243]S. Schaab and T. Granzow, "Temperature dependent switching mechanism of ($Pb_{0.92}La_{0.08}$)($Zr_{0.65}Ti_{0.35}$)O_3 investigated by small and large signal measurements", Applied Physics Letters **97**, 132902 (2010).

[244]D. Shim, J. Pak, K. Nam, and G. Park, "Enhanced fatigue characteristics of sol–gel derived PZT thin films", Journal of Alloys and Compounds **449**, 32–35 (2008).

[245]T. Mihara, H. Watanabe, and C. A. P. D. Araujo, "Evaluation of imprint properties in sol-gel ferroelectric Pb(Zr,Ti)O_3 thin-film capacitors", Japanese Journal of Applied Physics **32**, 4168–4174 (1993).

[246]X. J. Lou, H. J. Zhang, Z. D. Luo, F. P. Zhang, Y. Liu, Q. D. Liu, A. P. Fang, B. Dkhil, M. Zhang, X. B. Ren, and H. L. He, "Effect of polarization fatigue on the Rayleigh coefficients of ferroelectric lead zirconate titanate thin films: Experimental evidence and implications", Applied Physics Letters **105**, 102907 (2014).

[247]M. D. Losego and J. P. Maria, "Reproducibility and ferroelectric fatigue of lead zirconate titanate thin films deposited directly on copper via a composite gel architecture", Journal of the American Ceramic Society **93**, 3983–3985 (2010).

[248]D. Damjanovic and M. Demartin, "The Rayleigh law in piezoelectric ceramics", Journal of Physics D: Applied Physics **29**, 2057–2060 (1996).

[249]D. Damjanovic and D. V. Taylor, "Contributions to the nonlinear dielectric and piezoelectric response of ferroelectric thin films and ceramics", Ferroelectrics **221**, 137–146 (1999).

[250]J. Glaum, T. Granzow, and J. Rödel, "Evaluation of domain wall motion in bipolar fatigued lead-zirconate-titanate: A study on reversible and irreversible contributions", Journal of Applied Physics **107**, 1–6 (2010).

[251]S. Bhattacharyya, S. Saha, and S. Krupanidhi, "Investigation of reversible and irreversible polarizations in thin films of $SrBi_2(Ta_{0.5}, Nb_{0.5})_2O_9$", Thin Solid Films **422**, 155–160 (2002).

[252]D. Bolten, O. Lohse, M. Grossmann, and R. Waser, "Reversible and irreversible domain wall contributions to the polarization in ferroelectric thin films", Ferroelectrics **221**, 251–257 (1999).

[253]F. Griggio, S. Jesse, A. Kumar, O. Ovchinnikov, H. Kim, T. N. Jackson, D. Damjanovic, S. V. Kalinin, and S. Trolier-McKinstry, "Substrate clamping effects on irreversible domain wall dynamics in Lead Zirconate Titanate thin films", Physical Review Letters **108**, 157604 (2012).

[254]G. Holzlechner, D. Kastner, C. Slouka, H. Hutter, and J. Fleig, "Oxygen vacancy redistribution in $PbZr_xTi_{1-x}O_3$ (PZT) under the influence of an electric field", Solid State Ionics **262**, 625–629 (2014).

[255]N. D. Browning, J. P. Buban, Y. Ito, R. F. Klie, and Y. Lei, "Atomic scale analysis of oxygen vacancy segregation at grain boundaries in ceramic oxides", Microscopy and Microanalysis **7**, 308–309 (2001).

[256]K. McKenna and A. Shluger, "The interaction of oxygen vacancies with grain boundaries in monoclinic HfO_2", Applied Physics Letters **95**, 222111 (2009).

[257]A. Lindman, E. E. Helgee, B. J. Nyman, and G. Wahnström, "Oxygen vacancy segregation in grain boundaries of BaZrO3 using interatomic potentials", Solid State Ionics **230**, 27–31 (2013).

[258]T. Schenk, A. Bencan, G. Drazic, O. Condurache, N. Valle, B. E. Adib, N. Aruchamy, T. Granzow, E. Defay, and S. Glinsek, "Enhancement of ferroelectricity and orientation in solution-derived hafnia thin films through heterogeneous grain nucleation", Applied Physics Letters **118** (2021).

[259]T. Schneller, R. Waser, M. Kosec, and D. Payne, "Chemical solution deposition of functional oxide thin films", **9783211993**, 1–796 (2013).

[260]S. Hoffmann, U. Hasenkox, R. Waser, C. L. Jia, and K. Urban, "Chemical solution deposited $BaTiO_3$ and $SrTiO_3$ thin films with columnar microstructure", MRS Online Proceedings Library **474**, 9–14 (1997).

[261]T. Pečnik, A. Benčan, S. Glinšek, and B. Malič, "Tailoring the microstructure and dielectric properties of $Ba_{0.5}Sr_{0.5}TiO_3$ thin films by solution-based processing in the frame of the microstructural zone model", Journal of Alloys and Compounds **743**, 812–818 (2018).